NAWCWD TP 8811

Groundwater Resource Sustainability: Modeling Evaluation for the Naval Air Weapons Station, China Lake, California

Prepared by
David McGraw, Rosemary Carroll, Greg Pohll,
Jenny Chapman, Steve Bacon, and Richard Jasoni
Desert Research Institute
Nevada System of Higher Education
Reno, Nevada

SEPTEMBER 2016

NAVAL AIR WARFARE CENTER WEAPONS DIVISION
CHINA LAKE, CA 93555-6100

Naval Air Warfare Center Weapons Division

FOREWORD

This report documents the development of a calibrated transient groundwater model for the Indian Wells Valley, California, ground water basin. Under current rates, pumping exceeds basin yield by a factor of three to five. The result is a decline in groundwater levels, water quality degradation, and the possibility of land subsidence. A calibrated transient groundwater model is developed here to predict groundwater level changes in the future. A chemical transport model and subsidence model are linked to the transient flow model to provide insight into the water quality and subsidence effects of groundwater withdrawal. The report considers the long-term effects of water pumping in the Indian Wells Valley by using the model to consider future conditions as a result of current pumping rates continuing their trend into future years. Finally, results are presented of an Interferometric Synthetic Aperture Radar (InSAR) study that created 92 interferograms for the Indian Wells Valley as a means to measure surface deformation associated with ground subsidence.

The work upon which this report is based has been conducted as part of the Naval Air Warfare Center Weapons Division (NAWCWD) Range Sustainment Office's continuing efforts to define and mitigate potential mission encroachments. The work outlined in the report is intended to both help mitigate future impacts to the NAWCWD China Lake Research, Development, Test, and Evaluation (RDT&E) mission, and to also provide a tool to enable informed decisions as the Indian Wells Valley works toward the establishment of a Groundwater Sustainability Plan for the basin in accordance with the California Sustainable Groundwater Management Act.

This report has been reviewed by M. L. Boggs, Dr. A. E. Sabin, and CDR B. J. Longbottom, CEC.

Approved by
T. DOWD, *Director*
NAVAIR Ranges
21 September 2016

Under authority of
B. K. COREY
RDML, U.S. Navy
Commander

Released for publication by
J. L. JOHNSON
Director for Research and Engineering

NAWCWD Technical Publication 8811

Published by ..... Technical Communication Office
Collation ..... Cover, 113 leaves
First printing ..... 62 paper, 15 electronic media

REPORT DOCUMENTATION PAGE

Form Approved
OMB No. 0704-0188

1. REPORT DATE *(DD-MM-YYYY)*	**2. REPORT TYPE**	**3. DATES COVERED** *(From - To)*
21-09-2016	Final Evaluation Report	01-December-2013 – 16 August 2016

4. TITLE AND SUBTITLE

(U) Groundwater Resource Sustainability: Modeling Evaluation for the Naval Air Weapons Station, China Lake, California

5a. CONTRACT NUMBER
N/A

5b. GRANT NUMBER
N/A

5c. PROGRAM ELEMENT NUMBER
N/A

6. AUTHOR(S)
David McGraw, Rosemary Carroll, Greg Pohll, Jenny Chapman, Steve Bacon, and Richard Jasoni

5d. PROJECT NUMBER
N/A

5e. TASK NUMBER
N/A

5f. WORK UNIT NUMBER
N/A

7. PERFORMING ORGANIZATION NAME(S) AND ADDRESS(ES) AND ADDRESS(ES)

Desert Research Institute
Nevada System of Higher Education
2215 Raggio Parkway,
Reno, Nevada, 89512

8. PERFORMING ORGANIZATION REPORT NUMBER
50018

9. SPONSORING / MONITORING AGENCY NAME(S) AND ADDRESS(ES)
Naval Air Warfare Center Weapons Division
NAVAIR Ranges (Code 52000MD)
130 Easy Rd Stop 3002
China Lake, CA 93555-6109

10. SPONSOR/MONITOR'S ACRONYM(S)
N/A

11. SPONSOR/MONITOR'S REPORT NUMBER(S)
NAWCWD TP 8811

12. DISTRIBUTION / AVAILABILITY STATEMENT
DISTRIBUTION STATEMENT A: Approved for public release; distribution is unlimited.

13. SUPPLEMENTARY NOTES
The contents of this document are reproduced in facsimile.

14. ABSTRACT
This report documents the development of a calibrated transient groundwater model for the Indian Wells Valley, California, ground water basin. Under current rates, pumping exceeds basin yield by a factor of three to five. The result is a decline in groundwater levels, water quality degradation, and the possibility of land subsidence. A calibrated transient groundwater model is developed here to predict groundwater level changes in the future. A chemical transport model and subsidence model are linked to the transient flow model to provide insight into the water quality and subsidence effects of groundwater withdrawal. The report considers the long-term effects of water pumping in the Indian Wells Valley by using the model to consider future conditions as a result of current pumping rates continuing their trend into future years. Finally, results are presented of an Interferometric Synthetic Aperture Radar (InSAR) study that created 92 interferograms for the Indian Wells Valley as a means to measure surface deformation associated with ground subsidence.

15. SUBJECT TERMS
groundwater level; groundwater transient model; Indian Wells Valley, California, groundwater; Interferometric Synthetic Aperture Radar (InSAR); land subsidence; water quality

16. SECURITY CLASSIFICATION OF:			**17. LIMITATION OF ABSTRACT**	**18. NUMBER OF PAGES**	**19a. NAME OF RESPONSIBLE PERSON**
					M. L. Boggs
a. REPORT	**b. ABSTRACT**	**c. THIS PAGE**	SAR	212	**19b. TELEPHONE NUMBER** *(include area code)*
UNCLASSIFIED	UNCLASSIFIED	UNCLASSIFIED			760-939-4404

Respectfully submitted,
Desert Research Institute

David McGraw, M.S.
Assistant Research Scientist

Rosemary Carroll, Ph.D.
Assistant Research Professor

Greg Pohll, Ph.D.
Research Professor

Jenny Chapman, M.S.
Research Scientist

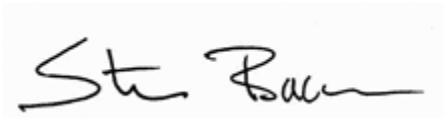

Steve Bacon, P.G., C.E.G.
Associate Research Scientist

Richard Jasoni, Ph.D.
Associate Research Scientist

EXECUTIVE SUMMARY

The Indian Wells Valley groundwater basin in California has been in overdraft since the 1960s. The primary consumption of groundwater is for municipal and agricultural uses. Under current rates, pumping exceeds basin yield by a factor of three to five. The result is a decline in groundwater levels, water quality degradation, and the possibility of land subsidence. A calibrated transient groundwater model is developed here to predict groundwater level changes in the future. A chemical transport model and subsidence model are linked to the transient flow model to provide insight into the water quality and subsidence effects of groundwater withdrawal.

The calibrated model is an update and improvement of an existing groundwater model. The most significant improvement is the better reproduction of observed drawdown rates in wells within the valley, which is achieved because of conceptual changes to the model and the use of a pilot-point calibration method. The changes include better quantification of mountain block recharge and playa evaporation rates, increased horizontal and vertical discretization of the original model, and allowing interbasin flow out of the model domain toward the east. Additionally, municipal, agricultural, and domestic pumping data were compiled, updated, corrected, and then added to a single database.

The model was calibrated to conditions observed before the beginning of significant pumping. Water levels in 1920 were used as the calibration objective function with horizontal hydraulic conductivity as the calibration parameter. Hydraulic conductivity was allowed to vary continuously throughout the model domain using the pilot-point approach. Good agreement was reached between simulated water levels and water levels observed during predevelopment conditions.

The steady-state model was used as the starting point for transient simulation of water level declines after the onset of significant pumping. This transient model incorporates the observed pumping rates in the basin. Storage parameters (specific yield and specific storage) were varied to calibrate the model to transient water levels for 1920 through 2010. The drawdown rate in selected monitoring wells was used as the objective function for calibration. The transient calibration methodology differs from that applied to previous transient models of Indian Wells Valley because the focus is on the drawdown rate rather than the absolute head, which aligns with the primary purpose of the model to predict drawdown in the future.

The transient calibration resulted in a much improved modeling tool for the prediction of drawdown throughout Indian Wells Valley (the previous model underpredicted drawdown in the city of Ridgecrest and overpredicted drawdown northeast of Ridgecrest). Three separate specific-yield zones with values ranging between 0.15 and 0.25 and a specific storage of 3×10^{-7} (1/ft) were found to yield the best agreement between simulated and observed groundwater hydrographs. Drawdown rates are predicted in the model with an average error of 0.3 ft/yr. Two alternative conceptual models of flow were evaluated to determine their effect on drawdown. The model of reduced recharge in the El Paso subbasin had a negligible effect, but the other conceptualization of hydraulic isolation between the shallow and deep aquifers had a significant effect that resulted in greater drawdown in the deep aquifer.

Volumetric groundwater flow rates from the flow model are linked directly to the solute transport model used to evaluate the effects of pumping on water quality. Total dissolved solids (TDS) are the measure of water quality in the transport model, which relies on 570 analyses of TDS for well water in the valley. The transport model is divided into two horizons, deep and shallow, and data density is sparse in

some areas, particularly in the deep horizon. This is addressed by inserting control points with interpolated TDS values that are consistent with the conceptual model for salinity distribution in the basin. Available time series salinity trends are replicated by the transport model, with increasing salinity simulated in areas adjacent to preexisting saline zones, located north and east of the municipal wells.

The flow model is also directly linked to a subsidence module to calculate compaction as a result of groundwater withdrawal. The subsidence model was calibrated to subsidence calculated from Interferometric Synthetic Aperture Radar (InSAR) observations of elevation changes in Indian Wells Valley over the last couple of decades. Although the model replicates the general magnitude of subsidence interpreted using InSAR (approximately one tenth of an inch per year), differences in spatial distribution suggest that the subsidence model lacks detail, particularly in terms of the properties and subsurface distribution of compressible fine-grained clay and silt deposits.

Most of the municipal supply wells are drilled relatively deep (hundreds of feet), but drawdown is a much nearer-term problem for domestic wells. A significant number of shallow domestic wells are at risk for serious functional problems or running dry within the next several decades based on the average domestic-well conditions of 78 feet (ft) of water above the bottom of the screen, which was reported by Todd Engineers (2014). The largest drawdown rate is forecast for the western side of the valley, north of the intersection of US 395 and State Highway 14. This region will experience decreases in water levels in excess of 20 ft within ten years (by 2025) and 50 ft within 25 years (by 2040) under status quo conditions.

Municipal wells in the eastern Ridgecrest area are likely to see increases in TDS of 200 mg/L over 85 years, which are higher than the forecasts for the NAWS wells because of Ridgecrest's proximity to shallow saline groundwater to the east.

(**NOTE**: The contents of this document are reproduced in facsimile.)

This page intentionally left blank.

CONTENTS

LIST OF FIGURES

LIST OF TABLES

LIST OF ACRONYMS

afy	Acre-feet per year
amsl	Above mean sea level
BBRM	Bootstrap brute-force recharge model
bgs	Below ground surface
CDWF	California Department of Fish and Wildlife
DHZ	Deep hydrogeologic zone
ET	Evapotranspiration
GCM	Global Climate Change Model
IHZ	Intermediate hydrogeologic zone
K	Hydraulic conductivity
Kx	Hydraulic conductivity horizontal ratio
Kz	Hydraulic conductivity vertical ratio
MAE	Mean absolute error
NAD	North American Datum
NAWS	Naval Air Weapons Station
PEST	Parameter Estimation Software
PET	Potential evapotranspiration
SHZ	Shallow hydrogeologic zone
Sfe	Elastic skeletal storage coefficient
Sfy	Inelastic skeletal storage coefficient
Ss	Specific storage
Sy	Specific yield
TDS	Total dissolved solids
USBR	United States Bureau of Reclamation
USGS	United States Geologic Survey
UTM	Universal Transverse Mercator

1.0 INTRODUCTION

Indian Wells Valley groundwater basin (Figure 1) is located in southeastern California on the western edge of the Basin and Range geologic province and it occupies portions of Inyo, Kern, and San Bernardino Counties. It is in the northwestern portion of the Mojave Desert, approximately 125 miles north of Los Angeles. Surface water resources in the region are minimal and all development relies on groundwater resources. Development in the valley includes the China Lake Naval Air Weapons Station (NAWS), the city of Ridgecrest, the communities of Inyokern and Pearsonville, and various rural residences. There is some agriculture in the region and crops consist primarily of alfalfa and pistachio orchards. The limitations of sustainable groundwater resources in the valley were recognized as early as 1912 (Lee, 1912). Overdraft of groundwater resources began in the 1960s (Dutcher and Moyle, 1973) when groundwater pumping began to exceed basin yield, which is defined as that proportion of groundwater that can be extracted without causing undesirable effects (Bachman *et al.*, 2005). Overdraft continues today and groundwater pumping is estimated to exceed basin yield by a factor of three to five. As a result, groundwater levels are chronically dropping and concerns about water quality are increasing (Todd Engineers, 2014). Overdraft severity is deemed "critical," which is defined by the California Department of Water Resources (1980) as being the "continuation of present water management practices would probably result in significant adverse overdraft-related environmental, social, or economic impacts" (Todd Engineers, 2014).

Municipal and agricultural water use accounts for 70 to 80 percent of total groundwater pumping. Recent agricultural expansion has increased alfalfa fields from 870 acres to 990 acres and pistachio orchards from 300 to 2,500 acres (Todd Engineers, 2014). Water use by pistachio crops is projected to increase agricultural water demand by approximately 70 percent by 2025, when these orchards reach maturity (Todd Engineers, 2014). Water budget estimates suggest an overdraft of approximately 16,500 acre-feet per year (afy) in 2013 (Todd Engineers, 2014) and water conservation or recycling alone cannot offset this. Instead, a variety of mitigation measures are under investigation by local and regional agencies, with increasing focus on restricting land use and importing water (Todd Engineers, 2014). An Indian Wells Valley Land Use Management Plan has been recently adopted by the Kern County Board of Supervisors (May 13, 2015) that will implement zoning changes to restrict the expansion of agricultural activities in the valley but preserve the current and historical activities.

1.1 PURPOSE

If implemented, land-use changes and water importation will only reverse overdraft problems many years in the future. However, there is an immediate need for reliable information to support decisions and, in some cases, related infrastructure changes to manage the ongoing overdraft problem and provide support for planning complex and costly future actions. Although much valuable hydrogeologic research has focused on Indian Wells Valley (e.g., Kunkel and Chase [1969]; Berenbrock and Martin [1991]; and Tetra Tech EM, Inc. [2003a,b]) and several numerical models of groundwater flow have been developed (Clark, 1999; Brown and Caldwell, 2006, 2009), there is no quantitative tool available that has the fidelity to provide the decision support required. Therefore, DRI's objective is to update the existing Brown and Caldwell (2009) groundwater model to serve NAWS by answering the following questions:

- When will NAWS wells require deepening under either status quo (baseline) or decreased agricultural pumping?

- What is the timeline for water quality degradation in NAWS wells given either baseline or decreased agricultural pumping?
- If the timeline for well deepening and/or degradation is relatively soon, what is the optimal placement of wells to buy extra time before more costly alternative measures are required?
- What are the spatial and temporal predictions of land subsidence, particularly within the NAWS facility?

An update to the preexisting model is required to more accurately reproduce observed water level drawdown and add water quality and subsidence calculation capabilities. This will produce more robust forecasts of future conditions to allow NAWS to make informed decisions and evaluate alternative pumping scenarios and optimize well locations. Specific updates to the Brown and Caldwell (2009) model include: better quantification of mountain block recharge and playa evaporation rates, increased groundwater grid resolution in the horizontal and vertical directions, refined model layering to better represent aquifer units, altered boundary conditions to honor the conceptualization of eastward flow toward Salt Wells Valley, and pilot-point hydraulic parameterization to improve calibrated response in water levels and drawdown rates. Alternative conceptual models are also considered, including reduced recharge in the El Paso Basin area and isolation of the deep and shallow aquifers by a low-permeability clay horizon. A solute transport model and a subsidence model are linked to the groundwater flow model, which allows simulations of groundwater salinity related to the movement of water from lower-water-quality areas of the basin and subsidence related to groundwater withdrawal.

This report presents a revised steady-state groundwater flow model, a transient calibration that was developed using observed water level declines, and an examination of the effects of several alternative conceptual models. The solute transport and subsidence models are also described. The questions above are addressed by examining the effects of alternative futures on water levels, salinity, and subsidence in the model forecasts.

2.0 STUDY AREA

2.1 PHYSIOGRAPHY

The Indian Wells Valley project area (outlined in blue in Figure 1) occupies the southwestern edge of the NAWS property. China Lake is located along the eastern edge of Indian Wells Valley. The groundwater model domain is the Indian Wells Valley alluvial basin, which encompasses approximately 460 mi^2. The full extent of the hydrographic basin is bounded by the Sierra Nevada Mountains to the west, the Coso Range to the north, the Argus Range to the east, and the El Paso Mountains to the south (Figure 2). The mountain slopes dip steeply to the valley floor that in turn slopes gently to China Lake, which is usually a dry playa. Mountains are primarily granite bedrock with the Coso Range composed of some volcanic deposits. Because of the impermeable bedrock complexes of the surrounding mountain systems, the larger hydrographic basin receives no significant groundwater from beyond the topographic divides of the hydrographic basin and is therefore considered "closed." Large alluvial fan complexes stemming primarily from the Sierra Nevada Mountains, and to a lesser degree from the other mountain ranges, allow groundwater flow into the basin as mountain block recharge. Elevations range from a maximum of 8,300 feet (ft) above mean sea level (amsl) in the Sierra Nevada Mountains to 2,136 ft amsl at the China Lake playa.

2.2 CLIMATE

Annual precipitation varies between 4 inches per year (in/yr) on the valley floor and approximately 20 in/yr in the Sierra Nevada Mountains, based on the 1981 through 2010 annual average precipitation data developed by the PRISM Climate Group at Oregon State University (PRISM Climate Group, 2012) (Figure 3). Annual precipitation in excess of 10 in/yr is also seen in the Coso and Argus Ranges. The precipitation data are produced on an 800 meter (m) grid, and then contoured within the Indian Wells Valley hydrographic basin. The total area of the Indian Wells Valley hydrographic basin is 1,292,380 acres. Total annual precipitation volume is 576,751 afy. Temperatures in the basin range from over 100 °F to below freezing, with snow in the mountains lasting several weeks.

3.0 HYDROGEOLOGY AND CONCEPTUAL FLOW MODEL

Indian Wells Valley lies on the westernmost edge of the Basin and Range Province. During the Pleistocene epoch (1.8 million to 12,000 years ago), the region was much wetter and basins that are currently isolated (e.g., Rose Valley, Owens Valley, Indian Wells Valley, Salt Wells Valley, and Searles Valley; Figures 1 and 2) were all connected via the Owens River. The active movement of alluvial fan material off the Sierra Nevada Mountains and the reworking of basin sediments by the Owens River resulted in a complex distribution of well-sorted and poorly sorted deposits in the basin. Structurally, Indian Wells Valley is a half-graben (Monastero *et al.*, 2002) with depositional history controlled by mountain-block faulting and down-dropped valley characteristics to depths between 2,000 and 3,000 ft.

3.1 PREVIOUS STUDIES

Although numerous studies have been conducted in the Indian Wells Valley basin over the last 60 years, five comprehensive studies of the region are described with respect to their effect on the modeling effort reported here. Berenbrock and Martin (1991) provide a comprehensive catalogue of all available data in terms of hydraulic properties and aquifer stresses. They also developed a numerical flow model of the site. Brown and Caldwell (2009) identified several limitations with this early modeling effort. Specifically, the system was simulated as a quasi-three-dimensional system in which the playa groundwater discharge zone and the underlying basin sediments were conceptualized as individual hydrologic units but connected via the bottom sediments of the playa to effectively model the system in two dimensions. Additionally, boundary conditions and stresses applied to the system, specifically basin recharge, playa discharge and predevelopment groundwater use, needed updating based on more contemporary estimates and data.

Hydrogeologic information has been greatly improved in the Indian Wells Valley basin since the early 1990s. The United States Bureau of Reclamation (USBR, 1993) drilled 10 deep wells (1,910 to 2,024 ft deep) on the western side of the basin and NAWS added a geothermal test hole (SNORT-1) to a depth of 7,394 ft with wells screened to depths of 880 ft and 1,470 ft below ground surface (bgs) in the boring. The SNORT-1 has helped more accurately delineate sediment characteristics in the down-dropped valley block. Although sediments are in excess of 7,000 ft thick, those below 2,000 ft bgs cannot store and transmit sufficient water for groundwater development (USBR, 1993; Berenbrock and Martin, 1991). Additionally, several wells that range in depth between 700 and 800 ft have been installed in the southwestern portion of the basin. Tetra Tech EM, Inc., (2003a,b) added to the knowledge of the site by collecting water quality data—including isotopic age dating—and analyzing the effects of faults on groundwater flow.

The Brown and Caldwell (2009) model was the most representative numerical model of the aquifer system in Indian Wells Valley prior to the initiation of this project. It has been used to successfully replicate some of the regional hydrogeologic features and explore overdraft conditions. The major limitation of the Brown and Caldwell (2009) model is that it cannot accurately reproduce drawdown rates, which is a requirement for the model to be used to support water-resource decision making. Specifically, the model underpredicts drawdown within the city of Ridgecrest but overpredicted northeast of Ridgecrest, which indicates a spatial and temporal model bias, and model errors generally increase over time. Additionally, the model is not configured to address land subsidence and water quality degradation, which are critical aspects of overdrafting that must be considered for successful system management. The Brown and Caldwell (2009) model serves as the template for ongoing modifications to allow a more comprehensive assessment of groundwater withdrawal on water level drawdown and degradation.

3.2 REGIONAL GEOLOGY

The depth of water-producing sediments is believed to be limited to the upper 2,000 ft in Indian Wells Valley. These sediments are primarily derived from the Sierra Nevada Mountains and include clays, silt, sand, and gravel deposits in alluvial fan, fluvial, and lacustrine environments. The Argus Range and El Paso Mountains are considered a secondary source of alluvial sediments. Lithologic units are taken from Berenbrock and Martin (1991) who based their work on units mapped by Von Huene (1960), Zbur (1963), and Kunkel and Chase (1969). Broadly speaking, units are divided into consolidated and unconsolidated rocks. Consolidated rocks are typically low in permeability and porosity unless they are highly fractured. These rocks include the tertiary igneous and metamorphic rocks in the surrounding mountains, as well as the Miocene basalts near the El Paso Mountains. For the purposes of this study, consolidated rocks are not considered to be water-bearing units. In contrast, unconsolidated rocks have the potential to transmit water and are divided into four hydrostratigraphic features that are important for analyzing water budgets and developing a hydrogeologic conceptual model. These unconsolidated units are mapped across the project site in Figure 4 as alluvium, lacustrine, playa, and sand dunes. Berenbrock and Martin (1991) describe these units as follows:

- Alluvium consists of moderately to well-sorted gravel, sand, silt, and clay of Pleistocene and Holocene age and is considered to have a high permeability. The percentage of silt and clay increases toward the central portion of China Lake, which reduces permeability. These deposits include both older and younger alluvial deposits, alluvial fans, and elevated pediment veneers and stream terrace deposits. Alluvium extends across Indian Wells Valley and is thickest along the western and southern edges of the basin.
- Lacustrine deposits were described by Kunkel and Chase (1969) as containing silt and silty clay of Pleistocene age and exhibiting low permeability. This unit lies above the alluvium and is interbedded with the alluvial deposits in the central portion of the basin. Figure 5 delineates the extent of clay lacustrine deposits.
- Playa deposits of low permeability are of Holocene age and contain silt and clay with an occasional sand lens.
- Sand dune deposits are of Holocene windblown sand and less than 100 ft thick (Warner, 1975). These sands occur above the water table and do not contain any water.

Cross sections (Figure 6) show the relationship between highly permeable alluvial gravel units at/near the land surface along the western and southern edges of the model domain, alluvial thickness, and the extent of low-permeability lake deposits.

Hydrostratigraphic units are mapped into two principal aquifer units, which were defined by Kunkel and Chase (1969) as the shallow and deep (or main) aquifers. The shallow aquifer extends from land surface through the sand dune deposits, younger lacustrine deposits, and shallow alluvium. Fine sand, silt, and clay comprise the shallow aquifer, which results in low permeability that can confine (or partly confine) the deeper aquifer. Additionally, water quality is generally poor in the shallow aquifer with total dissolved solids (TDS) greater than 1,000 mg/L (Warner, 1975; Berenbrock, 1987). The base of the shallow aquifer is not well defined, but Berenbrock and Martin (1991) estimate that it slopes from 1,950 ft amsl at its western edge to 1,850 ft amsl in the vicinity of China Lake.

The deep aquifer is likely under hydraulically confined conditions in the eastern portion of the basin because of silt and clay from the overlying lacustrine and playa deposits, but otherwise it is mostly unconfined. The medium-to-coarse sands and gravels have an estimated saturated thickness of 1,000 ft (Kunkel and Chase, 1969) and are the main source of water to Indian Wells Valley because they generally produce adequate flow rates and TDS is less than 1,000 mg/L (Warner, 1975).

Several faults are present in the basin, but studies in the region (Berenbrock and Martin, 1991; Tetra Tech EM, Inc., 2003; Brown and Caldwell, 2009) indicate that faults internal to the project domain do not exert control on groundwater flow. Instead, flow is more likely controlled by clay and/or silt deposits, primarily the extensive lakebed clay that separates the shallow aquifer from the primary aquifer below China Lake playa.

3.3 GROUNDWATER LEVELS AND FLOW DIRECTIONS

In the hydrogeologic conceptual model for Indian Wells Valley, the groundwater source is derived from snowmelt and mountain block recharge from the Sierra Nevada Mountains, as well as from Rose Valley and Coso Valley basins. Groundwater inflows also enter Indian Wells Valley basin from the El Paso subbasin. Previous studies have conceptualized that groundwater outflows occur because of groundwater pumping as well as discharge from the playa as evapotranspiration. Included in the updated steady-state analysis, groundwater flow is allowed to move downgradient to Searles Valley. This outflow was added in response to the lower than expected observed TDS concentrations and the need to export TDS downgradient.

3.4 GROUNDWATER LEVEL DATABASE

The water level database was updated and refined from Brown and Caldwell (2009). Each location was plotted and evaluated for quality assurance. If errors were obvious (e.g., misplaced decimal points or transposed digits), then the dataset was corrected or the observation was removed if it was determined to be redundant. An observation was deemed redundant only if there were other points nearby with water levels around the same time frame. There are over 1,200 wells with water levels and approximately 12,000 individual values.

A digitized contour map for 1920 was also added to this database. Observed water levels prior to 1926 are used to calibrate the steady-state model. Data from 259 well locations are available for groundwater levels in 1920 and an additional 20 groundwater levels were digitized from interpolated values generated by Brown and Caldwell (2009) (Figure 7).

3.5 GROUNDWATER BUDGET

3.5.1 Mountain Front Recharge

Mountain front recharge is the primary source of water in Indian Wells Valley. Other sources of groundwater recharge have been suggested, but many of these water sources were found to be insignificant in terms of the overall water budget. For example, fluid sources from deep geothermal upwelling (Bean, 1989), subsurface inflow from the Sierra Nevada bedrock (east of the topographic divide) (Todd Engineers, 2014), leakage from the Los Angeles Aqueduct (Todd Engineers, 2014), and wastewater pond percolation were postulated (Todd Engineers, 2014) but not accepted as significant sources of water. This analysis focuses solely on groundwater recharge derived from precipitation in the higher elevations. Other sources of water, such as the reinfiltration of agricultural and municipal pumping, are fairly well documented and can be handled by assuming net groundwater pumping.

Given the physiographic setting, precipitation-based recharge in the western portion of the basin (from the Sierra Nevada Mountains) is likely the dominant source of groundwater recharge in the area. Brown and Caldwell (2009) also noted groundwater inflow in the northwestern portion of the groundwater model that originated from precipitation-based recharge west of Rose Valley in the Sierra Nevada Mountains. Additional recharge may be derived from the Coso Range, Argus Range, and the El Paso Mountains. Analysis of mountain block recharge included a review of 14 previous studies and a two-dimensional model built to assess the volumetric inputs quantitatively. Some of the previous studies were purposely excluded from the analysis because the techniques were outdated (Lee, 1913; Thompson, 1929) or the hypothesis presented had subsequently been rejected by numerous researchers (Austin, 1988; Thyne *et al.*, 1999).

3.5.1.1 Past Recharge Estimates

To facilitate a review of the numerous groundwater recharge estimates, Indian Wells Valley was divided into six recharge zones, as shown in Figure 8. The recharge zones were designed to be consistent with previously established recharge zones and are generally consistent with subwatershed areas. Past studies have constrained recharge estimates by assuming recharge into Indian Wells Valley will equal discharge by evapotranspiration (prior to groundwater development).

Lee (1912) developed one of the first estimates of groundwater recharge by assuming that under predevelopment conditions the groundwater recharge equals discharge. Therefore, estimates of groundwater discharge help to quantify the amount of recharge. Although the estimate of 27,000 afy of groundwater recharge was too large because there was little data to support the evapotranspiration rates, Lee (1912) did highlight evapotranspiration (ET) as the main discharge mechanism within the valley. Lee (1912) also produced a detailed map of phreatophytes, as shown in Figure 9.

Kunkel and Chase (1969) used the Lee (1912) phreatophyte map and updated evapotranspiration rates to estimate the total discharge from the valley for 1912 and 1953. The discharge areas are associated with the China Lake playa and the surrounding vegetation. Kunkel and Chase (1969) estimated total groundwater discharge from evapotranspiration to be 11,000 and 8,000 afy for 1912 and 1953, respectively. The 1912 discharge estimate developed by Kunkel and Chase (1969) is commonly used as the estimate of basin recharge because little groundwater pumping occurred during this period, and therefore discharge should equal recharge. The ET rates used in the analysis are based on a depth-to-water versus ET rate that was developed by H.F. Blaney of the U.S. Department of

Agriculture (Kunkel and Chase, 1969). Although the relationship is reasonable, no site-specific data are presented to validate the approach. The ET rates developed by Kunkel and Chase (1969) for bare playa areas range between 0.3 and 0.7 feet per year (ft/yr) (generally 0.4 to 0.5 ft/yr), with the depth to water averaging 3 to 4 ft. For comparison, Tyler *et al*. (1997) estimated ET rates for Owens Lake, California—located approximately 60 miles to the north and under artesian conditions—to be between 0.29 and 0.34 ft/yr using eddy covariance techniques. Therefore, the ET estimates developed by Kunkel and Chase (1969) may be overestimated by 33 to 67 percent.

Although Dutcher and Moyle (1973), St. Amand (1986), and Berenbrock and Martin (1991) maintained the 11,000 afy recharge estimates of Kunkel and Chase (1969) without modification in their studies, Bloyd and Robson (1971) calibrated a groundwater flow model by reducing the groundwater recharge estimate from 11,000 to 9,850 afy. They also adjusted the spatial distribution of the recharge such that approximately 64 percent (6,235 afy) of the recharge originates from the Sierra Nevada Mountains, 32 percent (3,170 afy) from the Coso and Argus Ranges, and 4 percent (400 afy) from the El Paso Mountains to the south.

Bean (1989) developed detailed estimates of the spatial distribution of groundwater recharge using the Bloyd and Robson (1971) recharge estimate of 6,300 afy for the Sierra Nevada Range. They also determined that an additional 2,500 afy of recharge occurs from the Sierra Nevada west of the topographic divide, which is an assertion that since then has been largely disproven. The estimate of recharge from Rose Valley of 400 afy is based on a transmissivity of 18,000 gallons per day per foot, but the cross-sectional area and gradient are not provided. The estimate of 2,000 afy for the Coso Basin area appears to be taken directly from Thompson (1929). The estimate of 1,000 afy recharge for the Argus Range and 400 afy for the recharge from the El Paso range was taken from Bloyd and Robson (1971). Bean (1989) also included additional groundwater recharge from leakage from the Los Angeles Aqueduct (900 afy), leakage from the Indian Wells Valley Water District distribution system (500 afy), and wastewater pond percolation (1,000 afy). According to Bean (1989), the total groundwater recharge is 10,000 afy (which excludes the anthropogenic sources and flows from Sierra Nevada Mountains west of the topographic divide).

Berenbrock and Martin (1991) developed a three-dimensional groundwater flow model for the Indian Wells Valley that included recharge estimates. They assumed the total mountain-front recharge to be 9,900 afy, which was derived from Bloyd and Robson (1971). Berenbrock and Martin (1991) did change the spatial distribution of recharge for each mountain range based on the stream-drainage area above 4,500 ft in the Sierra Nevada Range and above 5,000 ft in the other mountain ranges. This yielded 6,300 afy, 3,200 afy, and 400 afy for the Sierra Nevada, Coso/Argus, and El Paso Ranges, respectively. The spatial and/or temporal distribution of recharge was not adjusted during model calibration.

Likewise, Watt (1993) used the Bloyd and Robson (1971) recharge total, but redistributed recharge based on the percentage of pinyon-juniper woodland area in each recharge watershed as a percentage of the total pinyon-juniper area in all the potential recharge watersheds. Based on this recharge distribution procedure, the annual recharge from the Coso and Argus Ranges is 1,000 afy and 8,900 afy for the Sierra Nevada Range.

Bauer (2002) conducted a localized study for Rose Valley and determined that 3,300 afy of groundwater exits Rose Valley into Indian Wells Valley. Bauer (2002) assumed that surface discharge from Little Lake infiltrates and ultimately flows into Indian Wells Valley as groundwater. Daniel B. Stephens (2011) developed a groundwater flow model of Rose Valley in support of Conditional Use Permit 2007-003 to extract water from two wells on the Coso Hay Ranch, LLC, property. The model was updated from a version that was created by MHA (2008) in support of a draft environmental impact review. The MHA (2008) model appeared to be essentially an updated model originally created by Brown and Caldwell (2006). Daniel B. Stephens (2011) also developed a watershed model to estimate groundwater recharge within Rose Valley. The watershed model yielded a groundwater recharge estimate of 4,500 afy from the Sierra Nevada, Argus, and Coso Ranges and focused recharge along surface water drainages within Rose Valley. Additional groundwater recharge (1,300 afy) was estimated from the transient groundwater model at South Haiwee Reservoir and downstream (outflow losses and irrigation return flows). Estimates of groundwater outflow from Rose Valley to Indian Wells Valley ranged between 3,500 and 3,900 afy with smaller outflows during years of increased agricultural pumping.

Anderson *et al*. (1992) developed a relationship between annual precipitation volume and groundwater recharge. The equation is given as:

$$\log Q_{rech} = 0.98 \log P - 1.40, where\ P > 8" \quad (1)$$

where Q_{rech} is groundwater recharge (afy) and P is the average annual precipitation (afy), but only for areas above 8 in/yr. Figure 10 shows the relationship developed by Anderson *et al*. (1992), including the data, regression, and uncertainty bounds. The Anderson *et al*. (1992) relationship was used to estimate groundwater recharge using the 1981 through 2010 average annual precipitation derived from the PRISM Climate Group (2012). Precipitation volumes were calculated by multiplying the area between precipitation contours (contour interval = 2 in/yr) by the mean precipitation. The entire Indian Wells Valley hydrographic basin was included in the analysis and the calculations are shown in Table 1. Using the estimated precipitation volume (129,861 afy) in the regression equation yields an estimate of groundwater recharge of 4,100 afy. The graphical relationship shown in Figure 10 was used to determine the upper and lower bounds of the recharge estimate (refer to blue lines in Figure 10), which are 700 afy and 15,000 afy, respectively.

Brown and Caldwell (2009) developed independent estimates of precipitation within Indian Wells Valley. They assumed that 15 percent of the precipitation above 4,500 ft yields groundwater recharge. Based on an empirical relationship developed for Owens Valley (Danskin, 1998), they assumed that elevations ranging from 4,500 to 6,500 ft have an average annual precipitation of 8 in/yr (decreased from 10 in/yr as determined from the Owens Valley study). Above 6,000 ft they predicted an annual average precipitation of 10 in/yr. The total area associated with precipitation above 8 in/yr was estimated to be 89,846 acres and total precipitation volume of 62,701 afy. Brown and Caldwell (2009) assumed that 15 percent of the precipitation becomes recharge, which results in approximately 9,400 afy. They also assumed an additional 1,500 afy of groundwater flow originating from the area to the northwest (including Rose and Coso Valleys). Their conceptual analysis of recharge yielded approximately 11,000 afy. During the model calibration process, they subsequently decreased the recharge by 2,100 afy for a total of 8,900 afy. The spatial distribution of recharge within the Brown and Caldwell (2009) model was 5,900 afy from the Sierra Nevada Mountains, 300 afy from the Coso Range, 1,600 afy from the

Table 1. Calculated precipitation volumes and groundwater recharge from the relationship developed by Anderson *et al*. (1992).

Precip Lower Bound (in)	Precip Upper Bound (ft)	Precip Centroid (in)	Precip Centroid (ft)	Area (m^2)	Area (acres)	Precip Vol (afy)
8	10	9	0.75	489,270,865	120,901	90,676
10	12	11	0.92	379,661,834	93,816	85,998
12	14	13	1.08	128,722,738	31,808	34,459
14	16	15	1.25	30,445,006	7,523	9,404
10	18	14	1.17	22,945,598	5,670	6,615
18	20	19	1.58	12,466,326	3,080	4,877
20	22	21	1.75	317,513	78	137
22	24	23	1.92	-	-	
				Total:	133,147	129,861

Best Estimate	Recharge:	4,085
Lower bound	Recharge:	700
Upper bound	Recharge:	15,000

Argus Range, 50 afy from the El Paso Mountains, and 1,000 afy from Rose Valley. It is not clear how Brown and Caldwell (2009) developed the interbasin flow estimate from Rose Valley. In their earlier model, Brown and Caldwell (2006) estimated approximately 2,100 afy of groundwater flow from southern Rose Valley to Indian Wells Valley.

It is noted that Brown and Caldwell (2009) also used the relationship developed by Anderson *et al*. (1992) to develop a secondary estimate of recharge in Indian Wells Valley. Although the equation states that the precipitation volume should be calculated for areas with annual precipitation in excess of 8 in/yr, Brown and Caldwell (2009) performed the calculation with precipitation in excess of 10 in/yr for elevations above 6,000 ft, which resulted in a recharge estimate of 420 afy. The equation developed by Anderson *et al*. (1992) was used to recalculate the recharge using precipitation in excess of 8 in/yr, which resulted in a recharge estimate of 4,100 afy and a 95 percent confidence interval that ranged from 700 to 15,000 afy.

Todd Engineers (2014) reviewed numerous hydrogeologic reports and developed a detailed summary of groundwater recharge estimates as well their own estimates, which were primarily based on expert judgment and the reliability of the previous studies. They developed a range of estimates for total groundwater recharge from 7,700 to 11,000 afy with most of the uncertainty coming from the Sierra Nevada recharge (3,100 to 5,900 afy). Their estimates for recharge from the Coso Range, Argus Range, and El Paso Mountains are 300 afy, 1,600 afy, and 50 afy, respectively. They also assumed 1,600 afy to 2,100 afy of deep percolation from agricultural irrigation (originally derived from groundwater pumping).

Todd Engineers (2014) assumed additional recharge occurred from leakage from the Indian Wells Valley Water District distribution system in the amount of 80 afy. Their estimates of total recharge range between 6,100 and 8,900 afy with an average of 7,500 afy, not including the irrigation excess (which is derived from groundwater pumping) and water distribution leakage.

Todd Engineers (2014) provided detailed arguments against the larger Bauer (2002) estimates of groundwater flow from Rose Valley and determined that the 1,000 afy estimate used by Brown and Caldwell (2009) was more appropriate. They suggested that Bauer (2002) used measured discharge below Little Lake during unusually wet years (1997 and 1998), took measurements during the winter that were extrapolated to the rest of the year, omitted the smallest measurement when calculating the average, and did not describe the stream gauging method. Additionally, one of the measurements appears to be anomalous. Todd Engineers (2014) did not reference the modeling studies of Brown and Caldwell (2006) or Daniel B. Stephens (2011) that yield estimates of 2,100 afy and 3,700 afy, respectively, from Rose Valley.

3.5.1.2 Updated Recharge Estimate

Total recharge and its spatial distribution in Indian Wells Valley are updated using an empirical relationship between precipitation and natural groundwater recharge originally developed for Nevada basins. The first of such models was established in Water Resource Bulletin No. 8 (Maxey and Eakin, 1949) and remains a common technique for estimating recharge in Nevada today. Updated, daughter techniques—such as the Nichols method (2000) and Epstein *et al*. (2010) bootstrap brute-force recharge model (BBRM)—are also available. The Nichols (2000) method generally yields erroneously large recharge estimates, and therefore is not used in this analysis. The Maxey and Eakin (1949) method relies on the Nevada-specific precipitation map, and therefore cannot be used in the California basin of Indian Wells Valley.

The Maxey-Eakin (1949), Nichols (2000), and BBRM are simple, additive linear models that can rapidly estimate the quantity of water recharging aquifer storage at the basin scale. These models lump many physical processes into one set of coefficients. Mathematically, the empirical model of Epstein *et al*. (2010) is given as:

$$Y = \sum_{i=1}^{N} \beta_i P_i, \tag{2}$$

where N is the number of precipitation zones, Y is predicted recharge (afy), β_i is the recharge coefficient (dimensionless) for a given precipitation zone (i), and P_i is the annual zonal precipitation estimate (afy).

The BBRM is an optimized algorithm developed to calibrate empirical models by incorporating measurement error in precipitation, recharge variability, and regression model uncertainty (Epstein *et al*., 2010). The BBRM relies on the PRISM precipitation map (PRISM Climate Group, 2012). Although the PRISM map covers the entire United States, the BBRM is calibrated to ninety Nevada hydrographic areas with independently derived recharge estimates. The resulting β-coefficient means, standard deviations, and 95 percent confidence intervals are provided in Table 2. In a comparison of the BBRM with Maxey-Eakin (1949) and Nichols (2000) within Nevada basins, the Maxey-Eakin (1949) was found to produce the lowest error for basins with low-expected recharge, but the mean behavior of the BBRM was capable of explaining the highest percentage of recharge variability. The BBRM β confidence intervals were found to increase substantially for basins with large precipitation rates.

Table 2. BBMR β-coefficients and descriptive statistics for individual precipitation zones (modified from Epstein *et al*. [2010])

	β_i			
P_i	mean	st.dev.	LCI[a]	UCI[b]
<10	0.019	0.011	0.000	0.041
10<=p<20	0.049	0.012	0.029	0.074
20<=p<30	0.195	0.129	0.040	0.482
p>=30	0.629	0.278	0.127	0.999

[a]95 percent lower confidence interval

[b]95 percent upper confidence interval

Using the BBRM approach, recharge calculations for Indian Wells Valley recharge are shown in Table 3. The analysis assumes that the transference of Nevada empirically derived β terms is appropriate for these eastern California basins. Additionally, PRISM maps associated with the 30-year average annual precipitation from 1981 through 2010 at the 800 m resolution are used to define zonal precipitation for all empirical models despite not being used directly in the derivation of the β-coefficients. Two separate calculations are performed: (1) groundwater recharge is excluded from the basin floor where precipitation is less than 8 in/yr and (2) groundwater recharge occurs over all precipitation zones. The range in calculated recharge is 9,300 afy to 29,000 afy, depending on the assumptions used. The BBRM lower 95 percent confidence interval becomes 5,800 afy to 12,000 afy, depending on the exclusion or inclusion of precipitation zones less than 8 in/yr.

Table 3. Calculated precipitation volumes and groundwater recharge from the relationship developed by Epstein *et al*. (2010).

Precip Lower Bound (in)	**Precip Upper Bound (in)**	**Precip Centroid (in)**	**Precip Centroid (ft)**	**Area (acres)**	**Precip Vol (afy)**	**Rech Coef**	**Recharge (afy)**
0	8	4	0.33	1,029,502	343,167	0.019	19,561
8	10	9	0.75	120,901	90,676	0.019	2,297
10	12	11	0.92	93,816	85,998	0.049	4,597
12	14	13	1.08	31,808	34,459	0.049	1,559
14	16	15	1.25	7,523	9,404	0.049	369
16	18	17	1.42	5,670	8,032	0.049	278
18	20	19	1.58	3,080	4,877	0.049	151
20	22	21	1.75	78	137	0.195	15
			Total:	**1,292,380**	**576,751**		**28,826**
			Total w/out < 8":	**262,878**	**233,584**		**9,265**

Subwatersheds were also investigated individually to assess spatial distribution, but only for the scenario in which recharge does not occur along the basin floor (i.e., p<8 in/yr). Specifically, the Sierra Nevada Range is calculated to generate 5,200 afy, the Coso/Argus Ranges to generate 4,100 afy, and the El Paso Mountains produce no mountain block recharge. Excluding p<8 in/yr yields a total annual recharge equal to 4 percent of total annual precipitation.

In addition to using the BBRM, a two-dimensional model was used to further assess the total groundwater recharge into Indian Wells Valley and refine its spatial distribution. The purpose of the model was to adjust the magnitude and spatial distribution of recharge until there was a general agreement between the simulated and measured predevelopment (1920 to 1921) water levels. A MODFLOW (Harbaugh, 2005) model was constructed with an active area identical to the active area developed by Brown and Caldwell (2009) (see the model domain in Figure 2). The model was simulated with a constant saturated thickness and transmissivity distribution, which was presented in Dutcher and Moyle (1973, Plate 4). The transmissivity map (Figure 11) developed by Dutcher and Moyle (1973) is based on local aquifer tests (McClelland, 1964), driller's logs, and selected specific capacity tests that were converted to transmissivity using a simple regression equation.

The boundary conditions for the model included mountain block recharge, groundwater evapotranspiration (ET), and outflow toward Searles Valley. Four recharge zones were used to facilitate the calibration process. The recharge zones included Sierra Nevada South, Sierra Nevada North, Rose Valley, and the combined Coso and Argus Ranges (see Figure 8). The El Paso Range was assumed to have no significant groundwater recharge. Discharge by ET was simulated for all of the ET discharge zones shown in Figure 9, but for simplicity, a single depth to water versus ET relationship was used. The depth to water versus annual ET rate relationship for the 25 percent vegetative cover derived by Kunkel and Chase (1969) was used to parameterize the segmented ET package within MODFLOW (Figure 12). A specified head boundary condition was used to simulate potential groundwater outflow to Salt Wells Valley (Figure 13).

A trial-and-error calibration procedure was performed by adjusting the magnitude of the groundwater recharge for each of the four recharge zones until there was a general agreement between the simulated and measured 1920 to 1921 water levels. These water level measurements were obtained digitally from the Brown and Caldwell (2009) groundwater model, but were originally published in Dutcher and Moyle (1973, Plate 2). The calibration of the groundwater model yielded groundwater recharge of 1,500 afy, 2,100 afy, 2,400 afy, and 1,200 afy for the Sierra Nevada South, Sierra Nevada North, Rose Valley, and Coso/Argus recharge areas, respectively. Total groundwater recharge within Indian Wells Valley determined in this manner is 7,100 afy. The model has a mean absolute error (MAE) of 6.6 m and a relative error of approximately 3 percent. The largest errors (both positive and negative) are found in the El Paso subbasin. These errors might be caused by the southern Sierra Nevada recharge zone being applied over a large area, even though recharge might be focused around the large surface-water drainage feature located at the northern portion of this recharge zone.

3.5.1.3 Recharge Summary

Table 4 summarizes the groundwater recharge estimates for the various studies. Excluding anthropogenic recharge sources, the range in the total estimate from all mountain sources is 4,100 to 11,000 afy. Four of the studies produced confidence intervals ranging from 700 to 15,000 afy. The mean

Table 4. Summary of recharge estimates for Indian Wells Valley.

MOUNTAIN BLOCK RECHARGE									
SIERRA NEVADA									
Source	**South (afy)**	**North (afy)**	**Rose Valley (afy)**	**Coso (afy)**	**Argus (afy)**	**El Paso (afy)**	**Total (afy)**	**Total Lower Bound (afy)**	**Total Upper Bound (afy)**
Kunkel and Chase, 1969								11,000	15,000
Bloyd and Robson, 1971	6,200		45	3,200		400	9,800		
Dutcher and Moyle, 1973							11,000		
St. Amand, 1986							11,000		
Bean, 1989	6,300		400	2,000	1,000	400	10,000[1]		
Berenbrock and Martin, 1991	6,300			3,200		400	9,900		
Watt, 1993	8,900			1,000			9,900		
Bauer, 2002			3,300						
Daniel B. Stephens, 2011			3,700[3]						
Brown and Caldwell, 2006			2,100						
Brown and Caldwell, 2009	5,900		1,000	300	1,600	50	8,900		
Anderson *et al*., 1992							4,100	700	15,000
Todd Engineers, 2014	3,100 - 5,900		1,000	300	1,600	50	7,500[4]	6,100	8,900
Epstein *et al*., 2010	5,200				4,100		9,300	5,800	12,000
Numerical Analysis	1,500	2,100	2,400	1,200			7,100		
Best Estimate	1,500	2,100	2,400	1,600		50	7,700		

Notes:

1. Total does not include the additional 2,500 afy from the Sierra Nevada Range west of the topographic divide and anthropogenic sources (2,400 afy).
2. All numbers are rounded to two significant figures.
3. Midpoint of range provided (3,500-3,900 afy).
4. Assumes midpoint for Sierra Nevada North and South recharge and excludes their estimates of recharge from excess irrigation and Indian Wells Valley water distribution leakage.

mountain block recharge from all studies is 8,900 afy. The mean recharge estimate from the Sierra Nevada South and Sierra Nevada North zones is 5,900 afy. The mean recharge estimate for Rose Valley is 1,800 afy. Combining the Coso and Argus Ranges, the mean recharge estimate is 2,400 afy. The mean recharge estimate for the El Paso Mountains is 260 afy.

Three of the four recharge estimates (Berenbrock and Martin, 1991; Brown and Caldwell, 2009; and Epstein *et al*., 2010) are in general agreement with recharge volumes ranging between 9,300 and 11,000 afy. The Anderson *et al*. (1992) regression equation yielded the smallest estimate at 4,100 afy, but the other three estimates are within the confidence interval of the Anderson (1992) method. There is less agreement on the partitioning of the recharge among the three subareas. Using the groundwater model developed for this study as the primary basis for the spatial distribution of recharge, the best estimates are 1,500 afy, 2,100 afy, 2,400 afy, and 1,600 afy for the Sierra Nevada North, Sierra Nevada South, Rose

Valley, and Coso/Argus Ranges, respectively. The addition of 50 afy from the El Paso Mountains is added from estimates presented by Brown and Caldwell (2009) and Todd Engineers (2014). The total volume of mountain block recharge is 7,700 afy.

According to Todd Engineers (2014), wastewater from the treatment plant evaporates and then percolates into the shallow groundwater system. Because thick clay layers separate the shallow aquifer from the principal aquifer between the wastewater treatment plant and China Lake playa, essentially none of the percolated water contributes to the yield of the principal aquifer (Todd Engineers, 2014). Additional groundwater recharge in the amount of 80 afy can be attributed to leakage from the Indian Wells Valley Water District distribution system. Other sources—such as the reinfiltration of water pumped for agricultural and municipal use—can be handled by assuming net groundwater pumping, and therefore do not need to be directly considered in the groundwater recharge budget.

3.5.2 Groundwater Pumping

The steady-state groundwater model was calibrated to water levels measured in 1920. Although a small amount of domestic groundwater pumping may have occurred prior to 1920 (<1,000 afy), the steady-state model assumes no significant groundwater pumping.

3.5.2.1 Groundwater Pumping Database 1920 to 2025

As part of project objectives, a groundwater pumping database was developed to represent historical (1920 through 2013) pumping and future pumping projections (2014 through 2025). Each historical pumping well was evaluated and assigned to a category: private domestic, Searles Valley Minerals, municipal, NAWS, or agricultural. Individual wells were then verified using existing databases from Brown and Caldwell (2009) and aerial photographs. Historical pumping totals for each category were digitized from Todd Engineers (2014, Figure 9) based on the United States Geologic Survey (USGS) estimates of historical pumping from 1920 to 1974 and the Indian Wells Valley Water District rates from 1975 to 2013. Water use for 2013 is estimated to be approximately 23,700 afy (Todd Engineers, 2014), with the Indian Wells Valley Water District, Inyokern CSD, and alfalfa using approximately 67 percent of this total. Within each category, historical data for individual wells are used if available. If historical data for individual wells are not available, then nonagricultural pumping totals are divided evenly among the appropriate wells.

Agricultural wells are assigned rates according to the well's corresponding agricultural use (alfalfa or pistachios) and the rates for each agricultural type reported by Todd Engineers (2014). Agricultural use is calculated based on cropland identified in a Geographic Information System maintained by NAWS and it is current as of 2014. A total of 989 acres is assigned as alfalfa and 3,283 acres as pistachios (including acreage identified as under development). These acreages differ somewhat from the 2013 estimates of Todd Engineers (990 for alfalfa and 2,500 for pistachios) and also from those in the Kern County planning EIR report (1,467 for alfalfa and 3,322 for pistachios, which also include acreage under development).

Agricultural groundwater pumping rates are based on plant consumptive needs, improved technology, and irrigation inefficiency (e.g., spray evaporation and deep percolation). Applied water to alfalfa ranges between 7 and 11 ft/yr (i.e., afy/acre = ft/yr) and the value of 8 ft/yr is used for groundwater pumping. In the first year, pistachio seedlings use 0.25 ft/yr. After 12 years, they reach maturity and consume approximately 5 ft/yr. It is assumed that the increase is linear from year 1 to year 12, and then maintains at 5 ft/yr. The estimated potential groundwater pumping by 2025 is 35,000 afy, which is consistent with the estimates by Todd Engineers (2014).

3.5.3 Evapotranspiration

Evapotranspiration (ET) from the playa is the principal predevelopment groundwater outflow from Indian Wells Valley. Assuming steady-state conditions prior to significant groundwater pumping requires that groundwater outflows equal groundwater inflows. Therefore, ET losses combined with interbasin groundwater outflow to Searles Valley must equal mountain block recharge inflows of 7,650 afy. Adjusting for interbasin groundwater outflow (~200 afy) establishes an ET loss of 7,450 afy during predevelopment groundwater conditions.

Kunkel and Chase (1969) developed estimates of ET using the spatial extent of ET zones from Lee (1912) and multiplying these areas by predefined ET rates for each zone. A relationship between ET rate and depth to water for various plant cover percentages was developed based on the suggestions of H.F. Blaney, a well-respected irrigation engineer with the Department of Agriculture. The analysis yielded ET estimates of 11,000 and 8,000 afy for 1912 and 1953, respectively.

Berenbrock and Martin (1991) developed estimates of ET using techniques similar to Kunkel and Chase (1969). The ET zones and associated rates were dependent on the vegetation cover (e.g., free-standing water versus salt grass versus moist soil) and the maximum rate was 1.5 ft/yr. Their initial estimate assumed 9,850 afy of ET in 1920.

Additional vegetation mapping was done to determine if vegetation changes have occurred since the 1912 survey. The principle dataset used for the delineation of vegetation presented here is from the 2013 California vegetation map of the Mojave Desert region by Menke *et al*. (2013). This dataset consists of high-resolution vegetation classification in support of the desert renewable energy conservation plan of the California Department of Fish and Wildlife (CDWF). Vegetation mapping was performed between 2011 and 2012 and followed Federal Geographic Data Committee and National Vegetation Classification Standards. The classification was based on a combination of previous survey and classification work, along with the application of expert-based, on-screen digitizing techniques in ArcGIS using the true-color, color-infrared 2010 one-meter National Agricultural Imagery Program imagery in conjunction with ancillary data and imagery sources. Office-based mapping was followed by field verification and map accuracy assessments. Attributes of vegetation map polygons include vegetation type, percent cover, exotics, development disturbance, and other attributes (Figure 1). The attributes for percent cover are coded with numeric values to represent ranges of percent cover class.

The mapping was restricted to the phreatophyte zones defined by Lee (1912). The CDWF vegetation survey did not cover all of the previously defined phreatophyte area, so a portion of the geomorphic map of China Lake Basin from Bacon *et al*. (2015) in Bullard *et al*. (2015) was used to map vegetation in the areas that were not covered within the phreatophyte boundary.

The geomorphic map of China Lake Basin was mapped at scales between 1:2,000 and 1:5,000 during two phases in 2012 and 2014 using color imagery and principle component analysis of high-albedo areas, such as playa surfaces with bare ground. Because desert regions typically have distinctive vegetation patterns and associations that reflect soil-geomorphic landscape position (e.g., Michaud *et al*. [2013]), the boundaries of the geomorphic units were used with a high-degree of confidence to map vegetation by correlating to adjacent CDWF vegetation map units. Vegetation map correlations were broadly confirmed by visual inspection with the use of color imagery acquired in May 2010.

The resulting vegetation map is shown in Figure 15. The classification of vegetation-type and bare ground in addition to percent cover from this analysis can be considered a relatively high-resolution assessment of the distribution of vegetation and bare ground at the time of acquired imagery and subsequent field verification between 2010 and 2014.

A detailed comparison of the Lee (1912) vegetation map (Figure 9) and the map shown in Figure 15 suggests that the major difference is the addition of greasewood along the west/northeast boundary and a small section in the southwest. These areas are highlighted with light-brown polygons in Figure 15. The areas currently covered with greasewood previously contained pickleweed and saltgrass. Root depths of pickleweed and saltgrass are typically limited to 10 ft or less (Kunkel and Chase, 1969). Maximum rooting depth of greasewood has been reported at various sites ranging from 15 to 20 ft (Meinzer, 1927; ICWD/LADWP, 1989; Donovan *et al*., 1996; Chimner and Cooper, 2004), with one report of a maximum depth of 57 ft (Meinzer, 1927).

Two vegetation zones were used to simulate the depth to water versus ET in the groundwater model. The first zone represents the larger zone, which consists primarily of bare soil (playa), pickleweed, and saltgrass. This area is represented by all vegetation types outside of the greasewood unit. The maximum ET rate for this zone is 0.48 m/day (5.7 ft/yr) and ET terminates when the water table is greater than 3 m (10 ft) bgs. The second zone represents the greasewood unit shown in Figure 15 with a maximum ET rate of 0.002 m/day (2.4 ft/yr) and maximum rooting depth of 10 m (33 ft). Both vegetation units used a nonlinear functional shape between depth to water and ET rate, as shown in Figure 12.

An eddy covariance station was installed at the south end of China Lake playa in September 2014 to provide site-specific data for transient model calibration. Eddy fluxes of latent energy were calculated as the covariance between turbulent fluctuations of the vertical wind speed and water vapor density derived from Reynolds (block) averaging of 30-minute blocks of data. The sonic anemometer's coordinate system was numerically rotated during each averaging period by applying a double rotation, aligning the longitudinal wind component into the main wind direction, and forcing the mean vertical wind speed to zero (Kaimal and Finnigan, 1994; Wohlfahrt *et al.*, 2008). Frequency response corrections were applied to raw eddy fluxes to account for low-pass (lateral and longitudinal sensor separation, sensor time response, and scalar and vector path averaging) and high-pass (block averaging) filtering (Massman, 2000, 2001) using a site-specific, cospectral reference model (Massman and Clement, 2004; Wohlfahrt *et al*., 2005). Experimentally derived frequency response correction factors (Aubinet *et al*., 2000, 2001) were used to assess the validity of the theoretical low-pass filtering correction method detailed in Wohlfahrt *et al*. (2005). Finally, fluxes were corrected for the effect of air density fluctuations in accordance with Webb *et al*. (1980).

Half-hourly flux data were quality controlled in a five-step filtering procedure. First, periods were identified when the eddy covariance system was not working properly because of adverse environmental conditions (usually rain) or instrument malfunction. Second, half-hourly values that were comprised of less than 93 percent of the full complement of measured tenth-of-a-second values (full complement = 18,000 values) were removed. Third, data were subjected to the integral turbulence test (Foken and Wichura, 1996) and accepted only on the condition that they did not exceed the target value (Foken *et al*., 2004) by more than 60 percent (Wohlfahrt *et al*., 2008). Fourth, data were subjected to the angle of attack test (beta, β, the angle between the wind vector and horizontal), which identifies errors in data resulting from the imperfect cosine response of sonic anemometers. Data were excluded when the angle of attack was greater than 20º (Geissbühler *et al*., 2000; Gash and Dolman, 2003). Finally, data were excluded

when the automatic gain control (AGC) of the infrared gas analyzer (IRGA) was greater than 10 percent of the specific baseline value for each instrument. Increases from baseline AGC typically result from rain, snow, or ice accumulation on the surface of the lens of the IRGA and result in errors in water vapor density values.

Data gaps (30-minute time steps; both daytime and nighttime values) for each site, resulting from filtered or missing data, were filled using a site-specific regression equation of ET versus net radiation. Gap filling using a site-specific regression using net radiation is a conservative approach compared with other gap filling methods, such as linear interpolation or the mean diurnal variation method with a time window of one month (Falge *et al*., 2001). These methods tend to result in overestimation of nighttime ET. Monthly ET values were calculated for months in which measurements were not taken. Monthly ET was calculated using the ratio of ET for months with measured ET values to potential evapotranspiration (PET) for months without measured ET. Gap filling methods were also used when precipitation fell to ensure that the ET measurements were representative of groundwater ET.

Systematic uncertainty of ET estimates derive primarily from the collective effects of inherent instrument measurement errors on the large density corrections (Webb *et al.*, 1980; Webb, Pearman, and Leuning Correction [WPL]) that need to be applied to half-hourly ET values when measuring with open-path sensors under conditions of large sensible heat exchange (Wohlfahrt *et al.*, 2008). Uncertainty introduced by applying the WPL correction under the range of inherent measurement errors for each instrument (sensor) was estimated by defining a likely relative uncertainty for each independent parameter (instrument measurement), and then applying this uncertainty to calculate annual ET. Assuming that the various component uncertainties are independent, the combined uncertainty from the WPL correction was calculated by taking the square root of the sum of the squared individual uncertainties. Based on past experience with long-term sensor stability and the manufacturer's specifications, the water vapor density and static air pressure were assigned uncertainties of 10 percent (Wohlfahrt *et al*., 2008) and air temperature was assigned an uncertainty of 2 percent. Uncertainty in the sensible heat flux may arise because the sensible heat flux was measured based on speed-of-sound measurements, which has been shown by Loescher *et al*. (2005) to deviate from sensible heat flux derived from measurements of air temperature using a fast-response platinum resistance thermometer by up to 10 percent for this specific sonic anemometer model.

Alternatively, Ham and Heilman (2003)—again for the same anemometer model used in this study—found extremely close correspondence between sonic- and thermocouple-derived sensible heat flux measurements. Additional uncertainty of the sensible heat flux arises from the choice of coordinate system (Lee *et al*., 2004) and from the necessary (small) frequency response corrections (Massman, 2001). Based on the research findings presented above and some preliminary sensitivity tests with different coordinate systems, a 5 percent uncertainty for the sensible heat flux was assumed. Similar to the sensible heat flux, a 5 percent uncertainty for latent heat flux was assumed to reflect uncertainties based on the choice of the coordinate system and frequency response corrections, which are based on a site-specific cospectral reference model (Massman and Clement, 2004; Wohlfahrt *et al*., 2005) and have been validated against the experimentally derived frequency response correction factors following Aubinet *et al*. (2000) and Aubinet *et al.* (2001) that were described in Wohlfahrt *et al*. (2005) and Wohlfahrt *et al.* (2008). Based on this information, 5 percent uncertainty is justified and not nearly as large as the upper range of potential errors in frequency response correction factors (30 percent) reported by Massman and Clement (2004).

The area of interest footprint was calculated using the footprint model of Hsieh *et al.* (2000) to estimate the upwind distance and compass direction that represented 90 percent of the surface flux for each half-hour period ($X_{90\%}$). Close agreement between modeled and measured data from arid and agricultural areas has shown the model to be valid and provides reliable footprint data (Hsieh *et al.*, 2000).

$$X_{90\%} = \frac{-D\,|L|^{(1-P)}\,Z_u^P}{k^2 \ln(0.90)} \quad \textbf{Error! Bookmark not defined.} \tag{3}$$

where k is the von Karman constant (0.4), L is the Obukhov length, and Z_u is the length scale calculated as:

$$Z_u = \frac{Z_m\,u\,k}{u_*} \tag{4}$$

where Z_m is the measurement height, u is the mean wind speed, and D and P are stability-dependent coefficients:

D = 0.28; P = 0.59 for unstable conditions ($Z_u/L < -0.04$)

D = 0.97; P = 1.00 for near-neutral conditions ($-0.04 < Z_u/L < 0.04$)

D = 2.44; P = 1.33 for stable conditions ($Z_u/L > 0.04$)

Each calculated point, or footprint distance and direction (that corresponds to an individual 30-minute ET value), was then plotted in ArcGIS and a polygon circumscribed on the outside of the collective set of points within the area of interest (predefined as the phreatophyte area shown in Figure 15). Evapotranspiration for the area of interest was then calculated using ET values that were within the polygon, and therefore represent ET only from the area of interest. Evapotranspiration values that were removed during this process were gap filled using the gap-filling method previously described. Given the station location, most of the ET measurements were representative of the bare playa zone, which is shown in Figure 15.

Estimated monthly ET rates are shown in Table 5. Monthly ET rates range between 0.1 and 0.7 inches with largest rates in winter months. Although ET estimates on rainy days were removed, ET continues for a few days following a precipitation event. Therefore, groundwater ET estimates during the significant periods of precipitation could be overestimated. Annual ET is estimated to be 4.5 inches. Annual groundwater ET could be as low as 2.4 inches if elevated ET measurements are removed for a longer period after precipitation events. It is difficult to convert the ET rates into volumetric rates over the entire phreatophyte zone. The eddy covariance measurements are primarily representative of bare playa. Extrapolating to other areas with higher vegetation density and spatially variable water levels would be speculative at best.

Table 5. Monthly ET and precipitation.

Month/year	ET (in)	Precipitation (in)
October 2014	0.20	0.00
November 2014	0.13	0.01
December 2014	0.50	1.23
January 2015	0.54	1.35
February 2015	0.67	0.92
March 2015	0.57	0.09
April 2015	0.43	0.02
May 2015	0.38	0.01
June 2015	0.29	0.00
July 2015[1]	0.30	n/a
August 2015[1]	0.28	n/a
September 2015[1]	0.22	n/a
Total:	**4.53**	**3.63**

Notes: 1) July, August, and September months were estimated based on the ratio of ET for months with measured ET values to PET for months without measured ET.

The ET rates are assumed to be a function of water table depth. Kunkel and Chase (1969) determined that ET declined from 11,000 to 8,000 afy between 1912 and 1953, largely because of declining water levels. With significant groundwater development between 1953 and the present, increased water table depths within the phreatophyte zone and associated decreases in ET discharge might be expected. Water level measurements were available over this period for three wells located in the phreatophyte zone, which is shown in Figure 16. Figure 17 shows the hydrographs for these three wells. Water levels have actually increased approximately 2 to 3 ft from 1950 through 2000.

Although water levels are not available over the period in which the eddy covariance data were collected, if it is assumed that water levels are approximately 7 to 8 ft bgs, then the measured ET rates are in general agreement with the relationship between depth to water and ET rate (see Figure 12). The ET rates are estimated to be 0.2 ft/yr at a water table depth of 7.5 ft. Eddy derived ET rates ranged between 60 and 115 mm/yr (0.2 and 0.4 ft/yr).

3.5.4 Interbasin Flow

Although some previous studies assume that all groundwater discharge from Indian Wells Valley is by ET (Lee, 1912), others note the possibility of interbasin groundwater outflow toward Salt Wells Valley, which is discussed below. The absence of a large accumulation of salinity in Indian Wells Valley suggests that the basin may not be hydrologically closed. To allow groundwater outflow, a constant head boundary condition of 2,182 ft (refer to Figure 13) was established as part of the two-dimensional model to adjust recharge volumes and distribution. This boundary condition is maintained in the three-dimensional steady-state model.

Most previous studies have considered subsurface outflow to Salt Wells Valley to be small or negligible. Kunkel and Chase (1969) estimate that 20 afy of groundwater could flow through the former surface outlet channel of China Lake, based on Darcy's law. Dutcher and Moyle (1973) estimated groundwater flow on the order of 50 afy. Bean (1989) estimated a larger rate of 200 afy, but noted that is a "guess." Prior groundwater models of the basin have assumed no subsurface outflow to Salt Wells Valley (Bloyd and Robson, 1971; Berenbrock and Martin, 1991; Brown and Caldwell, 2009), presumably because estimates were found to be relatively small.

Water levels within Indian Wells Valley are higher than in Salt Wells Valley, which indicates that interbasin groundwater flow is a possibility given large enough transmissivities. Additionally, some investigators have noted a similarity in water quality between the China Lake playa area and the western end of Salt Wells Valley (Tetra Tech EM, Inc., 2003b; TriEcoTt, 2012; Stoner, 2013). Todd Engineers (2014) point out that one must be careful when drawing conclusions about flow based on groundwater quality. Similar groundwater qualities would likely have developed during the Pleistocene, when the climate was much wetter and Indian Wells Valley and Salt Wells Valley were intermittently connected by surface flow (and periodically covered by one large lake) (Smith, 2009). Todd Engineers (2014) suggests that as the climate became drier during the past 10,000 years, the rate of groundwater movement decreased dramatically and preserved a "snapshot" of Pleistocene water quality. Todd Engineers (2014) ultimately conclude that outflow to Salt Wells Valley is 50 afy or less. If Indian Wells Valley behaved like a completely closed basin, salt would continue to accumulate in the playa area, which is observed in the other downstream basins, which have salinities approaching halite saturation (300,000 mg/L) and precipitation of halite and other salts. The TDS concentrations in the vicinity of the playa are limited to approximately 60,000 mg/L, which suggest that groundwater outflow exists to some degree.

TriEcoTt (2012) identified the potential for fracture flow between the eastern portion of Indian Wells Valley and Salt Wells Valley. Groundwater levels decrease 175 ft between the eastern edge of Indian Wells Valley and the western edge of Salt Wells Valley, which indicates that transmissivities may be low. However, small hydraulic head gradients (0.002) and hydraulic conductivities ranging between 0.3 and 10 feet per day (ft/d) suggest that a significant amount of groundwater flows in Salt Wells Valley, some of which could originate from inflow through bedrock fractures in addition to the local mountain front recharge.

A flow calculation was performed in Salt Wells Valley using the hydraulic and aquifer geometry information from TriEcoTt (2012). The hydraulic gradient was estimated to be 0.002, the aquifer thickness of 400 ft was estimated from the southeastern portion of the geologic cross section (Figures 2-3), aquifer width (12,500 ft) from the potentiometric map shown in Figures 2-4, and hydraulic conductivity ranged between 0.3 and 10 ft/d. The volumetric flux was calculated using Darcy's law and yields a range of 25 to 800 afy with the best estimate of 250 afy using the geometric mean of the six hydraulic conductivity measurements within Salt Wells Valley. It is difficult to determine how much of this estimated flow within Salt Wells Valley originates as mountain block recharge in the Argus Range versus underflow from Indian Wells Valley. Given the low elevation of the southern Argus Range it seems unlikely that a large percentage of this groundwater flow originates as mountain block recharge.

Austin (1988) and Thyne *et al.* (1999) suggest that groundwater might flow from Indian Wells Valley directly to Searles Lake Valley (beyond Salt Wells Valley). Erskine (1989) mentioned that there are substantial upward gradients in groundwater levels beneath Searles Lake. However, none of those studies present any data that support a conclusion that substantial amounts of groundwater flow occur through 10 miles of bedrock from Indian Wells Valley to Searles Lake Valley.

3.5.5 Basin-wide Budget 1920 Conditions (Predevelopment)

Section 3.5 of this report describes the hydrologic conditions of the Indian Wells Valley aquifer system prior to significant development of well fields and pumping for consumptive use after 1920. It is important to carefully and accurately capture predevelopment hydrologic conditions and to build a model that represents these steady-state conditions because the steady-state hydrologic model is the foundation for all subsequent modeling. Table 6 represents the best estimates for recharge and outflow from the Indian Wells Valley hydrographic basin prior to 1920. The Indian Wells Valley hydrographic basin is assumed to be in hydrostatic equilibrium, or steady state, which means that all water inflows are equal to all water outflows.

Table 6. Steady-state water budget for Indian Wells Valley.

Inflow	AFY	Source
Mountain Block Recharge		
Sierra Nevada North	1,500	BBRM method applied to 2-D groundwater model
Sierra Nevada South	2,100	BBRM method applied to 2-D groundwater model
Rose Valley	2,400	BBRM method applied to 2-D groundwater model
Coso/Argus Ranges	1,600	BBRM method applied to 2-D groundwater model
El Paso	50	Brown and Caldwell (2009); Todd Engineers (2014)
Total	**7,650**	

Outflow	AFY	Source
ET	7,450	Balance budget
Interbasin	200	TDS mass balance; 2-D groundwater model
Pumping Wells	0	Assumed pre-groundwater development
Total	**7,650**	

4.0 FLOW MODEL DEVELOPMENT

4.1 MODEL SELECTION

The groundwater flow model MODFLOW is a widely accepted, public domain model produced by the USGS. Brown and Caldwell (2009) used MODFLOW-2000 (Harbaugh *et al*., 2000), which has been upgraded to the more contemporary MODFLOW-2005 (Harbaugh, 2005). All versions of MODFLOW use the finite difference numerical method to obtain approximate solutions to the groundwater flow equation, in which a continuous system is broken into discrete points in both space and time and partial derivatives are replaced by the differences in head between these discrete points at the

center of each block, or cell. Cells are defined by their row and column (and by layer in three dimensions). Using the continuity equation, all flow into the cell minus the flow out of the cell is the change in water stored in the cell. All flow into and out of the model cell is represented by a set of linear, algebraic difference equations, with one equation written for each active cell in the model domain. Using the set of *n*-equations and *n*-unknowns, the system of equations is solved simultaneously for head in each actively modeled cell.

4.2 MODEL DOMAIN, LAYERING, AND DISCRETIZATION

The model domain (refer to Figure 2) is identical to that presented by Brown and Caldwell (2009). The land surface was obtained from a digital elevation model and contacts were interpolated from borehole geology and a three-dimensional geologic model and associated cross sections. Figure 18 shows the model grid in which cell size has been reduced from 1,340 ft (402 m) on a side in the original model by Brown and Caldwell (2009) to 820 ft (250 m). The number of rows and columns equals 231 and 207, respectively. Vertical refinement has also occurred by replacing the original four layers with six layers. Brown and Calwell (2009) used layers to represent (1) playa and lacustrine deposits; (2) the unconsolidated, younger alluvium; (3) older alluvium; and (4) the older basin fill. The current model added an additional layer to the unconsolidated, younger alluvium as well as the older basin fill. This was done to allow greater heterogeneity in material properties in the vertical direction because simulated water levels are highly sensitive to the distribution of clay lenses and to allow better estimates of average pore velocities for future transport simulations. Refinement of the uppermost layer (playa and lacustrine deposits) was not done to allow for wetting and drying because of water table fluctuations. The resulting number of active cells in the model domain is 19,051. The model is oriented in the north-south direction and georeferenced in the Universal Transverse Mercator (UTM) coordinate system, North American Datum (NAD) 1983, zone 11N.

4.3 INITIAL CONDITIONS

For the steady-state model, assigning appropriate initial water levels is not imperative. However, better accuracy of initial heads does allow more rapid convergence on the solution. Initial water levels were set at the top of each cell. The simulated steady-state water levels are then used in the transient model simulation as its initial condition.

4.4 HYDRAULIC PARAMETERS

Previously, Brown and Caldwell (2009) estimated hydraulic parameters using geologic logs from the Indian Wells Valley Groundwater Study (USBR, 1993) work performed by NAWS, which included driller logs of water wells drilled over the years, specific capacity tests, available aquifer tests, and literature values for the Basin and Range lithologies (Anderson and Freethey, 1995; Schwartz and Zhang, 2003). Brown and Caldwell (2009) ultimately developed a range of hydraulic properties for each of the four geologic units as follows:

- Playa and lacustrine deposits: hydraulic conductivity (K) range 0.1 to 100 ft/d; ratio of horizontal (Kx) to vertical (Kz) hydraulic conductivity (Kx:Kz) equal to 10; and specific yield 0.05 to 0.15.
- Unconsolidated, younger alluvium: K range 0.1 to 75 ft/d; ratio of Kx:Kz equal to 10; specific storage 0.00001 to 0.0001 per feet; and specific yield 0.05 to 0.12.

- Older alluvium: K range 0.1 to 75 ft/d; ratio of Kx:Kz equal to 10; specific storage 0.00001 to 0.0001 per feet; and specific yield 0.05 to 0.15.
- Older basin fill: K range 0.1 to 50 ft/d; ratio of Kx:Kz equal to 10; and specific storage 0.00001 to 0.0001 per feet.

The PEST (Parameter Estimation) software suite was used to automate the steady-state calibration process (Doherty, 2005; Doherty and Hunt, 2010). The pilot-point methodology (Doherty, 2003) was implemented within the PEST environment to develop a heterogeneous hydraulic conductivity field that yields an acceptable agreement between the simulated and measured hydraulic heads. The basis of the pilot-point method is to calibrate a reduced set of hydraulic conductivity points rather than each grid element. Doing so significantly reduces the number of unknowns in the calibration process while maintaining the appropriate level of spatial variability. The measured hydraulic conductivity values are used directly in the pilot-point process as fixed values. Other hypothetical points are added in areas without measurements and the automated process determines the hydraulic conductivities at these points. The hydraulic conductivity for all cells is determined by interpolating the measured and hypothetical values. The pilot-point algorithm was used for the following separate zones within the model domain:

1. Fine-grained sediment associated with China Lake
2. The southwest high-gradient zone
3. The remainder of Indian Wells Valley

Additional subdivision of the zones was necessary to improve the model calibration. The fine-grained sediment associated with China Lake was further subdivided into zones: layer 1, layer 2, layer 3, and layer 4 and pilot points were used to develop the distribution of K within these deposits. The southwest high-gradient zone was separated into four zones with no vertical heterogeneity that were each represented by a single parameter. The playa was split into four zones—layer 1, layers 2 and 3, layers 4 and 5, and layer 6—and used pilot points.

During the automated calibration process, the hydraulic conductivity was restricted to a reasonable range of values based on the hydrogeologic unit type. For example, the maximum hydraulic conductivity within the entire model was not allowed to exceed 330 ft/d. The minimum hydraulic conductivity value in the southwest high-gradient zone was set to 0.16 ft/d and held to 0.003 ft/d elsewhere. Figure 19 shows the calibrated hydraulic conductivity field at the surface as well as an east-west cross section (A-A') through the model domain. The ratio of Kx to Kz was lowered from the Brown and Caldwell (2009) value of 10 to a value of 3 to improve calibration. Storage parameters were developed as part of the transient model calibration process.

4.5 SOURCES AND SINKS

Sources and sinks refer to those water budget items in Table 6 that are delineated as part of the conceptual model development. Mountain block recharge is modeled as a specified flux boundary condition using the MODFLOW WEL package and represents a source of 7,650 afy. Fluxes are distributed linearly by area across each recharge zone. Evapotranspiration varies nonlinearly with depth to groundwater. Based on the steady-state calibration described below, 7,453 afy are lost through evapotranspiration and 197 afy are removed from the basin by interbasin groundwater outflow.

4.6 ALTERNATIVE MODEL CONCEPTUALIZATIONS

Beyond the base model, two additional model conceptualizations were investigated including:

- Reduced recharge in the El Paso Basin
- Isolation of the deep and shallow aquifers

The purpose of considering alternative conceptual models was to determine the effect on drawdown behavior of uncertain model features to determine if those uncertainties were important to consider when analyzing drawdown forecasts.

4.6.1 Reduced Recharge in the El Paso Basin

Previous hydrogeological investigations interpreted the high hydraulic gradient zone between El Paso Basin and Indian Wells Valley as a groundwater barrier (Kunkel and Chase, 1969). If this region truly acts as a barrier to 100 percent of groundwater flow, then groundwater recharge originating in El Paso Basin should not be counted as recharge to Indian Wells Valley. In an effort to simulate the effects of reduced groundwater flow from El Paso Basin, groundwater recharge from the El Paso Basin segment was reduced from 2,150 to 100 afy. This includes recharge from the El Paso and Sierra Nevada South recharge segments.

4.6.2 Isolation of the Deep and Shallow Aquifers

Tetra Tech EM, Inc., (2003a) subdivided Indian Wells Valley into three distinct zones:

- Shallow hydrogeologic zone (SHZ)
- Intermediate hydrogeologic zone (IHZ)
- Deep hydrogeologic zone (DHZ)

Tetra Tech EM, Inc., (2003b) suggested that the IHZ and DHZ comprise the regional aquifer. All production wells occur in either the IHZ or DHZ. The saturated thickness of the SHZ ranges from 10 to 100 ft throughout the valley. The SHZ consists primarily of more permeable units such as sands and gravels. The IHZ consists of low-permeability lacustrine silts and clays. The thickness of the IHZ ranges from tens of feet to more than 1,000 ft thick. Although the IHZ consists mainly of low-permeability units, there are sand stringers that create transmissive water-bearing zones (TriEcoTt, 2012). The water-bearing zones are can produce groundwater in significant quantities (TriEcoTt, 2012).

The DHZ is primarily comprised of coarse sand and gravel with some interbedded clay and is the primary water-bearing zone of the regional aquifer (TriEcoTt, 2012). The bottom of the DHZ is defined by the contact with the underlying bedrock. The production wells in these areas are generally screened over multiple intervals between 220 and 1,015 ft bgs.

Isolation between the DHZ and SHZ is simulated by introducing a vertical anisotropy ratio (Kx/Kz) of 100 for layers 2 through 5. Using a larger anisotropy ratio is consistent with the fact that high-permeability water-bearing zones do exist in the IHZ, which implies that only vertical hydraulic conductivity is reduced.

5.0 STEADY-STATE FLOW MODEL CALIBRATION

Calibration used the PEST software (Doherty and Hunt, 2010) to optimize simulated water levels to the 1920 observed water levels by adjusting the spatial distribution of hydraulic conductivity. A discussion of pilot-point zones is provided in Section 4.4 on Hydraulic Parameters. Simulated heads are provided in Figure 20, which includes the calibration target error. Colored bars represent the error in model prediction with respect to the observed water level. Green error bars indicate that predicted water levels are within ± 6.6 ft (2 m) of the observed water level, yellow bars indicate an error less than ± 13.1 ft (4 m), and red bars indicate an error greater than 13.1 ft (4 m). Model predictive error is generally low in the main basin and higher in the southwestern, high-gradient portion of the domain where simulated water levels underpredict observed values. A regression of modeled versus observed water levels is provided in Figure 21. There are 279 observation points. The MAE is 1.7 ft (0.52 m) and the root mean squared error is 12.7 ft (3.87 meters). The relative error, which is defined as the ratio of the MAE and the total range in hydraulic head (simulated), is a more telling calibration metric. The steady-state model has a relative error of 1.6 percent. Typically, models that have a relative error less than 10 percent are deemed acceptable for predictive purposes. Models with a relative error less than 5 percent are considered excellent (Anderson *et al*., 2015).

The final steady-state water budget is only slightly modified from the conceptual model presented in Table 6. Mountain block recharge inflows equal 7,650 afy, whereas outflow is divided between interbasin groundwater outflow equal to 197 afy and evapotranspiration equal to 7,453 afy.

6.0 TRANSIENT FLOW MODEL CALIBRATION

Transient groundwater flow represents a dynamic system in which variable inflows, outflows, and groundwater storage change with time. In the modeling done to date, it is assumed that mountain block recharge (inflow) does not change. Variable pumping (outflow) is represented by observed or assumed pumping rates (discussed above) and interbasin flow (outflow) is controlled by the constant head boundary in the east. The remaining part of this dynamic system is the change in aquifer storage with time.

In the steady-state calibration described above, hydraulic conductivity values were modified to minimize the difference between simulated and observed heads. For transient calibrations, there are three primary hydraulic parameters available for continued calibration: hydraulic conductivity (K), specific yield (Sy) in unconfined layers, and specific storage (Ss) in confined layers. For the Indian Wells Valley transient model calibration, K was maintained from the steady-state model, whereas Ss and Sy were modified to match observed drawdown rates in wells. Drawdown rates were used as the calibration metric for the transient model instead of the absolute amount of drawdown because the magnitude of hydraulic head is generally controlled by the hydraulic conductivity and recharge. Automated calibration using hydraulic head magnitude can only lead to erroneous results if the solution tries to fix head offsets created by the steady-state model.

Transient conditions for calibration were simulated for the period 1920 through 2010. Seventy-three of the 562 monitoring wells contained in the transient calibration were used for drawdown calibration. Observed drawdown rates were computed by linear regression (for example, Figure 22). Simulated heads at monitoring wells were recorded for three values of Sy (0.1, 0.2, and 0.3) and four

values of Ss (3×10^{-8}, 3×10^{-7}, 3×10^{-6}, and 3×10^{-5}). Simulated drawdown rates for each calibration run were also computed using linear regression. For example, the slope of the drawdown of the observed water levels in well 26S39E05F01 between 1990 and 2010 is 0.0019 ft/d (refer to Figure 22) and the simulated drawdown slopes at this well for each calibration run are shown in Table 7 and Figure 23.

Table 7. Example of drawdown analysis for a range of Ss and Sy in well 26S39E05F01 for years 1990 to 2010. Observed drawdown slope is equal to 0.0019 ft/d.

Ss (1/ft)	Sy	Simulated drawdown slope (ft/d)
3.0E-08	0.1	0.0034
3.0E-08	0.2	0.0020
3.0E-08	0.3	0.0015
3.0E-07	0.1	0.0033
3.0E-07	0.2	0.0020
3.0E-07	0.3	0.0015
3.0E-06	0.1	0.0032
3.0E-06	0.2	0.0019
3.0E-06	0.3	0.0014
3.0E-05	0.1	0.0025
3.0E-05	0.2	0.0017
3.0E-05	0.3	0.0013

The objective is to find the calibration run (corresponding to a single Sy-Ss combination) that best matches observed slopes in the 73 selected monitoring wells. This is achieved by computing MAE between observed and simulated slopes for each run at each monitoring well and selecting the Sy-Ss combination with the lowest MAE.

For example, the MAE for a single calibration run would be computed using the equation below:

$$MAE = \frac{1}{n} \sum_{1}^{n} \{abs(\log(abs(S_{sim})) - \log(abs(S_{obs})))\} \quad (5)$$

where MAE = mean absolute error, n = number of monitoring wells, S_{sim} = drawdown slope (simulated), and S_{obs} = drawdown slope (observed). It was necessary to take the logarithm of the data to reduce the inherent bias of comparing values that span several orders of magnitude. The lowest MAE is 0.609 for Ss=3×10^{-8} (1/ft) and Sy=0.2. This MAE results from taking the difference in logs and has no units.

Figure 24 shows the spatial distribution of the differences in slope, which represents a goodness of fit for each monitoring well used in calibration. The blue points represent a reasonably good fit and the green and red points show that the simulated slope is higher than the observed slope. In those areas, the model will tend to overpredict drawdown.

Inspection of the slope differences with respect to Ss and Sy shows that the objective function is more sensitive to Sy than to Ss (see Table 7). Therefore, the Sy in layer 1 was divided into three zones with values of 0.15 or 0.25 (Figure 25) and Ss was increased to 3.0 x 10^{-7} (1/ft) for the confined layers 2 through 6 to improve calibration. This improved the MAE slightly from 0.609 to 0.593. Results using the updated Sy zones and Ss are shown for two wells: 25S38E13J01 (Figure 26) and 26S39E26B02 (Figure 27). Results for all wells used in calibration are included in Appendix A. The objective during calibration was to match the slope of the drawdown and not necessarily to match absolute heads. The simulated head in the model in the 1990s and 2000s is highly dependent on the initial conditions assumed for 1920. Steady-state calibration results show that simulated heads in 1920 are mostly within 20 ft of measured head. Allowing the transient simulated heads to vary by +/- 20 ft, combined with the overall agreement between simulated and observed drawdown slopes, suggests that the model is very well calibrated to transient heads.

The average error for the transient calibration is 0.3 ft/yr between simulated and measured drawdown rates (Figure 28). Model error is generally less than 1 ft/yr with only two locations exceeding this value. Although the transient calibration is very good throughout most of the model domain, drawdown error does increase in the southwest portion of Indian Wells Valley near the outlet of the El Paso subbasin. In this region, the simulated drawdown rates are larger than observed. Although this region is outside of the main groundwater pumping zone, additional calibration may be necessary to further refine the model.

The model-simulated water levels are relatively stable until approximately 1945, when groundwater pumping begins to escalate. Drawdown rates after approximately 1970 are relatively constant at approximately 1 ft/yr, which is in general agreement with measured data (see Figure 29).

6.1 Effect of Alternative Conceptualizations

A sensitivity analysis was performed to test the effect of two additional model conceptualizations on the simulated transient water levels. As described in Section 4.6, the two conceptualizations include:

- Reduced recharge in the El Paso Basin
- Isolation of the deep and shallow aquifers

Selected monitoring wells were used to qualitatively assess the effect of these alternative conceptual models on drawdown behavior. The locations of the selected monitoring wells are shown in Figure 30 and a typical comparison between the base model, alternative models, and observed water levels is show in Figure 31.

The reduction of groundwater recharge in El Paso Basin from 2,150 afy to 100 afy has very little effect on the predicted drawdown response. The main difference between the reduced recharge scenario and the base model is slightly lower heads at the beginning of the simulation. The drawdown response for the rest of the simulation is nearly identical to the base model, though the more recent (after 2000) drawdown rate does increase from 1.06 ft/yr in the base model to 1.11 ft/yr in the reduced El Paso recharge scenario. This relative lack of effect on the drawdown response is likely because the pumping rates are more than three times the recharge rate. The groundwater system continues to be in a significant deficit condition regardless of the recharge coming from El Paso Basin.

Isolation of the deep and shallow aquifer systems has a more significant impact on calculated drawdown. This conceptual model is simulated by using a large vertical anisotropy ratio (Kx/Kz) = 100. Under the isolated conditions, much greater drawdown is simulated for some wells in response to the post-1945 pumping increase than is either observed or simulated by the base model (Figure 31). The monitoring well presented in Figure 31 (26S39E26A01) is screened from 1,190 to 1,200 ft bgs (see Table 8).

Table 8. Screen depths for selected monitoring wells.

#	Well Name	Screen Top (ft)	Screen Bottom (ft)
1	26S39E26A01	1190	1200
2	BR-3 Shallow	650	670
3	26S39E27D MW-32 medium deep	1240	1260
4	27S40E06D01	580	700
5	BR-3 deep	1850	1870
6	BR-6 deep	1640	1660
7	NR-1 deep	1960	1980
8	NR-2 medium	1540	1560
9	26S39E19Q01	251	371
10	26S39E28C01	10	20
11	26S39E24M01	10	20
12	26S39E24Q01	10	20

The higher drawdown rates for the deep/shallow isolation scenario are associated with the deeper aquifer zones in the large production wells. By contrast, the simulated hydraulic heads are nearly identical in the base model and the deep/shallow isolation scenario in wells that are vertically separated from production horizons, such as well BR-3 (shallow) (Figure 32). This well is screened from 650 to 670 ft bgs, which is above the screened sections for the adjacent NAWS production wells (screened from 700 to 1,400 ft bgs; Table 9). Under the deep/shallow isolation model, drawdown magnitude is larger than the base model at depths associated with large production wells but similar drawdown rates are predicted at shallower depths.

In general, the drawdown rates simulated by the base model for deep monitoring wells located near large production wells are in better agreement with observed rates than the deep/shallow isolation conceptual model (Figures 33 to 42). Because deep monitoring wells are not present throughout the basin, the degree of isolation between the systems cannot be assessed everywhere. For example, there are no deep monitoring wells adjacent to the NAWS production wells to assess the degree of isolation between the shallow and deep systems in those areas. The alternative model results demonstrate that drawdown will be greater in areas with isolation between the systems.

Table 9. Screen depths for municipal and NAWS wells.

Owner	Well name	Screen Top Depth (ft)	Screen Bottom Depth (ft)
SVM	25S40E30D01	591	1236
SVM	26S39E25E01	790	1329
SVM	26S39E36G01	787	1363
SVM	27S40E04B03	405	1052
SVM	27S40E05D01	518	1340
China Lake Acres	26S39E26B	841	1365
China Lake Acres	26S39E26D	917	1463
China Lake Acres	26S39E27C	911	1453
City of Inyokern	26S39E19A00	788	1355
City of Inyokern	26S39E19H00	792	1375
City of Inyokern	26S39E20N01	792	1375
City of Inyokern	26S39E20N02	768	1371
City of Inyokern	26S39E30J01	726	1317
City of Inyokern	27S39E07R01	926	1458
City of Ridgecrest	26S40E29R	556	1275
City of Ridgecrest	26S40E34F	328	1073
City of Ridgecrest	26S40E34N01	225	260
City of Ridgecrest	27S40E04A01	333	1007
City of Ridgecrest	27S40E05H	515	1216
IWVWD	26S39E26	891	1414
IWVWD	26S39E27D01	906	1436
IWVWD	26S39E28R	895	1452
IWVWD	26S39E30K	666	1264
IWVWD	26S40E30C	627	1340
IWVWD	26S40E30K01	627	1340
IWVWD	26S40E32G	504	1320
IWVWD	26S40E32K	489	1329
IWVWD	26S40E33P04	452	1085
IWVWD	26S40E34P	165	192
IWVWD	27S39E04C	908	1437
IWVWD	27S39E08A	839	1424
IWVWD	27S39E08L01	975	1487
IWVWD	27S39E08L02	981	1493
IWVWD	27S40E06D01	474	1321
NAWS	26S39E19K01	759	1367
NAWS	26S39E19P02	693	1303
NAWS	26S39E20R01	832	1414
NAWS	26S39E21Q01	881	1438
NAWS	26S39E23H02	731	1321
NAWS	26S39E24P03	636	1221

7.0 TRANSPORT MODEL

7.1 MODEL PURPOSE

The well-documented presence of saline groundwater in portions of Indian Wells Valley raises the concern that drawdown may induce the migration of poorer quality water toward production wells. There is evidence of increasing salinity in some production wells, particularly in the southeastern Ridgecrest area (Berenbrock and Schroeder, 1994; Todd Engineers, 2014). A three-dimensional solute transport model was developed to predict the migration of TDS toward wells within Indian Wells Valley. The model uses measured TDS concentrations as an initial condition and then simulates TDS migration 85 years into the future. The results are presented as TDS concentrations through time at a few key supply wells and as spatial plots of TDS trends (i.e., increasing or decreasing concentration rates). An alternative conceptualization is simulated to determine the effect of high TDS fluid residing in low-permeability sediments adjacent to existing municipal wells.

7.2 INITIAL CONDITIONS

The hydrochemistry of groundwater in Indian Wells Valley has been evaluated by numerous workers and for various reasons. Identifying water-quality suitable for beneficial uses has been one focus, and using chemical and isotopic tracers to interpret groundwater flow directions has been another. These investigations have identified generally higher salinity groundwater in the eastern portion of the valley coincident with China Lake playa, moderate salinity in the northwestern portion of the basin toward Rose Valley, and scattered occurrences of moderate and high salinity in individual wells associated with clay horizons or geothermal zones.

For the transport model, TDS is used as the measure of groundwater salinity. The initial condition for the salinity distribution is defined by TDS values reported for groundwater wells throughout the valley. The primary data source is the hydrochemical database compiled by Guler (2002), which is largely comprised of data from the USGS. Records from Guler (2002) that include TDS and sample depth information located in the model area are also used. Samples reported by IWVCGTAC and Geochemical Technologies, Corp., (2008) were added to the dataset to supplement the Guler data both spatially and temporally. Of the 1,368 samples in Guler's 2002 database, 560 met the inclusion criteria, and 13 samples were added from IWVCGTAC and Geochemical Technologies, Corp., (2008). Locations with multiple TDS analyses were represented by the highest TDS reported. The salinity values represent measurements that span decades of time. Figure 43 shows the TDS data, which are represented by circles that are colored based on the TDS value, for samples collected from elevations greater than 500 m. Figure 44 shows the TDS data for samples collected from elevations less than 500 m.

In regions of the model domain where there are limited TDS data, control points were included to improve the interpolation. The control points are represented by colored squares in Figures 43 and 44. For the shallow measurements (elevation >500 m), control points were required in the far north and southwest portions of the model domain. In the far north portion of the domain control points were given a value of 1,300 mg/L based on measurements located south of this region. In El Paso Valley, TDS concentrations were assumed to be 450 mg/L, which is consistent with the measurement to the northeast.

In the deeper subsurface environment, more control points were needed to interpolate the full model domain. Specifically, control points were added in the north, east, and southeast portions of the model domain. In the north, control points were assumed to be 1,500 mg/L based on a measurement of 1,480 mg/L in the northwest. In the east central portion, four control points were added with a TDS concentration of 12,500 mg/L based on the measurement of 12,500 mg/L located just west of these points. Moving southward, a control point was added with a TDS concentration of 2,500 mg/L, which is consistent with the transition to lower concentrations as you approach the NAWS and other municipal wells in the region. There are two control points with concentrations of 750 mg/L in the southeastern portion of the valley. Less information is known about TDS concentrations in this region. In the southwest (El Paso region), concentrations were assumed to be 350 mg/L, which is consistent with the first measured TDS concentration point northeast of El Paso Valley.

The TDS concentration point data shown in Figures 43 and 44 are then interpolated to the finite difference grid to become initial conditions for the solute transport model. Kriging was used to interpolate the point data using a semivariogram structure with no nugget, a range of 1.1 km, and a sill (variance) of 1.9×10^7 $(mg/L)^2$ to fit the experimental semivariogram. Kriging interpolation was performed on the $\log_{10}$ of the TDS concentration data because of the large range of measured values.

The interpolated TDS concentration data with sample elevations greater than 500 m (Figure 43) was mapped to model layers 1 to 3 and those with elevations less than 500 m were mapped to layers 4 to 6. Although the elevation of the interface between layers 1 to 3 and 4 to 6 varies, it is at an approximate elevation of 500 m. The interpolated TDS concentrations for layers 1 to 3 are shown in Figure 45 and layers 4 to 6 are shown in Figure 46. The interpolated TDS patterns are generally consistent with the salinity patterns identified by previous works (e.g., Berenbrock and Schroeder [1994] and Morgan [2010]).

7.3 MODEL SELECTION

The MT3D software package (Zheng and Wang, 1999) was used to calculate the migration of TDS through the IWV aquifer. For simulating solute transport, MT3D is the industry standard software package and it has been tested and verified by numerous hydrogeologists. This model is used routinely and applied for this study using standard, generally accepted methodologies.

The MT3D package links directly with MODFLOW, which provides volumetric flow rates by finite difference cell. The base flow model was used to generate the volumetric flow rates into the future for the base transport model. For the alternative conceptualization, the base flow model was used but the hydraulic conductivity was reduced at one finite difference cell near two NAWS wells to represent a local clay unit. Therefore, in both scenarios the base model pumping schedule was assumed, which represents continuation of current groundwater use in the future (status quo).

7.4 MODEL PARAMETERS

The MT3D package requires a suite of transport parameters including dispersion coefficients, effective porosity, sorption parameters, and degradation constants. Longitudinal dispersion coefficients are thought to be a function of model scale. Given the large scale of the model domain and potential for TDS migration over large distances, the longitudinal dispersion coefficient was chosen as the maximum measured value of 1,000 m (see Gelhar *et al.* [1992]). The ratio of the horizontal transverse dispersion coefficient to the longitudinal coefficient is taken as 0.1 (Dullien, 1992). The ratio of the vertical

transverse dispersion coefficient to the longitudinal coefficient is taken to be 0.01. The effective porosity is the porosity available to fluid flow. The effective porosity was selected to be 0.2, which is typical for unconsolidated basin-fill aquifers (Stephens *et al.* [1998]).

Total dissolved solids were assumed to be conservative (nonsorptive and nondegrading), so the reactive transport modules within MT3D were not used. Although many of the components of TDS concentrations may be reactive, others such as chloride generally are not. The analysis presented here can be considered conservative because the simulated results may have higher concentrations and more rapid concentration increases than may occur in situ.

Although it is not critical to the simulated results, fluid recharge from the Sierra Nevada Range was assumed to have a TDS concentration of 67 mg/L, based on the average of samples in the recharge zone. Other values were tested, but it was found that migration distances were short enough within the 100 year simulation time to not affect concentrations at key pumping centers.

8.0 SUBSIDENCE ANALYSIS

Because groundwater use in Indian Wells Valley is three to four times higher than estimated recharge, the valley is susceptible to subsidence by aquifer depletion. Subsidence near NAWS facilities can negatively affect research and other activities.

Two methods were used to investigate subsidence and estimate future land surface effects if current pumping continues at its current rate. Interferometric Synthetic Aperture Radar (InSAR) was used to measure subsidence directly. The second method applies the subsidence package in MODFLOW to simulate subsidence because of groundwater extraction.

8.1 INSAR

Interferometric Synthetic Aperture Radar is a technique for mapping ground deformation using radar images of the Earth's surface that are collected from orbiting satellites. Radar data have been acquired in the Indian Wells Valley area since 1992 and, according to a study by Katzenstein (2013), the arid climate is favorable to InSAR processing. Katzenstein used multiple year, stacked radar results to identify subsidence for the periods 1992 to 2000 and 2005 to 2010. In that study, the observed subsidence rates for those periods were 2.6 and 2.7 mm/yr (0.10 and 0.11 in/yr), respectively, which suggests a constant deformation rate for the past 20 years. Additionally, Katzenstein concluded there were two main subsidence bowls (Figure 53) in the valley. These bowls appear to be influenced or controlled by regional faults. Figure 54 shows a profile of the land surface through these subsidence bowls.

8.2 SUBSIDENCE MODELING WITH MODFLOW

To simulate subsidence, the Indian Wells Valley MODFLOW groundwater model was used with the Subsidence and Aquifer-System Compaction Package for Water-Table Aquifers (SUB; Hoffmann *et al.*, 2003). The SUB Package simulates elastic (recoverable) compaction and expansion, and inelastic (permanent) compaction of compressible fine-grained beds (interbeds) within the aquifers. Interbeds are assumed to: (1) consist of highly compressible (non-consolidated) clay and silt deposits, (2) be of insufficient lateral extent to be a confining unit, (3) have relatively small thickness, and (4) have significantly lower hydraulic conductivity than the surrounding sediments. All of these assumptions are reasonable for the hydrostratigraphic environment of Indian Wells Valley. The deformation of the

interbeds is caused by head or pore-pressure changes, and therefore by changes in effective stress within the interbeds. If the change in effective stress is less than the preconsolidation stress of the sediments, the deformation is elastic; if the change in effective stress is greater than the preconsolidation stress, the deformation is inelastic (Hoffman *et al.* 2003).

A large source of uncertainty in simulating subsidence comes from parameterization of the subsurface properties. Specifically, the location and compressibility of the fine-grained interbeds is largely unknown. Therefore, the distribution of specific yield in the upper aquifer layer in the flow model was used as a general indicator of compressibility for the calibration process. The determination of specific yield is described in the groundwater modeling section above.

8.2.1 Calibration

Modeled subsidence was calibrated to the InSAR-interpreted subsidence through trial and error adjustments of skeletal specific storage parameters to match maximum subsidence rates within the entire model domain. The location of subsidence was not considered in the calibration process because the sparsity in subsidence parameter data only supports basin-wide estimates.

Specific parameters in the SUB package relevant to the calibration process are the preconsolidation head (parameter code HC), elastic and inelastic skeletal storage coefficients (Sfe and Sfv), and starting compaction. In the no-delay interbeds (those assumed to react instantly to changes in stress), HC was assumed to be land surface; Sfe was calibrated to 5.0×10^{-5} and 1.5×10^{-4}, for the zones associated with specific yield values of 0.25 and 0.15, respectively (see Figure 25). The calibrated Sfy parameter was adjusted to 5.0×10^{-4} and 1.5×10^{-3}, for the zones associated with specific yield values of 0.25 and 0.15, respectively (see Figure 25). The initial effective stress was calculate based on the initial position of the water table and the overburden pressure of the sediment. For the delay interbeds (exhibiting time-dependent compaction), the starting head was assumed to be the same as land surface, and the starting preconsolidation head was assumed to be 50 meters bgs. The equivalent interbed thickness, which was used for computational convenience in the SUB package and to account for a large number of interbeds of different thicknesses, was assumed to be 5.0 meters.

Calibration results for the two observed time periods (1992 to 2000 and 2005 to 2010) are shown in Figure 55 and 56. Although the magnitude of subsidence from water supply well pumping generally matches, its location differs. In general the model over-predicts subsidence associated with agricultural pumping relative to the InSAR measurements. In the model calculated subsidence is centered on the supply wells, whereas the InSAR results suggest that most subsidence occurs farther north toward the playa sediments. The differences between measured and simulated subsidence is likely due to the fact that the model does not have a detailed description of horizontal heterogeneities associated with soil mechanical properties. Additional factors would include the compressible clay interbeds that stretch from the production well area to the north that are not simulated in the model, or the InSAR elevation changes may be related to tectonic (i.e. faulting) rather than subsidence events.

9.0 SUMMARY OF MODEL DEVELOPMENT

This study has updated and improved a groundwater model of Indian Wells Valley for use as a decision support tool to address the problems of excessive drawdown, decreasing water quality, and land subsidence. Improvements were made in the representation of mountain block recharge, evapotranspiration, and historical pumping. A small amount of interbasin flow was also added to the model.

The model was calibrated under steady-state conditions from 1920 to obtain good agreement between simulated and observed water levels under predevelopment conditions. The revised calibration used a continuously varying hydraulic conductivity field to simulate the heterogeneous conditions. The steady-state model was used as the base for a transient simulation in which storage parameters were used to calibrate to the observed water level drawdown rates.

The transient calibration methodology differed from previous efforts by focusing on drawdown rates rather than absolute heads because the main purpose of the model is to predict drawdown in the future. Previous modeling efforts exhibited significant spatial bias in the predicted water levels. The Brown and Caldwell (2009) model underpredicted drawdown within the city of Ridgecrest and overpredicted drawdown northeast of Ridgecrest. These issues were resolved in the current version of the model and drawdown rates were predicted with an average error of 0.3 ft/yr. The transient calibration performed favorably in most areas of the model domain, including major groundwater pumping centers (Ridgecrest and agricultural areas). Although the model did not perform as favorably in the region between the El Paso subbasin and Indian Wells Valley, this area may be less important in terms of long-term drawdown effects.

Two alternative conceptual models were evaluated to determine their effect on drawdown calculations. The alternative of reduced recharge in the El Paso subbasin region has negligible influence on drawdown rates and need not be considered a significant uncertainty in model forecasts. Conversely, simulating hydraulic isolation between the shallow and deep aquifer zones leads to larger drawdown rates in the deep aquifer zone in response to pumping. Although monitoring well data from the deep production zone is better matched by the base conceptual model, it is spatially limited and isolation between the deep and shallow systems cannot be ruled out in some areas of Indian Wells Valley. Therefore, the alternative model of isolated deep and shallow systems should be carried forward as an uncertainty in model forecasts.

A chemical transport model was developed to investigate the potential for water-quality degradation caused by drawdown cones intercepting zones of saline water in the basin. The transport model is divided into two horizons, deep and shallow, with salinity represented by analyses of TDS. Although 570 TDS analyses were available, the sparsity of salinity data in some model regions was addressed by inserting control points with interpolated TDS values that were additionally consistent with the conceptual model for salinity distribution in the basin. Available time series salinity trends are replicated using the transport model, with increasing salinity simulated in areas adjacent to the preexisting saline zones north and east of the municipal wells.

Subsidence effects are modeled using a MODFLOW module designed to link the flow model and subsidence calculations. The subsidence model was calibrated to subsidence calculated based on InSAR observations of elevation changes in Indian Wells Valley. Although the general magnitude of subsidence interpreted using InSAR is replicated by the model, differences in spatial distribution suggest that the subsidence model is lacking in parameterization details.

10.0 DRAWDOWN, SALINITY, AND SUBSIDENCE FORECASTS

One of the primary purposes for increasing the fidelity of the Indian Wells Valley groundwater model is to answer the question of when NAWS supply wells might require deepening under status quo conditions. The quality of the steady-state and transient calibrations indicate that the updated flow model

is acceptable for such predictive use. The base model and two alternative conceptualizations were used to simulated current groundwater use into the future. The first alternative conceptualization included increased isolation between the deep and shallow aquifers. The second alternative tested the impact of global climate change. Forecasts of water-quality degradation because of saline water incursion into pumping areas and land subsidence related to groundwater withdrawals are also developed for the base groundwater flow model.

Simulated groundwater levels for the base model and the two alternative conceptualizations are shown for all NAWS production wells in Figures 58 through 63. Table 10 provides the predicted year in which the simulated water level drops below the top and bottom of the screen in NAWS production wells for the status quo scenario and the alternative conceptual models. Note that the model-grid resolution (820 ft on a side) prevents accurately capturing near-well drawdown effects such that the forecasts are more applicable for the surrounding aquifer rather than immediately adjacent to the well bore.

Table 10. Predicted year in which simulated water level drops below top and bottom of the NAWS production well screen for three conceptual models.

NAWS Well	Year to top of screen			Year to bottom of screen		
	Base	Isolation Alt.	Global Climate Change	Base	Isolation Alt.	Global Climate Change
26S39E19K01	2440	2329	2423	2982	2839	2946
26S39E19P02	2376	2264	2362	2920	2767	2892
26S39E20R01	2485	2336	2466	3009	2833	2972
26S39E21Q01	2534	2396	2514	3036	2893	2998
26S39E23H02	2487	2323	2468	3059	2868	3019

A map of the spatial distribution of simulated drawdown rate for the base model is shown in Figure 64. Corresponding maps of drawdown magnitude for 10, 25, 50, and 100 years into the future are shown in Figures 65 through 68. Note that the initial hydraulic head condition for the drawdown calculations is the end of 2014.

10.1 BASE MODEL GROUNDWATER LEVEL PREDICTIONS

The status quo condition assumes the continuation of current groundwater use, modified as needed to accommodate maturation of existing young pistachio orchards. The calibrated transient model simulated pumping and associated drawdown into the future. The largest drawdown rate is predicted in the western portion of Indian Wells Valley, which is coincident with agricultural pumping for pistachio orchards, and also in the area south of Inyokern (Figure 29 and 64). A general swath of drawdown rates higher than 1 ft/yr occurs throughout the southwestern portion of Indian Wells Valley proper (not including the El Paso subbasin) where the majority of the valley's production wells are located. Predicted drawdown rates under current conditions near NAWS wells range from 1.01 to 1.12 ft/yr. At this rate, water levels will not drawdown to the proximity of the top of the NAWS well screens for hundreds of years (year 2376 or later) (Table 10).

Domestic wells are likely to be affected much sooner. According to Todd Engineers (2014), the average water level in domestic wells in Indian Wells Valley is 78 ft above the bottom of the screen. Water levels at the western side of the basin (the general area of the intersection of US 395 and State Highway 14) are forecast to decrease in excess of 20 ft within 10 years (by 2025) and 50 ft within 25 years (by 2040). Well-specific conditions will depend on the depth of the well, properties of the aquifer (for example, greater drawdown south of Inyokern is associated with lower permeability in the aquifer in that area), and proximity to significant pumping operations.

10.1.1 Salinity Forecasts

Forecasts of salinity changes were developed for an 85 year horizon. The simulated TDS concentrations in year 2100 for layer 4 and layer 2 are shown in Figure 47 and 48, respectively. After 85 years, the simulated spatial distribution of TDS concentrations is very similar to the initial condition because of low fluid velocities. In layer 4, which is equivalent to the screen elevation of many of the municipal wells, the main change in TDS concentration between the initial condition and 2100 is a slight southward movement of the high TDS (>5,000 mg/L) zone beneath the main playa. The low TDS zone around the NAWS wells remains relatively stable. The differences between the initial condition and simulated TDS concentrations in 2100 are minimal in layer 2. The lowest TDS concentration zone adjacent to the NAWS wells becomes slightly smaller as higher-salinity water slowly encroaches toward the high-capacity wells in this region.

Figure 49 shows the TDS concentration trend (mg/L/yr) in layer 4 of the model. Layer 4 is at an equivalent elevation to many of the municipal wells. Therefore, TDS trends from layer 4 reflect potential changes in TDS concentrations in many of the water supply wells within Indian Wells Valley. Figure 49 shows trends in three categories a) <0 in blue, b) 0 to 10 in yellow, and c) 10 to 50 mg/L/yr in red. Regions shown in yellow and red are those that might experience increasing TDS concentrations. For context, the municipal well locations are also shown and there are no red areas (highest potential for increasing TDS concentrations) that overlap with municipal wells.

The highest TDS increases are along the eastern edge of Indian Wells Valley and a large region in the central portion of the NAWS testing area. These regions of expected TDS increases are associated with higher TDS concentrations in the shallow sediments and slightly lower TDS concentrations at depth. Because deeper TDS measurements are limited beneath the playa, the simulated TDS increases in this region may be an artifact of the assumptions used to generate the initial conditions. Regardless, it would be useful to gain additional information on the depth of the high TDS plume north of Ridgecrest.

Figure 50 shows the simulated TDS concentration at a selected NAWS well, which brings the valley-wide salinity trends into perspective for specific wells. The TDS concentration is expected to increase moderately over the simulation period with an increase of approximately 40 mg/L in the 85 year simulation period. A similar plot is shown in Figure 51 for one of the eastern municipal wells in Ridgecrest, where concentrations are expected to increase more rapidly. At this location, TDS concentrations increase by approximately 200 mg/L in the 85 year simulation.

10.1.2 Subsidence Forecasts

The calibrated groundwater/subsidence model was used to predict the magnitude and location of subsidence using the base groundwater flow model. Simulations were executed for 50- and 100-year time frames. Results are displayed in Figure 57. The model forecasts approximately one foot of additional

subsidence in 100 years, or approximately 3.0 mm/year. Although this rate corresponds with the observed rates from InSAR described above the location of the larger simulated subsidence rates are not always in the same location as those measured with InSAR.

10.2 ALTERNATIVE CONCEPTUALIZATION (1): ISOLATION BETWEEN SHALLOW AND DEEP AQUIFERS

As stated previously, an alternative conceptual model simulating a lack of hydraulic connection between shallow and deep aquifers was found to significantly affect drawdown rates in the deep aquifer. Available drawdown observations are not well simulated in the alternative model, but the model is carried forward into this predictive analysis because isolation between aquifer zones may occur in areas without adequate observation wells. As in the simulation of the historical period, this alternative scenario results in significantly more drawdown in the future compared with the base status quo simulation (Figures 58 through 63 and Table 10). This is because of the larger initial drawdown for the isolation alternative when significant pumping began in the late 1940s. The water levels do not fully recover, so even though the future drawdown rate is not very different from that of the other scenarios, the head remains approximately 100 ft lower. Therefore, drawdown will reach the NAWS well screens 100 to 150 years earlier.

A related alternative conceptualization was simulated in the transport model to determine the potential effect of a low-permeability clay horizon with high TDS fluid being adjacent to a NAWS production well. The localized clay deposit was inserted in the model in a single layer at an elevation (model layer 4) equivalent to the screen interval for two NAWS wells, as shown in the inset in Figure 52. The deposit was represented by one model cell (820 ft on edge) that was approximately one-half mile from two NAWS wells. This distance was selected to be far enough away so the response would not be instantaneous, but close enough that an effect from the high TDS fluid in the clay deposit might be expected. The hydraulic conductivity of the clay deposit was assumed to be $3x10^{-4}$ ft/day, which is typical for fine-grained deposits (Freeze and Cherry, 1979). The TDS concentration in the clay deposit was assumed to be 5,000 mg/L, which is well above measured concentrations in this area of the valley.

The result of the alternative salinity conceptualization can be seen in the lower graph in Figure 52. Introduction of a low-permeability clay deposit with high TDS fluid causes increased TDS concentrations after approximately one decade compared with the TDS concentrations for the simulation without the clay. The difference in the TDS concentrations at the NAWS well with and without the saline clay lens peak after 40 to 50 years, but the difference is only 10 mg/L TDS. The simulation suggests that localized clay deposits are not likely to significantly increase TDS concentrations at production wells unless they are spatially extensive, which would provide a larger mass of salt.

10.3 ALTERNATIVE CONCEPTUALIZATION (2): GLOBAL CLIMATE CHANGE SCENARIO

A future of reduced groundwater recharge affects the base simulation by changing the assumed mountain block recharge. Global Climate Model (GCM) predictions were assumed to apply after 2020. The GCM predictions reduce recharge in the model linearly from 100 percent of normal in 2020 to 84 percent of normal in 2120. There is little difference in head or drawdown slope between the base simulation and the model using the GCM predictions (Figures 58 through 63 and Table 10). This is to be expected because the effect of the GCM scenario is a reduction in mountain block recharge by a maximum of 16 percent, but the total amount of recharge is small compared with agriculture and municipal pumping.

11.0 DISCUSSION

Groundwater levels in Indian Wells Valley are declining at approximately 1 ft/yr. Based on forecasts of groundwater drawdown under six different future scenarios, water production from the NAWS supply wells will be unaffected by continuing basin overdraft for at least several hundred years. This outcome reflects the considerable depth of the NAWS wells and the volume of groundwater stored in the Indian Wells Valley basin during the period prior to overdraft. Similarly, increases in salinity in the NAWS wells because of drawdown inducing the incursion of salty groundwater from areas north and east is forecast to be a slow process that will have a limited effect on NAWS well-water quality for at least one hundred years. Subsidence because of groundwater withdrawals is estimated to amount to a decrease in elevation of one foot in the next hundred years, but there are substantial uncertainties in both the model forecast and current subsidence observations.

Most of the municipal wells in Indian Wells Valley have well screens placed deep within the aquifer, but there are some completed at shallower depths that will be affected by the water level decline sooner than the NAWS wells. The situation of domestic wells is more critical throughout Indian Wells Valley. According to Todd Engineers (2014), the water level is below the top of the well screen for nearly one-third of the domestic wells, which creates a risk of corrosion and pump cavitation because of air entrainment in the water. Todd Engineers (2014) also reports that these wells have less than 80 ft of water above the bottom of their screen on average. Serious functional problems, if not running dry, will be encountered by most domestic wells during the next several decades unless wells are deepened or replaced by deeper wells.

Todd Engineers (2014) identified three pathways by which high TDS groundwater can reach a water supply well that initially had low TDS: (1) laterally from the China Lake area, (2) vertically from below, and (3) internally from clay deposits. Modeling results indicate that high TDS water may migrate laterally from the China Lake area, but the concentration increases at water supply wells will be relatively slow. Maximum increases may be on the order of 200 mg/L by 2100 and occur on the eastern side of Ridgecrest. The TDS concentrations could reach the Environmental Protection Agency's lower standard (500 mg/L) for TDS in 15 years (it is important to note that the TDS maximum contaminant level is a non-mandatory, secondary standard for aesthetic and taste considerations). The simulation results do not indicate that significant TDS will migrate from depth to contaminate water supply wells. Simulation of localized clay deposits containing high TDS fluid did not increase TDS concentrations in adjacent water supply wells in any significant manner (increase of 10 mg/L).

Overlaid on these predictions are uncertainties regarding aquifer properties and uncertainties in future conditions. The model results suggest that the aquifer property or process contributing the most uncertainty to all of the forecasts is the hydrostratigraphy of clay lenses. Drawdown forecasts are sensitive to the degree of isolation between the shallow and deep aquifer systems, which is a function of low-permeability clay horizons. If localized aquifers are isolated by clay lenses, more drawdown is experienced by the deep aquifer. Essentially, the water-producing horizon has less storage under the isolation scenario. A comparison of drawdown rates observed in Indian Wells Valley wells with rates calculated by models with and without aquifer isolation indicates that, basin-wide, the system is best represented without isolating the deep and shallow aquifers. Nonetheless, the high degree of spatial variability that is characteristic of alluvial and lacustrine sediments suggests it is likely that communication between the deep and shallow aquifers is

restricted in some portions of the basin. The absence of deep piezometers to monitor water levels adjacent to the NAWS wells' production zones prevents determining the degree of isolation. If isolated conditions exist, whether at the NAWS or other deep production wells, drawdown will be more rapid and intercept the well screens sooner, potentially by 100 years or more.

The spatial distribution of clay interbeds and their mechanical properties are critical to predictions of land subsidence as groundwater is withdrawn, but are largely unknown for the valley subsurface. Subsidence calibration data are also uncertain as a result of the complexity of interpreting cause and effect for InSAR-detected elevation changes. For example, InSAR alone cannot distinguish between an elevation change caused by subsidence and one caused by tectonic processes.

Clay lenses present an uncertainty in the water quality forecasts because they have the potential to retain saline water, which can migrate to pumping wells if the clay lenses are extensive enough and close enough to a production well. The existing distribution of salinity in valley aquifers is another important uncertainty for the salt transport predictions, particularly for the deep horizon (elevations <1,600 ft).

Other uncertainties in the groundwater system are of lesser importance. Considerable attention has been paid here and in previous work to reduce uncertainty in groundwater recharge. That uncertainty is now reasonably constrained and groundwater pumping so far exceeds recharge that the drawdown predictions are relatively insensitive to moderate changes in recharge rate, which is demonstrated by the simulation of a future global climate change scenario.

12.0 CONCLUSIONS

- Navy wells are deep enough that they are unlikely to be adversely hydraulically affected by declining water levels for a couple of hundred years.
- Moderate increases in salinity (40 mg/L) can be expected at the Navy wells over the next 85 years as drawdown intercepts saline groundwater to the north and east.
- Land subsidence as a result of groundwater withdrawal has the potential to proceed at a rate of 2 to 3 mm/yr (approximately one foot in 100 years), but both magnitude and location are highly uncertain because of data limitations.
- Installation of deep monitoring wells adjacent to the Navy wells would provide valuable information for reducing uncertainty in drawdown predictions and for monitoring ongoing declines.
- Most domestic wells, and a few municipal wells, are at risk from declining water levels within the next few decades.
- Greater declines in water quality because of increasing salinity can be expected in the eastern parts of the valley and the central portion of the NAWS testing area. An increase in TDS of 200 mg/L is forecast for municipal wells east of Ridgecrest by year 2100.
- Reduction in recharge from global climate change does not significantly affect drawdown forecasts.

13.0 FIGURES

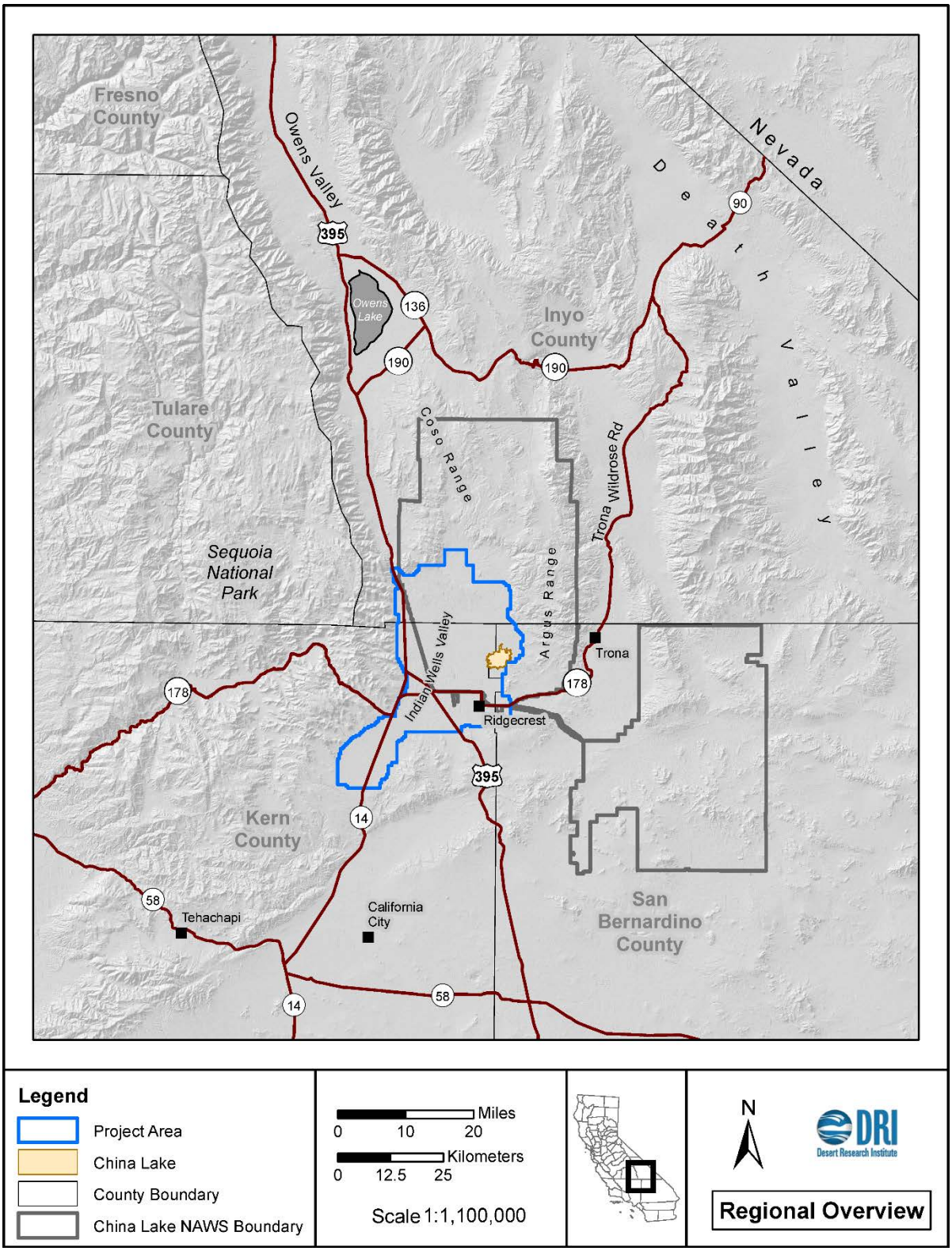

Figure 1. Indian Wells Valley location and regional overview.

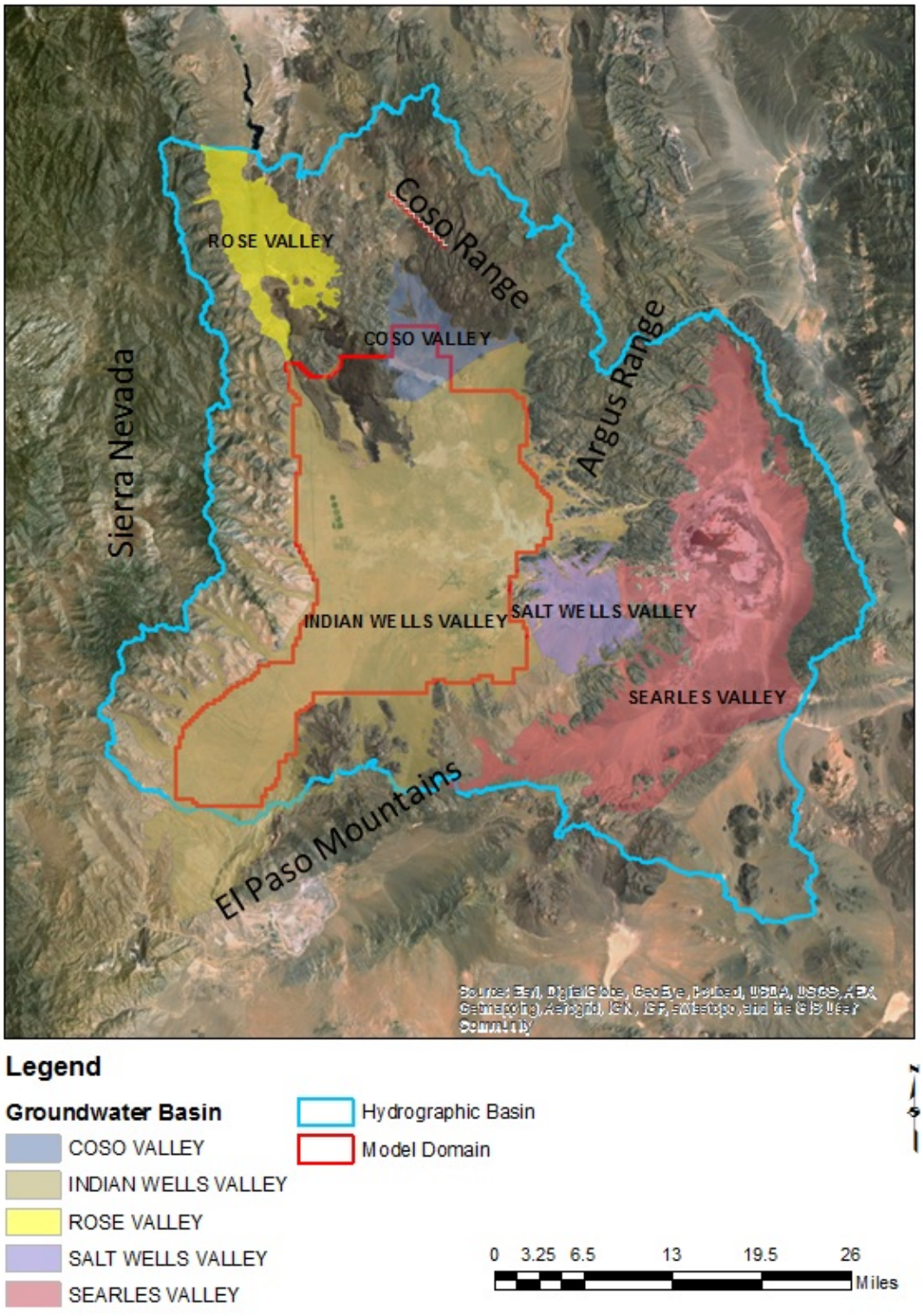

Figure 2. Hydrographic study boundary, encompassing the connected hydrographic basins of Rose, Coso, Indian Wells, Salt Wells, and Searles Valleys. The model domain (shown in red) includes Indian Wells Valley and a portion of Coso Valley.

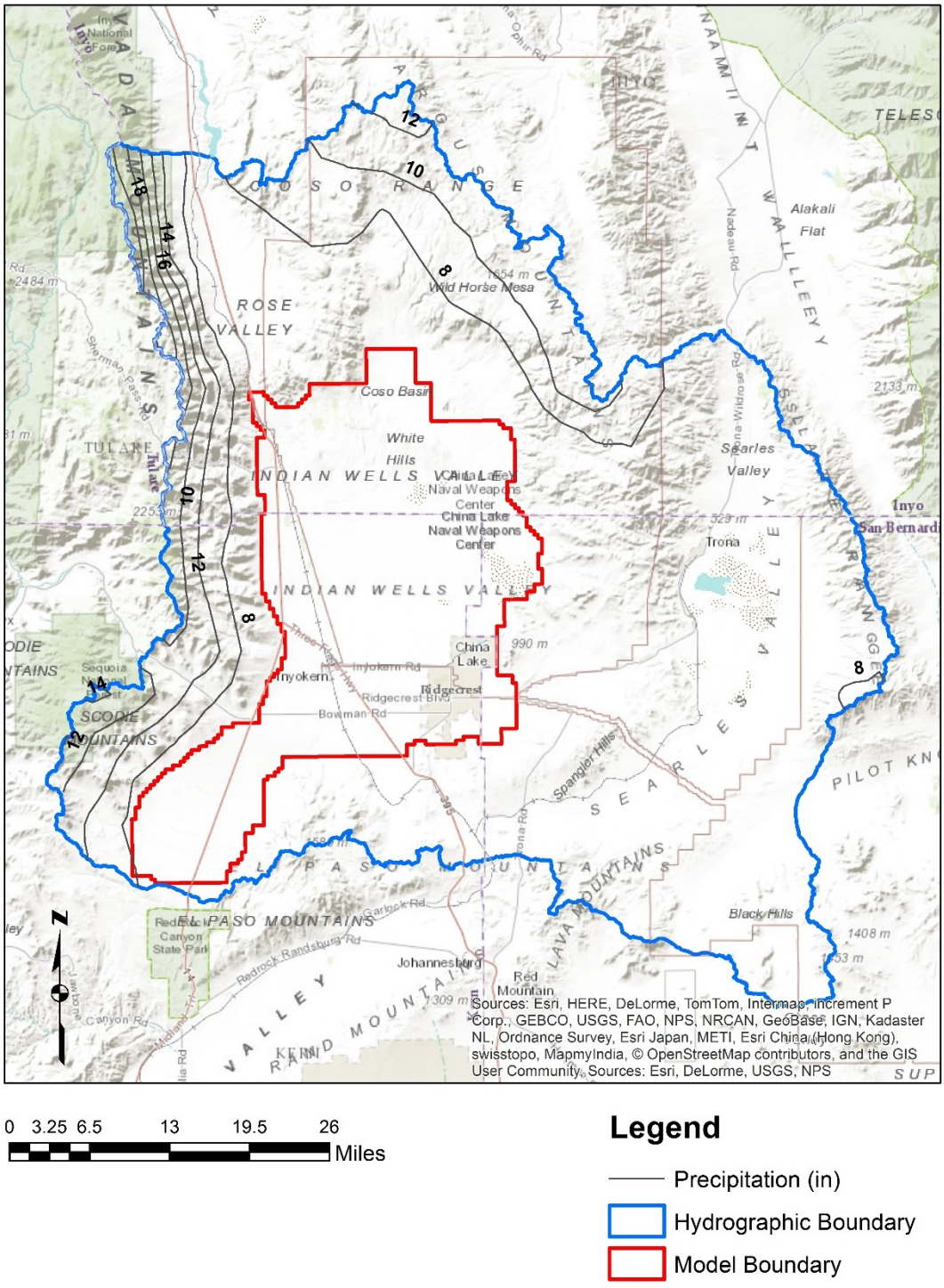

Figure 3. PRISM 30-year average annual precipitation two inch contours, 1981 to 2010.

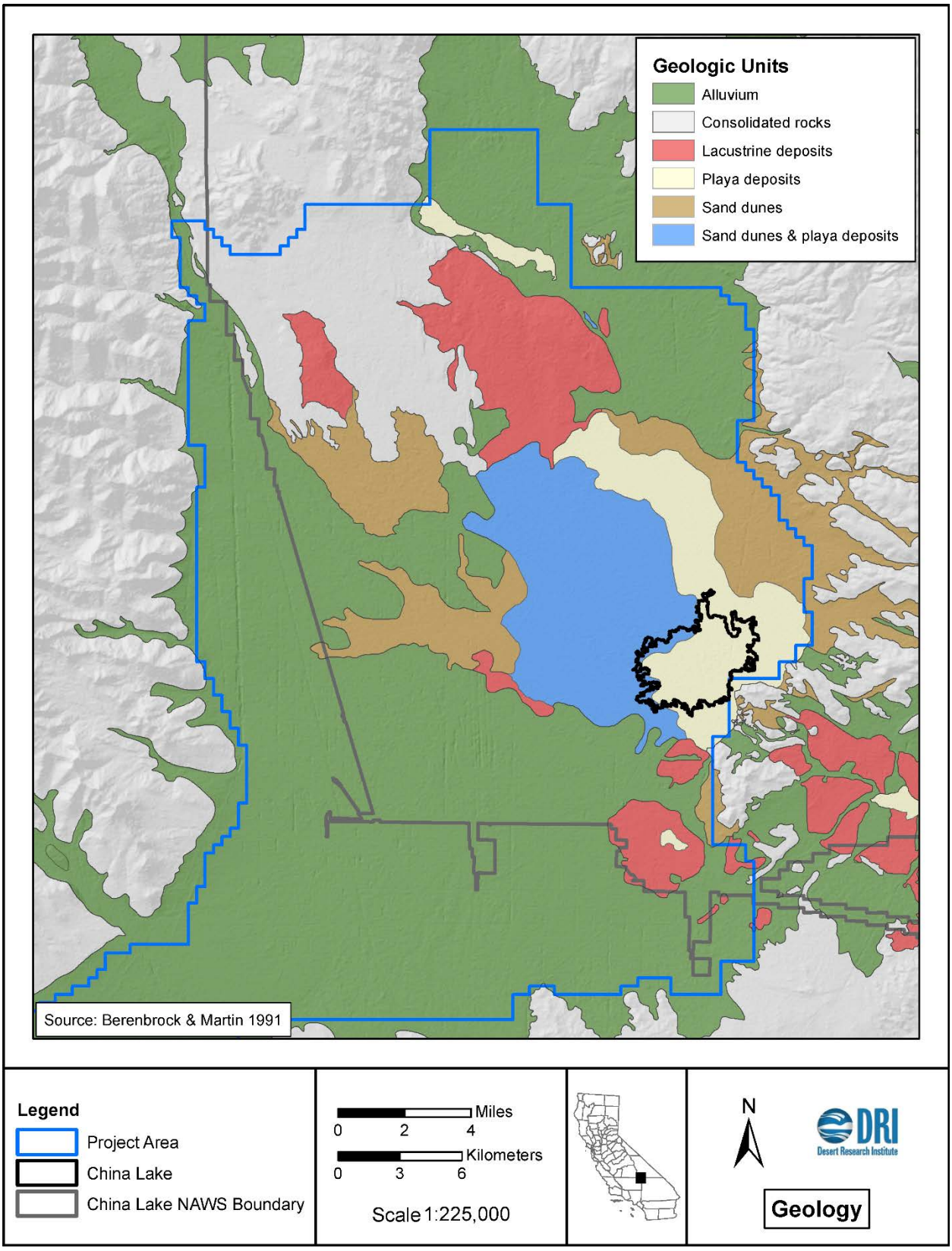

Figure 4. Surface geology of Indian Wells Valley (Berenbrock and Martin, 1991).

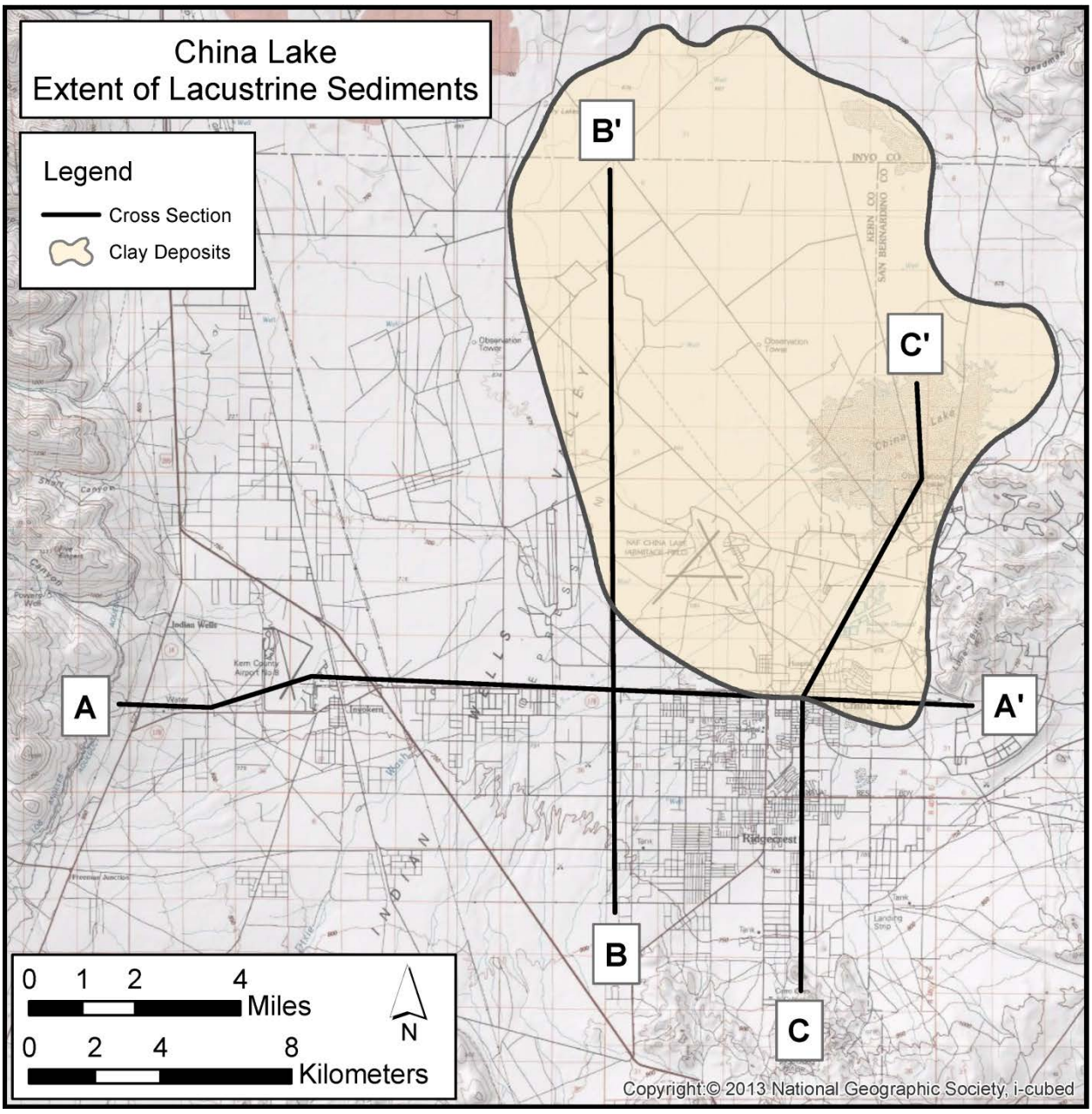

Figure 5. Spatial extent of clay lacustrine deposits in Indian Wells Valley. Cross sections (A-A', B-B', and C-C') are provided in Figure 6. Adapted from Kunkel and Chase (1969).

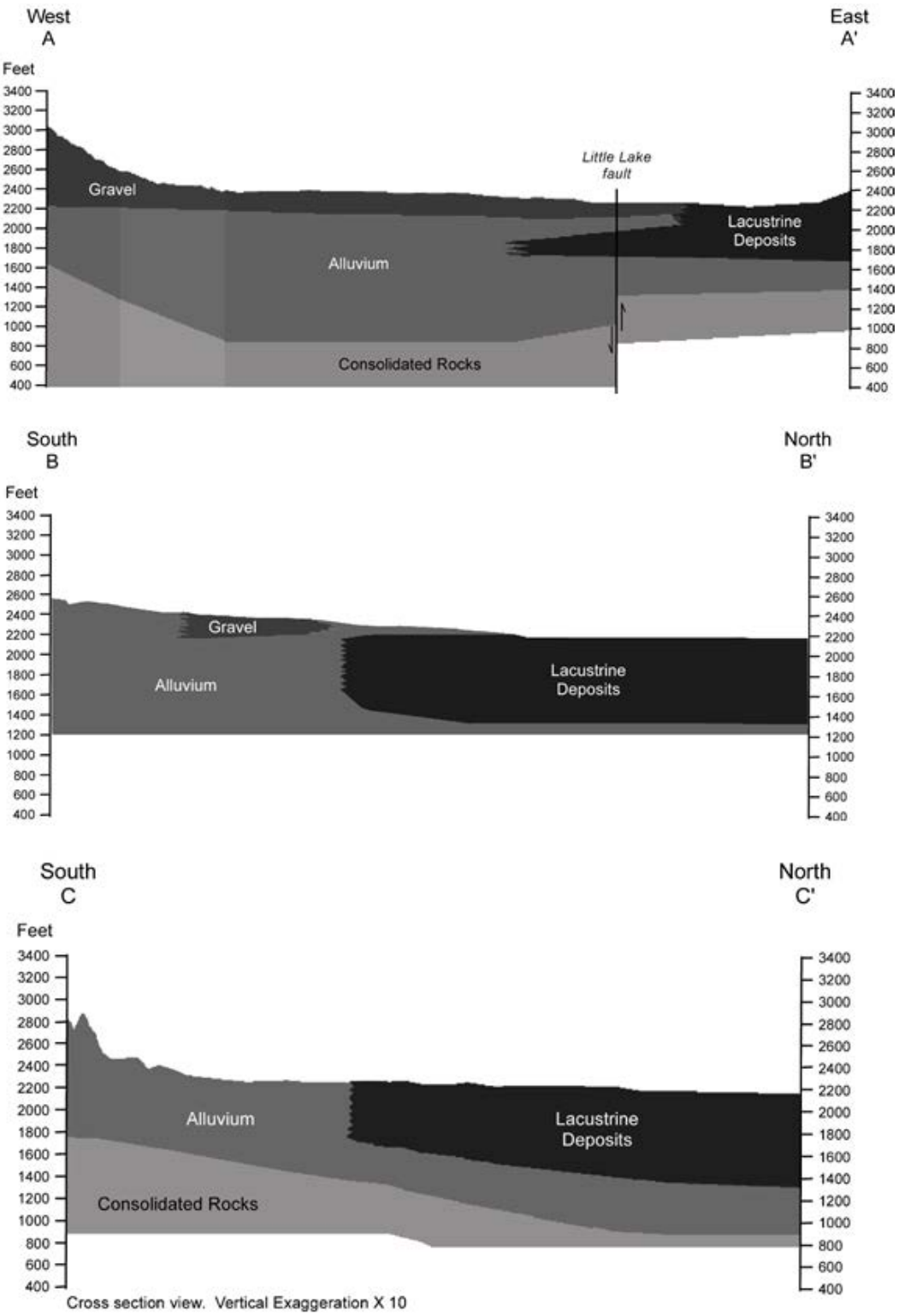

Figure 6. Cross sections identified in Figure 5 delineating clay lacustrine deposits from alluvium, gravel, and consolidated rocks. Adapted from Kunkel and Chase (1969).

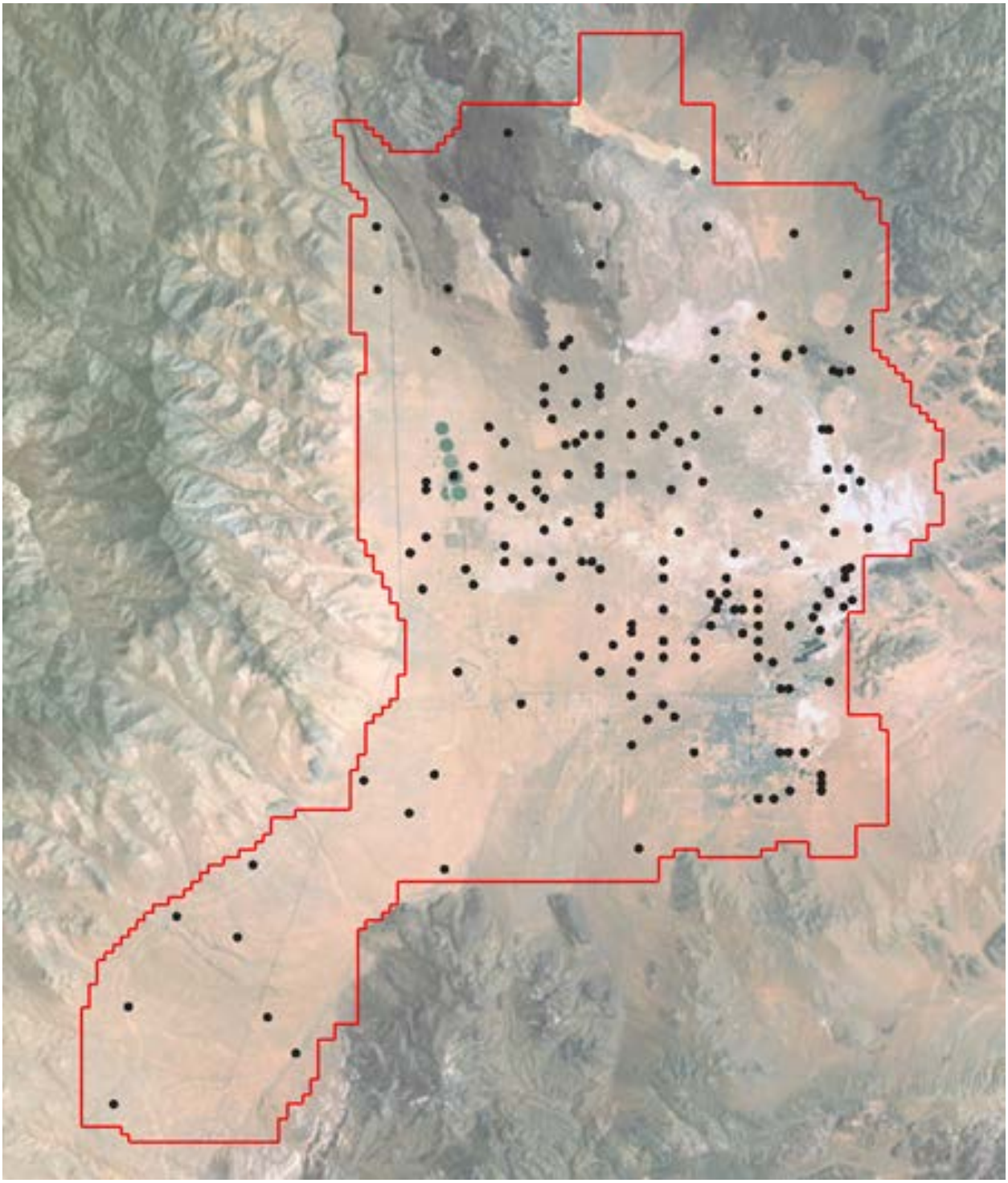

Figure 7. Observed water level locations prior to 1926 used in the steady-state model. It is assumed that early groundwater development from these wells was not significant, so they are used to represent pregroundwater development conditions.

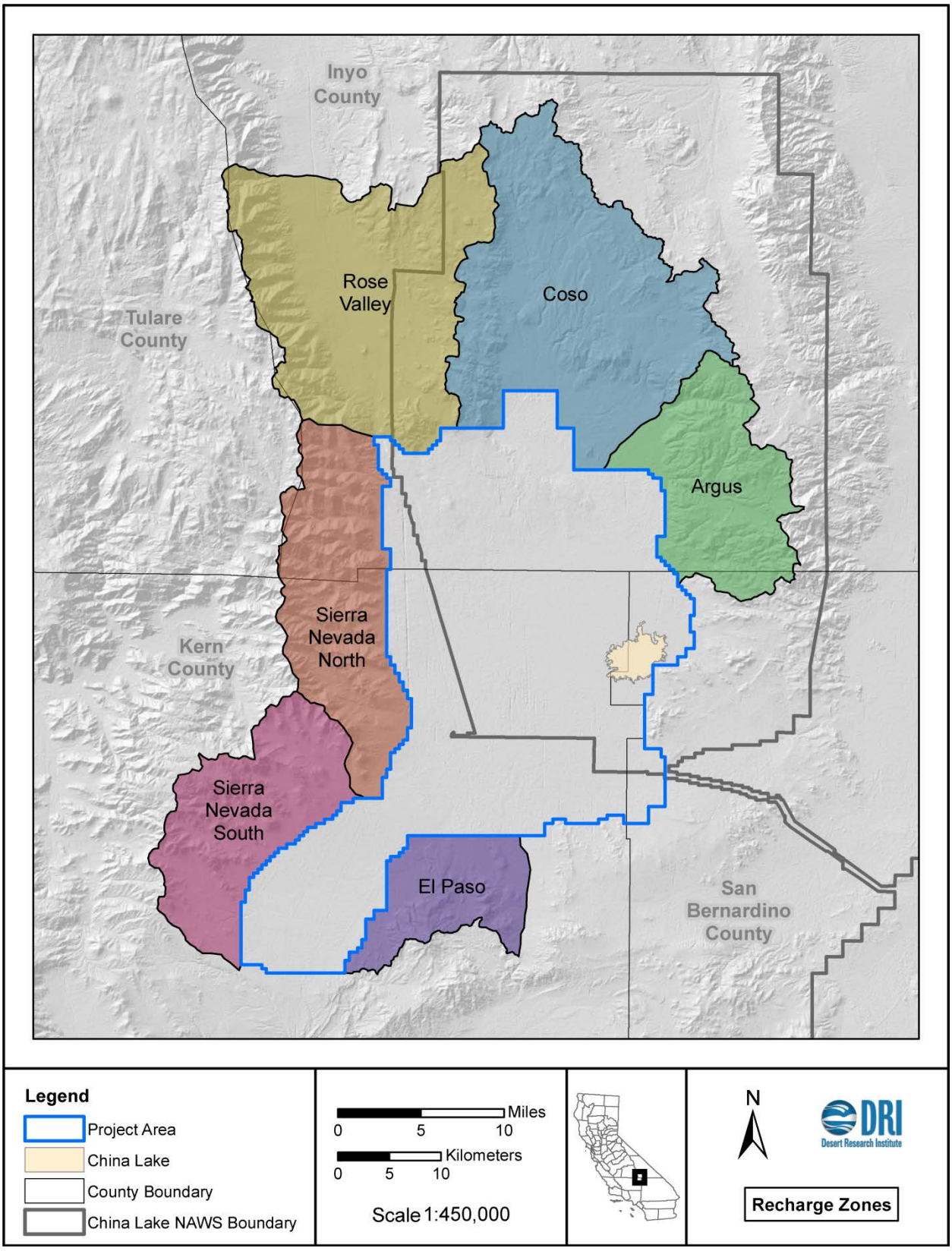

Figure 8. Six delineated mountain block recharge zones.

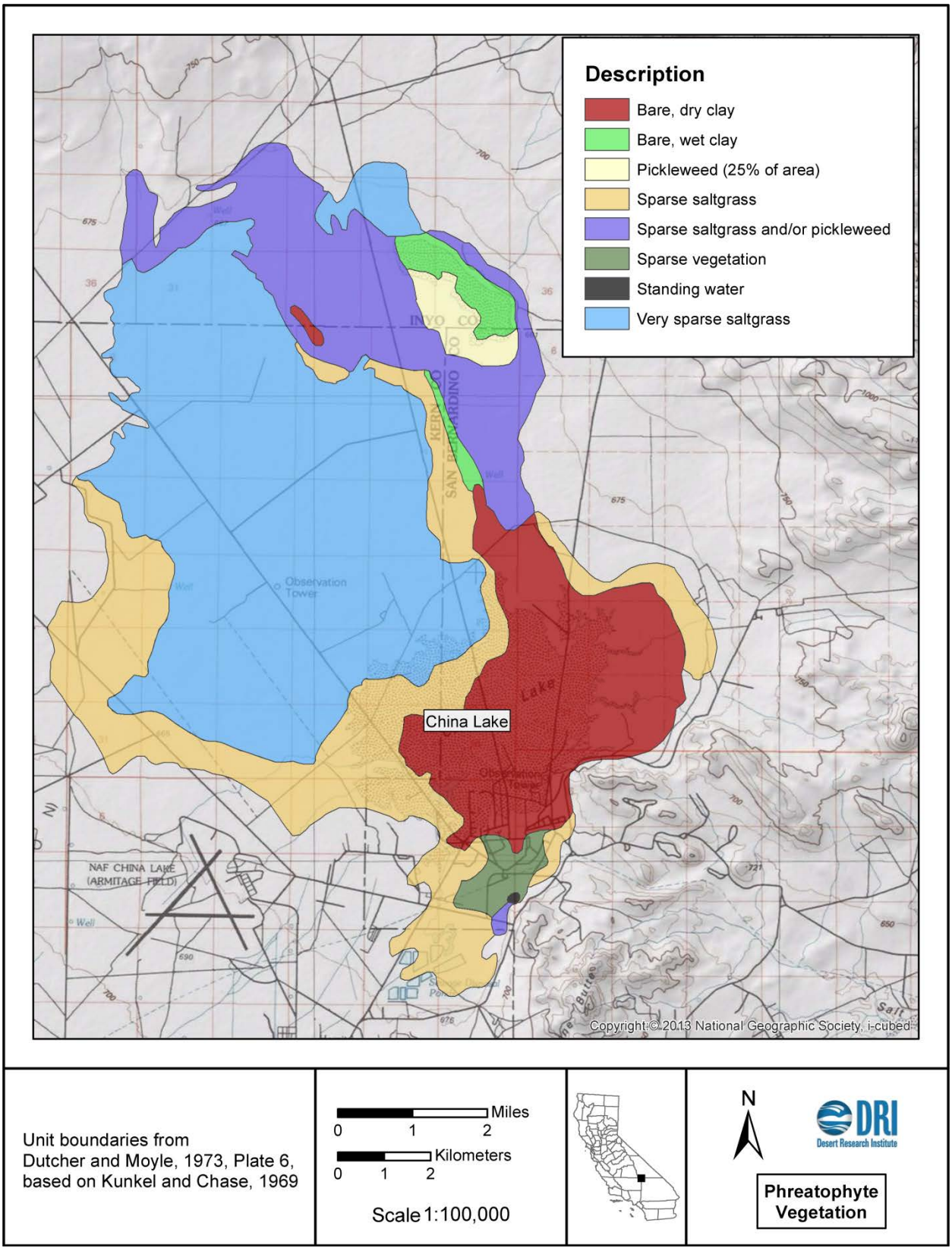

Figure 9. Phreatophyte vegetation zones for evapotranspiration groundwater discharge analysis (modified from Lee [1912]).

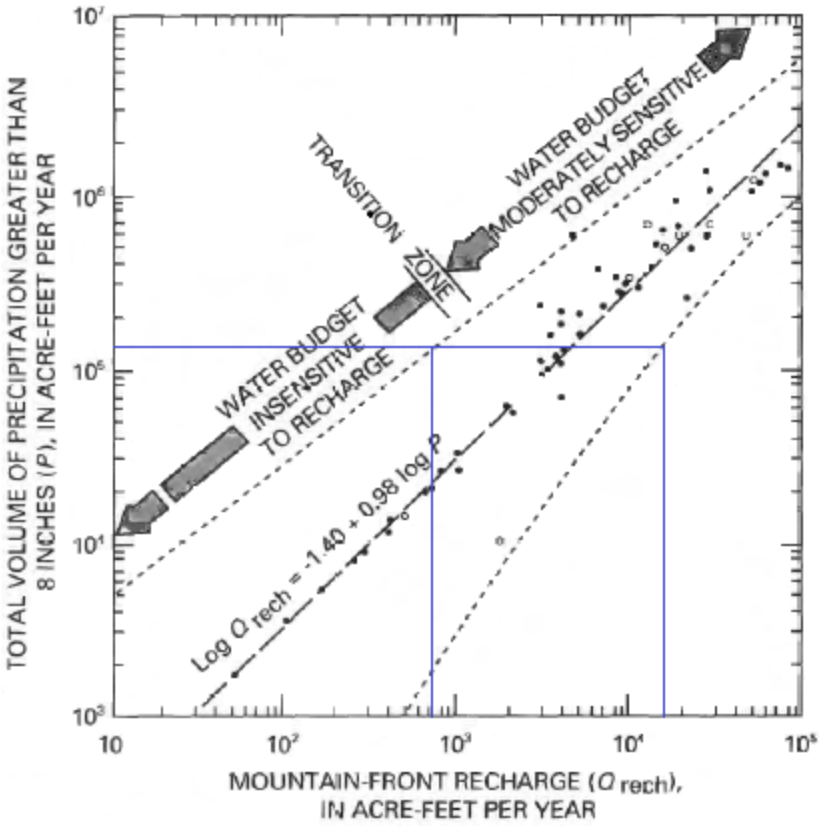

Figure 10. Relationship between annual precipitation volume and annual recharge (developed by Anderson *et al*. [1992]).

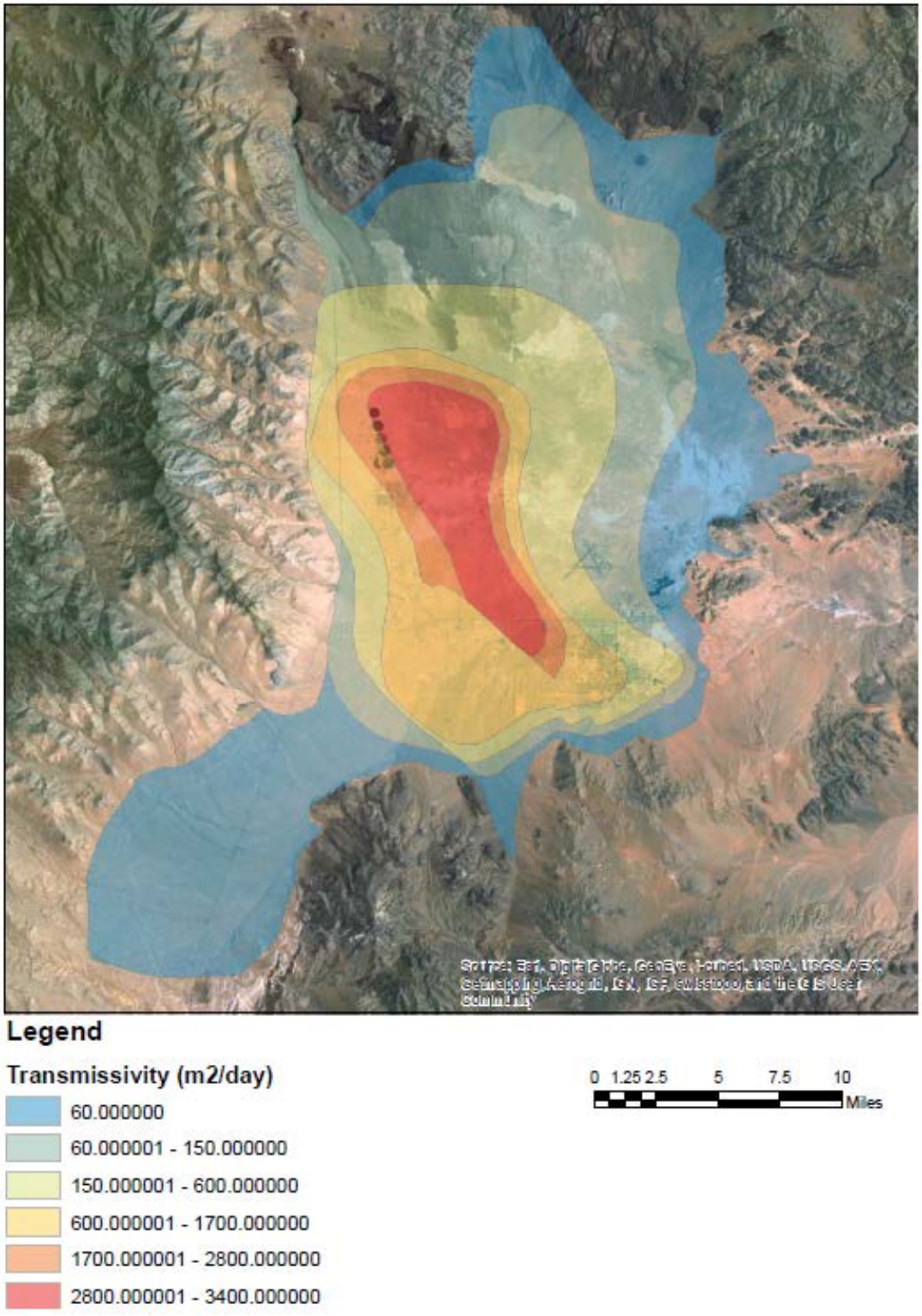

Figure 11. Distribution of transmissivity based on Dutcher and Moyle (1973).

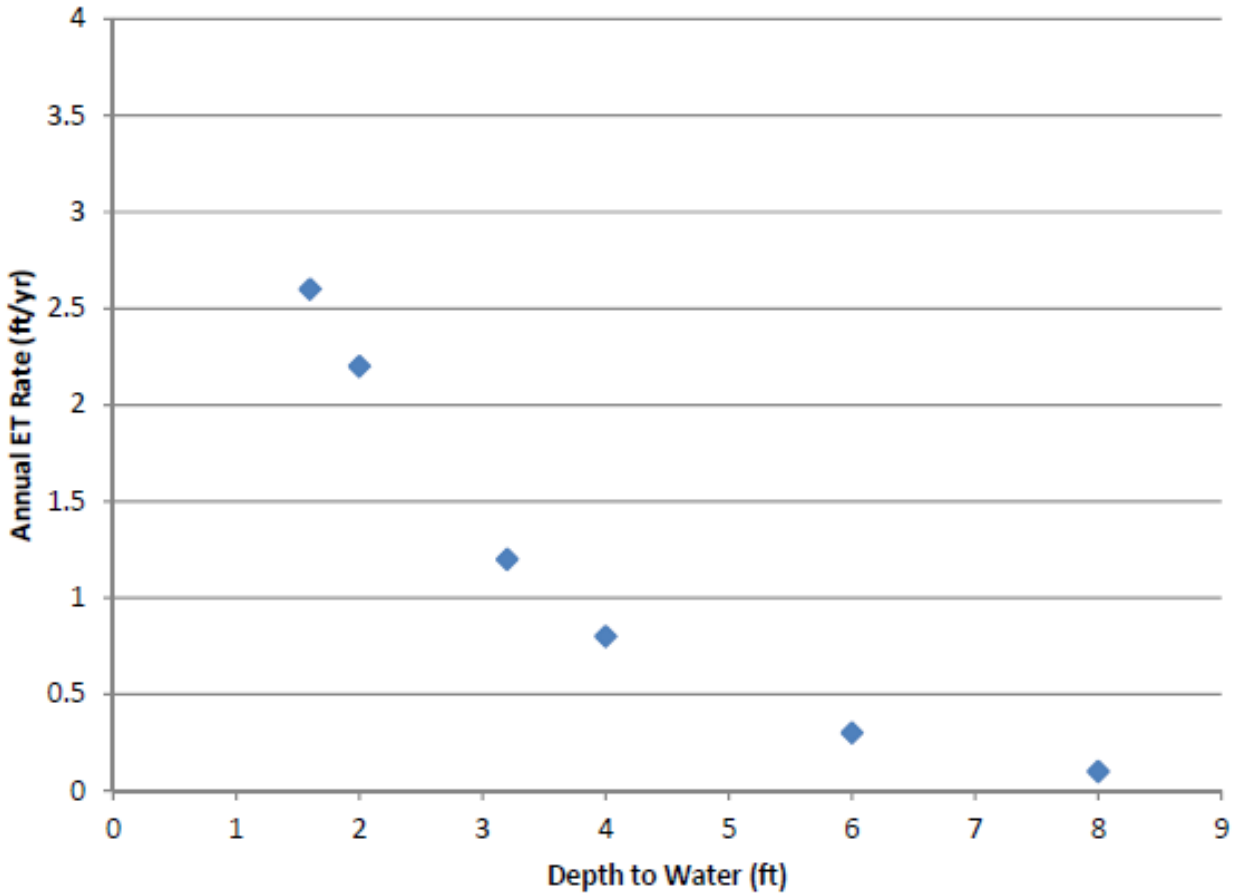

Figure 12. Depth to water table versus annual evapotranspiration rate obtained from Kunkel and Chase (1969) for the 25 percent vegetative cover.

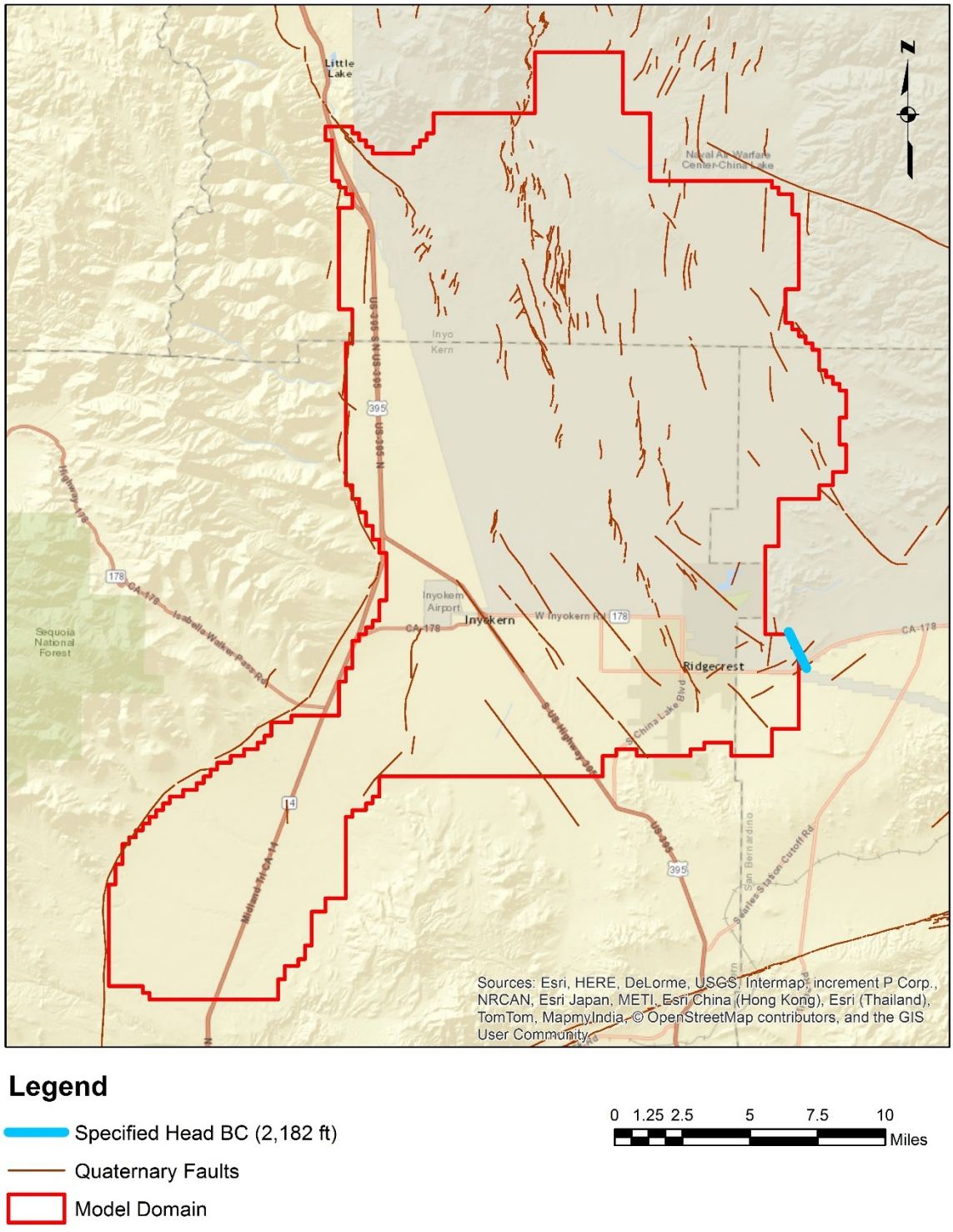

Figure 13. Specified head boundary condition of 2,182 ft to allow groundwater flow to Salt Wells Valley.

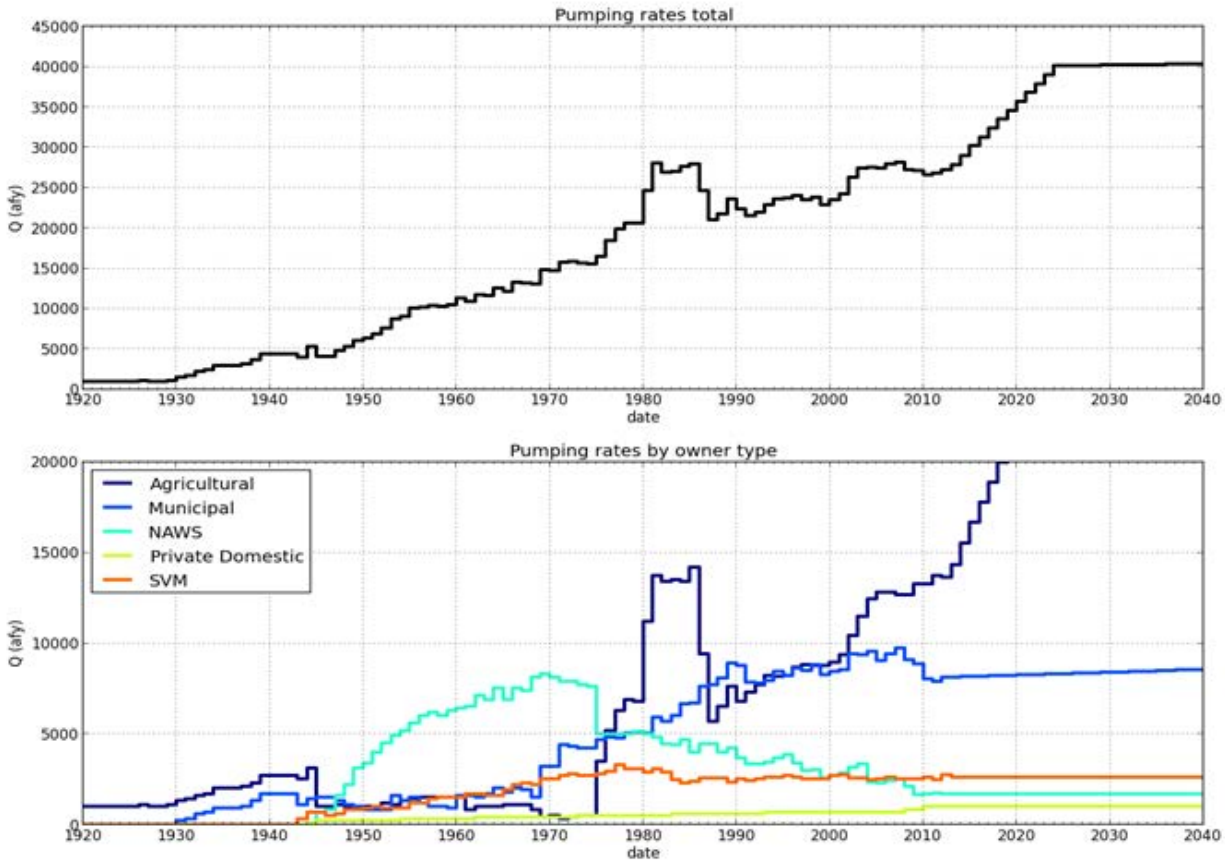

Figure 14. Historical and estimated annual pumping rate totals (Q, afy) by water use category. Pumping rate data obtained from Brown and Caldwell (2006) and Todd Engineers (2014).

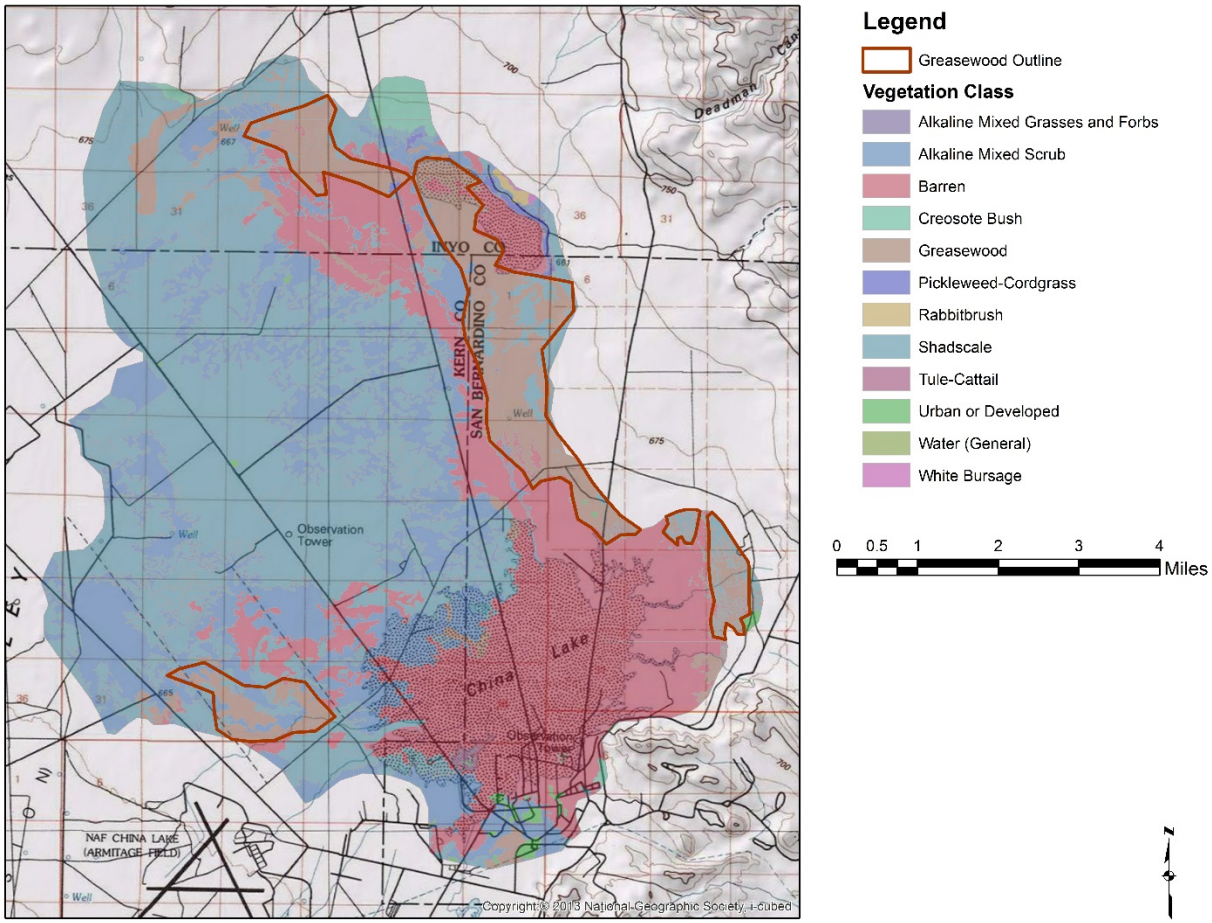

Figure 15. Map showing the distribution of vegetation and bare ground within the area of evapotranspiration (ET) used in the groundwater model. Mapping is based on the 2013 vegetation survey of Menke *et al*. (2013) and correlation to geomorphic map units of Bacon *et al*. (2015) in Bullard *et al*. (2015).

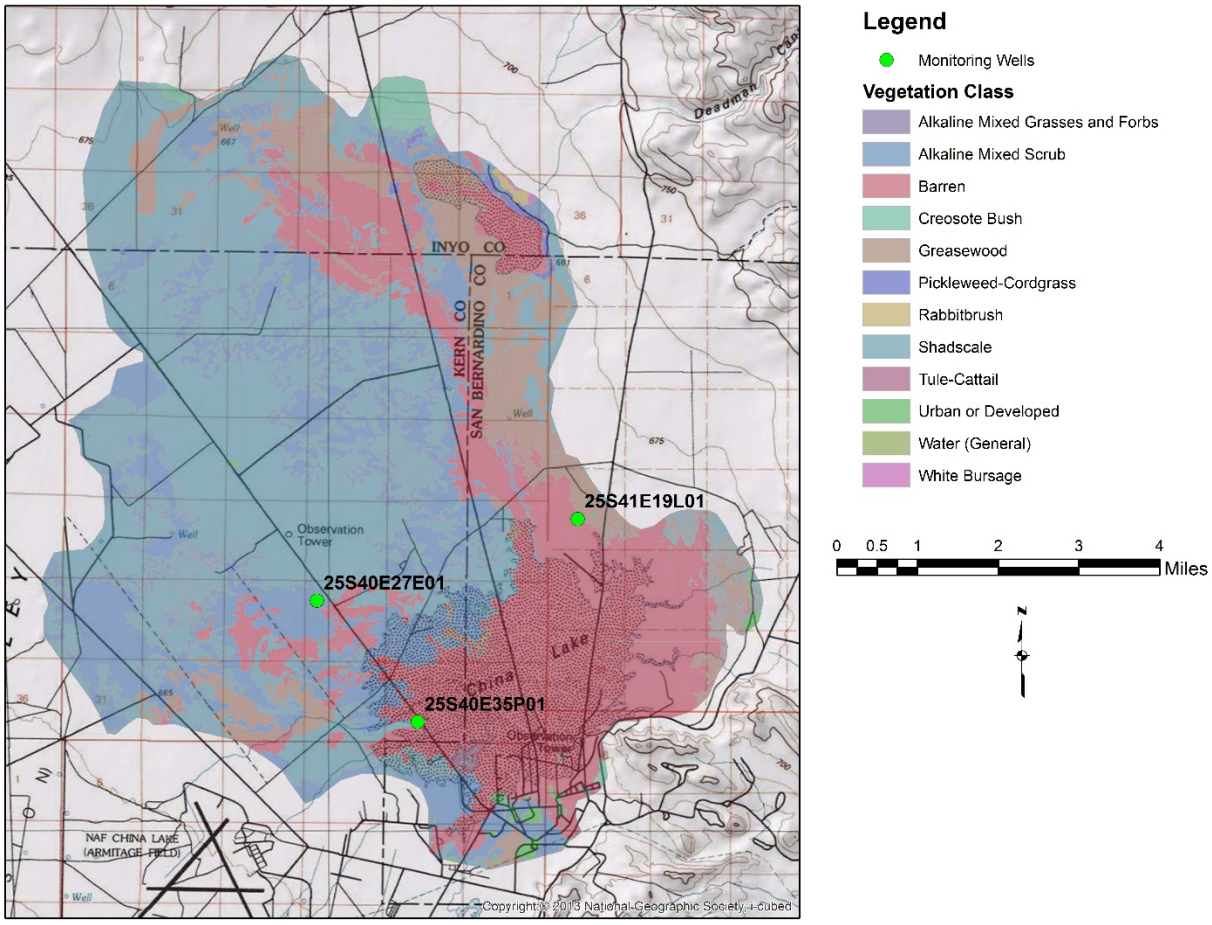

Figure 16. Shallow monitoring wells located in ET zone.

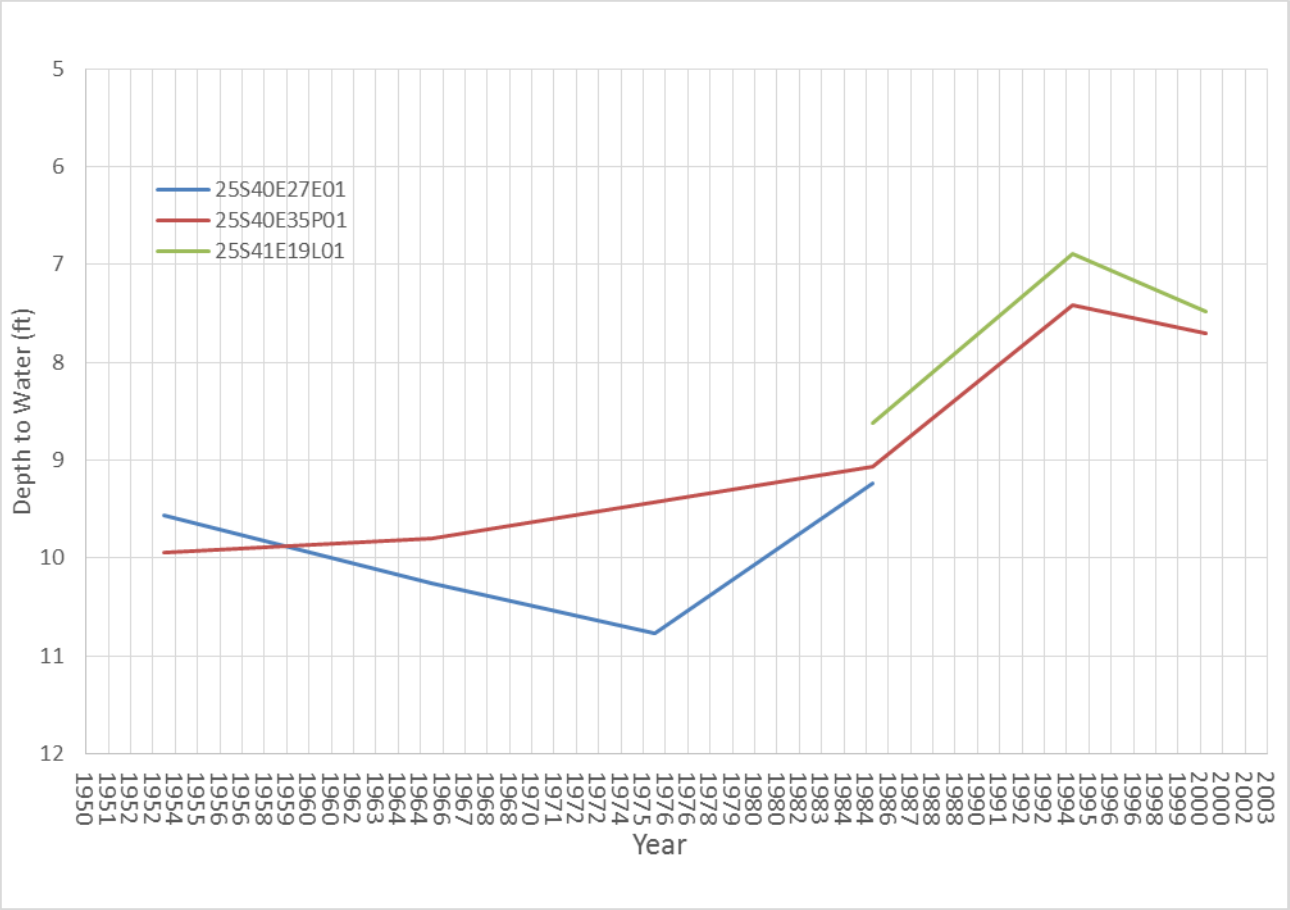

Figure 17. Depth to water (ft) for three monitoring wells located within ET zone used in groundwater model.

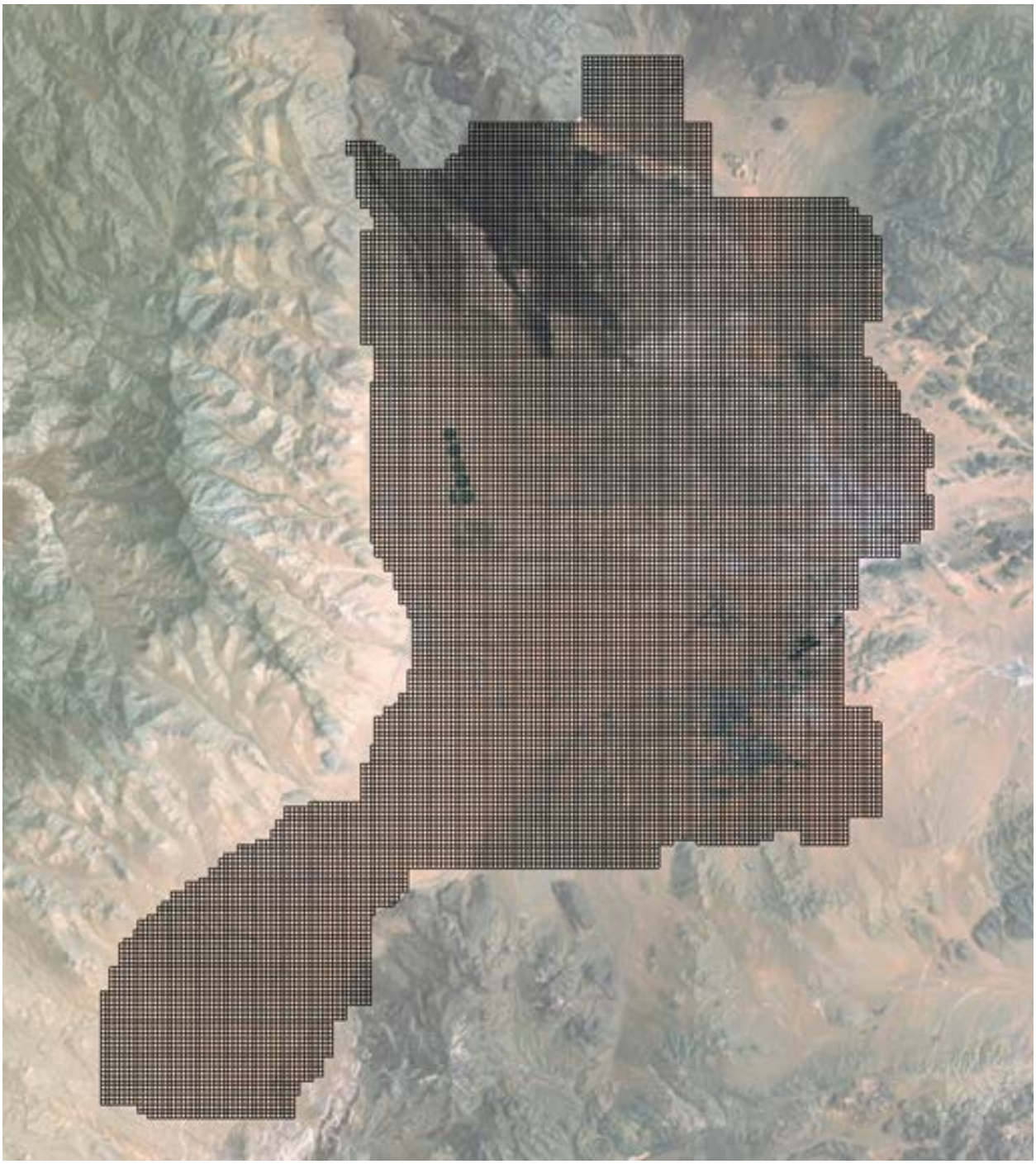

Figure 18. MODFLOW finite difference grid. Cell size is 820 ft (250 m) on a side. This represents the refined grid for the model compared with the larger grid used in the Brown and Caldwell (2009) model.

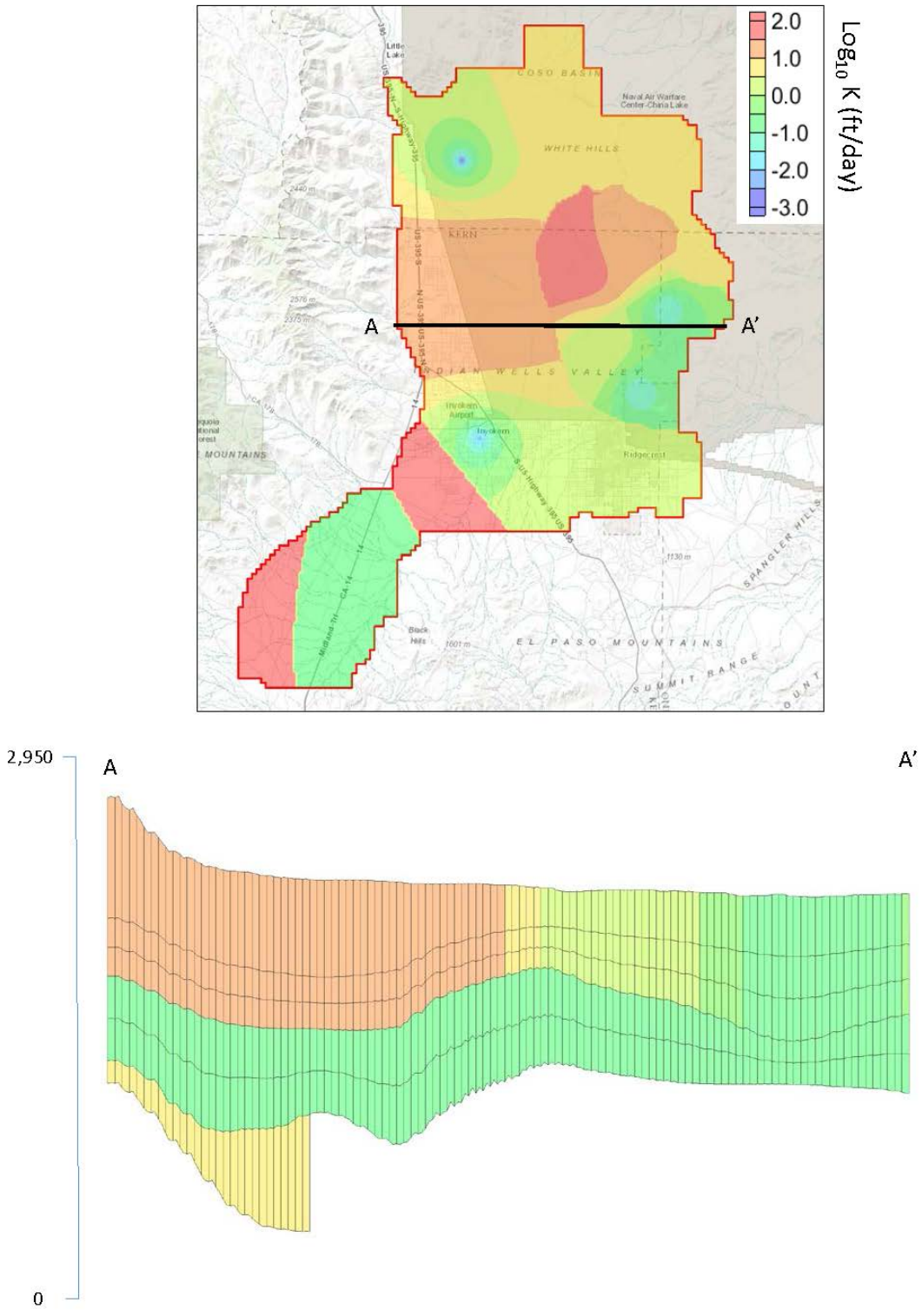

Figure 19. Hydraulic conductivity (K) zones determined using pilot-point calibration for the steady-state model. Plan view map depicts the three uppermost layers. Note that hydraulic conductivity values are $\log_{10}$ transformed with original units in ft/d.

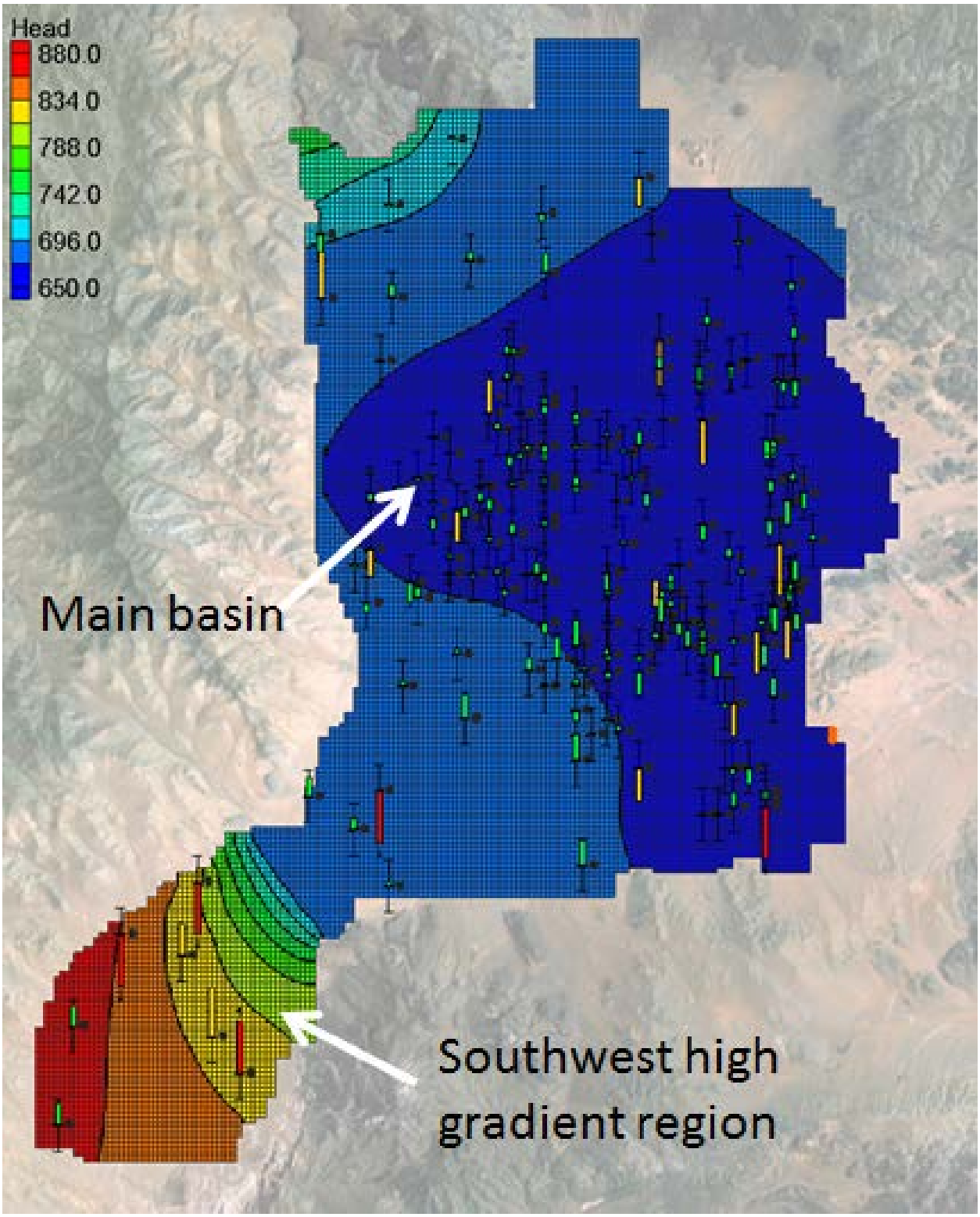

Figure 20. Steady-state modeled heads with error in target values shown with error bars. Green indicates error less than 6.6 ft, yellow indicates error less than 13.1 ft, and red indicates error greater than 13.1 ft.

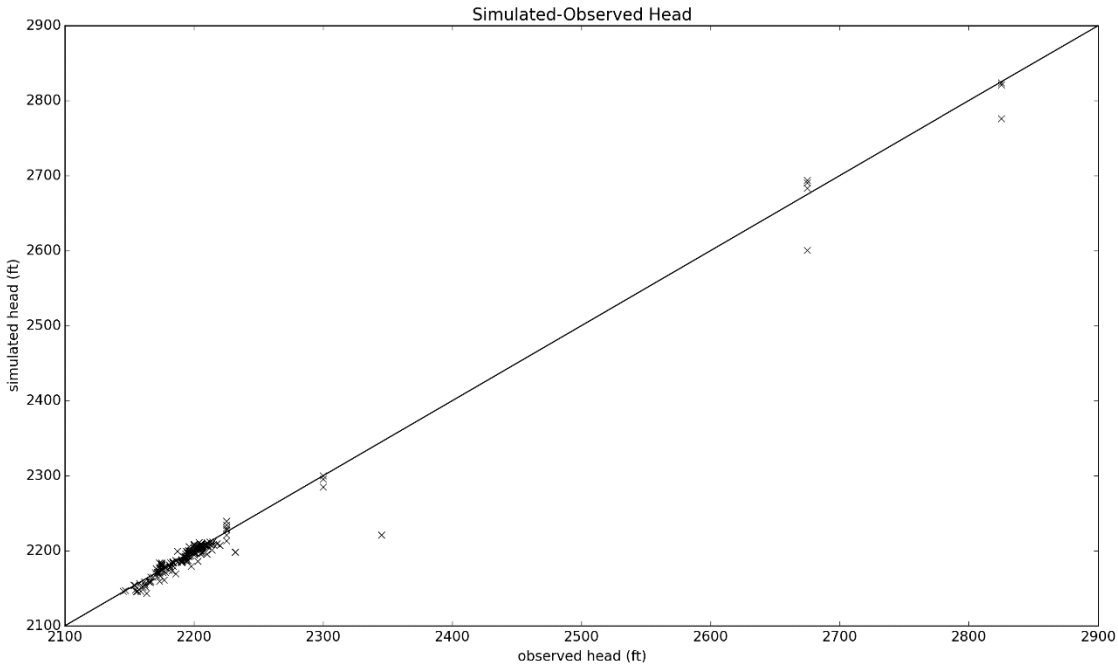

Figure 21. Simulated versus observed head for the steady-state model.

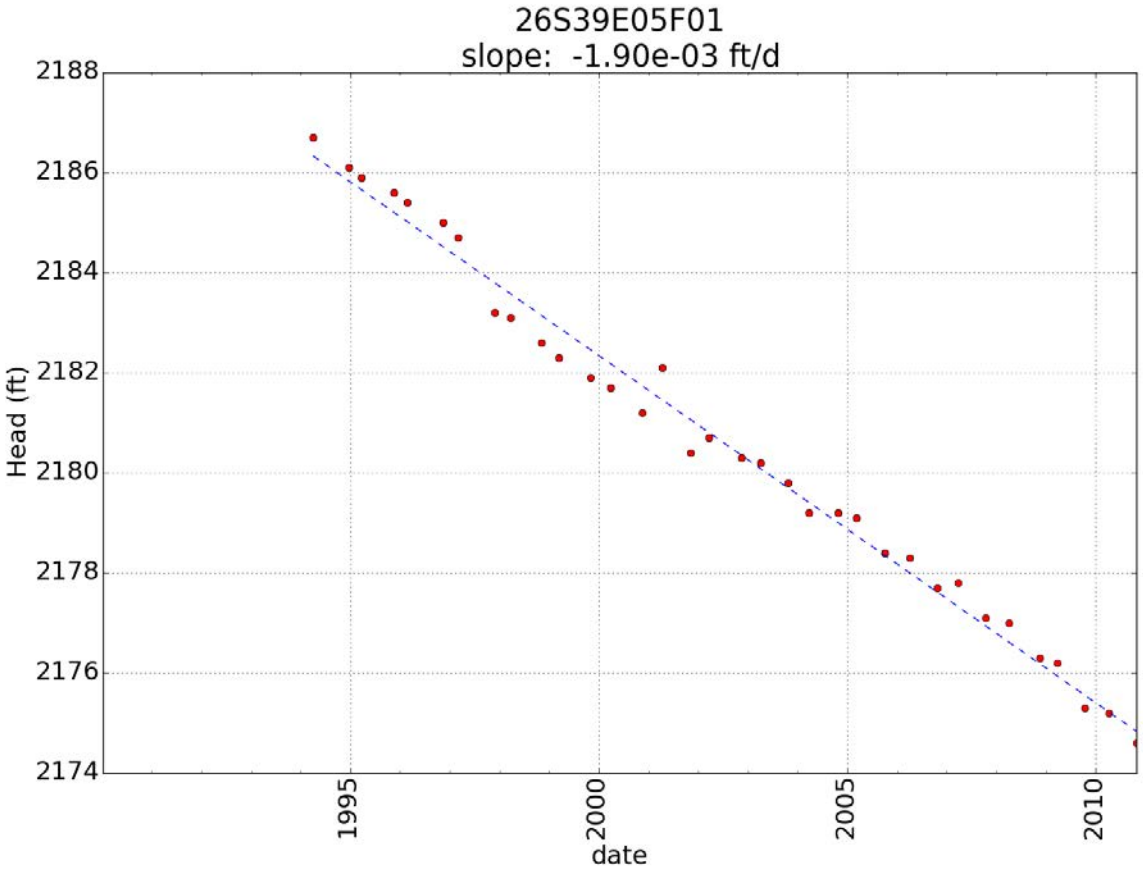

Figure 22. Example of observed drawdown analysis in well 26S39E05F01 for 1990 to 2010. Slope of the drawdown curve in this example is 0.0019 ft/d.

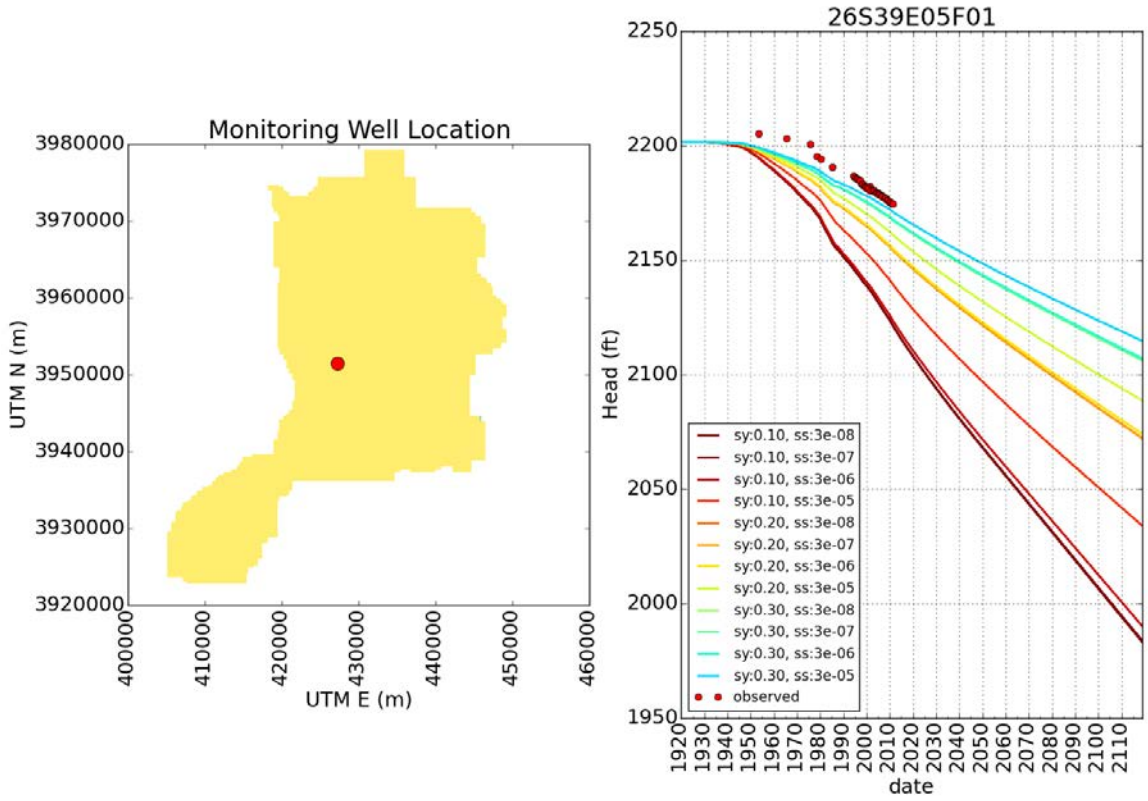

Figure 23. A comparison of drawdown curves for well 26S39E05F01 for years 1990 to 2010 over a range of Ss-Sy combinations.

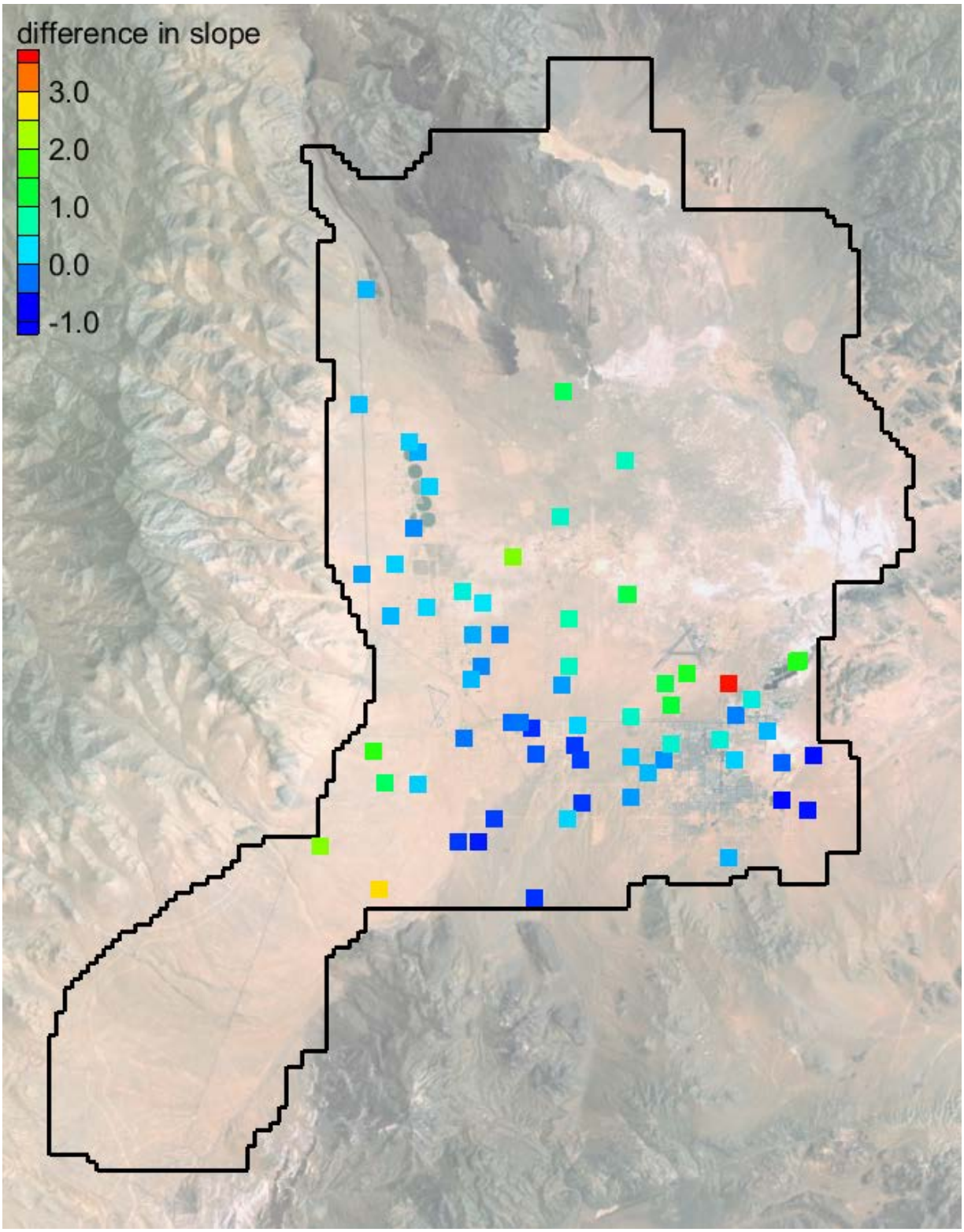

Figure 24. Spatial distribution in prediction error of observed drawdown slope. Error is in log-space so that each unit of error represents one-order of magnitude.

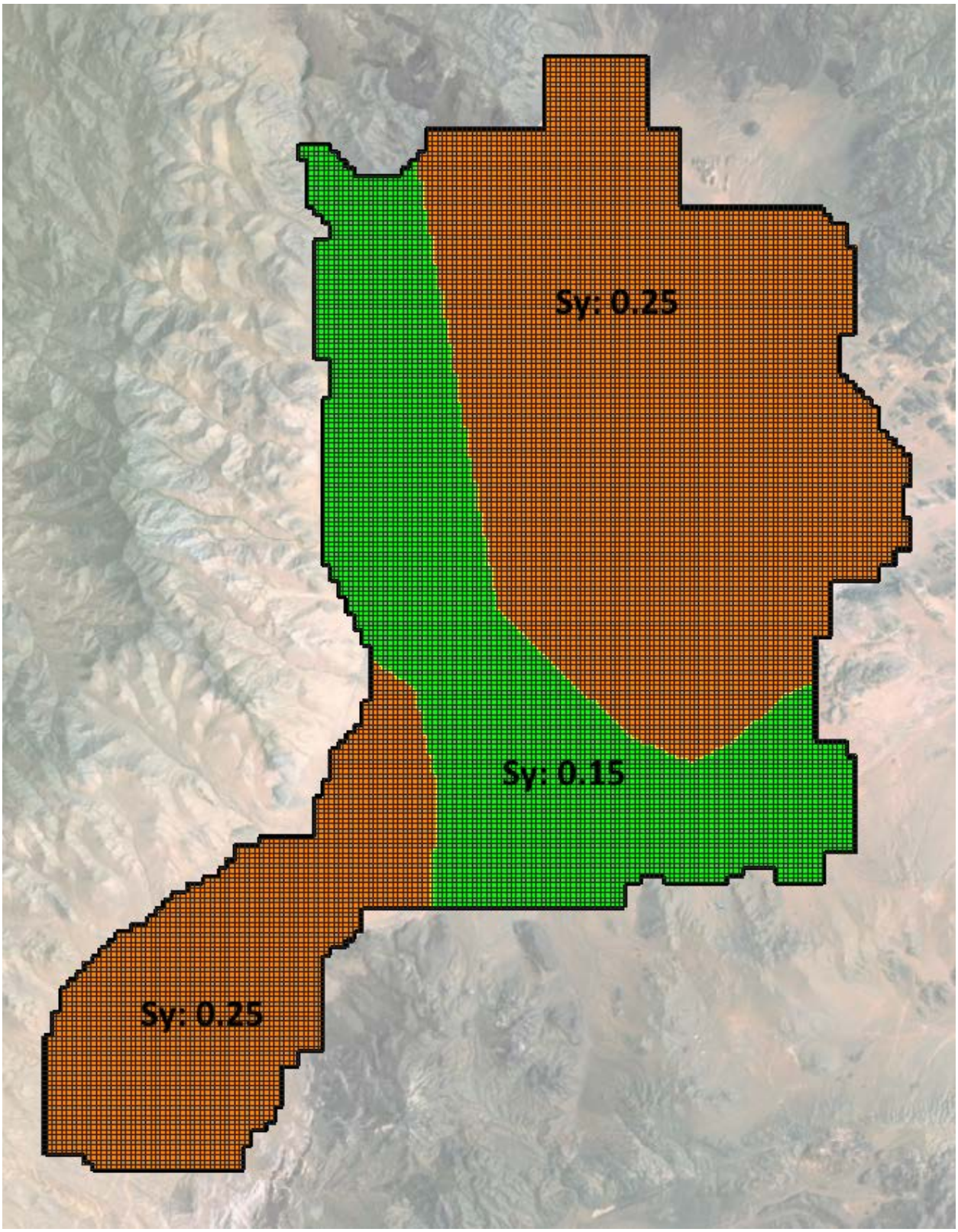

Figure 25. Zones of Sy used in all layers of the model.

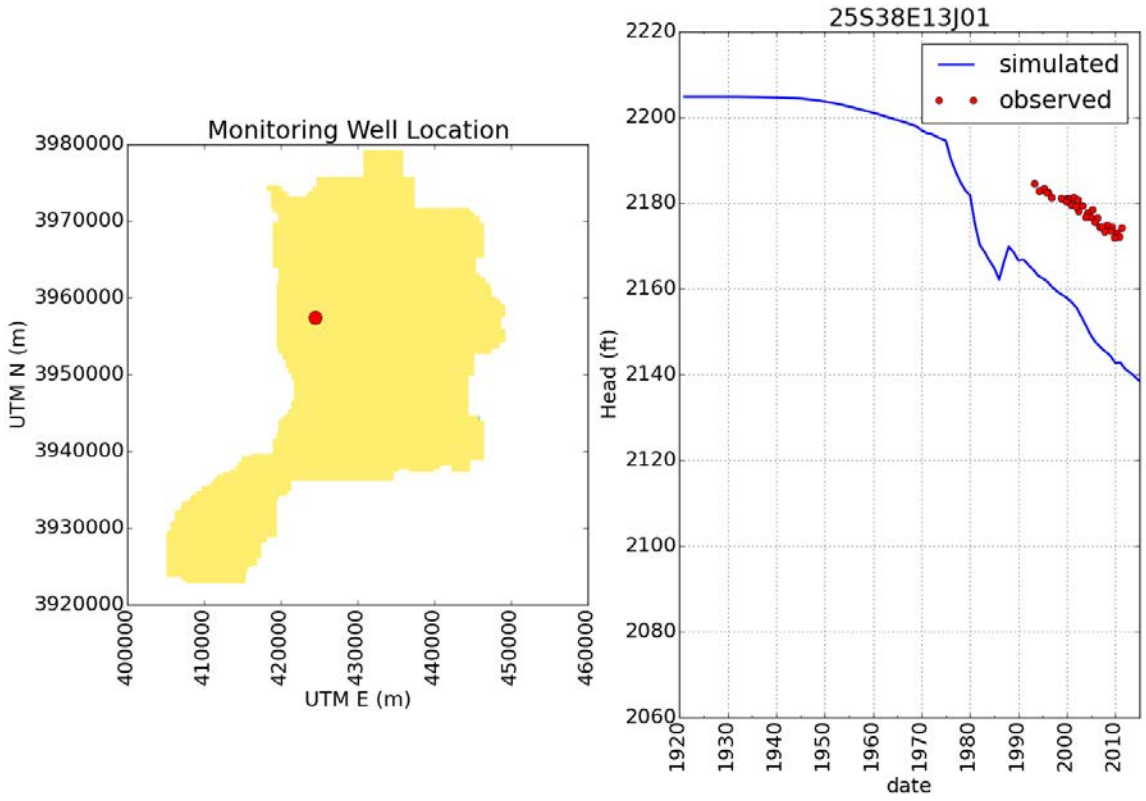

Figure 26. Comparison of simulated and observed drawdown in well 25S38E13J01.

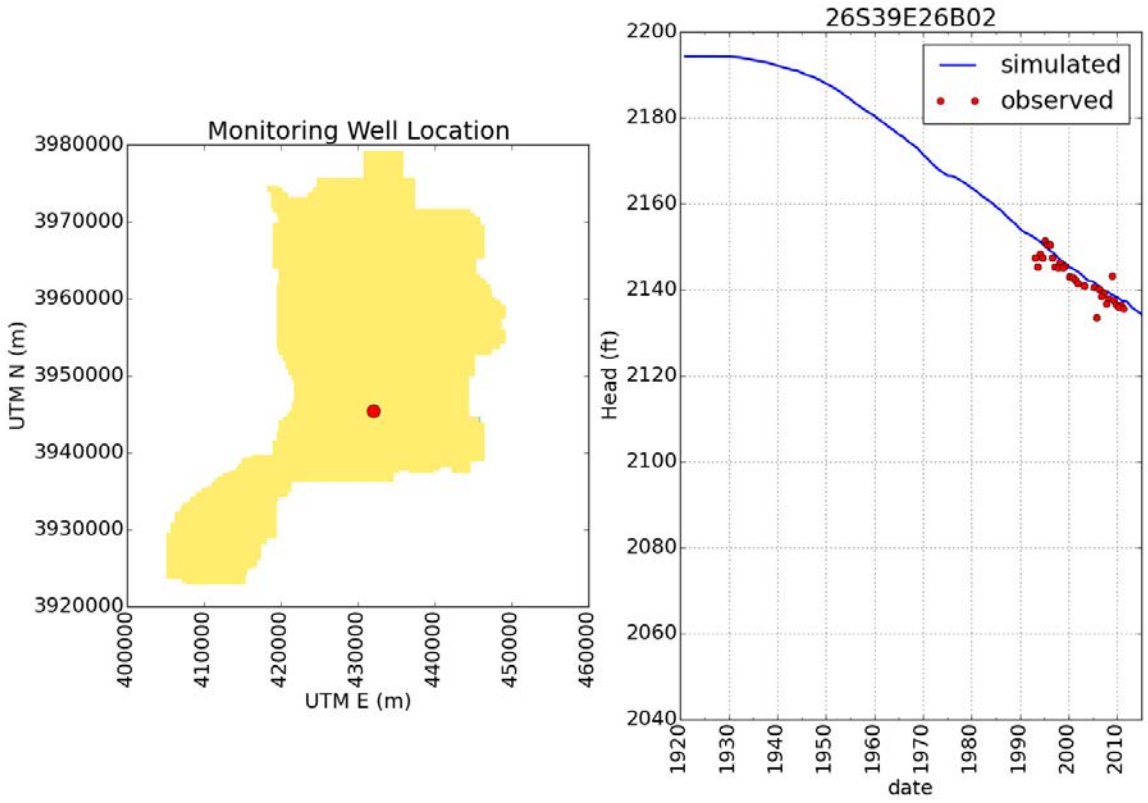

Figure 27. Comparison of simulated and observed drawdown in well 26S39E26B02.

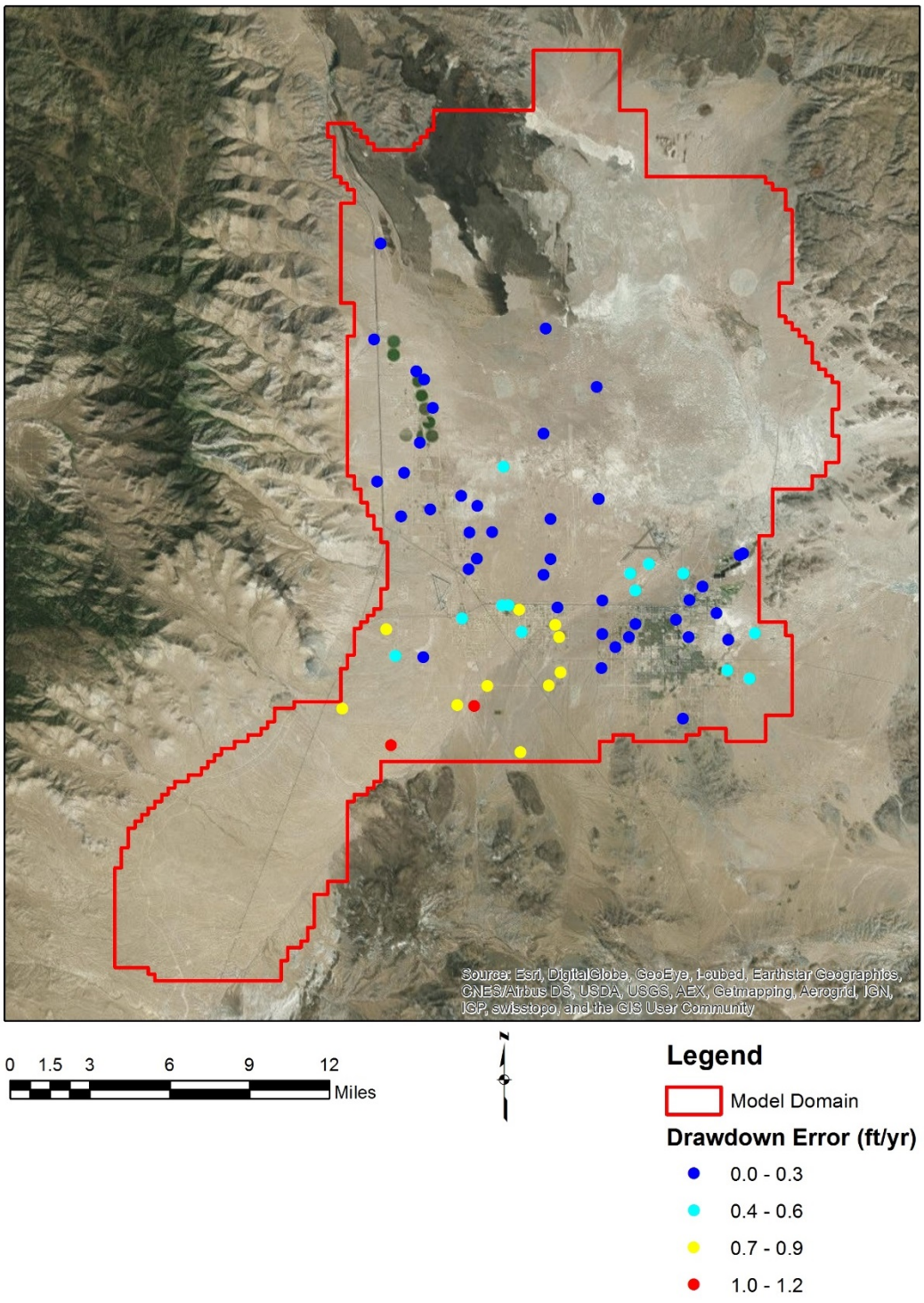

Figure 28. Updated spatial distribution in prediction error of observed drawdown slope using zones in layer 1 for Sy and Ss = 3.0E-07 (1/ft). Red circles indicate wells with error greater than one order of magnitude.

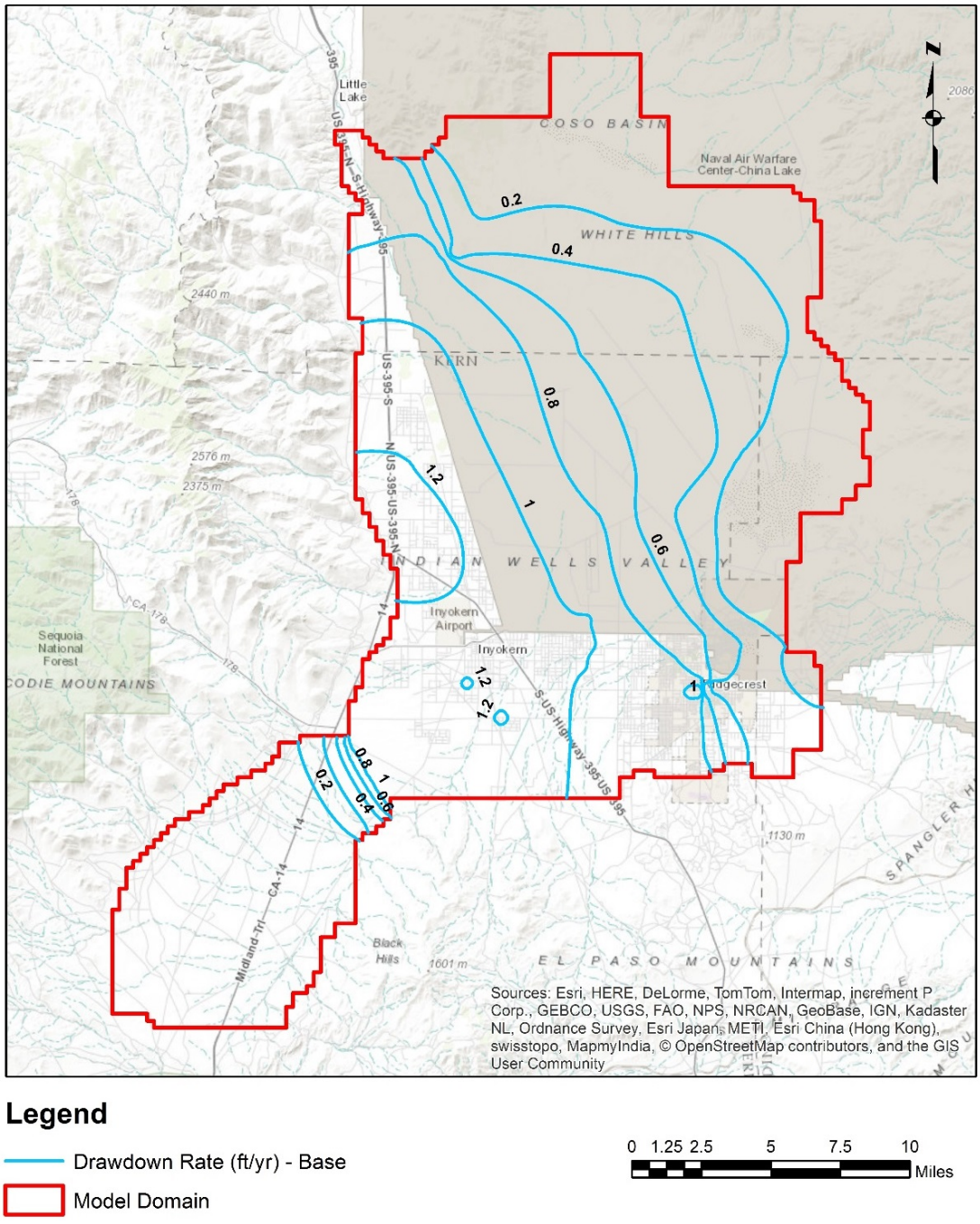

Figure 29. Predicted annual drawdown rate (ft/yr) between 2010 and 2120

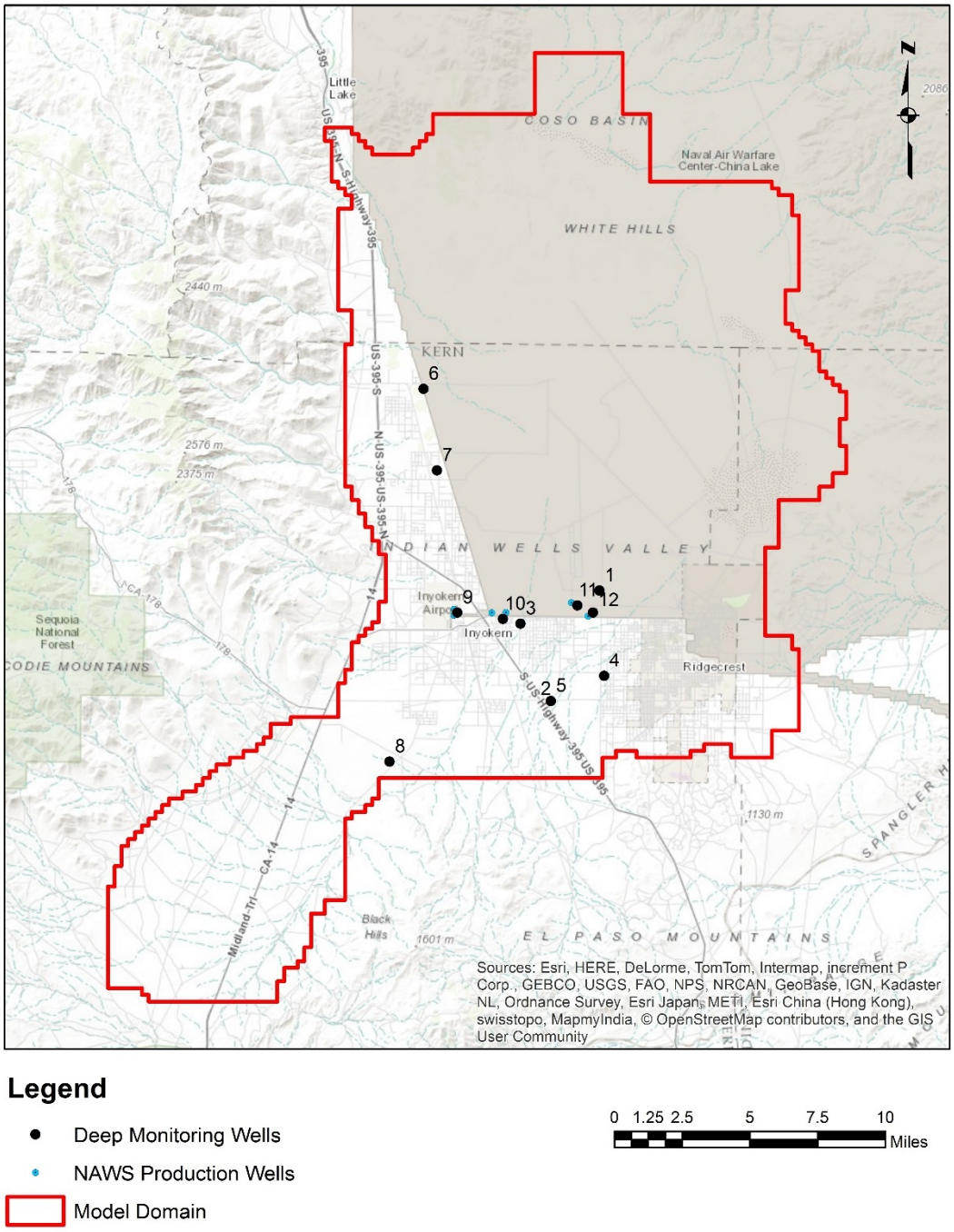

Figure 30. Selected monitoring wells used to evaluate the alternative conceptualizations. The locations of the NAWS production wells are also shown.

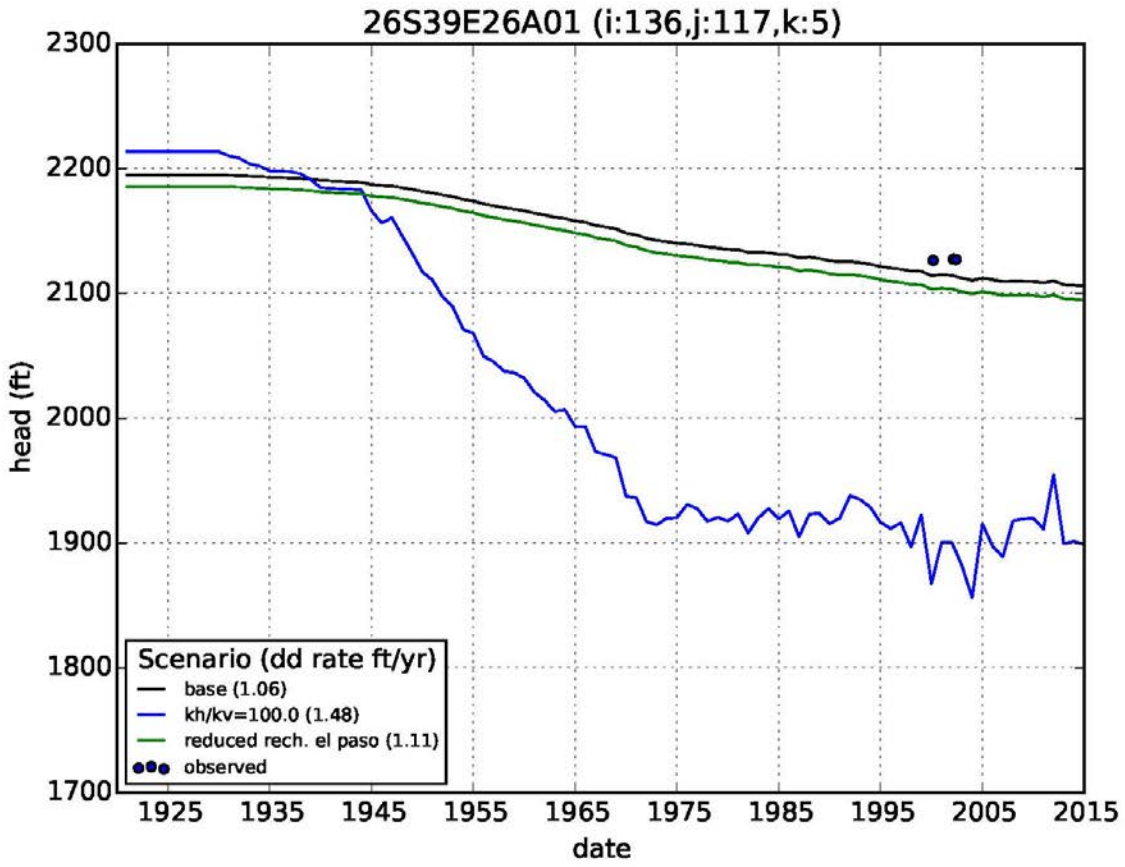

Figure 31. Simulated hydraulic head for the base model and two alternative conceptualizations at monitoring well 26S39E26A01 (labeled #1 on Figure 30). The alternative conceptual models include an isolated deep and shallow aquifer (simulated with an increased Kx/Kz= 100) and reduced recharge in the El Paso Basin. Note that kh/kv as shown in the legend is equivalent to Kx/Kz as noted in the caption.

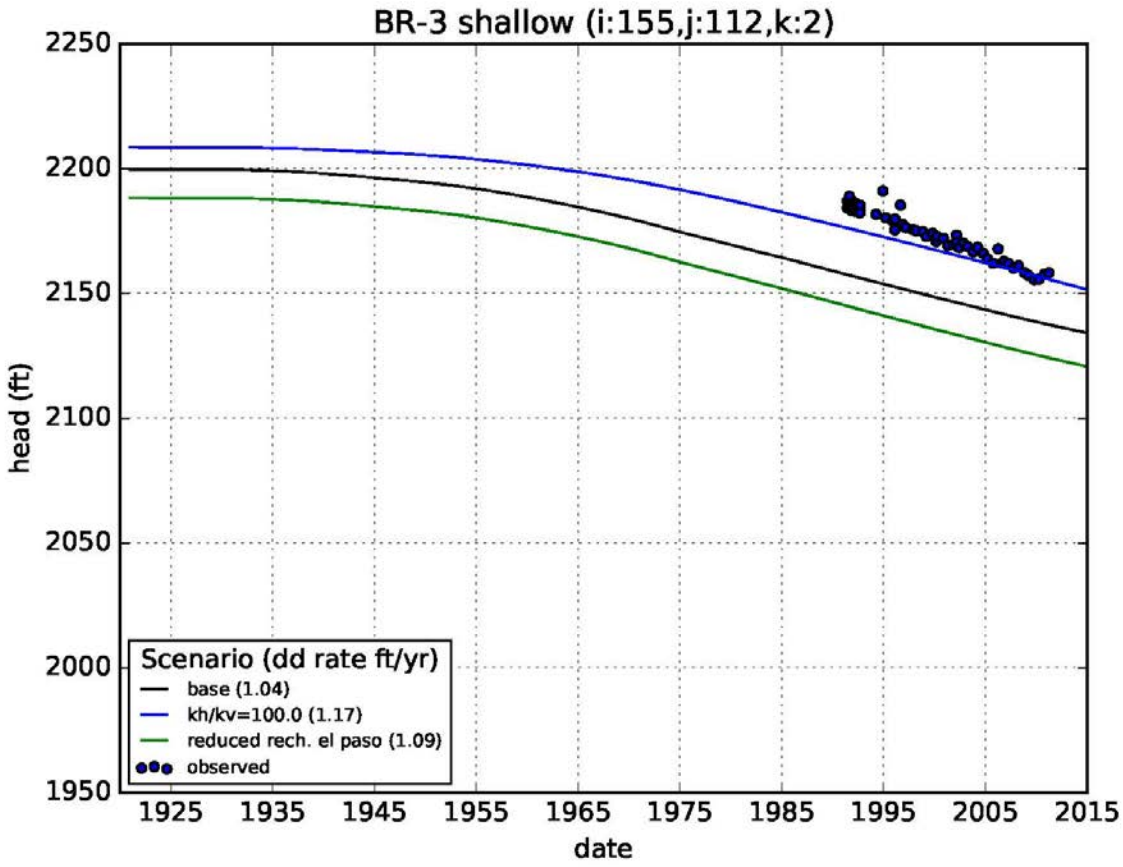

Figure 32. Simulated hydraulic head for the base model and two alternative conceptualizations at monitoring well BR-3 shallow (labeled #2 on Figure 30). The alternative conceptual models include an isolated deep and shallow aquifer (simulated with an increased Kx/Kz = 100) and reduced recharge in the El Paso Basin. Note that kh/kv as shown in the legend is equivalent to Kx/Kz as noted in the caption.

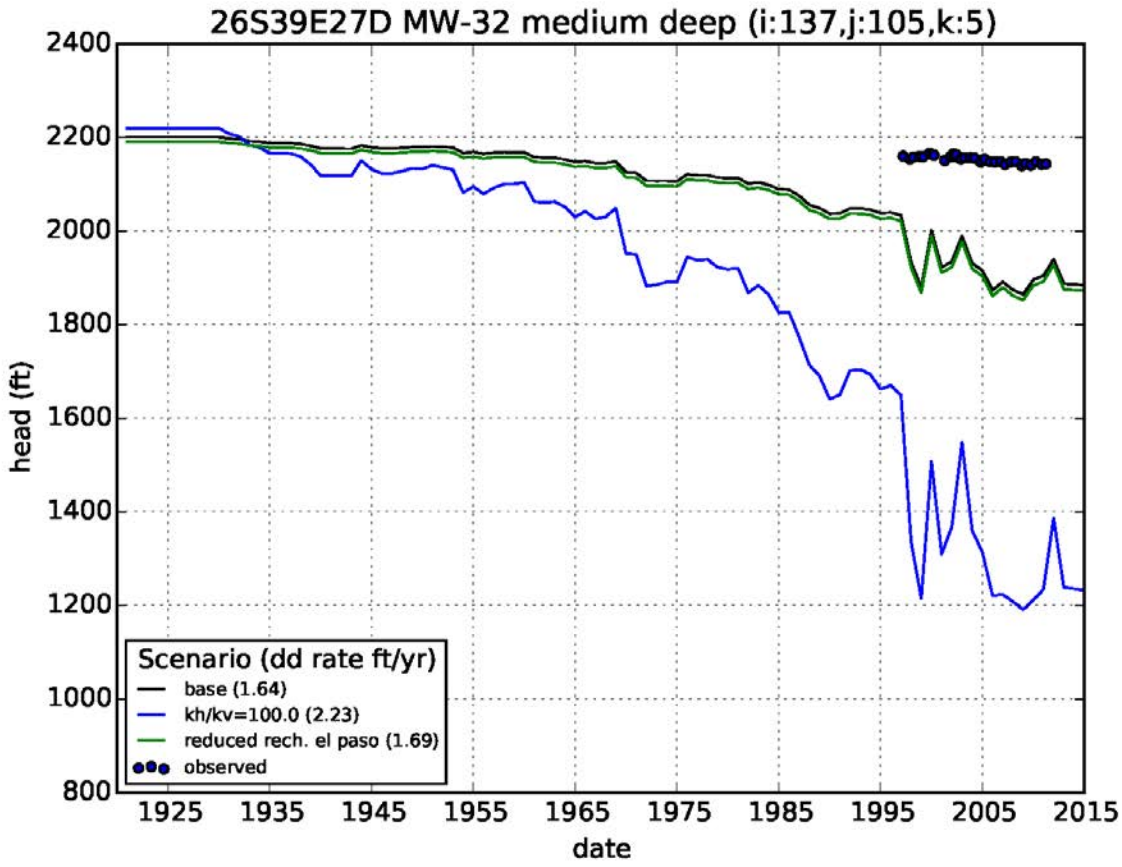

Figure 33. Simulated hydraulic head for the base model and two alternative conceptualizations at monitoring well 26S39E27D (labeled #3 on Figure 30). The alternative conceptual models include an isolated deep and shallow aquifer (simulated with an increased Kx/Kz = 100) and reduced recharge in the El Paso Basin. Note that kh/kv as shown in the legend is equivalent to Kx/Kz as noted in the caption.

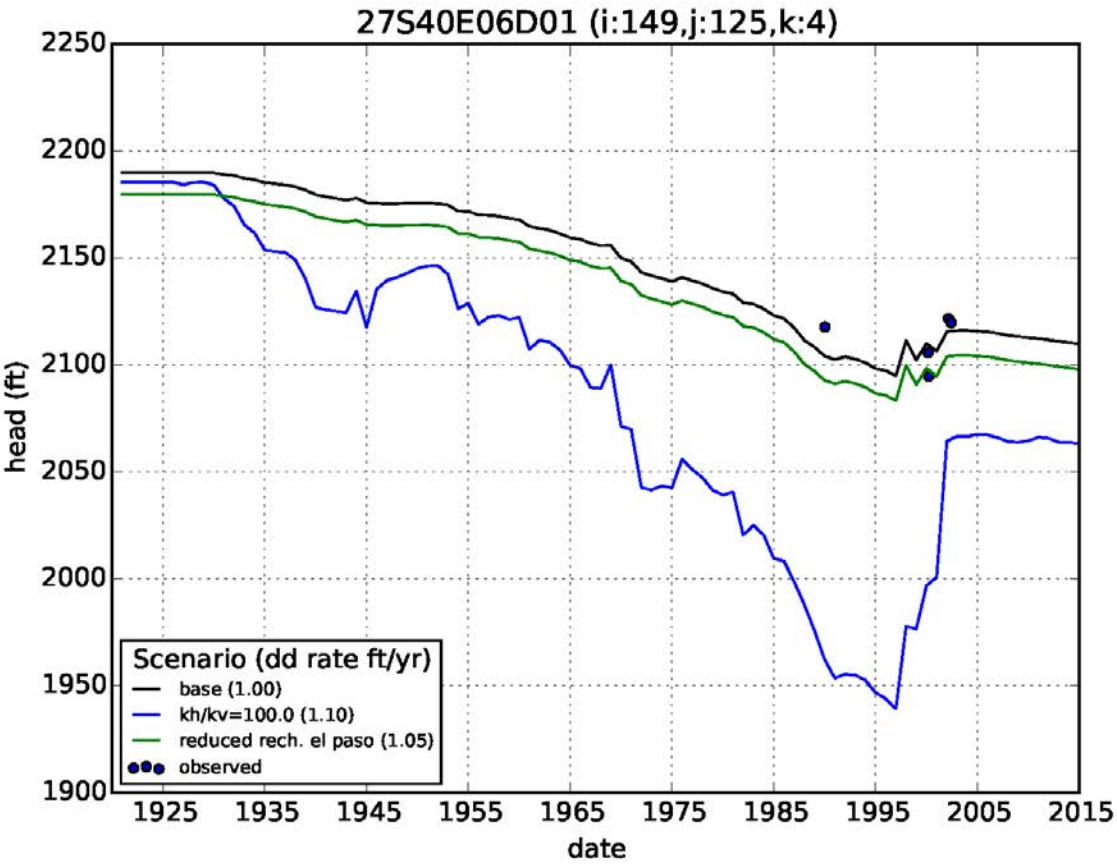

Figure 34. Simulated hydraulic head for the base model and two alternative conceptualizations at monitoring well 27S40E06D01 (labeled #4 on Figure 30). The alternative conceptual models include an isolated deep and shallow aquifer (simulated with an increased Kx/Kz = 100) and reduced recharge in the El Paso Basin. Note that kh/kv as shown in the legend is equivalent to Kx/Kz as noted in the caption.

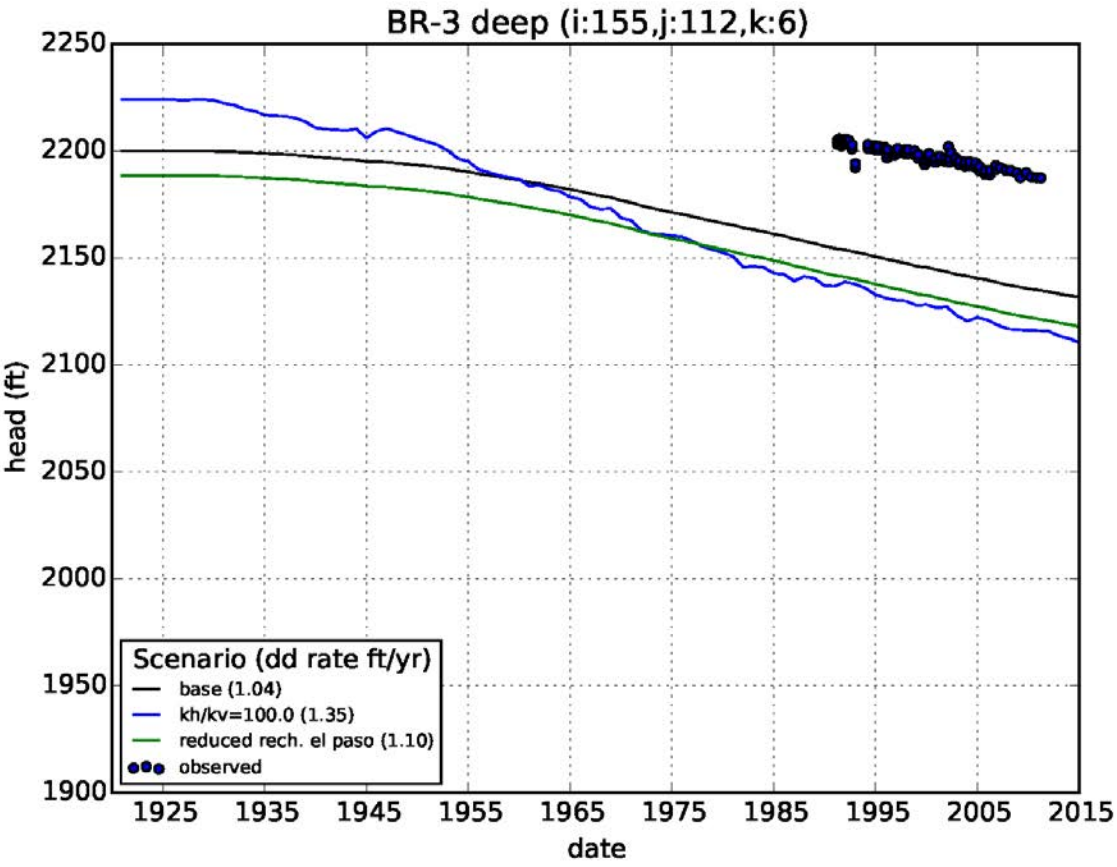

Figure 35. Simulated hydraulic head for the base model and two alternative conceptualizations at monitoring well BR-3 deep (labeled #5 on Figure 30). The alternative conceptual models include an isolated deep and shallow aquifer (simulated with an increased Kx/Kz = 100) and reduced recharge in the El Paso Basin. Note that kh/kv as shown in the legend is equivalent to Kx/Kz as noted in the caption.

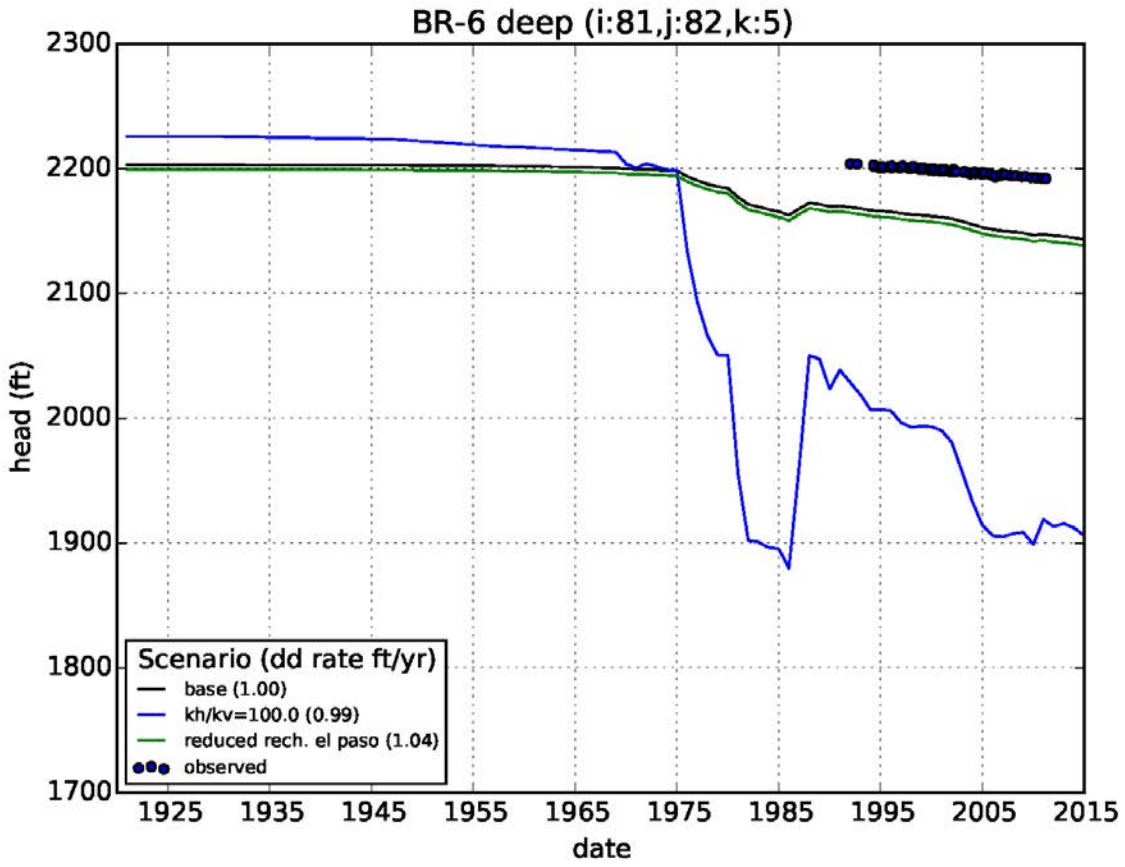

Figure 36. Simulated hydraulic head for the base model and two alternative conceptualizations at monitoring well BR-6 deep (labeled #6 on Figure 30). The alternative conceptual models include an isolated deep and shallow aquifer (simulated with an increased Kx/Kz = 100) and reduced recharge in the El Paso Basin. Note that kh/kv as shown in the legend is equivalent to Kx/Kz as noted in the caption.

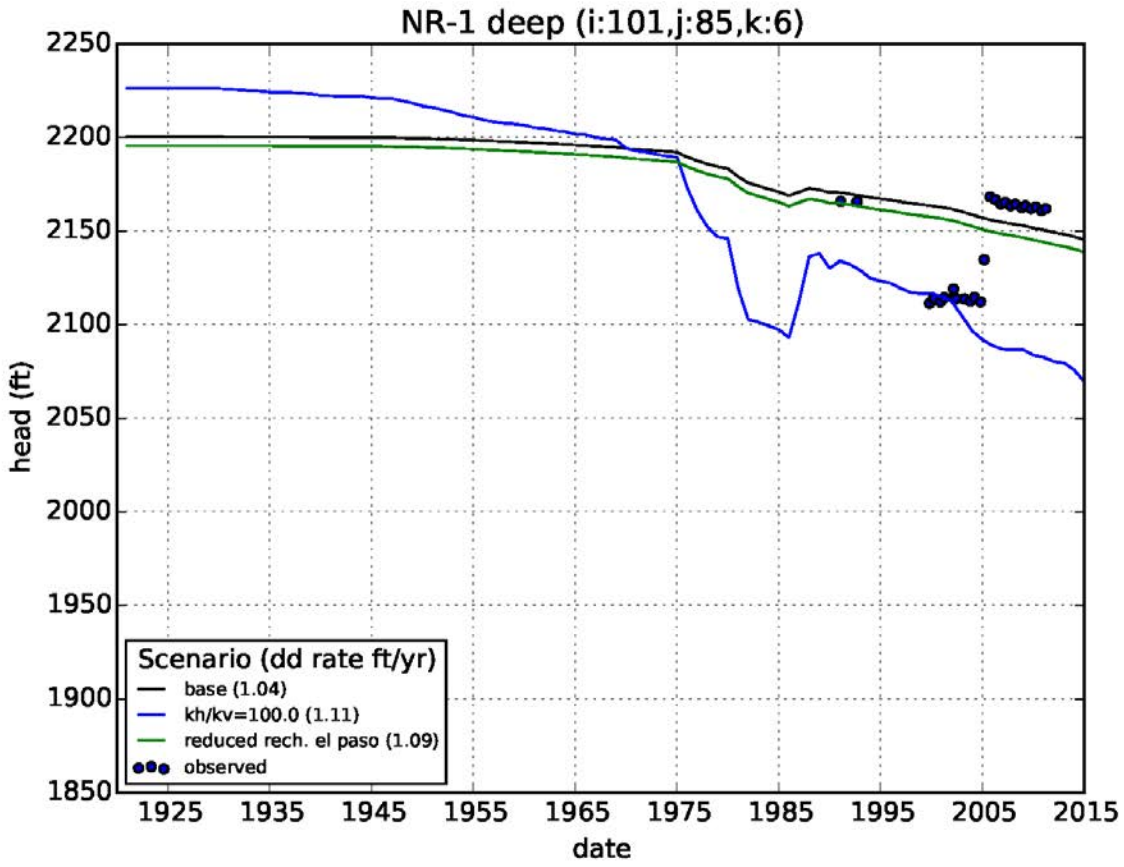

Figure 37. Simulated hydraulic head for the base model and two alternative conceptualizations at monitoring well NR-1 deep (labeled #7 on Figure 30). The alternative conceptual models include an isolated deep and shallow aquifer (simulated with an increased Kx/Kz = 100) and reduced recharge in the El Paso Basin. Note that kh/kv as shown in the legend is equivalent to Kx/Kz as noted in the caption.

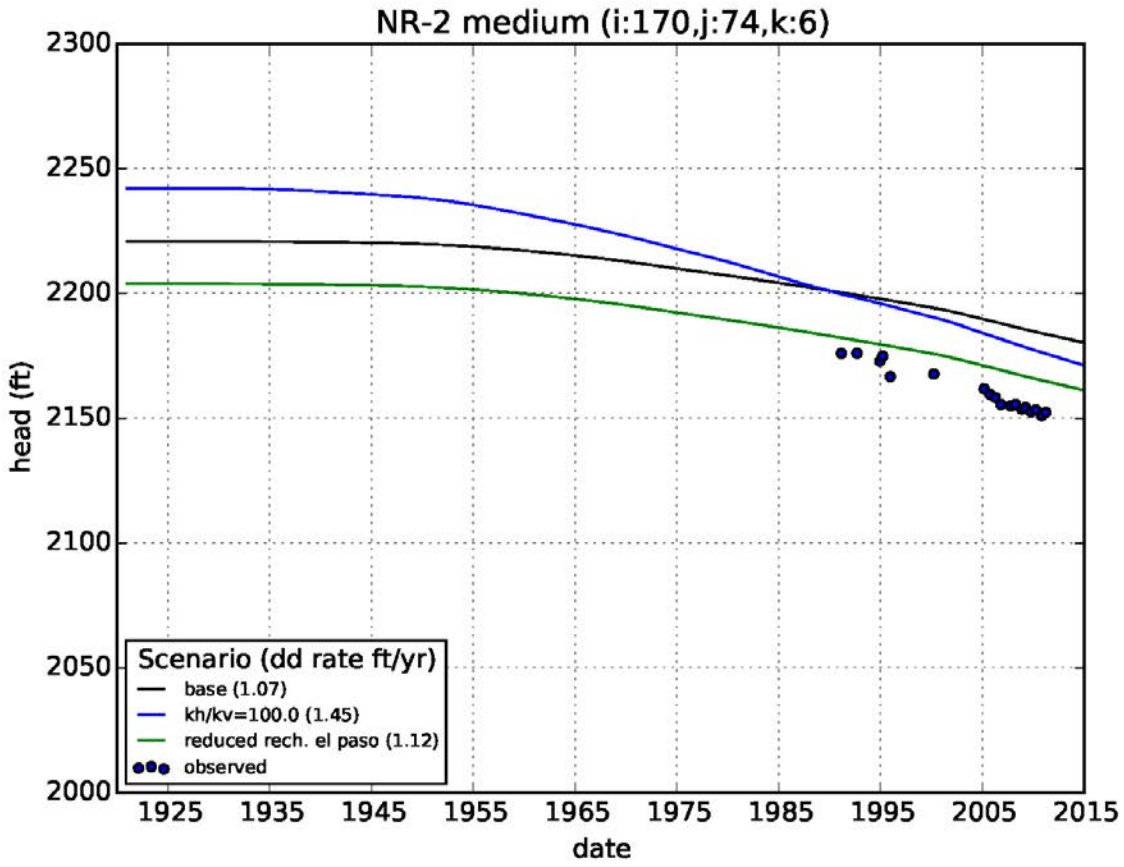

Figure 38. Simulated hydraulic head for the base model and two alternative conceptualizations at monitoring well NR-2 medium (labeled #8 on Figure 30). The alternative conceptual models include an isolated deep and shallow aquifer (simulated with an increased Kx/Kz= 100) and reduced recharge in the El Paso Basin. Note that kh/kv as shown in the legend is equivalent to Kx/Kz as noted in the caption.

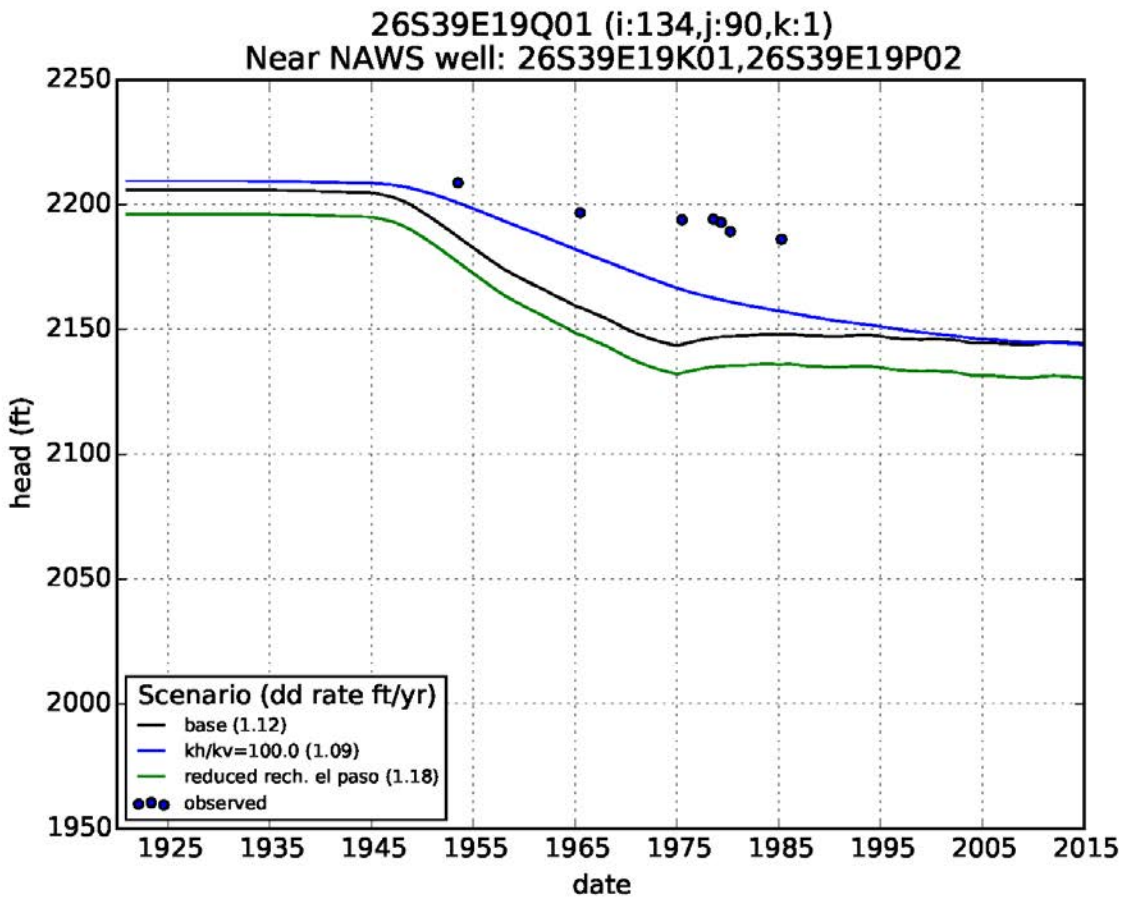

Figure 39. Simulated hydraulic head for the base model and two alternative conceptualizations at monitoring well 26S39E19Q01 (labeled #9 on Figure 30). The alternative conceptual models include an isolated deep and shallow aquifer (simulated with an increased Kx/Kz = 100) and reduced recharge in the El Paso Basin. Note that kh/kv as shown in the legend is equivalent to Kx/Kz as noted in the caption.

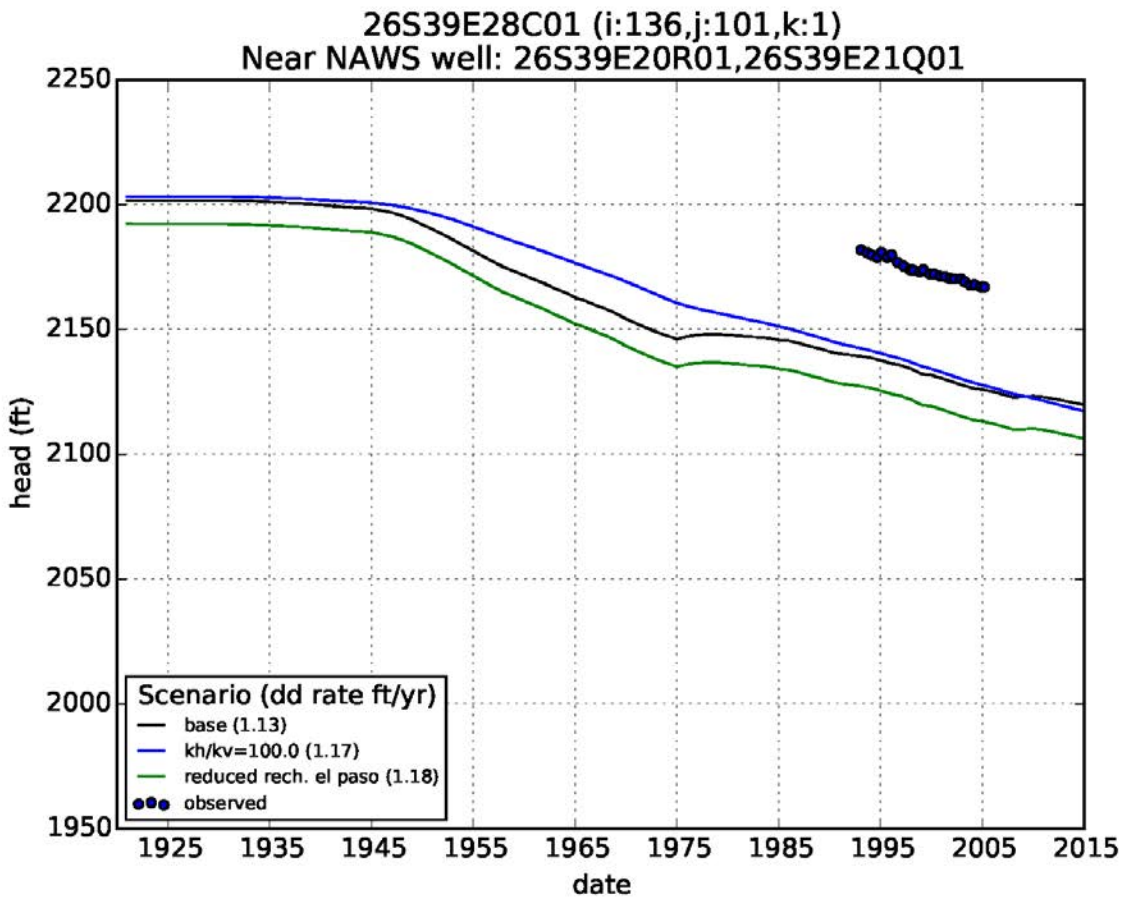

Figure 40. Simulated hydraulic head for the base model and three alternative conceptualizations at monitoring well 26S39E28C01 (labeled #10 on Figure 30). The two alternative conceptual models include an isolated deep and shallow aquifer (simulated with an increased Kx/Kz = 100) and reduced recharge in the El Paso Basin. Note that kh/kv as shown in the legend is equivalent to Kx/Kz as noted in the caption.

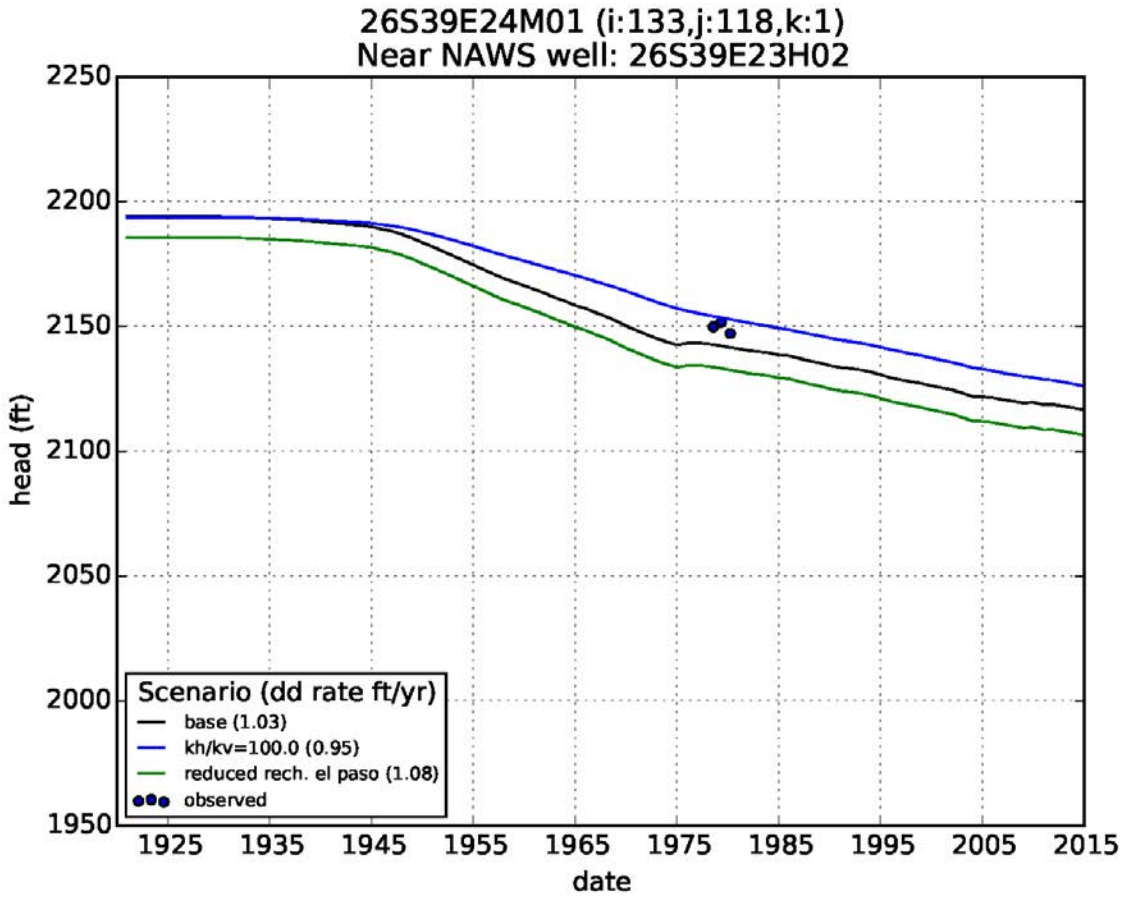

Figure 41. Simulated hydraulic head for the base model and two alternative conceptualizations at monitoring well 26S39E24M01 (labeled #11 on Figure 30). The alternative conceptual models include an isolated deep and shallow aquifer (simulated with an increased Kx/Kz = 100) and reduced recharge in the El Paso Basin. Note that kh/kv as shown in the legend is equivalent to Kx/Kz as noted in the caption.

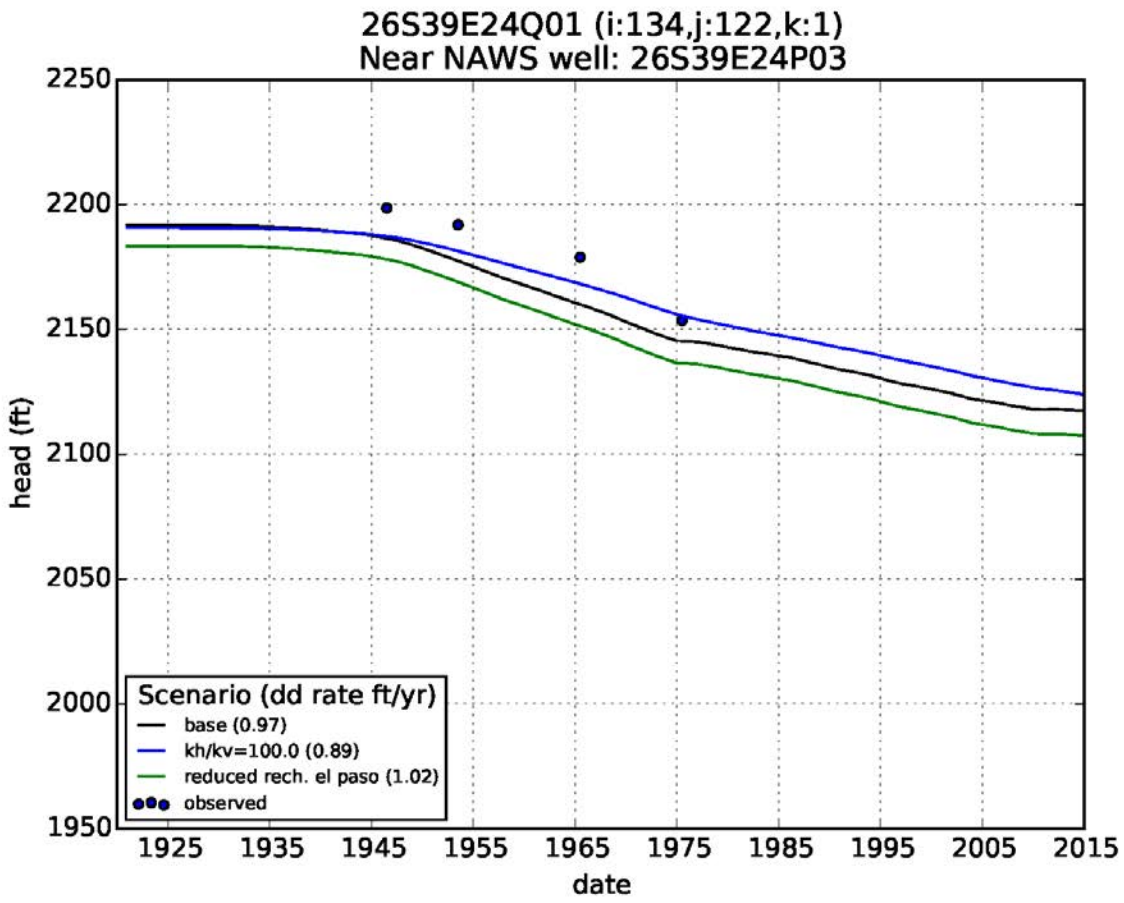

Figure 42. Simulated hydraulic head for the base model and two alternative conceptualizations at monitoring well 26S39E24Q01 (labeled #12 on Figure 30). The alternative conceptual models include an isolated deep and shallow aquifer (simulated with an increased Kx/Kz = 100) and reduced recharge in the El Paso Basin. Note that kh/kv as shown in the legend is equivalent to Kx/Kz as noted in the caption.

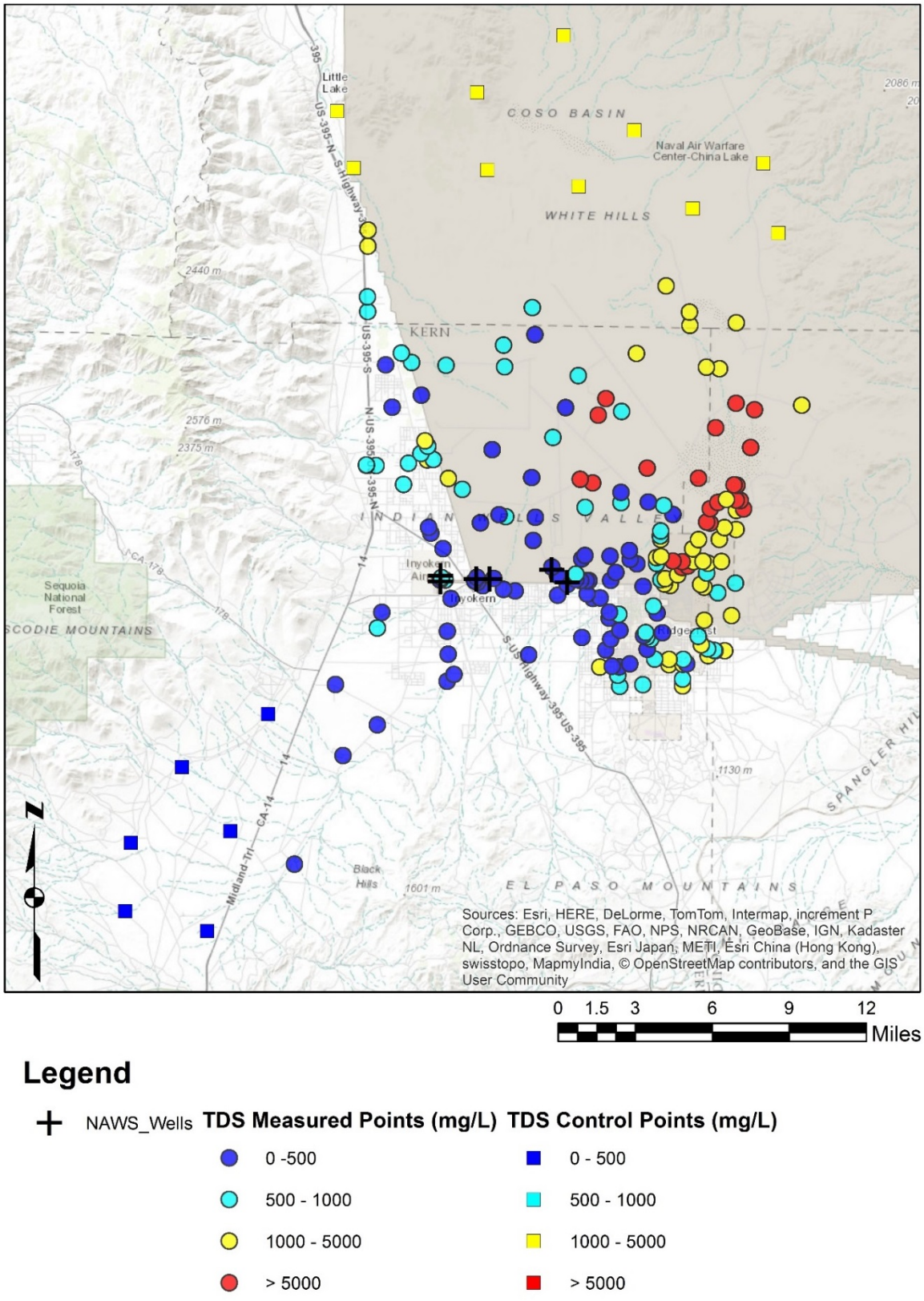

Figure 43. Data used to construct the TDS initial conditions for the shallow layers (i.e., elevation > 500 m).

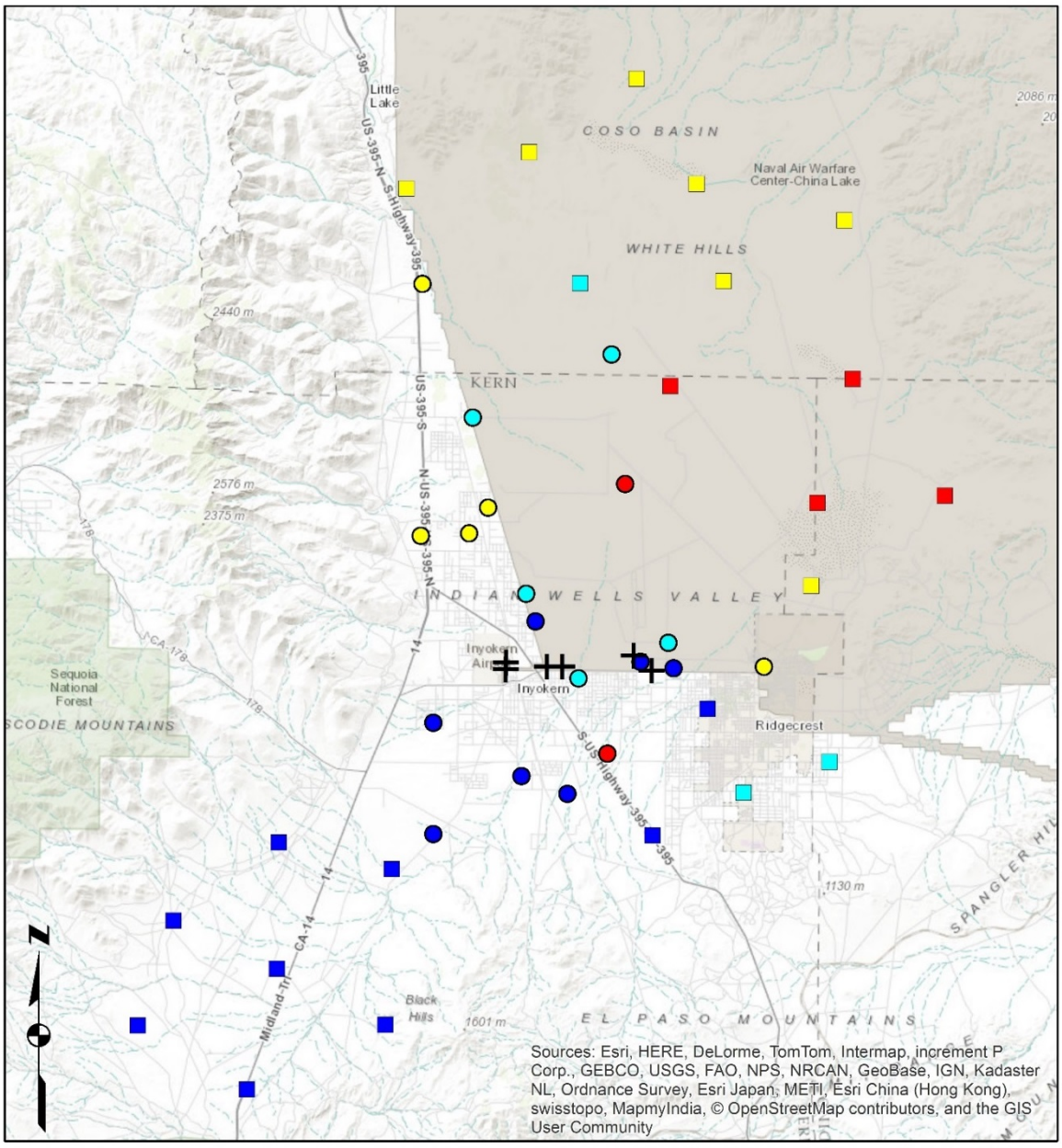

Figure 44. Data used to construct the TDS initial conditions for the deep layers (i.e., elevation < 500 m).

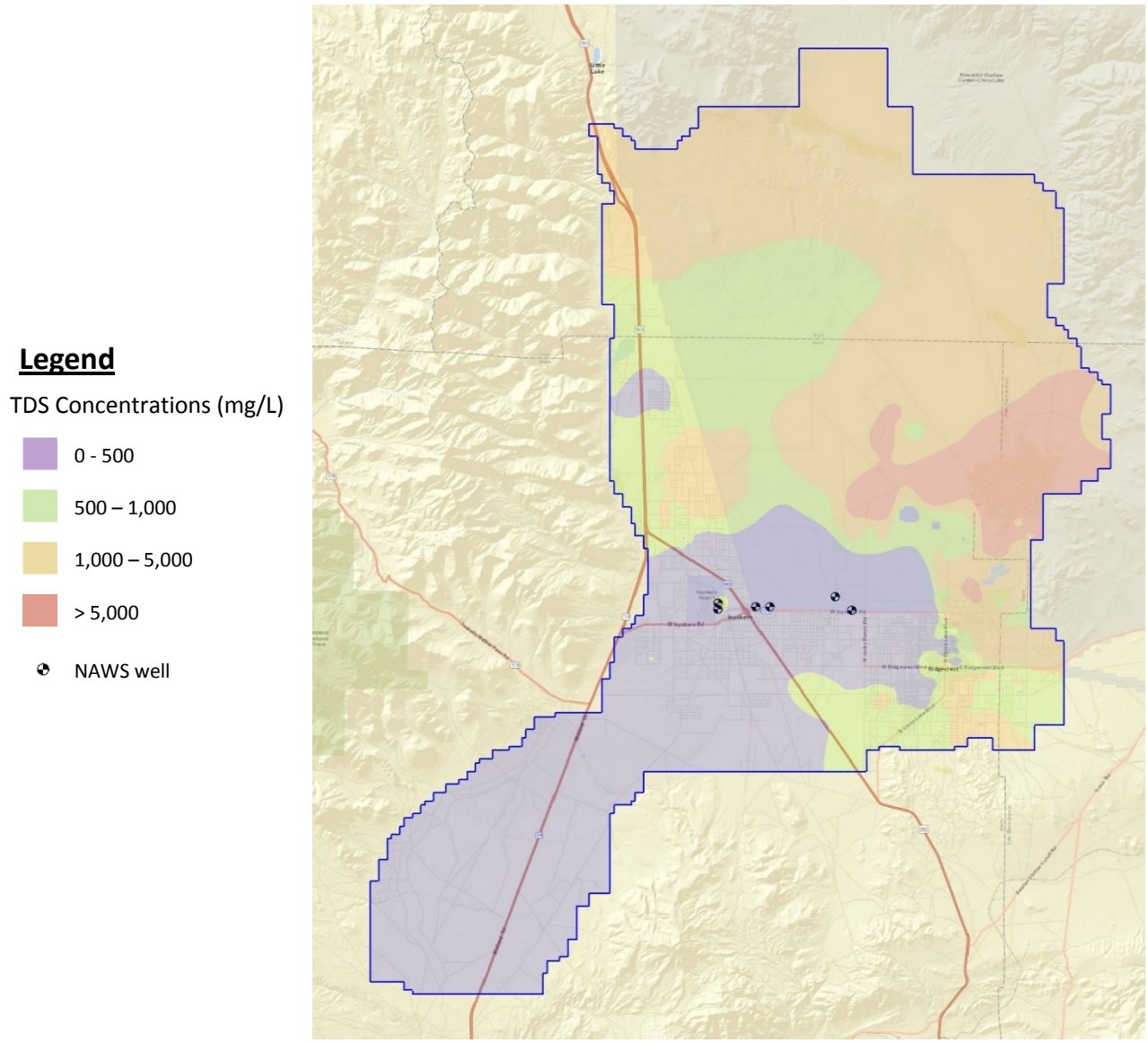

Figure 45. Initial condition for layers 1-3.

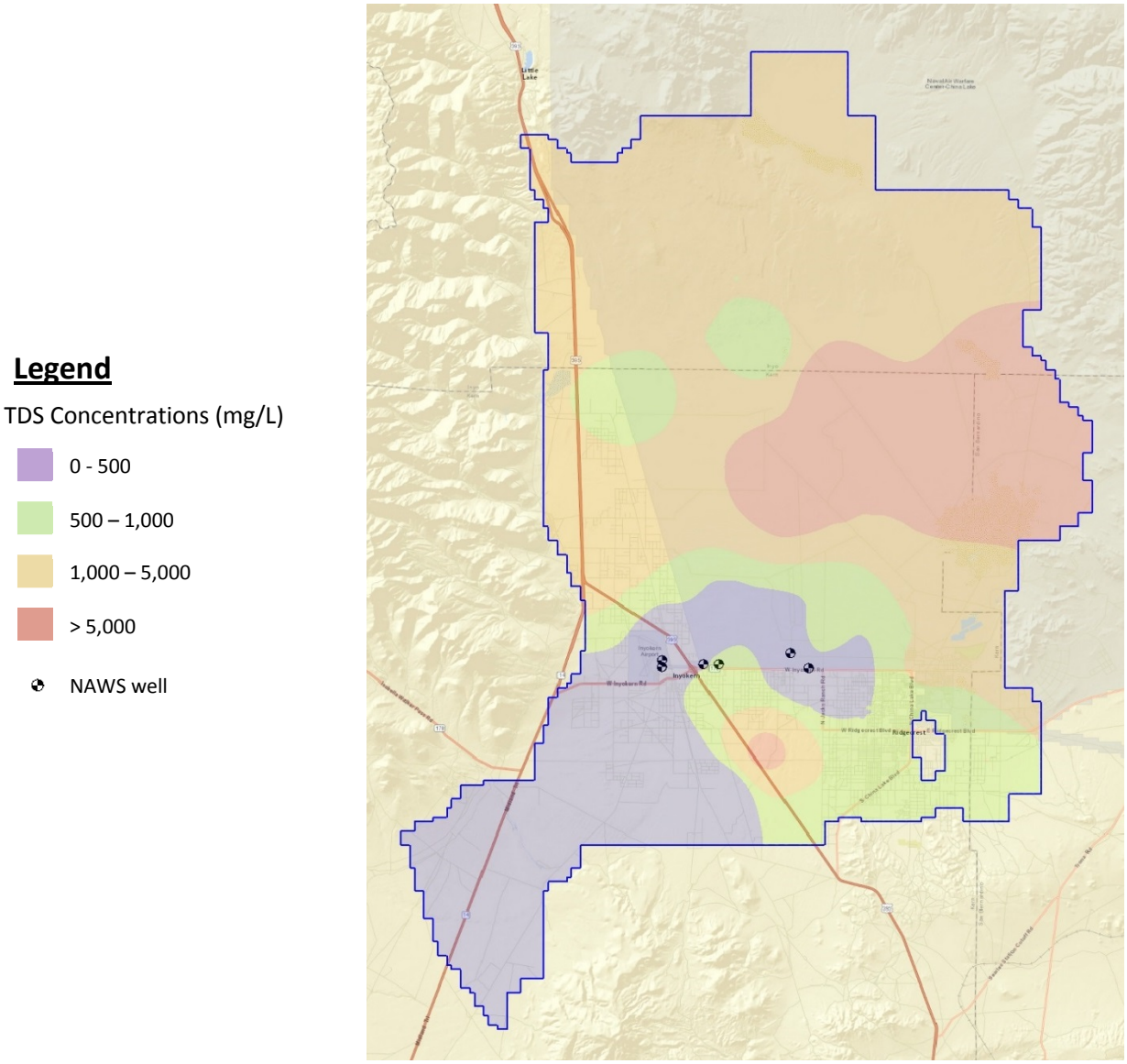

Figure 46. Initial condition for layers 4-6.

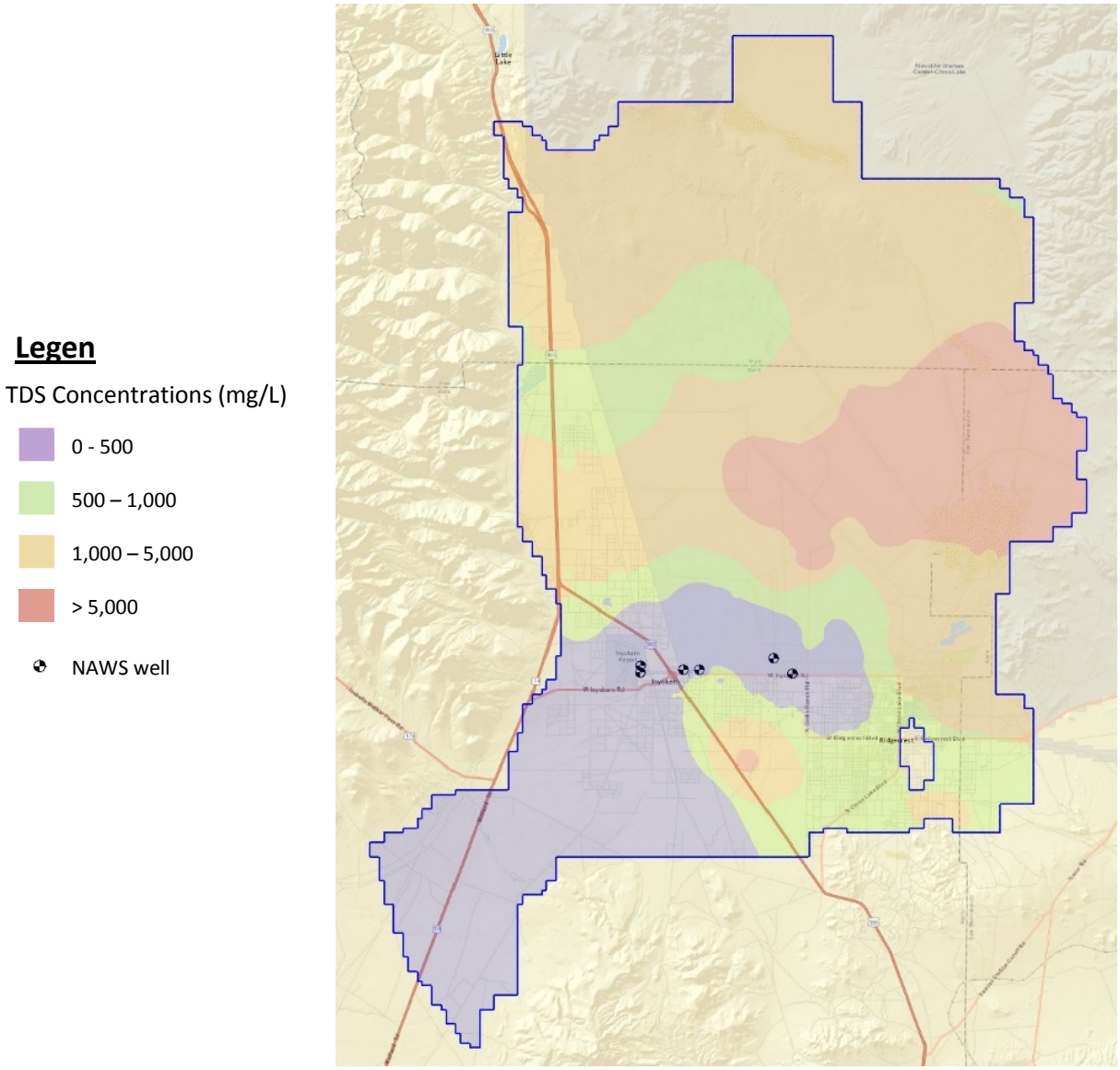

Figure 47. Simulated TDS concentration (mg/L) in 2100 in layer 4.

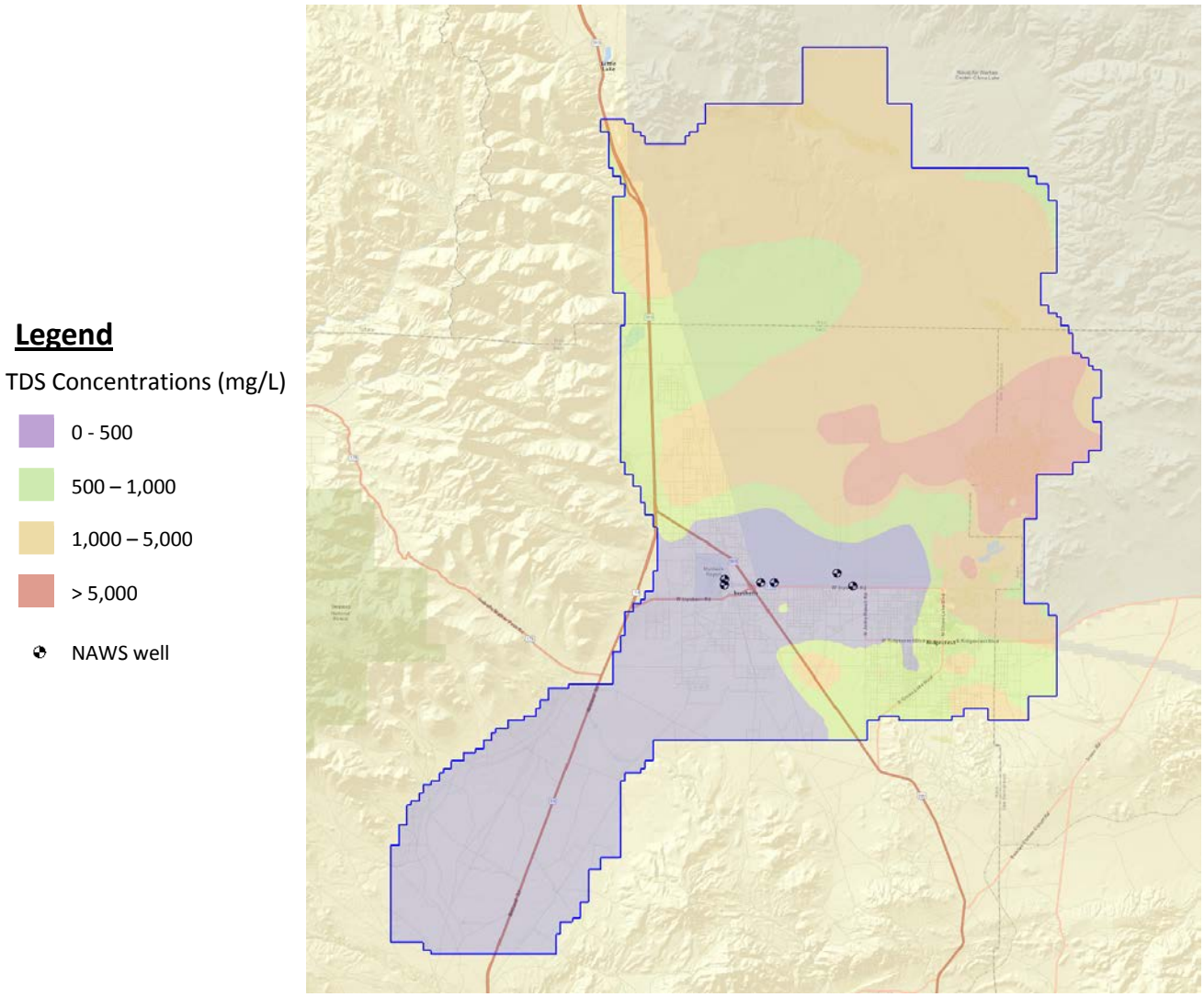

Figure 48. Simulated TDS concentration (mg/L) in 2100 in layer 2.

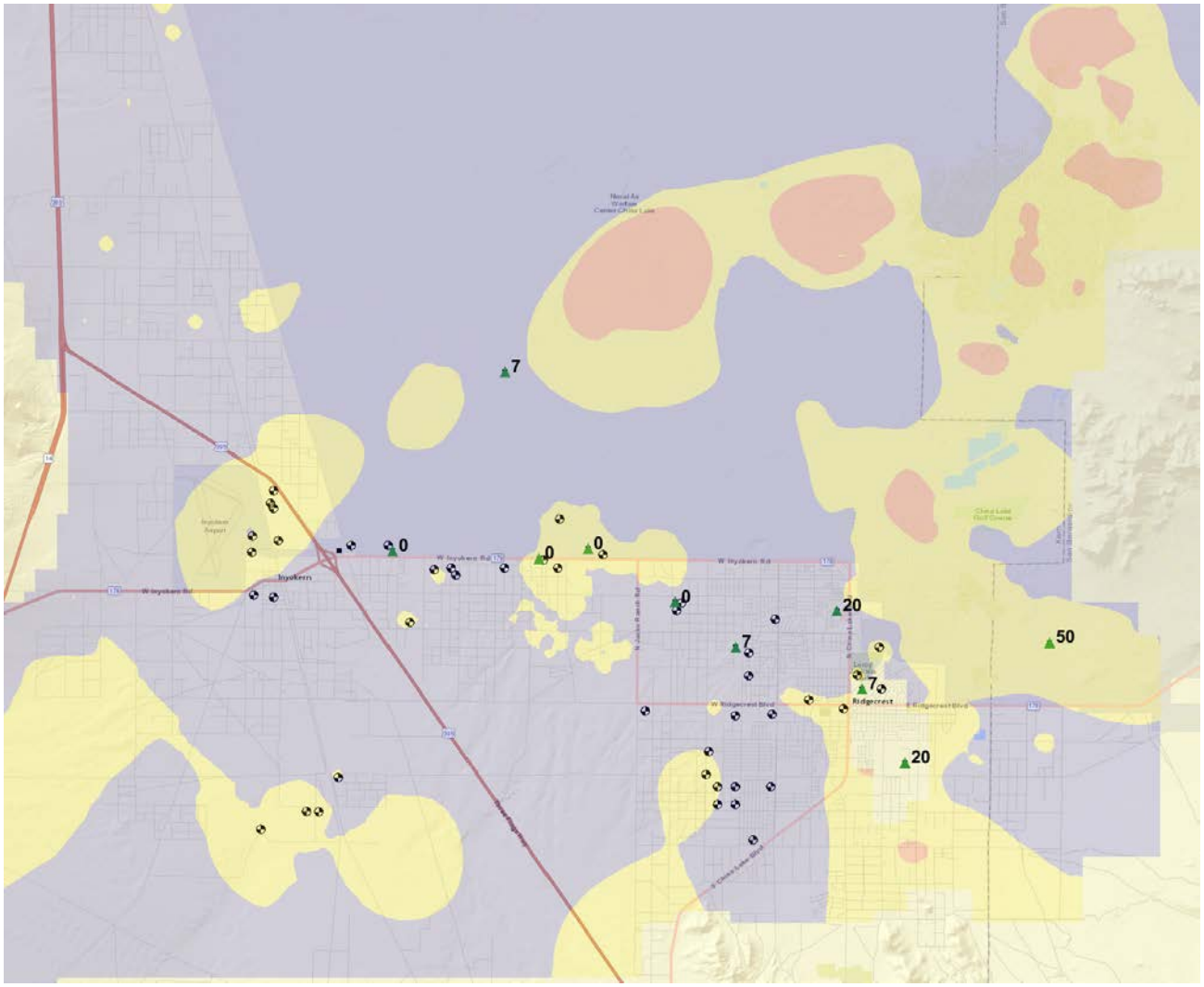

Legend

TDS Trend (mg/L/yr)

- < 0
- 0 - 10
- 10 - 50
- Municipal well
- Measured trend (mg/L/yr)

Figure 49. Simulated TDS concentration trends from 2020 – 2050 (mg/L/yr) in layer 4. Also shown are wells with previously recorded TDS trends. Note that positive trends indicate increasing concentrations while negative indicates decreasing concentrations.

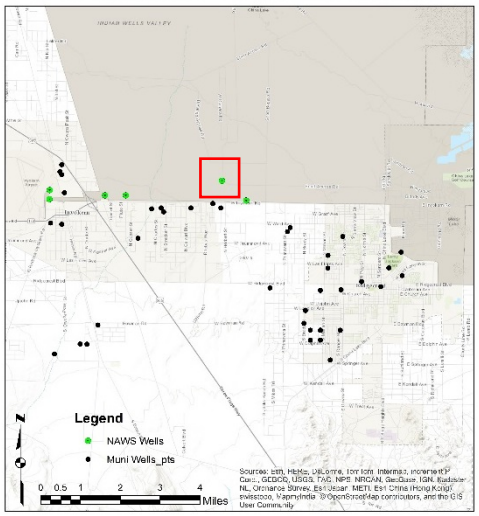

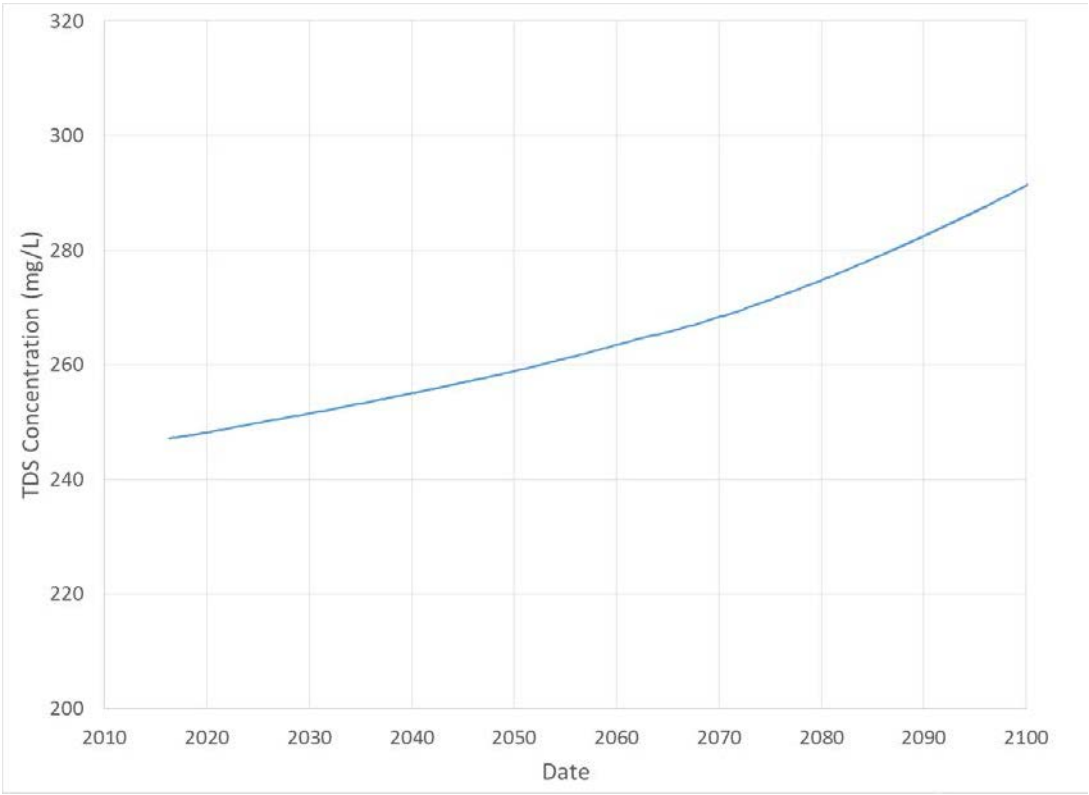

Figure 50. Simulated TDS concentration at location specified by red box.

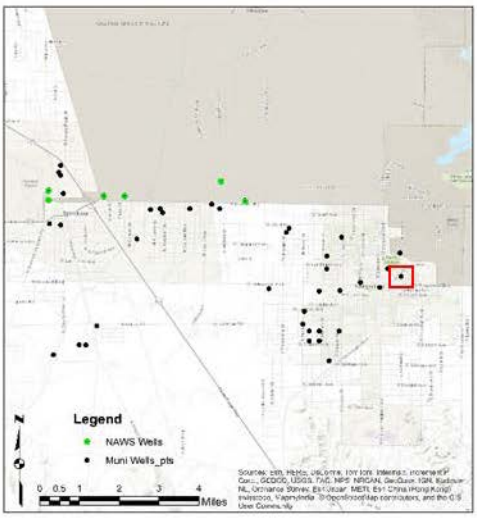

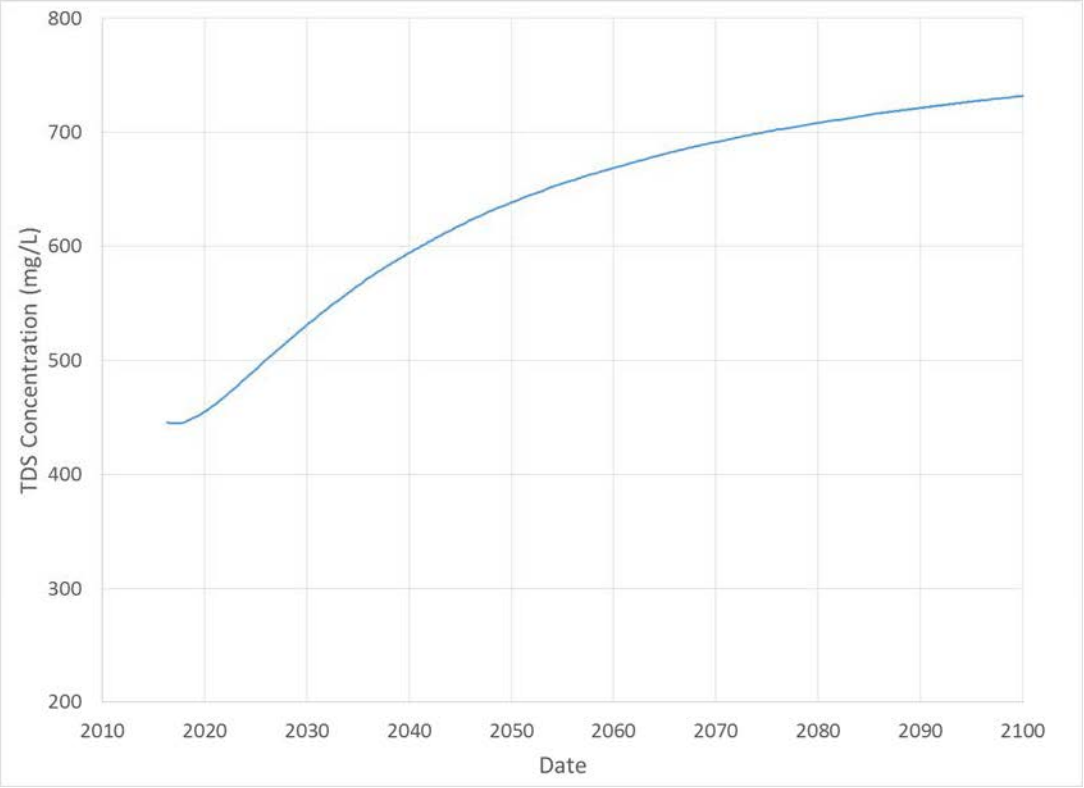

Figure 51. Simulated TDS concentration at location specified by red box.

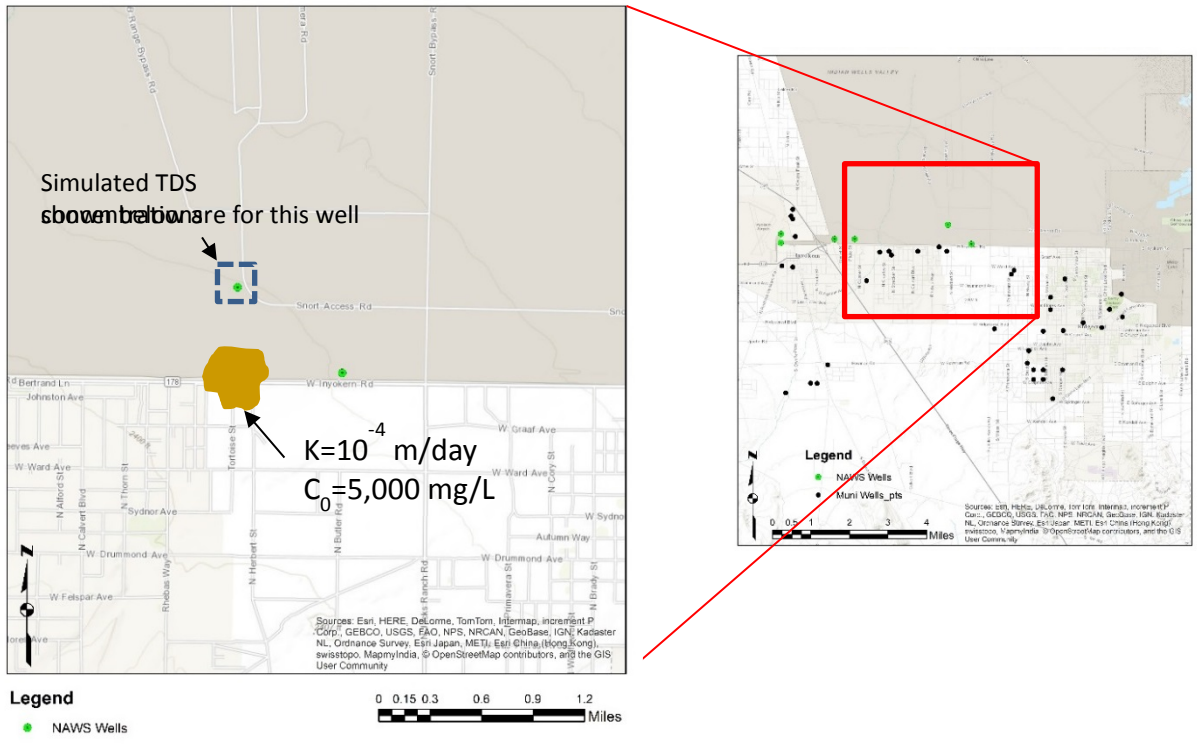

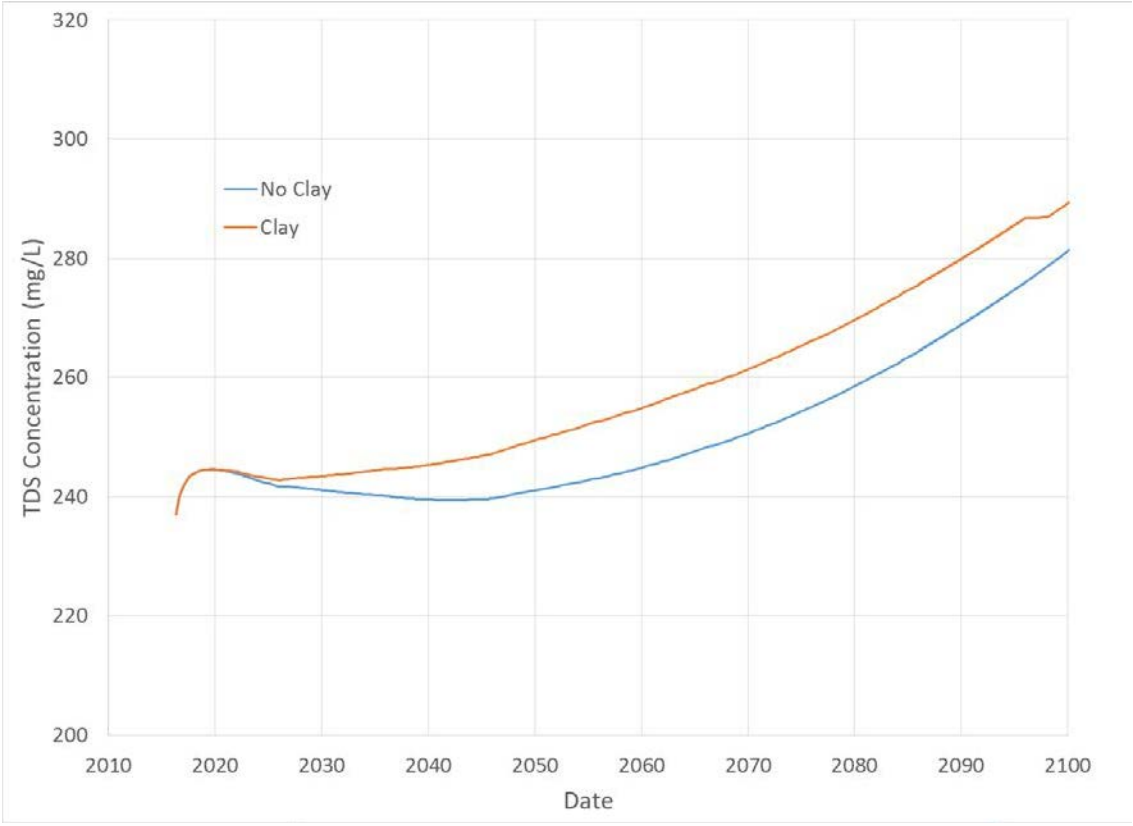

Figure 52. Simulated TDS concentration at NAWS well with and without adjacent low-permeability clay unit with high TDS concentration.

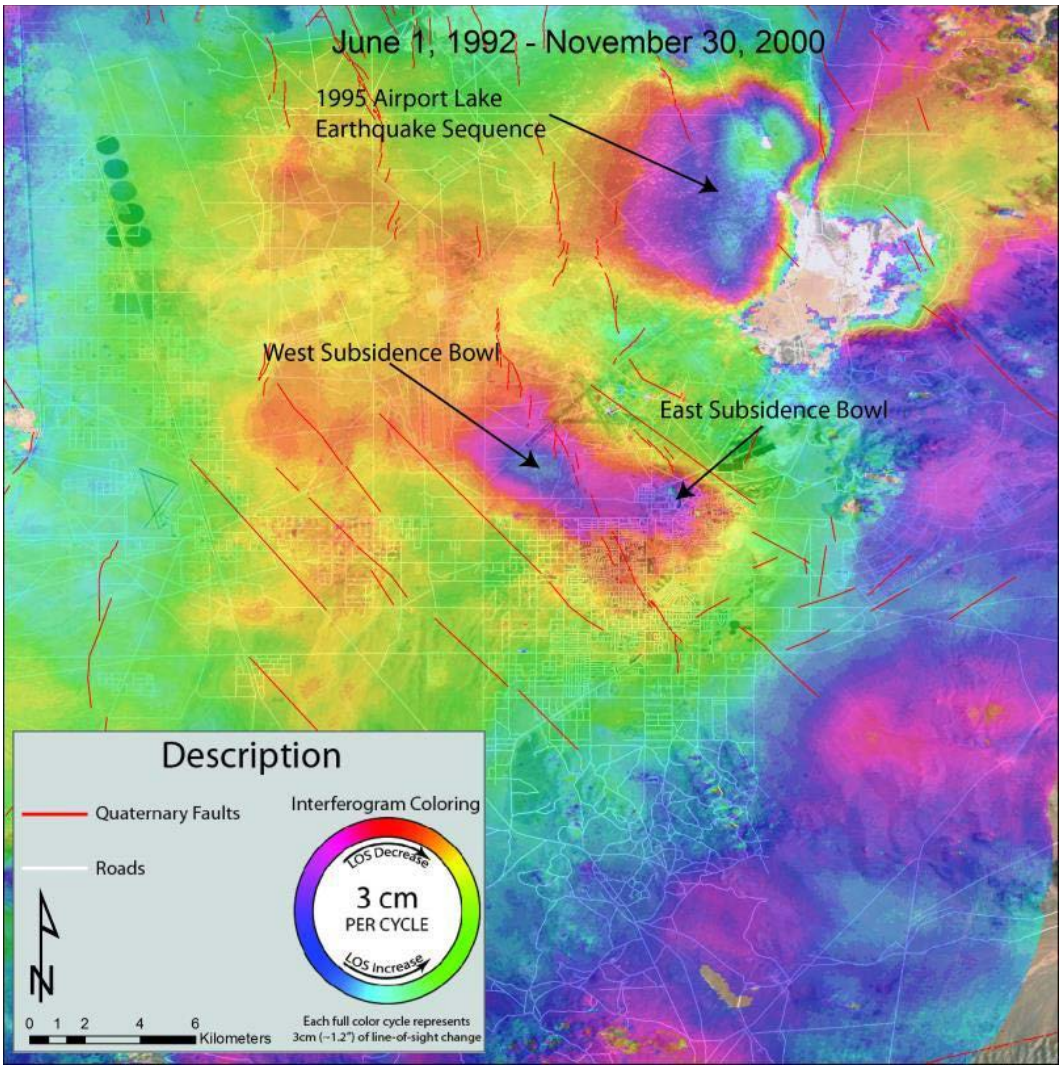

Figure 53. InSAR results, 1992 to 2000.

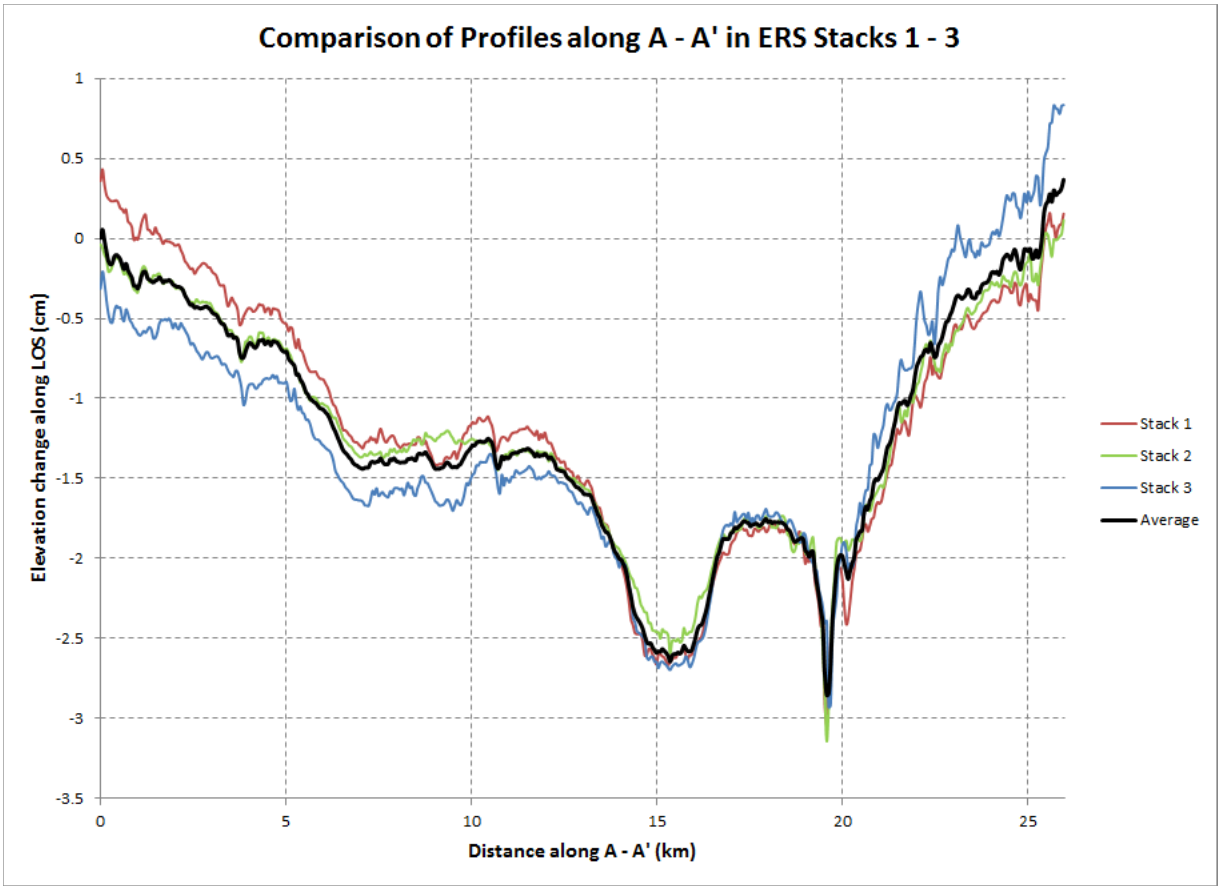

Figure 54. Land surface profile of subsidence from 1992 to 2000.

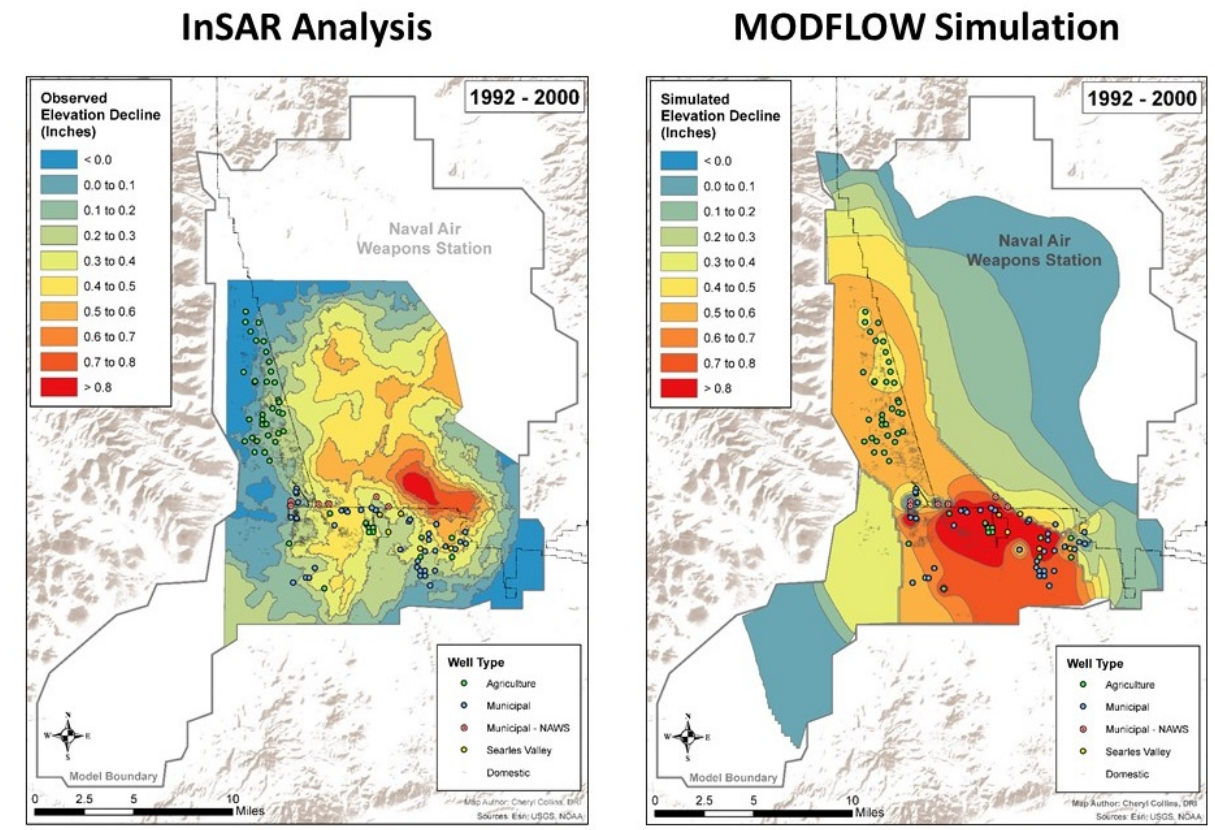

Figure 55. Observed and simulated subsidence, 1992 to 2000.

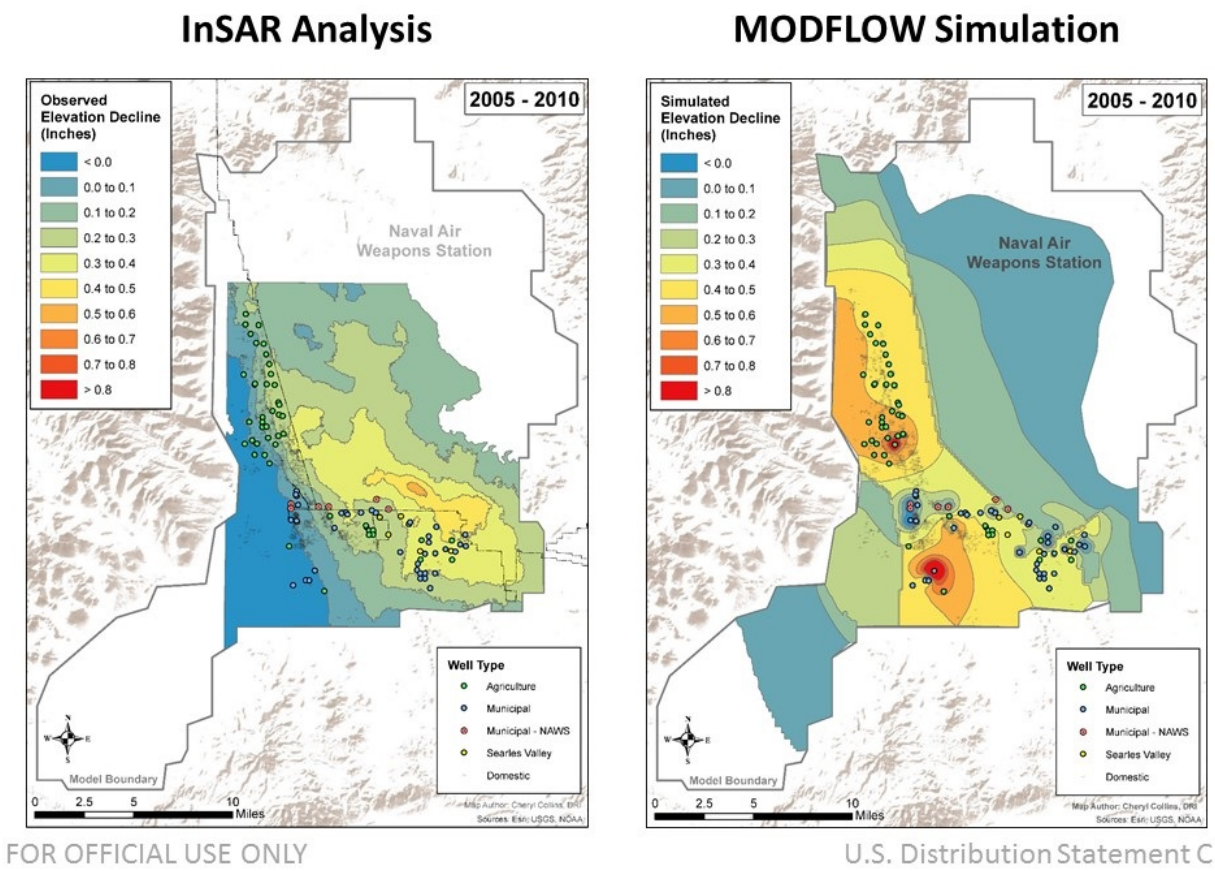

Figure 56. Observed and simulated subsidence, 2005 to 2010.

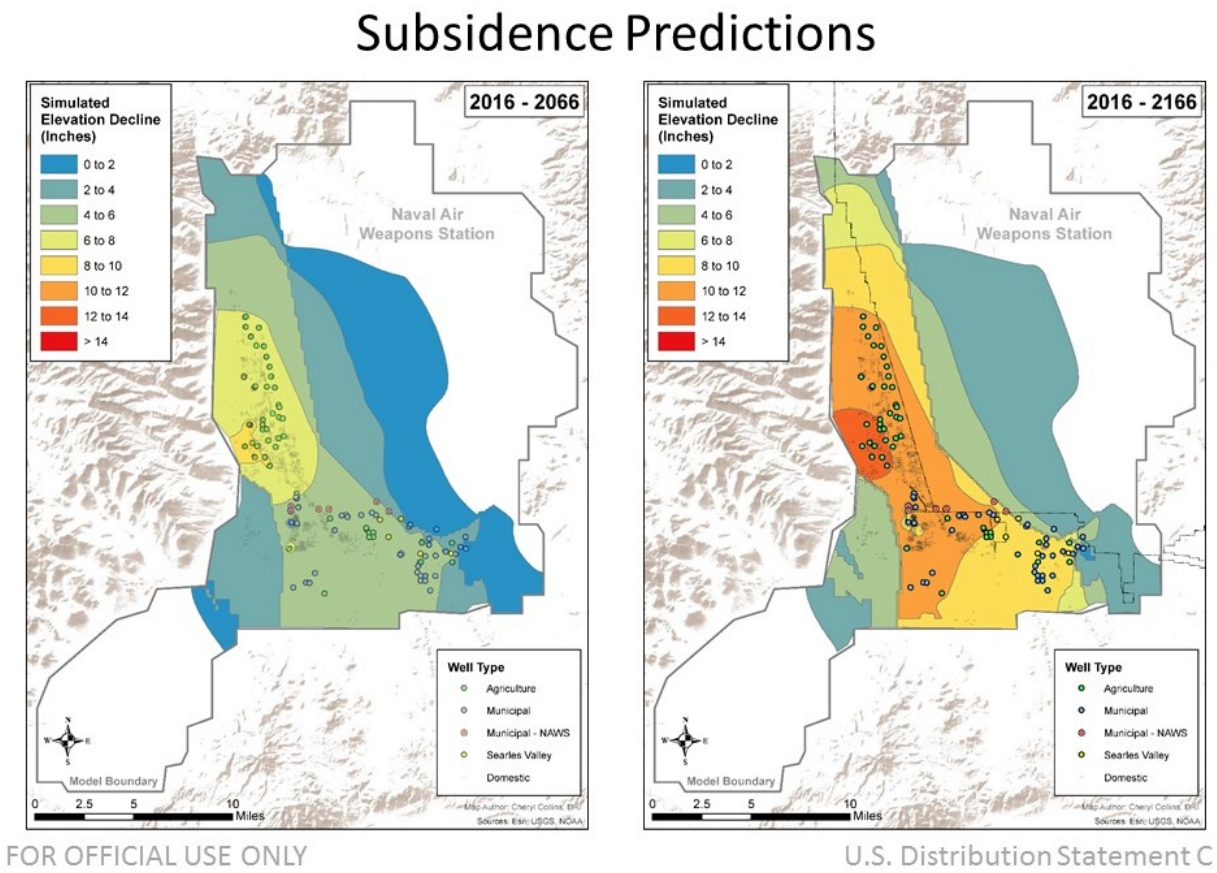

Figure 57. 50-year (left) and 100-year (right) subsidence predictions.

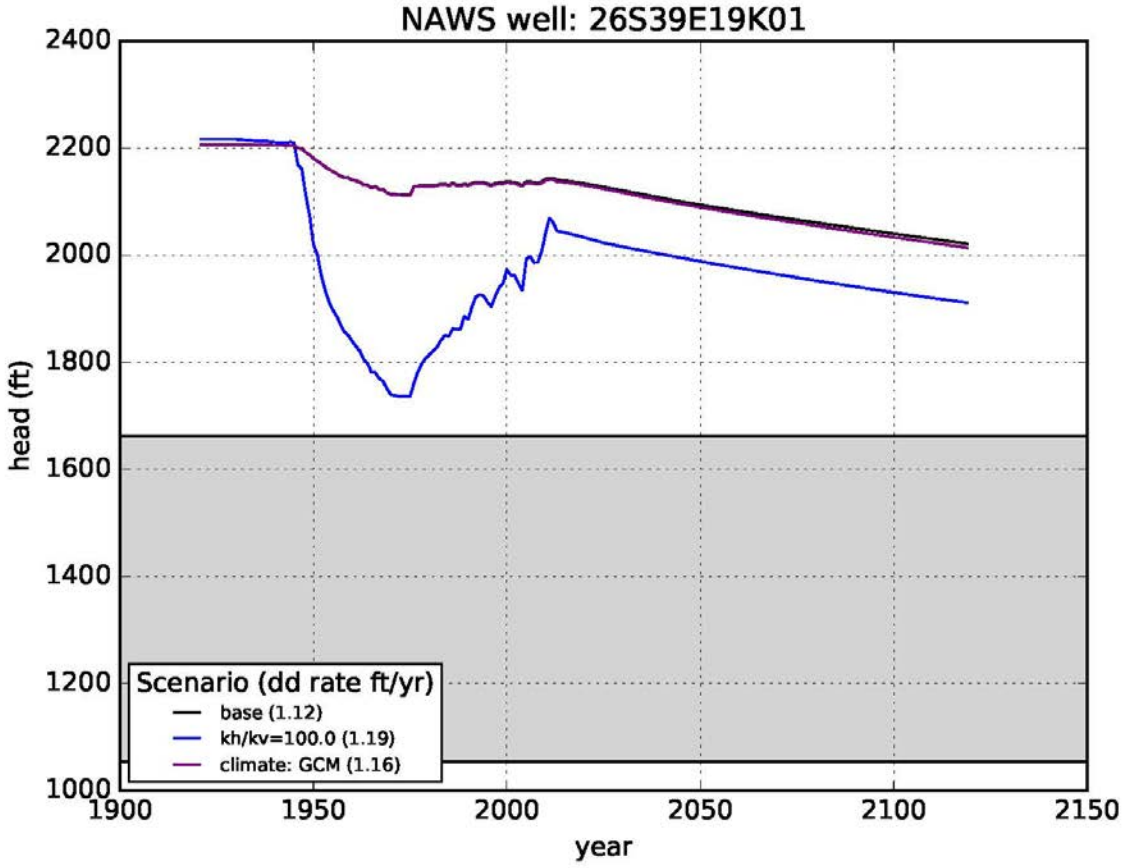

Figure 58. Simulated hydraulic head for NAWS well 26S39E19K01 with the well screen elevation shown in gray. Forecasts of hydraulic head are shown for three alternative future scenarios, all of which assume the continuation of current groundwater use in the future (status quo usage). In addition to the base transient model, the Kx/Kz=100 scenario isolates the deep and shallow aquifers and the climate:GCM scenario reduces future precipitation because of global climate change. The drawdown rate for each scenario is included in the legend. Note that kh/kv as shown in the legend is equivalent to Kx/Kz as noted in the caption.

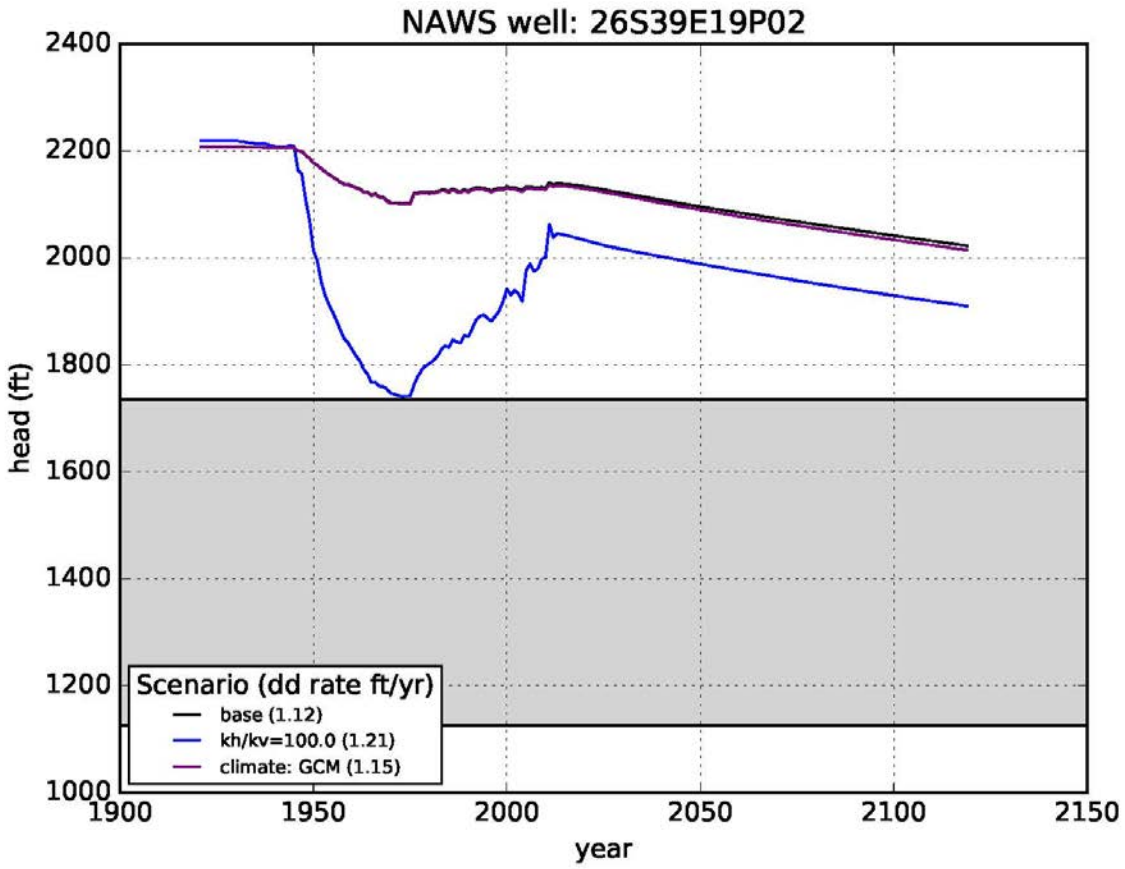

Figure 59. Simulated hydraulic head for NAWS well 26S39E19P02 with well screen elevation shown in gray. Forecasts of hydraulic head are shown for three alternative future scenarios, all of which assume the continuation of current groundwater use in the future (status quo usage). In addition to the base transient model, the Kx/Kz=100 scenario isolates the deep and shallow aquifers and the climate:GCM scenario reduces future precipitation because of global climate change. The drawdown rate for each scenario is included in the legend. Note that kh/kv as shown in the legend is equivalent to Kx/Kz as noted in the caption.

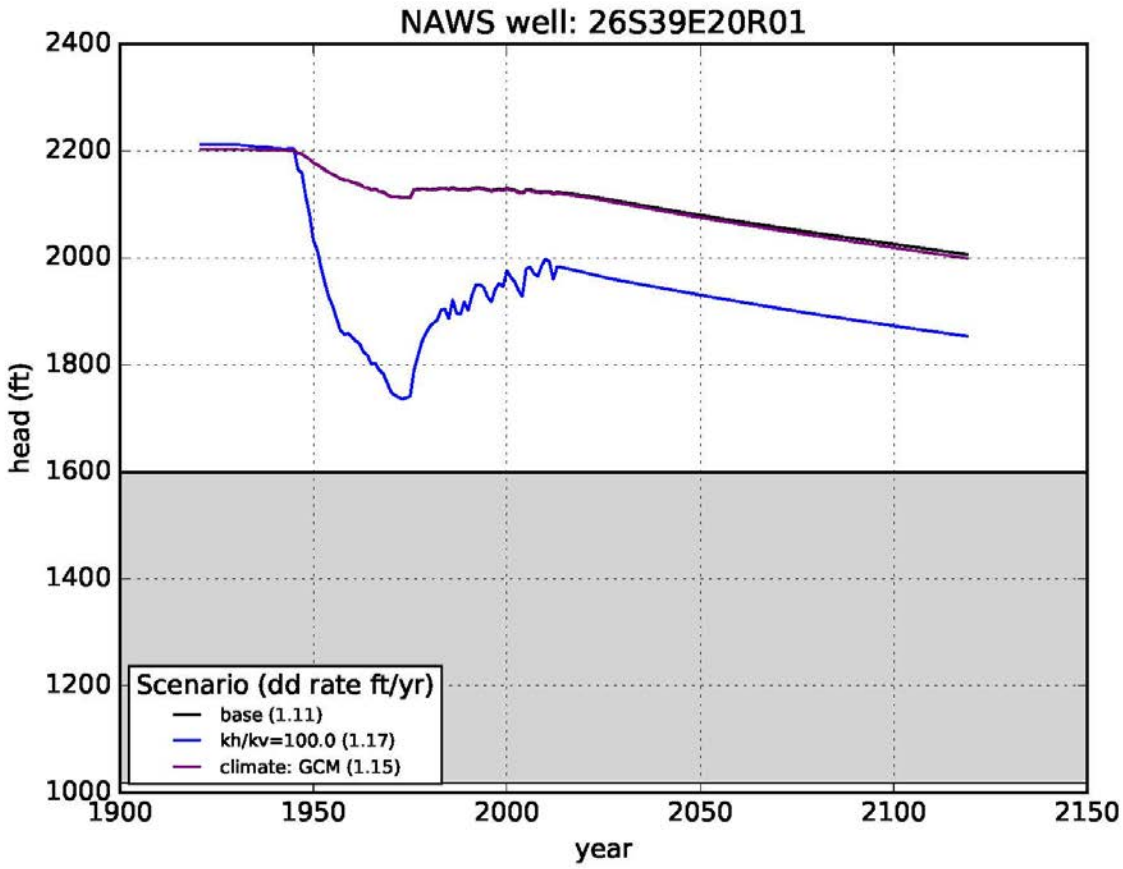

Figure 60. Simulated hydraulic head for NAWS well 26S39E20R01 with well screen elevation shown in gray. Forecasts of hydraulic head are shown for three alternative future scenarios, all of which assume the continuation of current groundwater use in the future (status quo usage). In addition to the base transient model, the Kx/Kz=100 scenario isolates the deep and shallow aquifers and the climate:GCM scenario reduces future precipitation because of global climate change. The drawdown rate for each scenario is included in the legend. Note that kh/kv as shown in the legend is equivalent to Kx/Kz as noted in the caption.

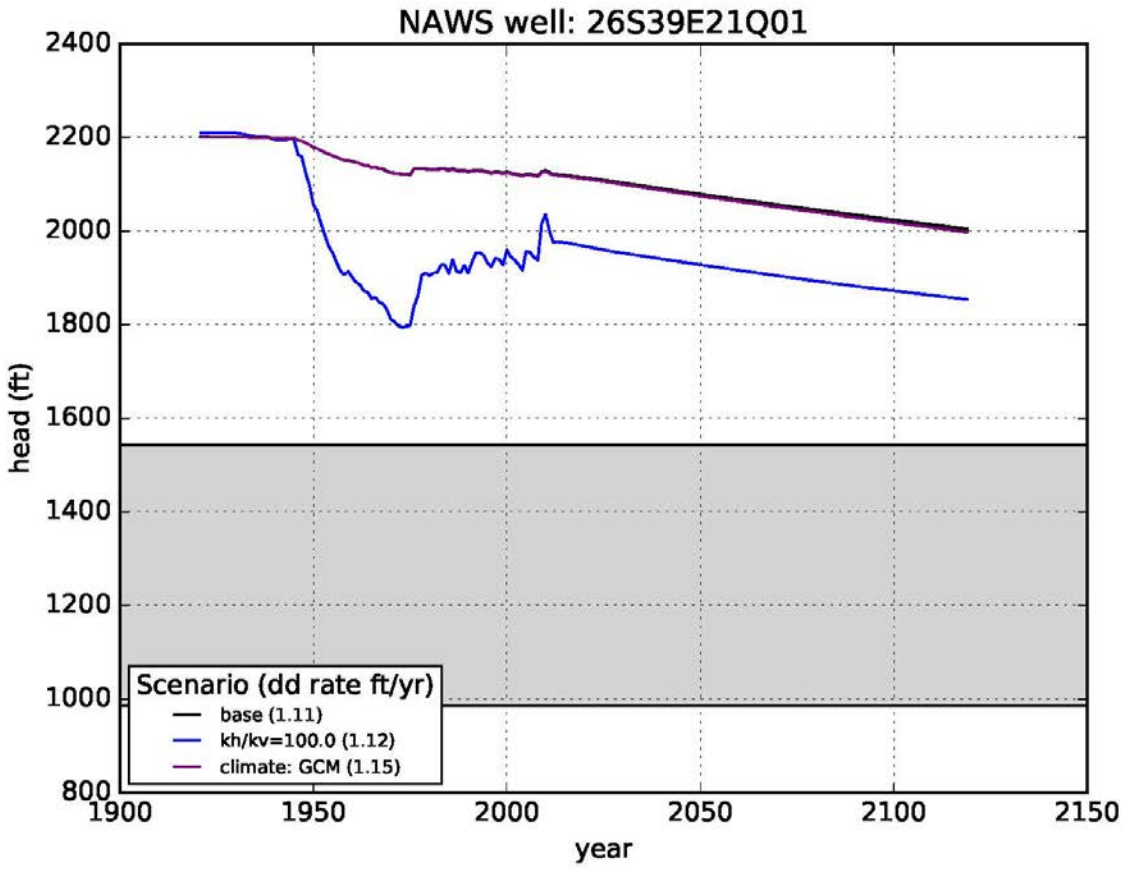

Figure 61. Simulated hydraulic head for location near NAWS well 26S39E21Q01 with well screen elevation shown in gray. Forecasts of hydraulic head are shown for three alternative future scenarios, all of which assume the continuation of current groundwater use in the future (status quo usage). In addition to the base transient model, the Kx/Kz=100 scenario isolates the deep and shallow aquifers and the climate:GCM scenario reduces future precipitation because of global climate change. The drawdown rate for each scenario is included in the legend. Note that kh/kv as shown in the legend is equivalent to Kx/Kz as noted in the caption.

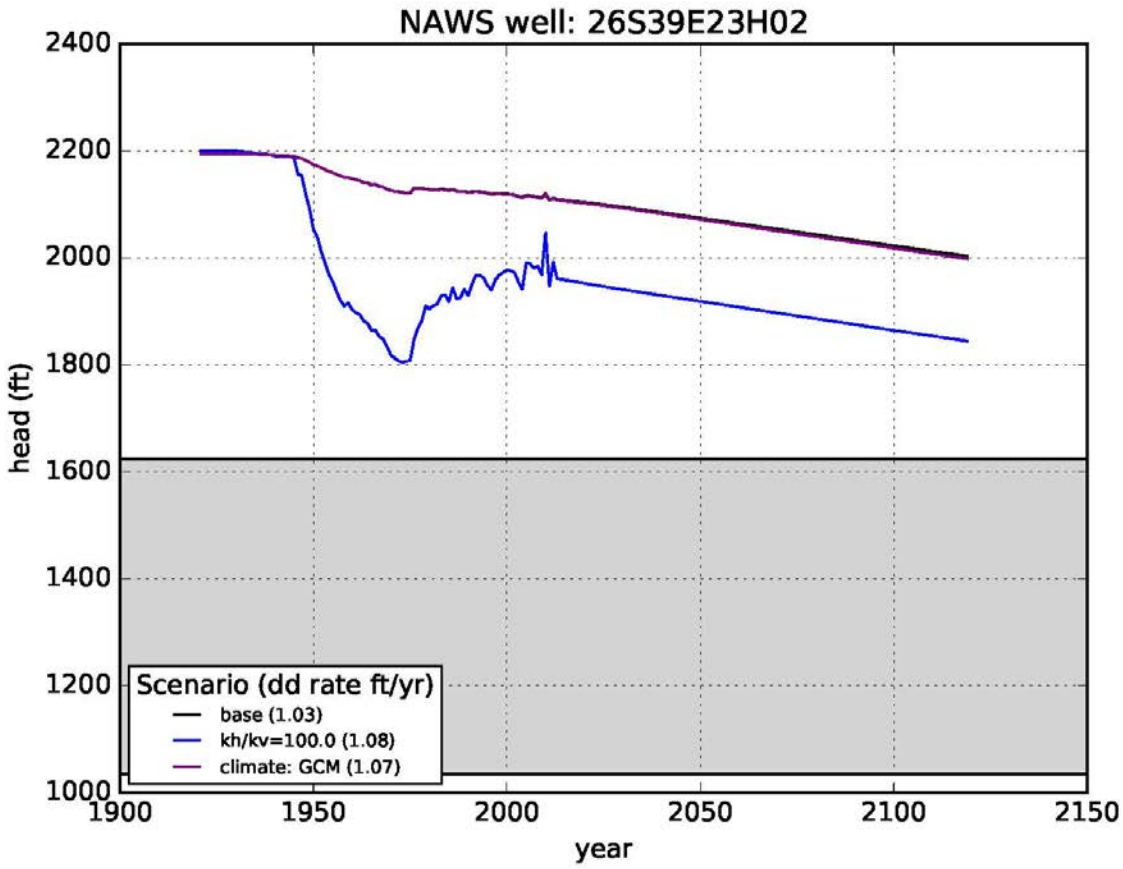

Figure 62. Simulated hydraulic head for NAWS well 26S39E23H02 with well screen elevation shown in gray. Forecasts of hydraulic head are shown for three alternative future scenarios, all of which assume the continuation of current groundwater use in the future (status quo usage). In addition to the base transient model, the Kx/Kz=100 scenario isolates the deep and shallow aquifers and the climate:GCM scenario reduces future precipitation because of global climate change. The drawdown rate for each scenario is included in the legend. Note that kh/kv as shown in the legend is equivalent to Kx/Kz as noted in the caption.

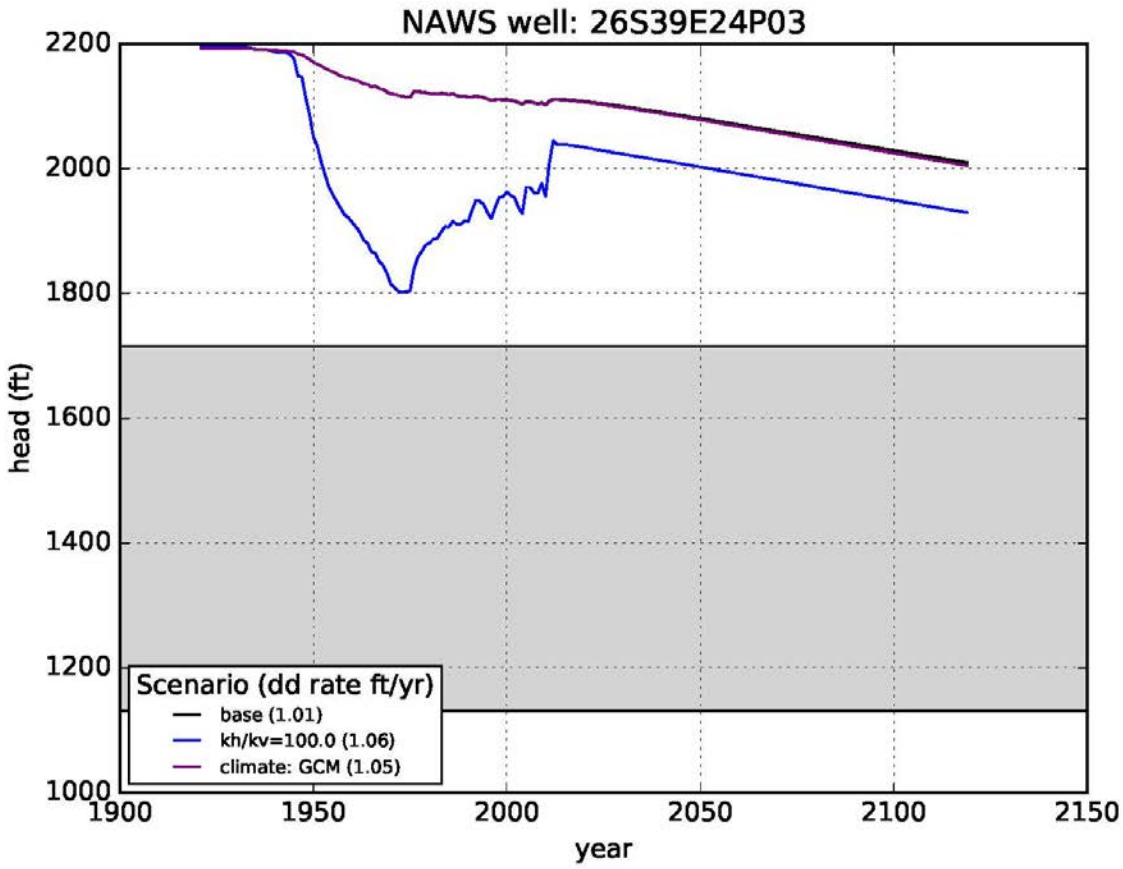

Figure 63. Simulated hydraulic head for NAWS well 26S39E24P03 with well screen elevation shown in gray. Forecasts of hydraulic head are shown for three alternative future scenarios, all of which assume the continuation of current groundwater use in the future (status quo usage). In addition to the base transient model, the Kx/Kz=100 scenario isolates the deep and shallow aquifers and the climate:GCM scenario reduces future precipitation because of global climate change. The drawdown rate for each scenario is included in the legend. Note that kh/kv as shown in the legend is equivalent to Kx/Kz as noted in the caption.

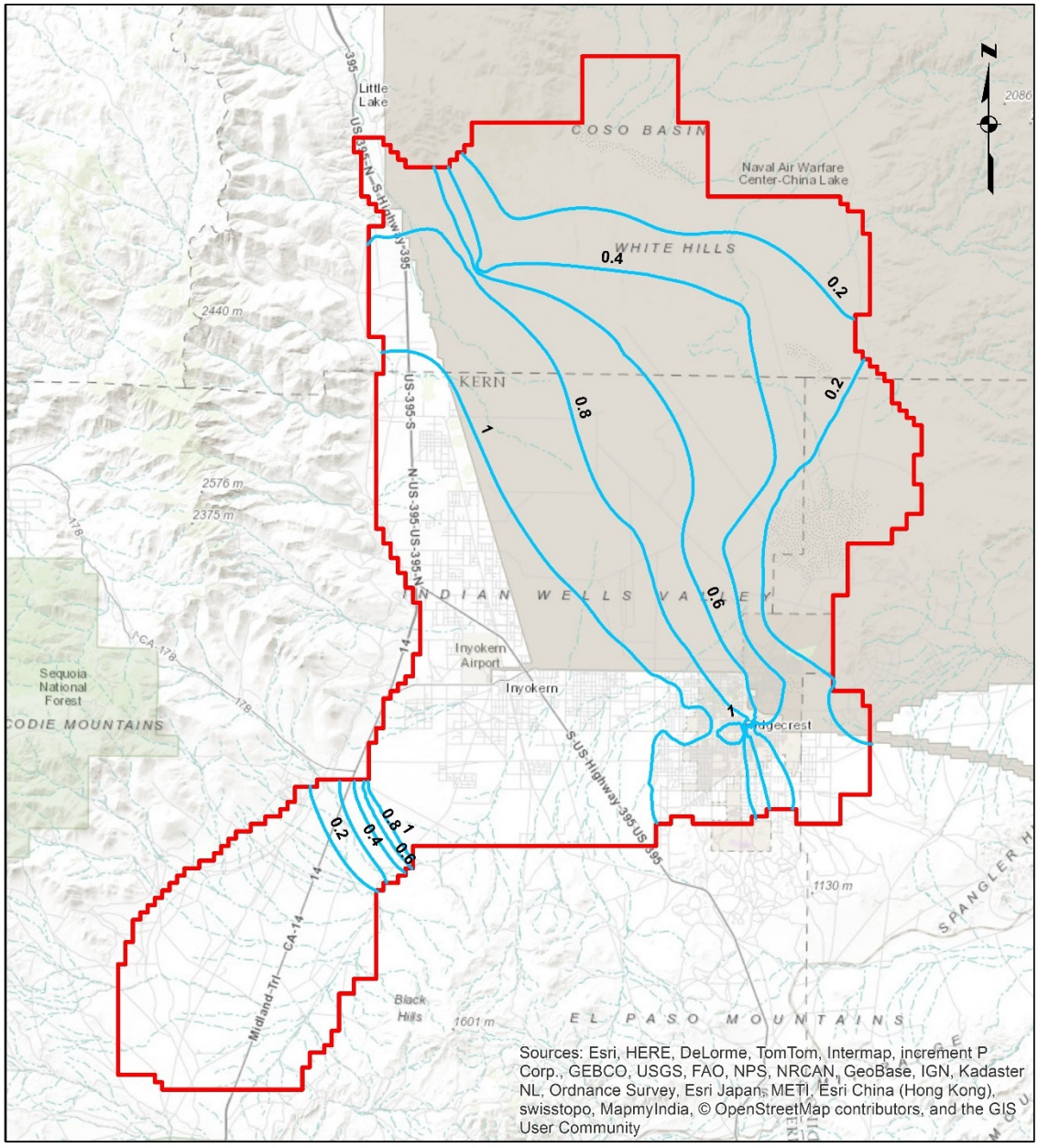

Figure 64. Simulated drawdown rates (ft/yr) for the base scenario over the period 2050 to 2123.

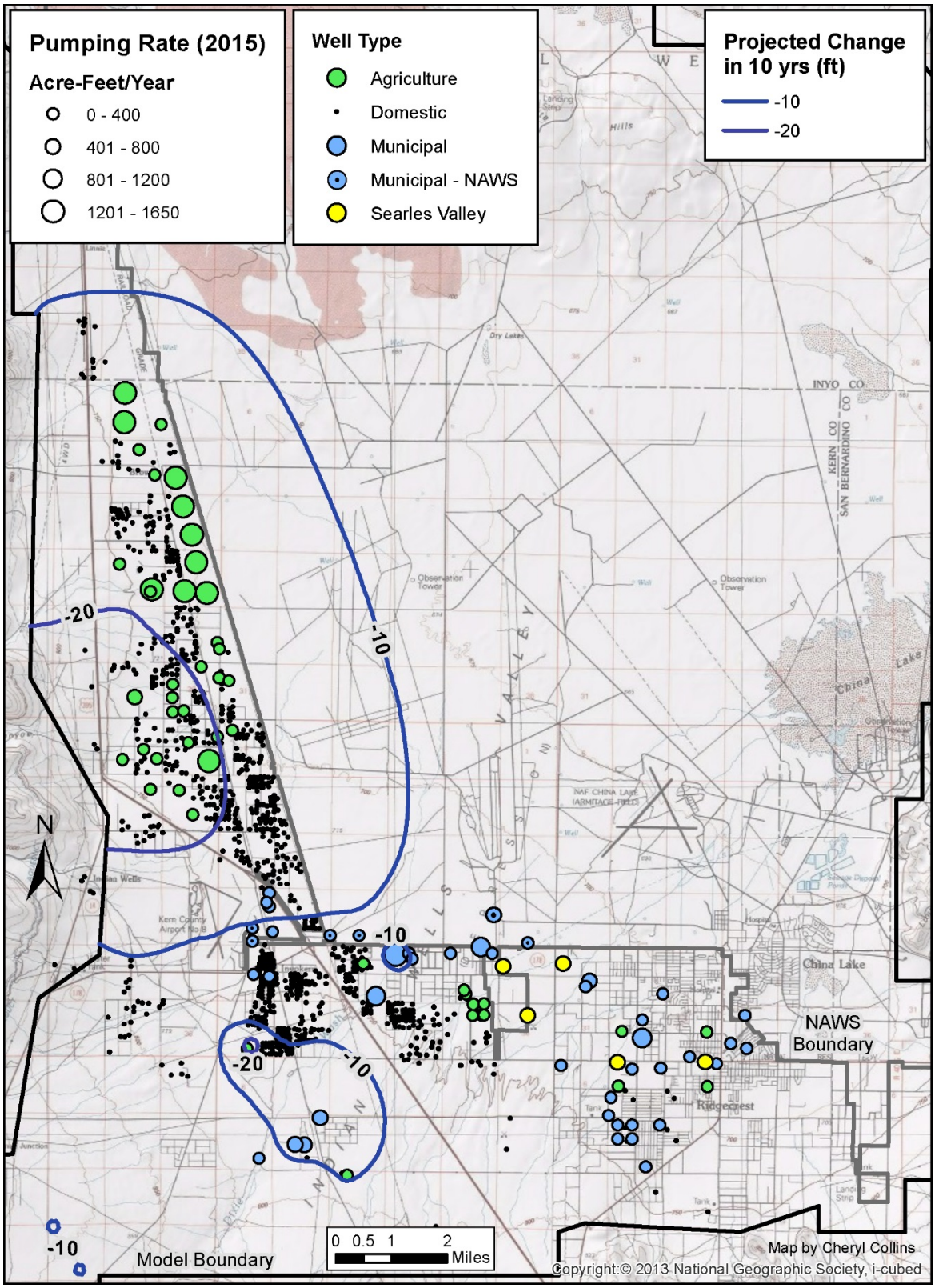

Figure 65. Total drawdown from 2014 to 2024 (10 years) for the base model.

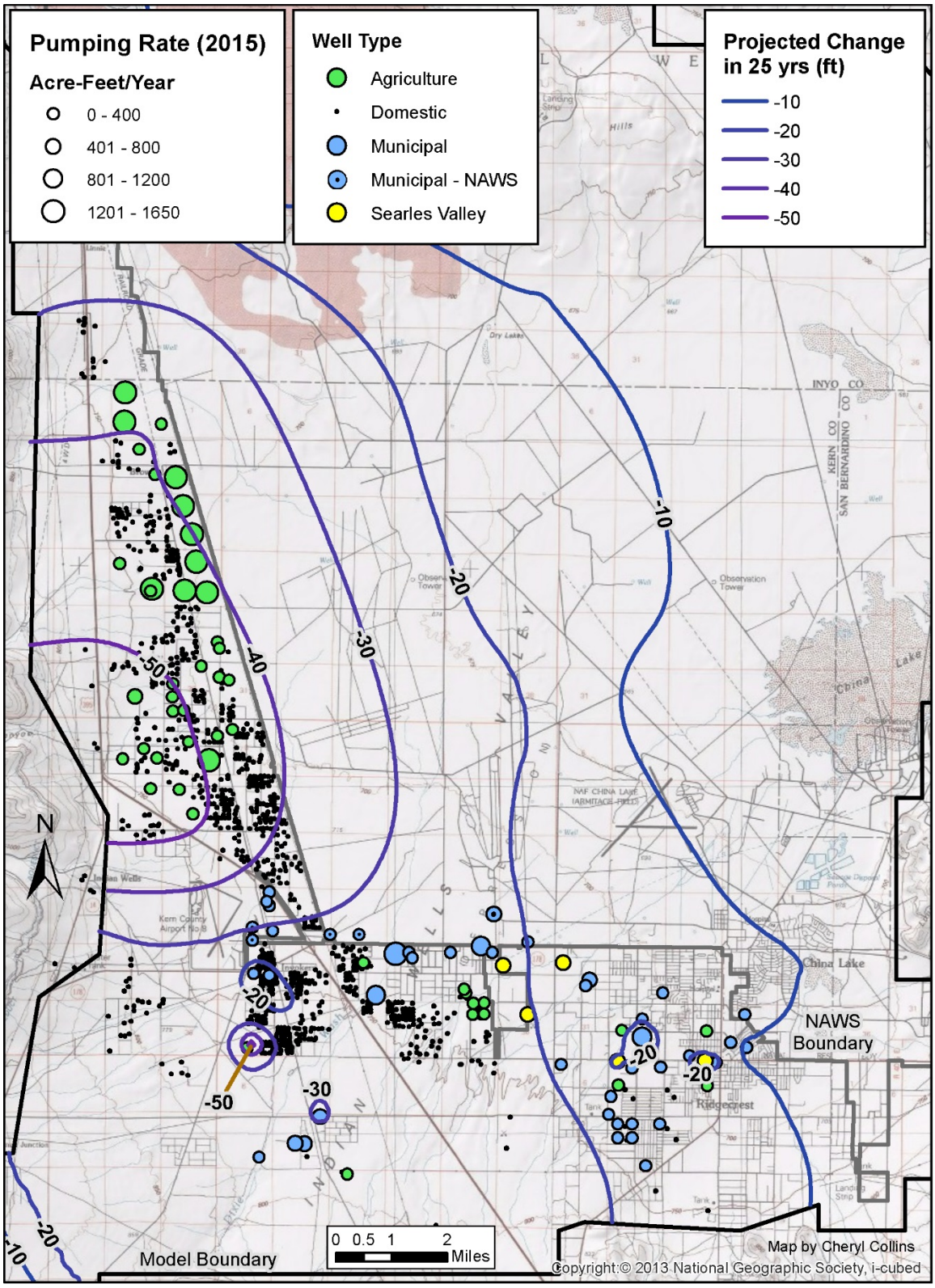

Figure 66. Total drawdown from 2014 to 2039 (25 years) for the base model.

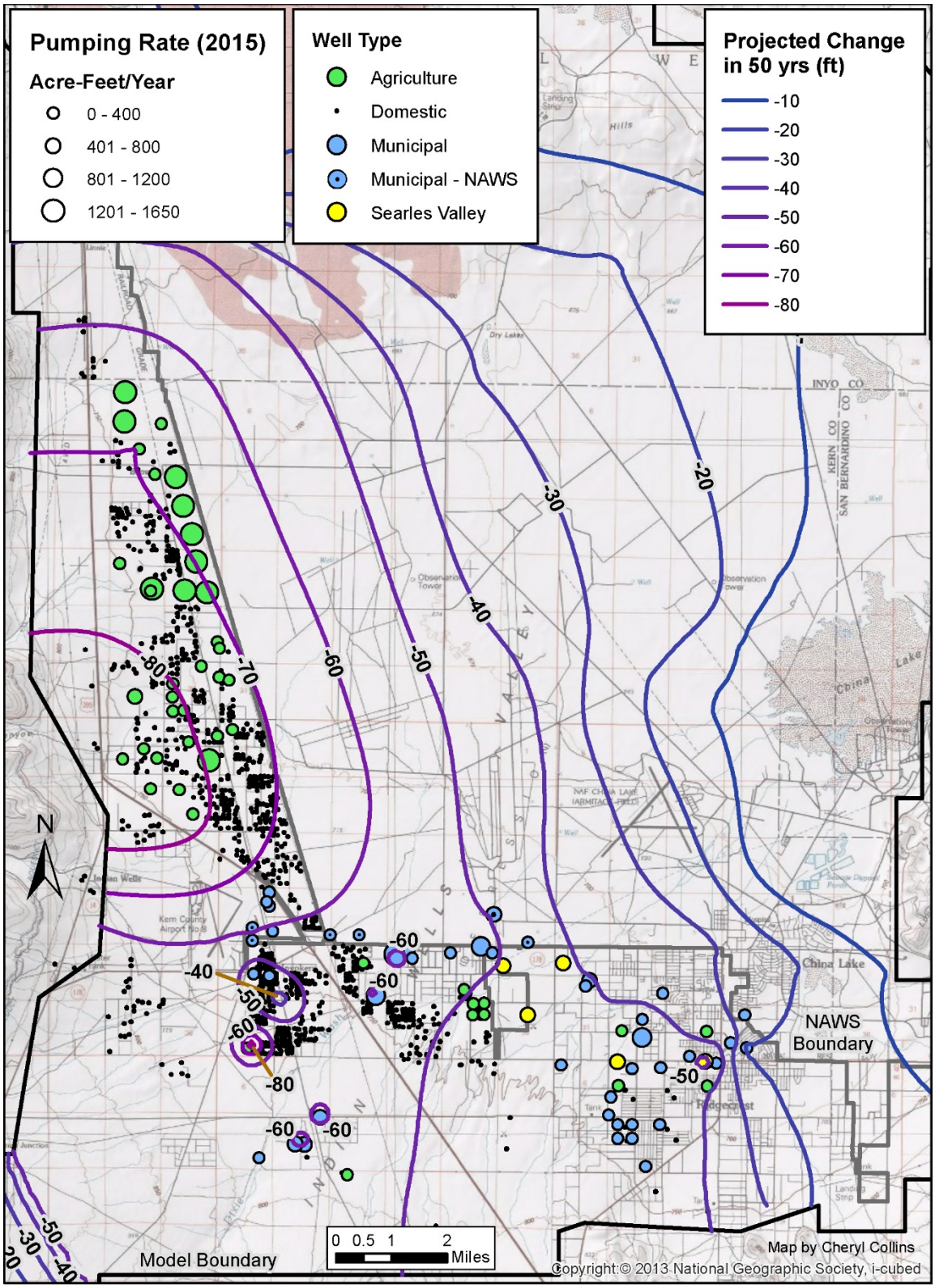

Figure 67. Total drawdown from 2014 to 2064 (50 years) for the base model.

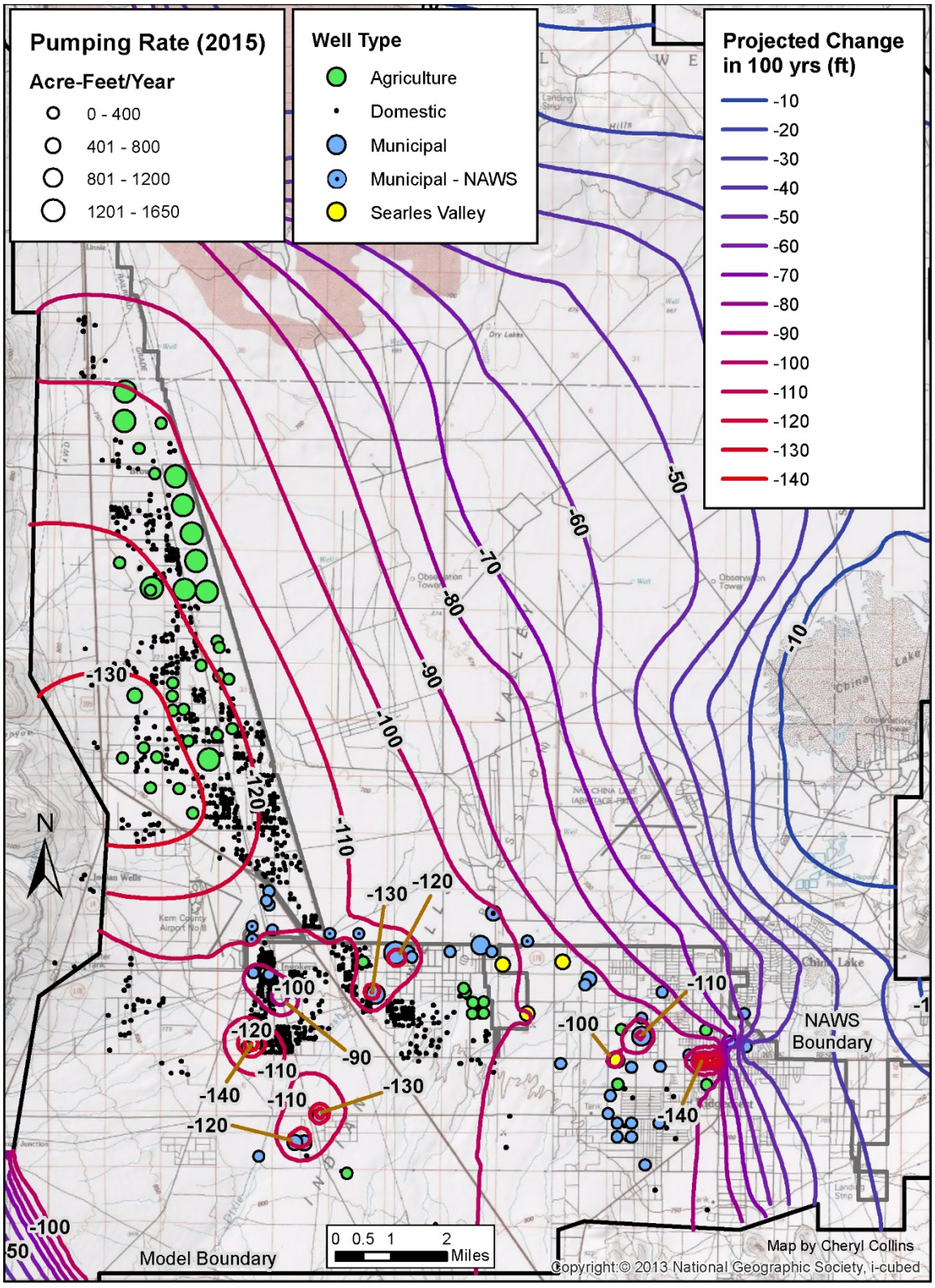

Figure 68. Total drawdown from 2014 to 2114 (100 years) for the base model.

14.0 REFERENCES

Anderson, T.W., Feethey, G.W., and Tucci, Patrick, 1992. *Geohydrology and Water Resources of Alluvial Basins in South-Central Arizona and Parts of Adjacent States.* United States Geological Survey Professional Paper 1406-B.

Anderson, T.W. and G.W. Freethey, 1995. Simulation of Ground-Water Flow in Alluvial Basins in South-Central Arizona and Parts of Adjacent States. United States Geological Survey Professional Paper 1406-D.

Anderson, M.P., W.W. Woessner, and R.J. Hunt, 2015. Applied Groundwater Modeling, Second Edition: Simulation of Flow and Advective Transport, Elsevier, New York, 564p.

Aubinet, M., B. Chermanne, M. Vandenhaute, B. Longdoz, M. Yernaux, E. Laitat, 2001. Long term carbon dioxide exchange above a mixed forest in the Belgian Ardennes. *Agricultural and Forest Meteorology*, **108**, 293–315.

Aubinet, M., A. Grelle, A. Ibrom U. Rannik, J. Moncrieff, T. Foken, A. Kowalski, P. Martin, P. Berbigier, C. Bernhofer, R. Clement, J. Elbers, A. Granier, T. Grünwald, K. Morgenstern, K. Pilegaard, C. Rebmann. W. Snijders, R. Valentini, and T. Vesala. 2000. Estimates of the annual net carbon and water exchange of forest: the EUROFLUX methodology. *Advances in Ecological Research*, **30**, 113–175.

Austin, C.F., 1988. Hydrology of Indian Wells Valley. China Lake, California, Naval Weapons Center, NWC Reg Memo 2606/103, document UN-CLASSIFIED.

Bacon, S.N., T.F. Bullard, K.D. Adams, and D.L. Decker, 2015. Geomorphic map of China Lake basin below 700 m elevation, Inyo, Kern, and San Bernardino counties, California. Map prepared by Desert Research Institute for Naval Air Warfare Center, Weapons Division, NAWS China Lake, March 2015, scale 1:50,000.

Bauer, C.M., 2002, "The Hydrogeolgy of Rose Valley and Little Lake Ranch, Inyo County, California," Master's Thesis, California State University, Bakersfield, California.

Bean, R.T., 1989. Hydrogeologic Conditions in Indian Wells Valley and Vicinity, Prepared for California Department of Water Resources, 56p.

Berenbrock, C., and P. Martin. 1991. "The Ground-Water Flow System in the Indian Wells Valley, Kern, Inyo, and San Bernardino Counties, California." USGS Water Resources Investigations Report 89-4191.

Berenbrock, C., and R.A. Schroeder, 1994. Ground-Water Flow and Quality, and Geochemical Processes, in Indian Wells Valley, Kern, Inyo, and San Bernardino Counties, California, 1987-88. U.S. Geological Survey, Water-Resources Investigations Report 93-4003.

Bloyd, R.M., and S.G. Robson, 1971. Mathematical groundwater model of Indian Wells Valley, California, U.S. Geological Survey Open-File Report, 36 p.

Brown and Caldwell, 2006, "Rose Valley Groundwater Model", Coso Operating Company, LLC, Rose Valley, California, April 10, 2006.

Brown and Caldwell. March 27, 2009. Indian Wells Valley basin groundwater model and hydrogeologic study. Final report. Prepared for Indian Wells Valley Water District, Ridgecrest, CA.

Bullard, T.F., S.N. Bacon, K.D. Adams, and D.L. Decker, 2015. Phase II: Geomorphic Map of the China lake Basin below 700 m in Support of cultural Resource Management at NAWS China Lake. Report prepared by Desert Research Institute for Naval Air Warfare Center, Weapons Division, NAWS China Lake, CA, March 2015. DRI Division of Hydrologic Sciences, NESEP Publication No. 50011, 58 p. + 2 appendices and map.

California Department of Water Resources (DWR). January 1980. Groundwater basins in California. Bulletin 118-80. Sacramento, CA.

Chimner, R.A., and D.J. Cooper, 2004. Using stable oxygen isotopes to quantify the water source used for transpiration by native shrubs in the San Luis Valley, Colorado U.S.A.: Plant and Soil, Vol. 260, p. 225-236.

Clark, A.L., 1999. A Groundwater Flow Model of Indian Wells Valley, California, Utilizing GMS with GIS Applications, Master's Thesis, Department of Hydrology and Water Resources, University of Arizona.

Danskin, W.R., 1998. Evaluation of the hydrologic system and selected water-management alternatives in the Owens Valley, California, USGS Water Supply Paper 2370-H

Doherty, J., 2003. Ground water model calibration using pilot points and regularization, Ground Water, 41(2), pp. 170-177.

Doherty, J., 2005. PEST, Model-Independent Parameter Estimation User Manual: 5th Edition, Watermark Numerical Computing, Australia.

Doherty, J.E., and R.J. Hunt, 2010, Approaches to highly parameterized inversion—A guide to using PEST for groundwater-model calibration: U.S. Geological Survey Scientific Investigations Report 2010–5169, 59 p

Donovan, L.A., J.H. Richards, and M.W. Muller, 1996, Water relations and leaf chemistry of Chrysothamnus nauseosus ssp. consimilis (Asteraceae) and Sarcobatus vermiculatus (Chenopodiaceae): American Journal of Botany, Vol. 83, No. 12, p. 1637-1646.

Dullien, F.A.L., 1992. Porous Media: Fluid Transport and Pore Structure, Academic, San Diego.

Dutcher, L.C., and W.R. Moyle, Jr. 1973. "Geologic and Hydrologic Features of the Indian Wells Valley, California." USGS Water Supply Paper 2007.

Epstein, B., G.M. Pohll, J. Huntington, and R.W.H. Carroll, 2010. Development and uncertainty analysis of an empirical recharge prediction model for Nevada's desert basins. Nevada Water Resources Association. 5(1): 1-22.

Falge E, D. Baldocchi, R.J. Olson , P. Anthoni, M. Aubinet, C. Bernhofer, G. Burba, R. Ceulemans, R. Clement, H. Dolman, A. Grainer, T. Grunwald, D. Hollinger, N. Jensen, G. Katul, P. Keronen, A. Kowalski, C. Ta Lai, B. Law, T. Meyers, J. Moncrieff, E. Moors, J. Munger, K. Pilegaard, U. Rannik, C. Rebmann, A. Suyker, J. Tenhunen, K. Tu, S. Verma, T. Vesala, K. Wilson, and S.Wofsy. 2001. Gap filling strategies for defensible annual sums of net ecosystem exchange. *Agricultural and Forest Meteorology*, **107**, 43–69.

Foken, Th., M. Göckede, M. Mauder, L. Mahrt, B. Amiro, W. Munger, 2004. Post-field data quality control. In: *Handbook of Micrometeorology* (eds Lee X, Massman W, Law B), pp. 181–208. Kluwer Academic Publishers, Dordrecht.

Foken, Th., B. Wichura, 1996. Tools for quality assessment of surface-based flux measurements. *Agricultural and Forest Meteorology*, **78**, 83–105.

Freeze, R.A, and J.A. Cherry, 1979. Groundwater, Prentice Hall, New Jersey, 604p.

Gash, J.H.C., and A.J. Dolman (2003), Sonic anemometer (co)sine response and flux measurement I. potential for (co)sine error to affect sonic anemometer-based flux measurements, *Agricultural and Forest Meteorology*, 119, 195–207.

Geissbühler, P., R. Siegwolf, and W. Eugster, 2000. Eddy covariance measurements on mountain slopes: the advantage of surface-normal sensor orientation over a vertical set-up. *Boundary-Layer Meteorology*, **96**, 317–392.

Gelhar, L.W., C. Welty, and K.W. Rehfeldt, 1992. A critical review of data on field-scale dispersion in aquifers, Water Resources Research, 28(7), pp.1955-1974.

Guler, C., 2002. Hydrogeochemical Evaluation of the Groundwater Resources of Indian Wells-Owens Valley Area, Southeastern California. Ph.D. Thesis prepared for Colorado School of Mines, Golden, Colorado.

Ham, J.M., and J.L. Heilman, 2003. Experimental test of density and energy-balance corrections on carbon dioxide flux as measured using open-path eddy covariance. *Agronomy Journal*, **95**, 1393–1403.

Harbaugh, A.W., 2005. MODFLOW-2005, the U.S. Geological Survey modular ground-water model - the Ground-Water Flow Process: U.S. Geological Survey Techniques and Methods 6-A16, variously p.

Harbaugh, A.W., E.R. Banta, M.C. Hill, and M.G. McDonald, 2000. MODFLOW-2000, The U.S. Geological Survey modular ground-water model -- User guide to modularization concepts and the Ground-Water Flow Process: U.S. Geological Survey Open-File Report 00-92, 121 p.

Hoffmann, J., S.A. Leake, D.L. Galloway, and A.M. Wilson, 2003. MODFLOW-2000 Ground-Water Model–User Guide to the Subsidence and Aquifer-System Compaction (SUB) Package. U.S. Geological Survey Ground-Water Resources Program. Open File Report 03-233.

Hsieh, C.I., G. Katul, T.W. Chi, 2000. An approximate analytical model for footprint estimation of scalar fluxes in thermally stratified atmospheric flows. *Advances in Water Resources*, **23**,765–772.

ICWD/LADWP, 1989, Root data collected at Inyo/Los Angeles permanent monitoring sites, October 1989. Inyo County Water Department and the Los Angeles Department of Water and Power. Bishop, California.

Indian Wells Valley Cooperative Groundwater Technical Advisory Committee and Geochemical Technologies Corporation, 2008, Installation and Implementation of a Comprehensive Groundwater Monitoring Program for the Indian Wells Valley, California. Prepared for Local Ground Water Assistance Program AB303.

IWVCGTAC and Geochemical Technologies Corp., 2008, see Indian Wells Valley Cooperative Groundwater Technical Advisory Committee and Geochemical Technologies Corporation, 2008.

Kaimal, J.C., and J.J. Finnigan, 1994. Atmospheric boundary layer flows: Their structure and measurement. *Oxford University Press*, New York, NY, pp. 289.

Katzenstein, K.W., 2013. Evaluating Potential Land Subsidence Induced by Groundwater Withdrawal from the Indian Wells Valley, CA Using InSAR. Geological Society of America *Abstracts with Programs.* Vol. 45, No. 7, p.775.

Kern County Planning and Community Development Department, 2015. Indian Wells Valley Land Use Management Plan, Draft Program Environmental Impact Report. Available at http://pcd.kerndsa.com/planning/environmental-documents/390-indian-wells-valley-land-use-management-plan.

Kunkel, F., and G.H. Chase, 1969. Geology and ground water in Indian Wells Valley, California, U.S. Geological Survey Open-File Report, 84 p.

Lee, C.H., 1912. Ground-water resources of Indian Wells Valley, California, California State Conservation Commission Report, p. 403-429.

Lee, X., J. Finnigan, U.K.T Paw, 2004. Coordinate systems and flux bias error. In: *Handbook of Micrometeorology* (eds. Lee X, Massman W, Law B), pp. 33–66. Kluwer Academic Publishers, Dordrecht.

Loescher, H.W., T. Ocheltree, B. Tanner , J. Liburdy, and B. Law., 2005. Comparison of temperature and wind statistics in contrasting environments among different sonic anemometer-thermometers. *Agricultural and Forest Meteorology*, **133**, 119–139.

Massman, W.J., 2000. A simple method for estimating frequency response corrections for eddy covariance systems. *Agricultural and Forest Meteorology*, **104**, 185–198.

Massman, W.J., 2001. Reply to comment by Rannik on ‘‘A simple method for estimating frequency response corrections for eddy covariance systems’’. *Agricultural and Forest Meteorology*, **107**, 247–251.

Massman, W.J., and R. Clement, 2004. Uncertainty in eddy covariance flux estimates resulting from spectral attenuation. In: *Handbook of Micrometeorology* (eds Lee X, Massman W, Law B), pp. 67–100. Kluwer Academic Publishers, Dordrecht.

Maxey, G.B., and T.E. Eakin, 1949. Ground water in White River Valley, White Pine, Nye and Lincoln Counties, Nevada. No. 8, State of Nevada Office of the State Engineer, prepared in cooperation with the United States Department of the Interior Geological Survey, Carson City, Nevada.

Meinzer, O.E., 1927, Plants as indicators of ground water: U.S. Geological Survey Water-Supply Paper 577, 95 p.

Menke, J., E. Reyes, A. Glass, D. Johnson, and J. Reyes, 2013. 2013 California Vegetation Map in Support of the Desert Renewable Energy Conservation Plan. Final Report. Prepared for the California Department of Fish and Wildlife Renewable Energy Program and the California Energy Commission. Aerial Information Systems, Inc., Redlands, CA.

MHA Environmental Consulting (MHA), 2008. Coso Operating Company Hay Ranch Water Extraction and Delivery System, Conditional Use Permit (CUP 2007-003) Application, SCH#2007101002, Draft EIR, Inyo County, California. Prepared for Inyo County Planning Department, Indepedence, California, July 2008.

Michaud, G.A., H.C. Monger, and D.L. Anderson, 2013. Geomorphic-vegetation relationships using geopedological classification system, northern Chihuahuan Desert, USA. Journal of Arid Environments 90, 45–54.

Monastero, F., J. Walker, A. Katzenstein, and A. Sabin. 2002. *Neogene Evolution of the Indian Wells Valley, East-Central California*, Geological Society of America, Memoir 195.

Morgan, T., 2010. Water Supply Improvement Plan Phase 1 and 2 Final Technical Memorandum, Project No. 27-1666. Prepared on behalf of Layne Christensen Company for Indian Wells Valley Water District.

Nichols, W.D., 2000. Regional Ground-Water Evapotranspiration and Ground-Water Budgets. Professional Paper 1628. United States Geological Survey, Reston, Virginia.

PRISM Climate Group, 2012. Oregon State University, http://prism.oregonstate.edu, created July 10, 2012.

Schwartz, F., and H. Zhang, 2003. *Fundamentals of Ground Water*. John Wiley & Sons, Inc., New York, New York.

Smith, G.I., 2009. *Late Cenozoic Geology and Lacustrine History of Searles Valley, Inyo and San Bernadino Counties, California.* U.S. Geological Survey Professional Paper 1727.

St. Amand, P., 1986. “Water Supply of Indian Wells Valley, California.” NWC TP 6404. NAWS, Ridgecrest, CA.

Stephens, D.B., 2011. Revised Groundwater Flow Model and Predictive Simulation Results, Coso Operating Company, Hay Ranch Water Extraction and Delivery System Conditional Use Permit (CUP 2007-003), Prepared for County of Inyo, Independence, Ca, 165p.

Stephens, D.B, K. Hsu, M.A. Prieksat, M.D. Ankeny, N. Blandford, T.L. Roth, J.A. Kelsey, and J.R. Whitworth, 1998. A comparison of estimated and calculated effective porosity, Hydrogeology Journal, 6, pp. 156-165.

Stoner, M., geologist, NAWS, 2013. E-mail to Gus Yates, hydrologist, Todd Engineers.

Tetra Tech EM, Inc. (TtEMI), 2003a. *Draft Basewide Hydrogeologic Characterization Summary Report. NAWS China Lake, California*. Prepared under CLEAN II Contract for Department of the Navy.

Tetra Tech EM, Inc. (TtEMI), 2003b. *Groundwater Management in the Indian Wells Valley basin, Ridgecrest, CA.* Albuquerque, NM. Prepared for East Kern County Resource Conservation District, Ridgecrest, CA.

Thompson, D.G., 1929. The Mojave Desert region, California, USGS Water-Supply Paper 578.

Todd Engineers, 2014. Indian Wells Valley Resource Opportunity Plan – Water Availability and Conservation Report, Submitted to Kern County Planning and Community Development Department, 89p.

Thyne, G.D., J.M. Gillespe, and J.R. Ostdick, 1999. Evidence for interbasin flow through bedrock in the southeastern Sierra Nevada, Geological Society of America Bull. 111 (11): 1600-1616.

TriEcoTt, joint venture, 2012. Technical justification for beneficial use changes for groundwater in Salt Wells Valley and shallow groundwater in eastern Indian Wells Valley. San Diego, CA. Prepared for: Department of the Navy, Naval Facilities Engineering Command Southwest, San Diego, California.

Tyler, S.W., S. Kranz, M.B. Parlange, J. Albertson, G.G. Katul, G.F. Cochran, B.A. Lyles, and G. Holder, 1997. Estimation of groundwater evaporation and salt flux from Owens Lake, California, USA, J. Hydrology, 200, 110-135.

U.S. Bureau of Reclamation, 1993. Indian Wells Valley Groundwater Project: USBR Technical Report Volumes I and II.

Von Huene, R.E., 1960. Structural geology and gravimetry of Indian Wells Valley, southeastern California: California State University, Los Angeles, Ph.D. thesis. 138 p.

Warner, J.W., 1975. Ground-water quality in Indian Wells Valley, California: U.S. Geological Survey Water Resources Investigations Report 8-75, 59 p.

Watt, D.E., 1993. "Estimating Recharge Distribution to Indian Wells Based on Vegetation Distribution in the Recharge Watersheds." Page 5 of Appendix I in "Indian Wells Valley Groundwater Project, Volume II, Technical Report." December.

Webb, E.K., G.I. Pearman, and R. Leuning, 1980. Correction of flux measurements for density effects due to heat and water vapour transfer. *Quarterly Journal of the Royal Meteorological Society*, **106**, 85–100.

Wohlfahrt, G., C. Anfang, M. Bahn , A. Haslwanter, C. Newesely, M. Schmitt, M. Drösler, J. Pfadenhauer, A. Cernusca. 2005. Quantifying nighttime ecosystem respiration of a meadow using eddy covariance, chambers and modeling. *Agricultural and Forest Meteorology*, **128**, 141–162.

Wohlfahrt, G., L.F. Fenstermaker, J.A. Arnone III, 2008. Large annual net ecosystem CO_2 uptake of a Mojave Desert ecosystem. *Global Change Biology*, **14**, 1475-1487.

Zbur, R.T., 1963. A geophysical investigation of Indian Wells Valley, California: U.S. Naval Ordnance Test Station, China Lake, California, NOTS Technical Publication 2795. 98 p.

Zheng, C., and P.P. Wang, 1999. MT3DMS: A Modular Three-Dimensional Mulitspecies Transport Model for Simulation of Advection, Dispersion, and Chemical Reactions of Contaminants in Groundwater Systems; Documentation and User's Guide, U.S. Army Corps of Engineers Contract Report SERDP-99-1, Vicksburg, Mississippi, 220 pages.

GLOSSARY OF HYDROGEOLOGIC TERMS

Acre-foot	Common unit for volume of water used or stored. It is the volume of water required to cover one acre of land to a depth of one foot. Equal to 325,851 gallons.
Hydraulic conductivity (K)	A proportionality constant in groundwater flow equations describing the capacity of rock to transmit water, analogous to electrical or thermal conductivity. Hydraulic conductivity is a function of both the porous medium and the fluid. The dimensions of K are $[L/T]$.
Permeability (k)	The ease with which fluid passes through a porous medium. It is a function of the medium alone and does not depend on the characteristics of the fluid. The dimensions of k are $[L^2]$.
Specific capacity	This is a measure of the productivity of a well, calculated as the yield of a well per unit of drawdown. The dimensions are [L^2/T; usually GPM/ft]
Specific storage (S_s)	The volume of water that a unit volume of aquifer releases from storage under a unit decline in hydraulic head. Water released from storage is produced by compaction of the aquifer due to increasing stress, and/or expansion of water caused by decreasing pressure, both a result of decline in head. Aquifer and fluid compressibility control storage. The dimensions of S_s are $[L]^{-1}$.
Specific yield (S_y)	The storage term for an unconfined aquifer, it is the volume of water an unconfined aquifer releases from storage per unit surface area of aquifer per unit decline in the water table. It is dimensionless.
Transmissivity	The rate at which water is transmitted through a unit width of an aquifer under a unit hydraulic gradient. It equals the hydraulic conductivity multiplied by the aquifer thickness. The dimensions of transmissivity are $[L^2/T]$.

This page intentionally left blank.

APPENDIX A: TRANSIENT CALIBRATION RESULTS FOR SELECTED WELLS

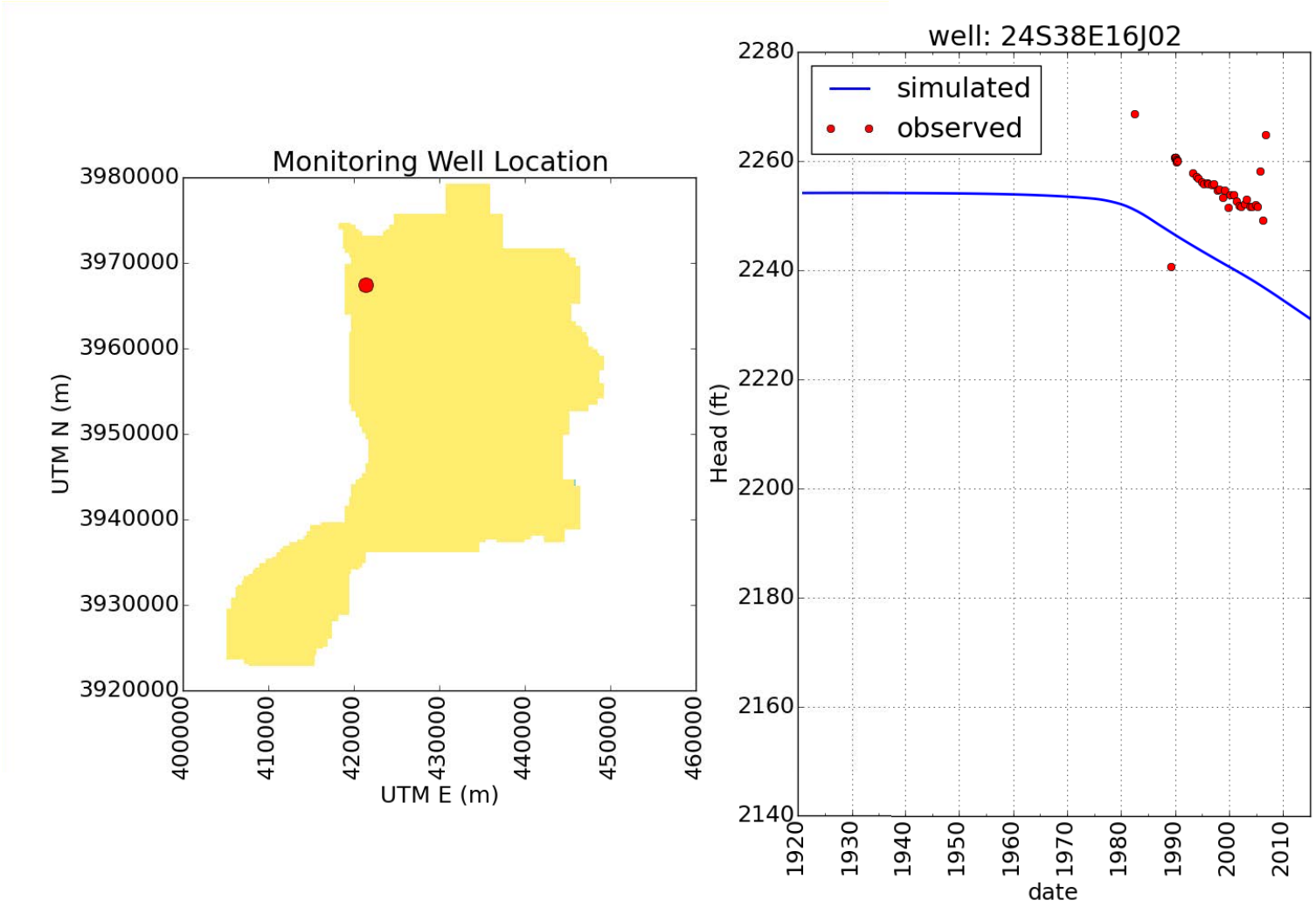

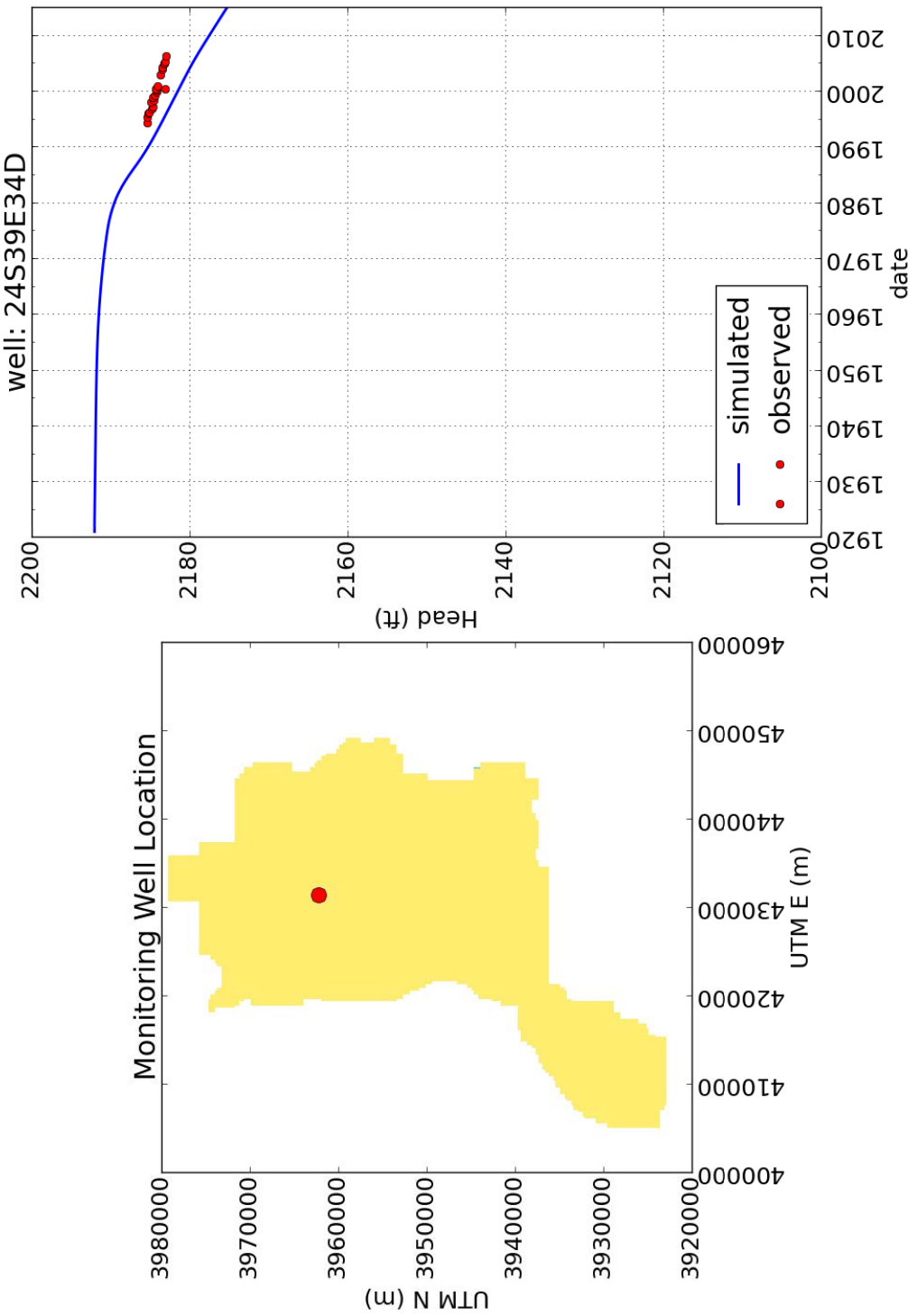
well: 24S39E34D
Head (ft)
2200
2180
2160
2140
2120
2100
1920
1930
1940
1950
1960
1970
1980
1990
2000
2010
date
simulated
observed
Monitoring Well Location
UTM N (m)
3980000
3970000
3960000
3950000
3940000
3930000
3920000
400000
410000
420000
430000
440000
450000
460000
UTM E (m)

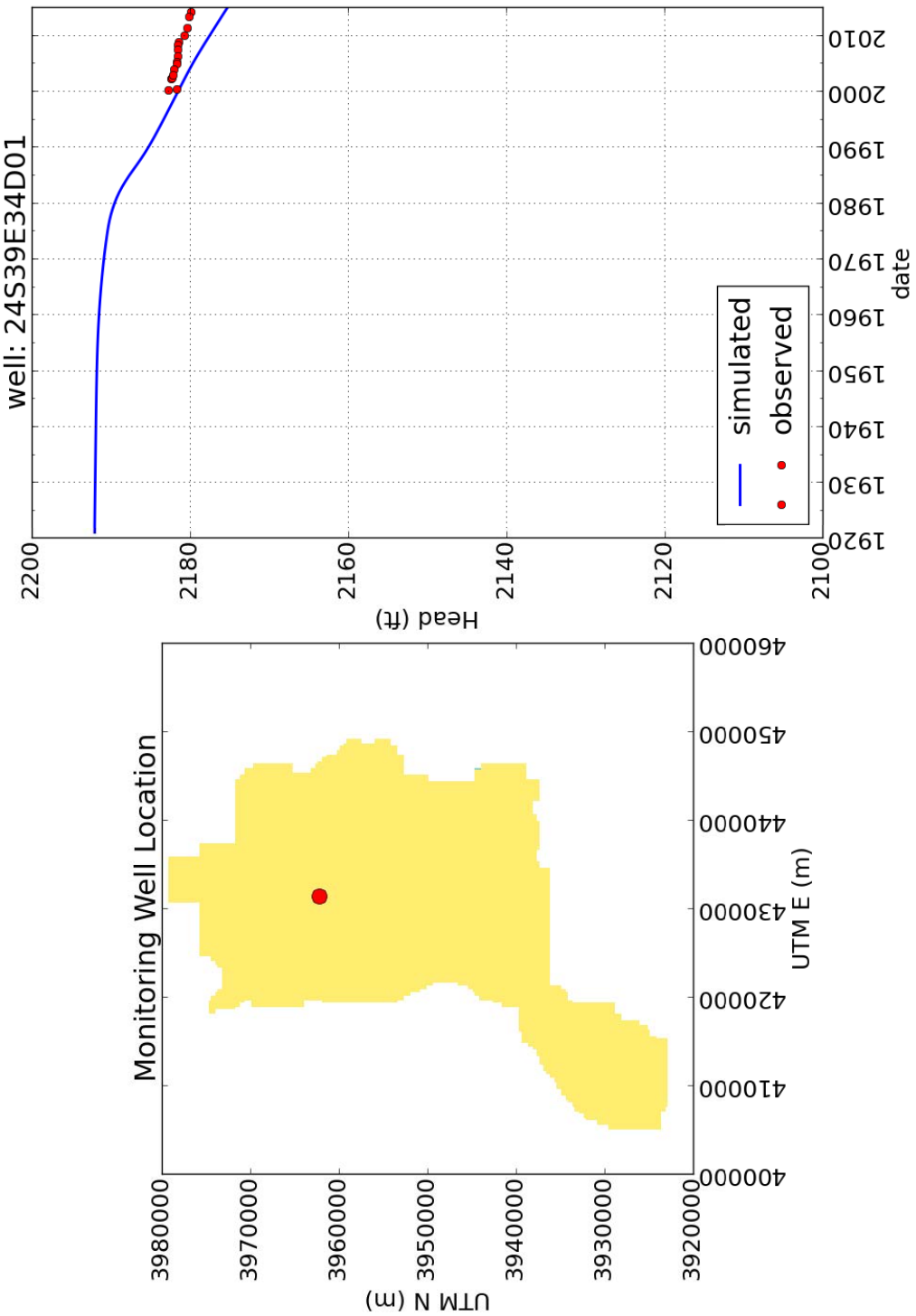
well: 24S39E34D01
Head (ft)
2200
2180
2160
2140
2120
2100
date
1920
1930
1940
1950
1960
1970
1980
1990
2000
2010
simulated
observed
Monitoring Well Location
UTM N (m)
3980000
3970000
3960000
3950000
3940000
3930000
3920000
UTM E (m)
400000
410000
420000
430000
440000
450000
460000

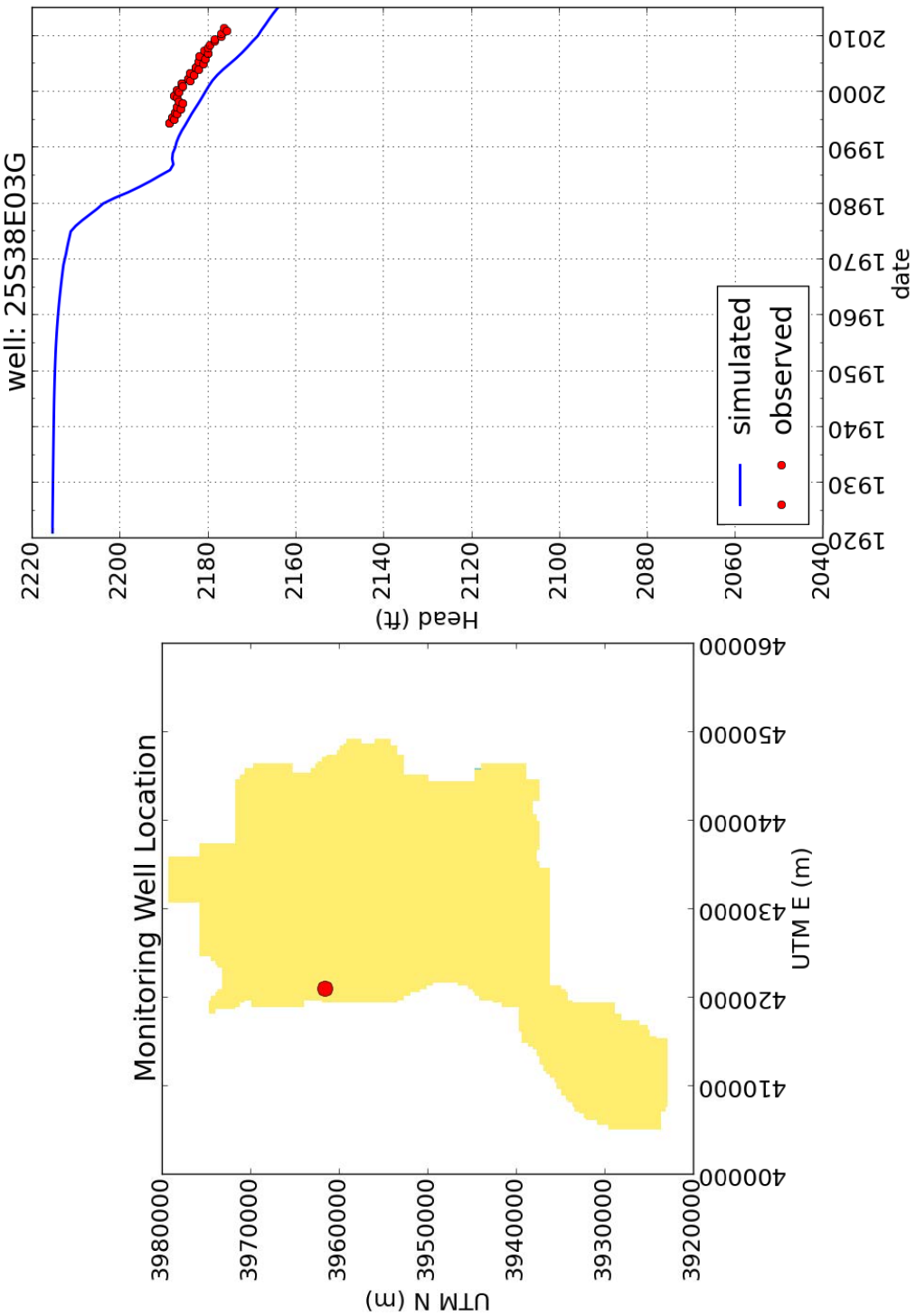
well: 25S38E03G
Head (ft)
2220
2200
2180
2160
2140
2120
2100
2080
2060
2040
date
1920
1930
1940
1950
1960
1970
1980
1990
2000
2010
simulated
observed
Monitoring Well Location
UTM N (m)
3980000
3970000
3960000
3950000
3940000
3930000
3920000
UTM E (m)
400000
410000
420000
430000
440000
450000
460000

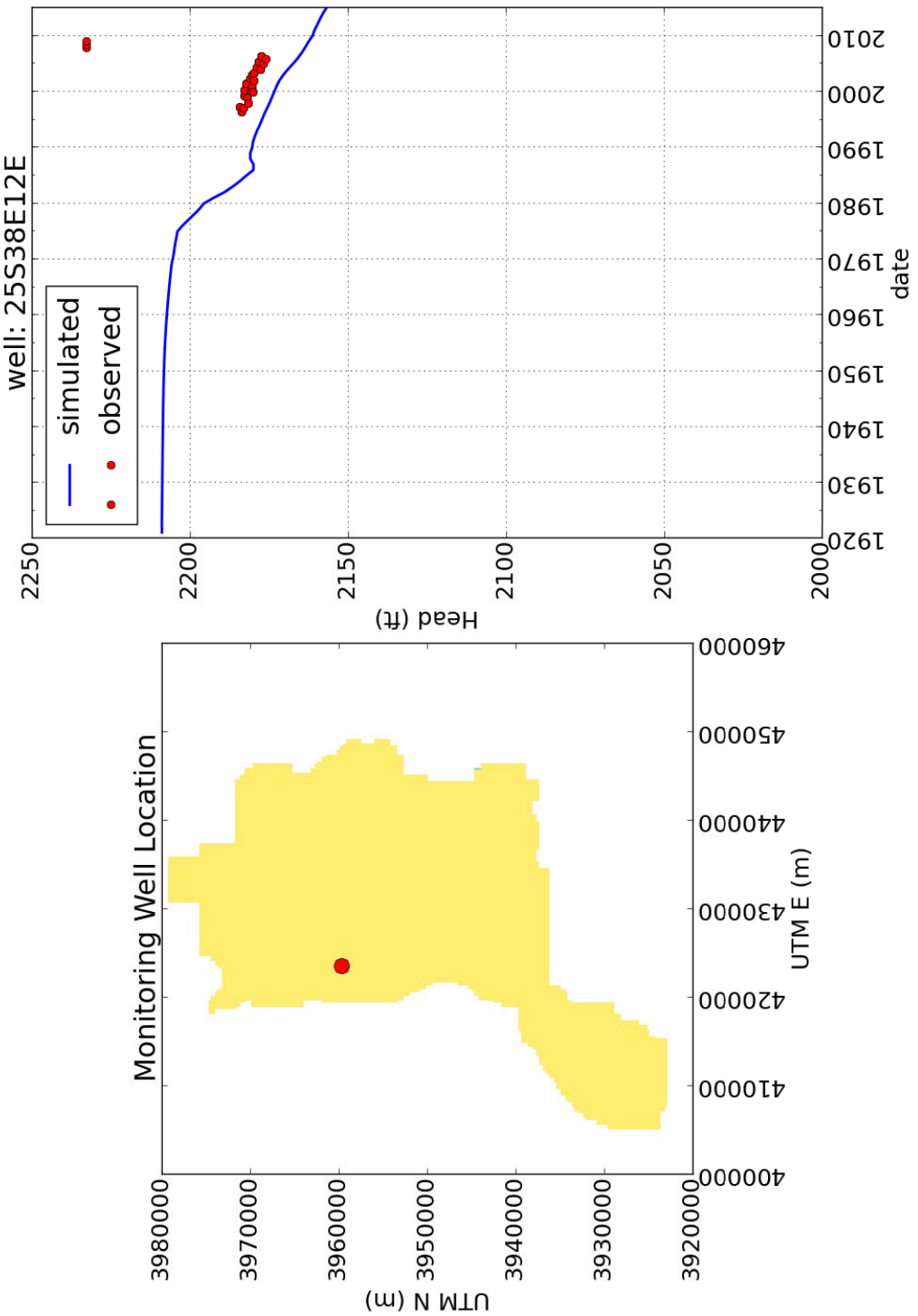
well: 25S38E12E
simulated
observed
Head (ft)
date
2250
2200
2150
2100
2050
2000
1920
1930
1940
1950
1960
1970
1980
1990
2000
2010
Monitoring Well Location
UTM N (m)
UTM E (m)
3980000
3970000
3960000
3950000
3940000
3930000
3920000
400000
410000
420000
430000
440000
450000
460000

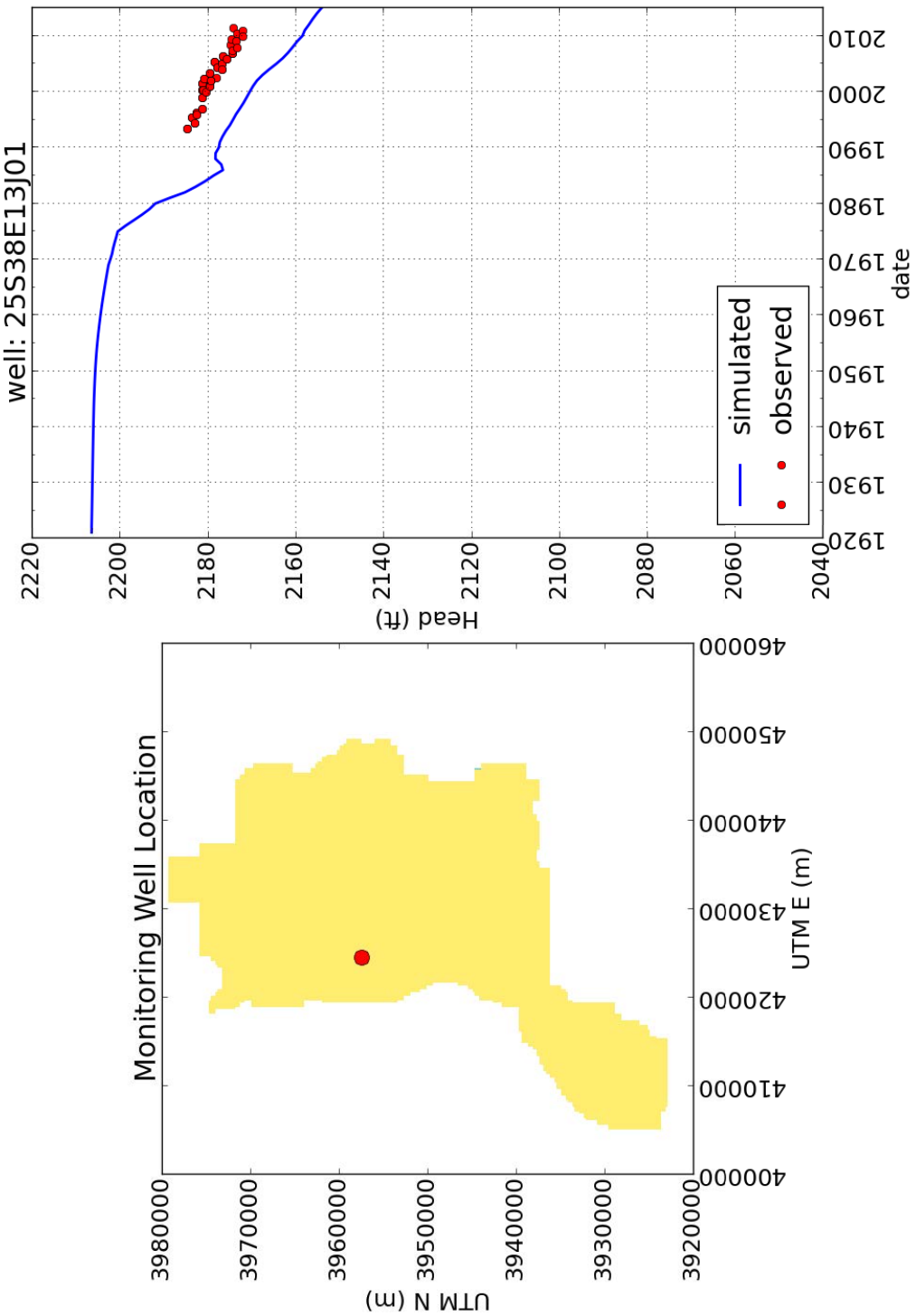
well: 25S38E13J01
Head (ft)
2220
2200
2180
2160
2140
2120
2100
2080
2060
2040
date
1920
1930
1940
1950
1960
1970
1980
1990
2000
2010
simulated
observed
Monitoring Well Location
UTM N (m)
3980000
3970000
3960000
3950000
3940000
3930000
3920000
UTM E (m)
400000
410000
420000
430000
440000
450000
460000

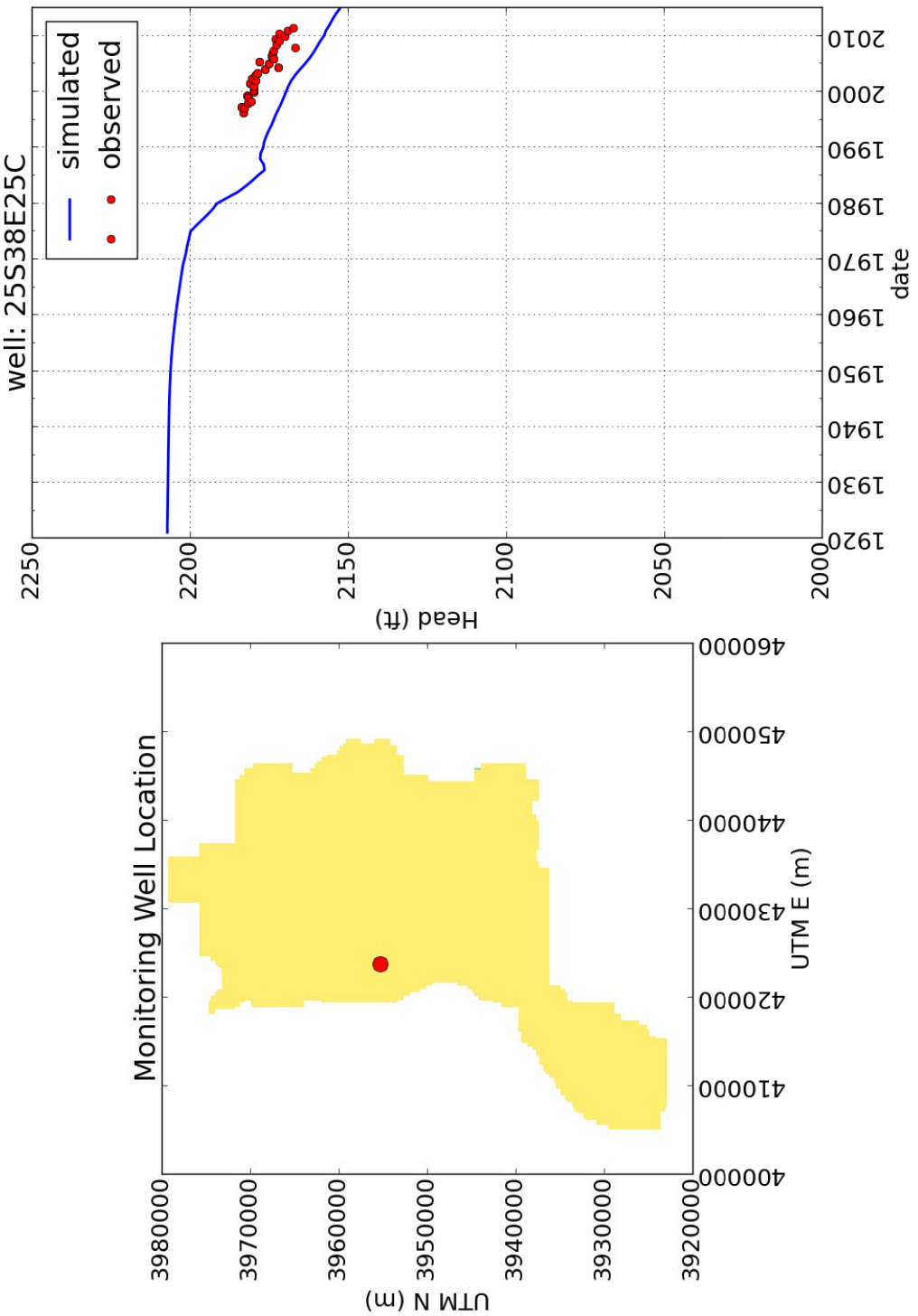
well: 25S38E25C
simulated
observed
Head (ft)
date
Monitoring Well Location
UTM N (m)
UTM E (m)

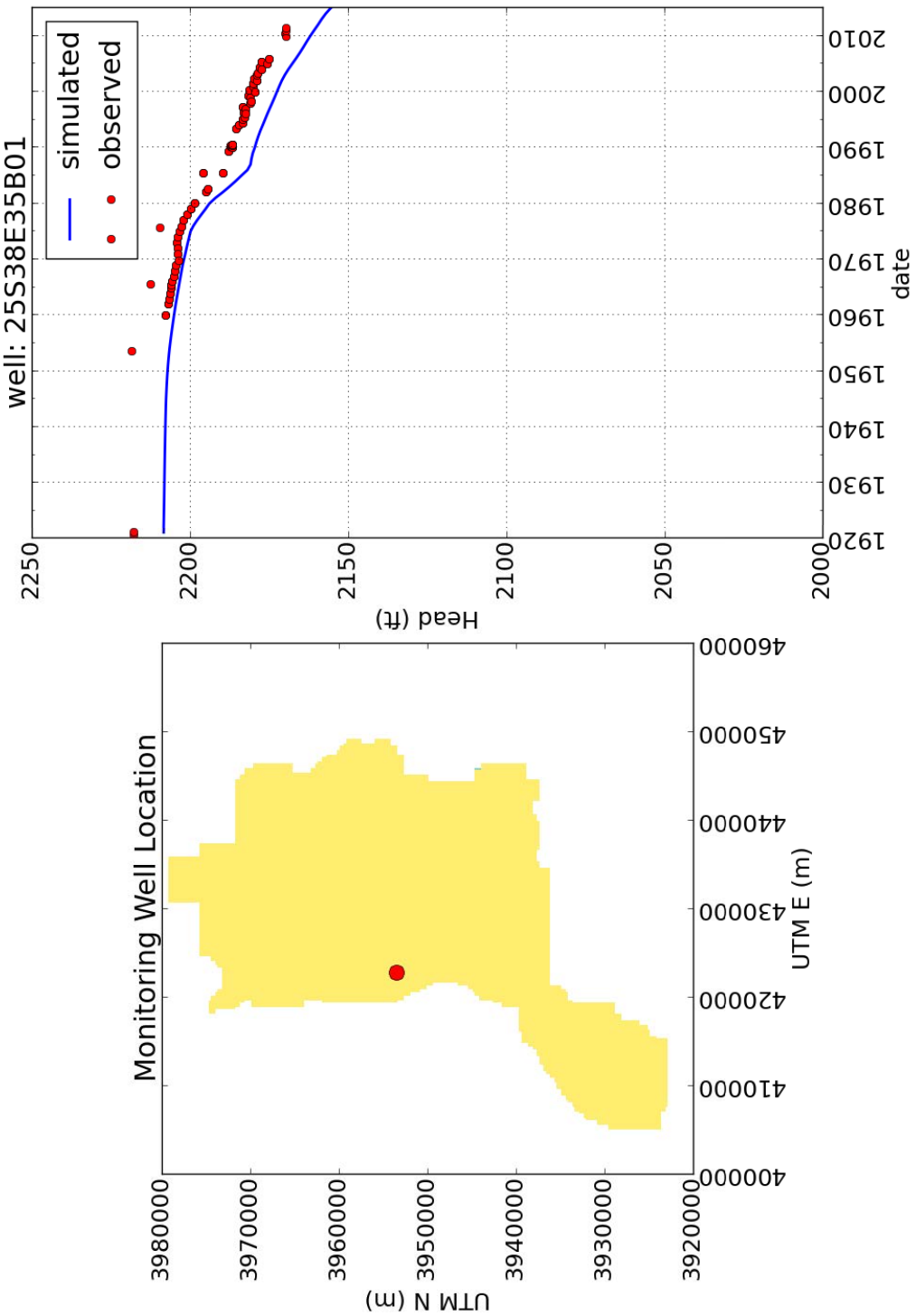
well: 25S38E35B01
simulated
observed
Head (ft)
date
2250
2200
2150
2100
2050
2000
1920
1930
1940
1950
1960
1970
1980
1990
2000
2010
Monitoring Well Location
UTM N (m)
UTM E (m)
3980000
3970000
3960000
3950000
3940000
3930000
3920000
400000
410000
420000
430000
440000
450000
460000

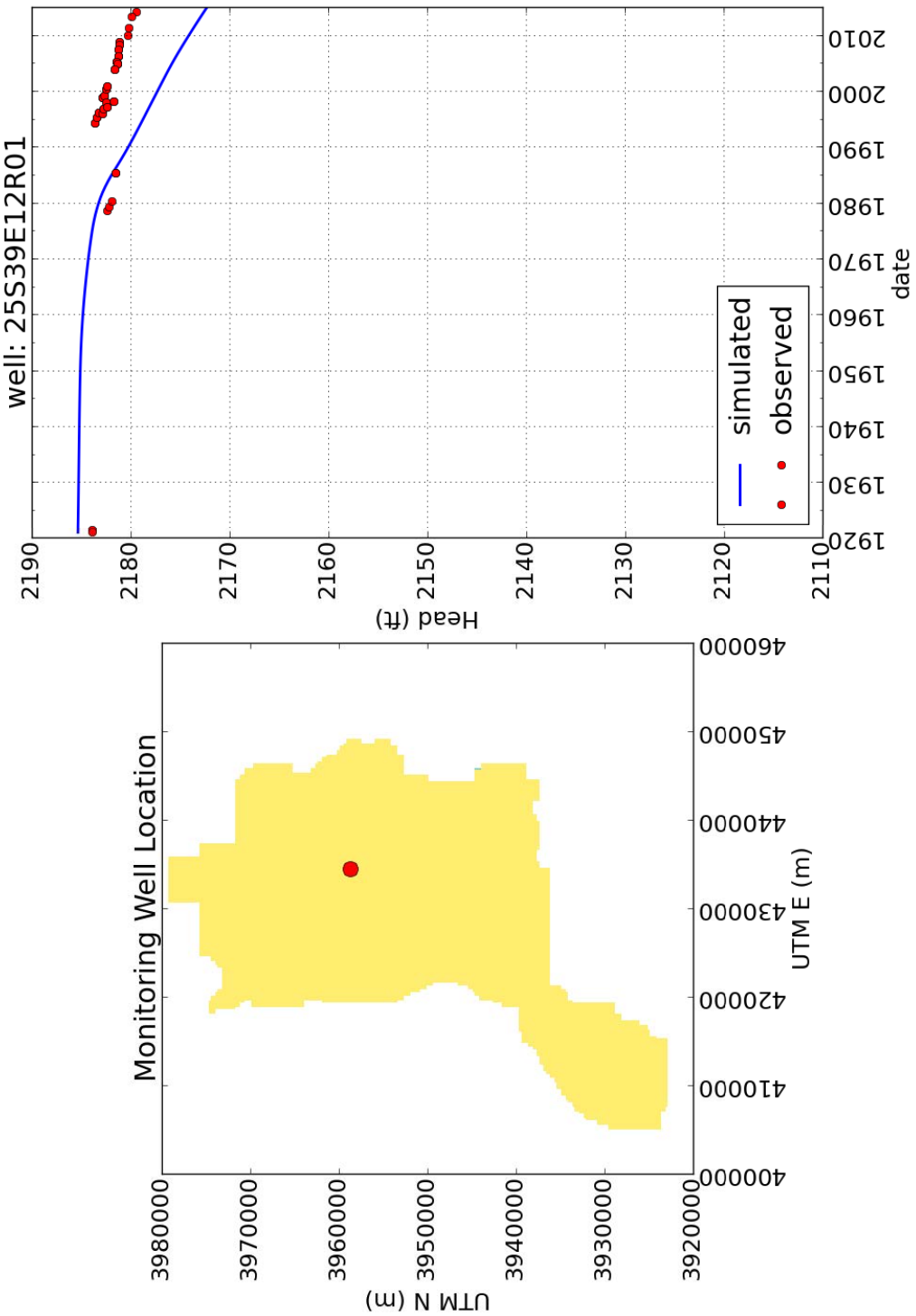
well: 25S39E12R01
Head (ft)
2190
2180
2170
2160
2150
2140
2130
2120
2110
date
1920
1930
1940
1950
1960
1970
1980
1990
2000
2010
simulated
observed
Monitoring Well Location
UTM N (m)
3980000
3970000
3960000
3950000
3940000
3930000
3920000
UTM E (m)
400000
410000
420000
430000
440000
450000
460000

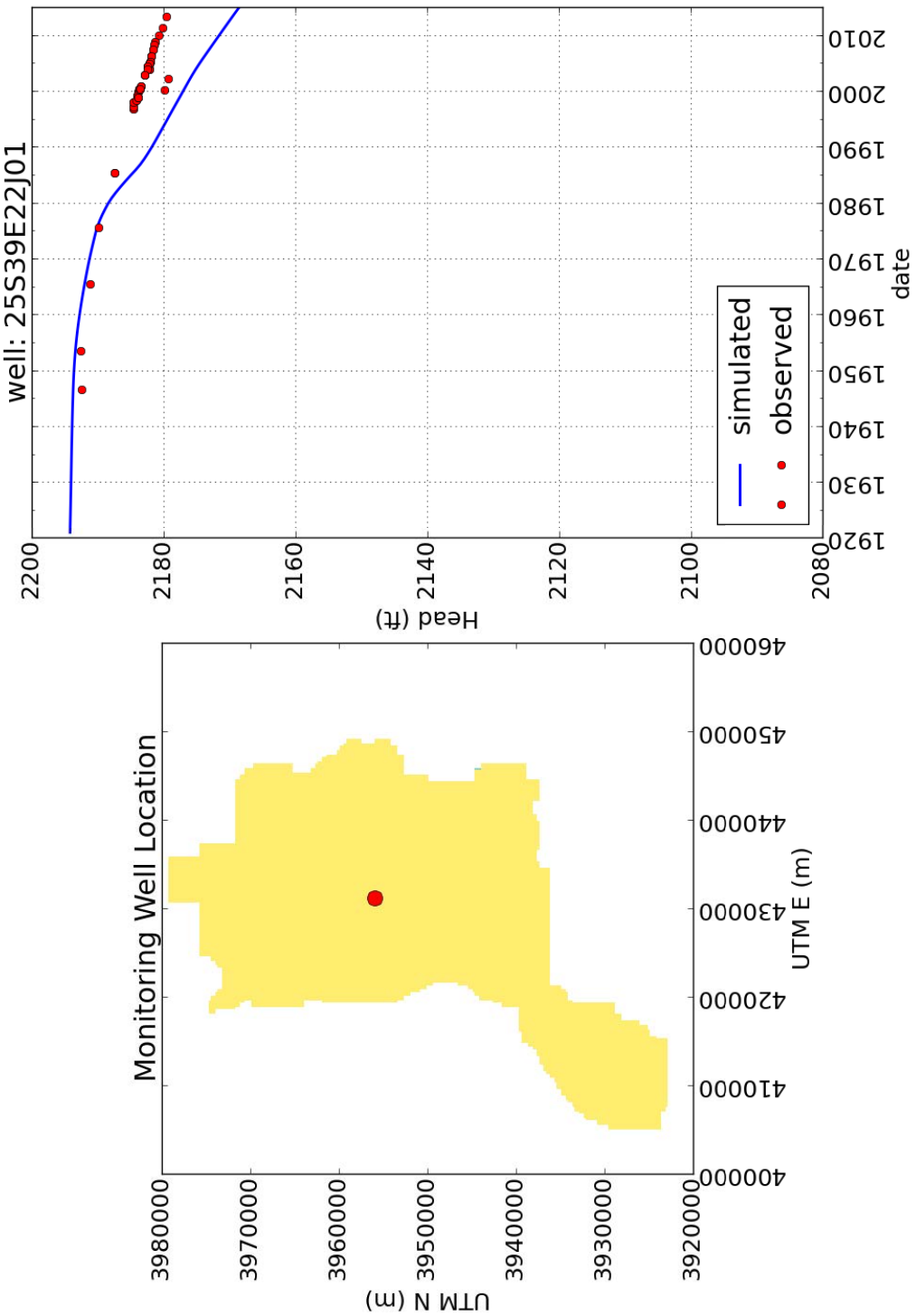
well: 25S39E22J01
Head (ft)
2200
2180
2160
2140
2120
2100
2080
date
1920
1930
1940
1950
1960
1970
1980
1990
2000
2010
simulated
observed
Monitoring Well Location
UTM N (m)
3980000
3970000
3960000
3950000
3940000
3930000
3920000
UTM E (m)
400000
410000
420000
430000
440000
450000
460000

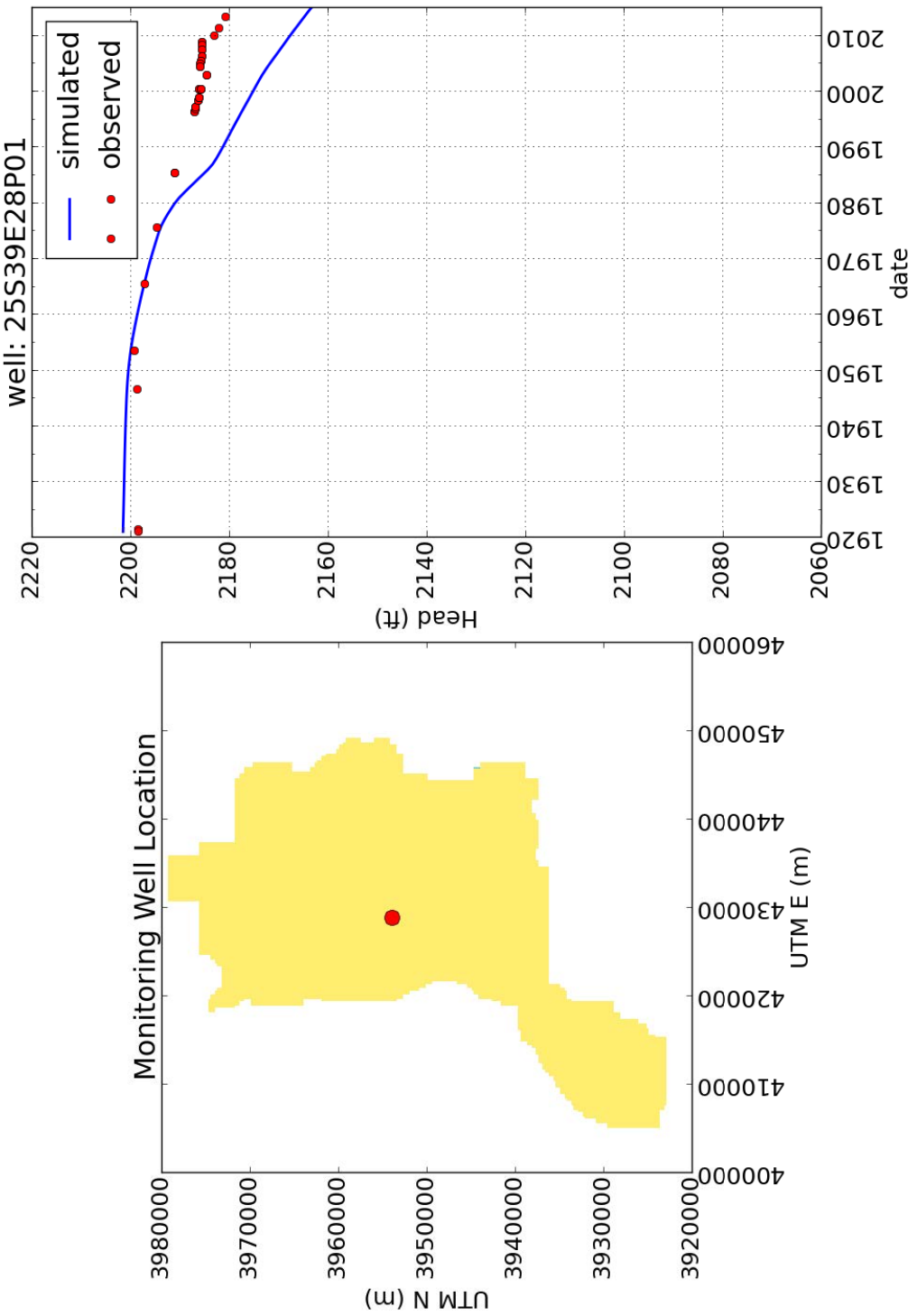
well: 25S39E28P01
simulated
observed
Head (ft)
date
2220
2200
2180
2160
2140
2120
2100
2080
2060
1920
1930
1940
1950
1960
1970
1980
1990
2000
2010
Monitoring Well Location
UTM N (m)
UTM E (m)
3980000
3970000
3960000
3950000
3940000
3930000
3920000
400000
410000
420000
430000
440000
450000
460000

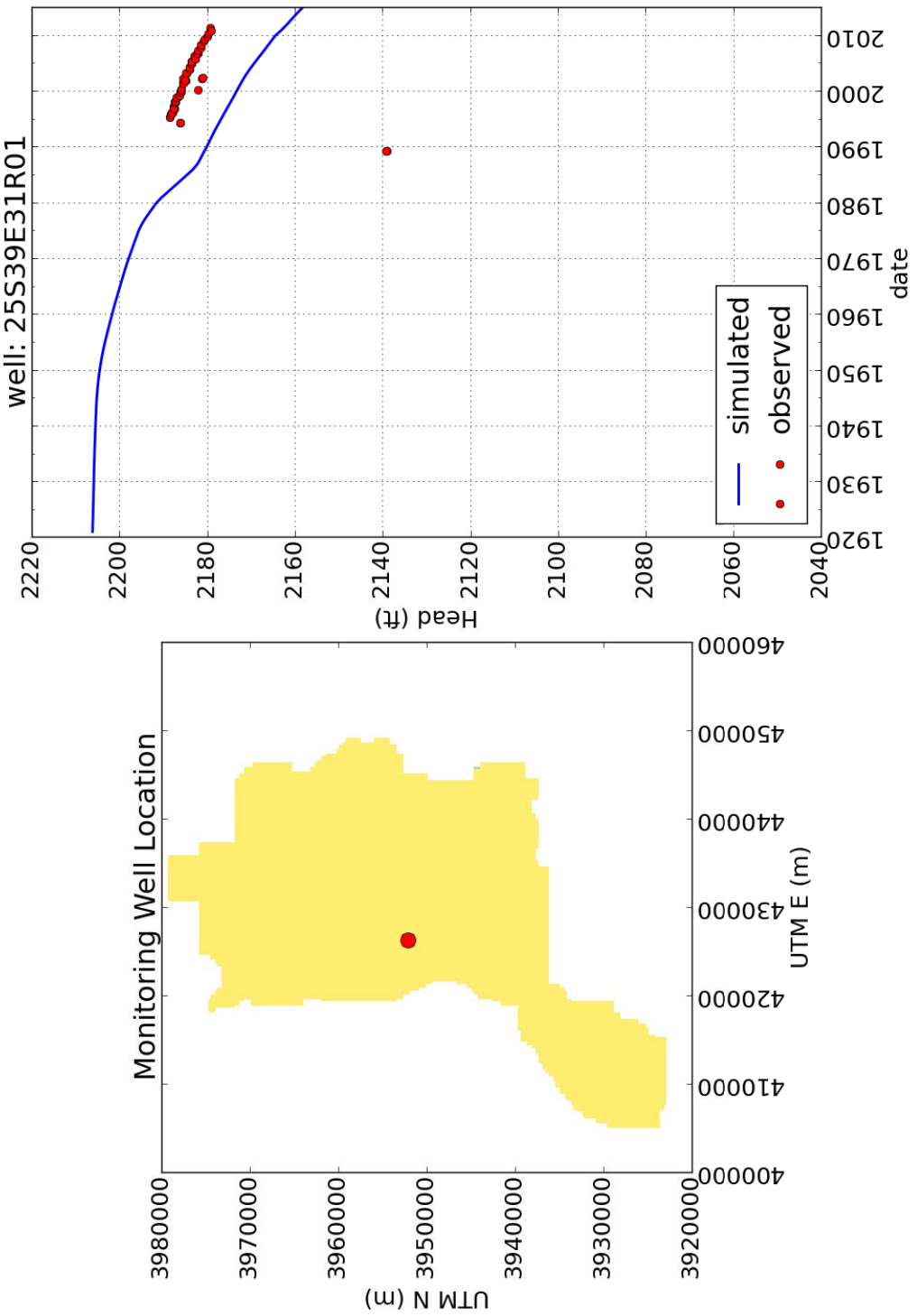
well: 25S39E31R01
Head (ft)
2220
2200
2180
2160
2140
2120
2100
2080
2060
2040
date
1920
1930
1940
1950
1960
1970
1980
1990
2000
2010
simulated
observed
Monitoring Well Location
UTM N (m)
3980000
3970000
3960000
3950000
3940000
3930000
3920000
UTM E (m)
460000
450000
440000
430000
420000
410000
400000

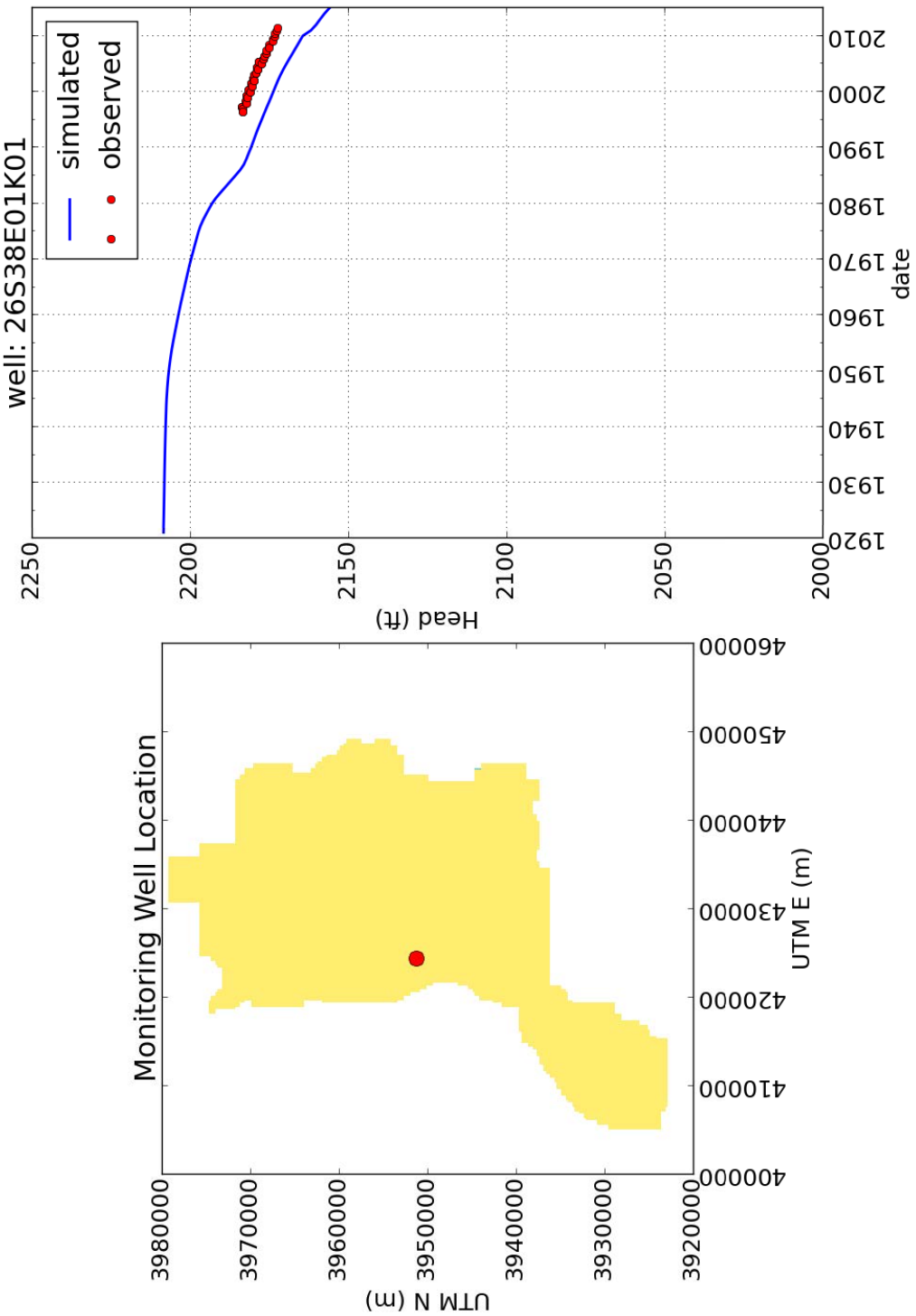
well: 26S38E01K01
simulated
observed
Head (ft)
date
2250
2200
2150
2100
2050
2000
1920
1930
1940
1950
1960
1970
1980
1990
2000
2010
Monitoring Well Location
UTM N (m)
UTM E (m)
3980000
3970000
3960000
3950000
3940000
3930000
3920000
400000
410000
420000
430000
440000
450000
460000

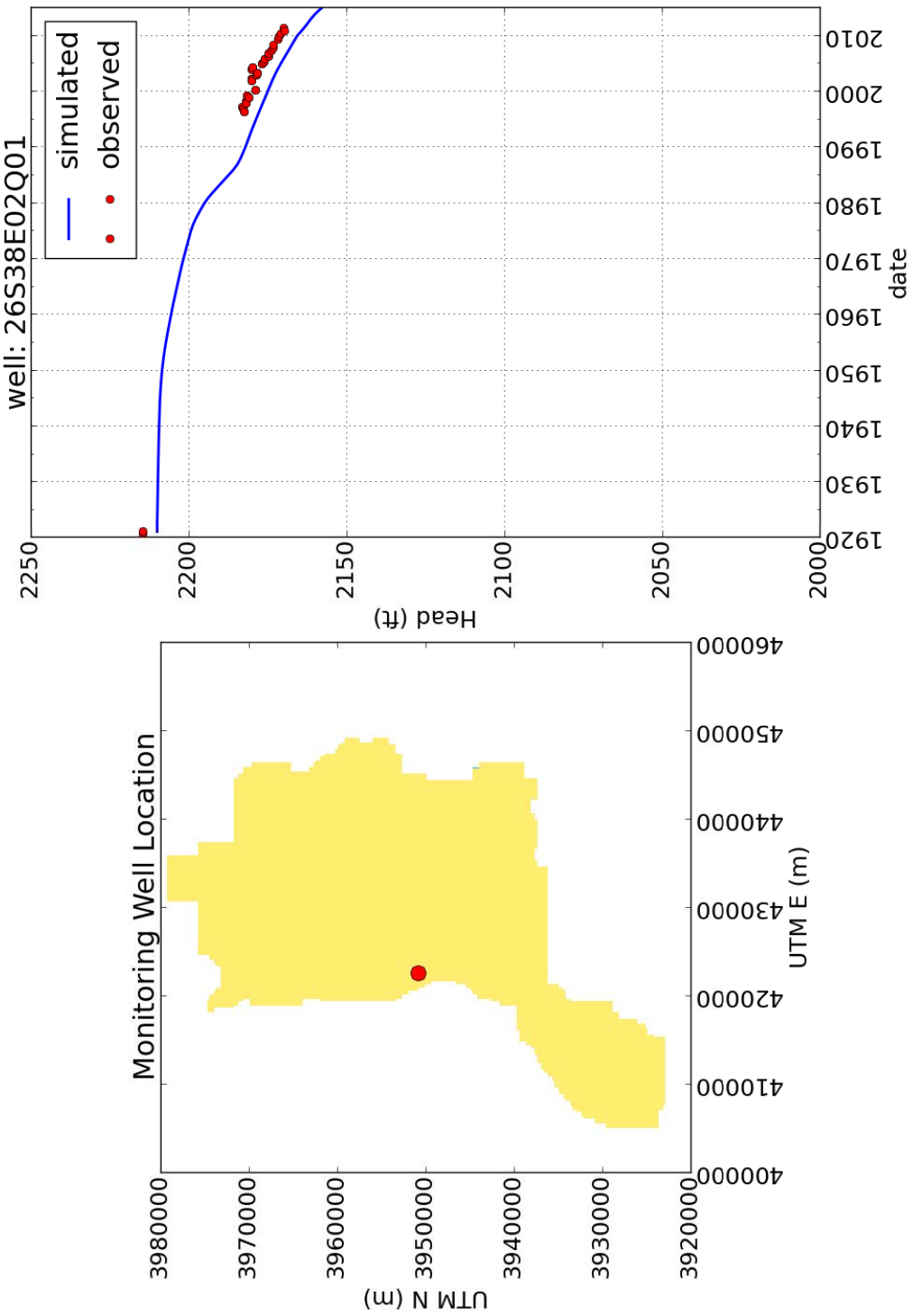
well: 26S38E02Q01
simulated
observed
Head (ft)
2250
2200
2150
2100
2050
2000
date
1920
1930
1940
1950
1960
1970
1980
1990
2000
2010
Monitoring Well Location
UTM N (m)
3980000
3970000
3960000
3950000
3940000
3930000
3920000
UTM E (m)
400000
410000
420000
430000
440000
450000
460000

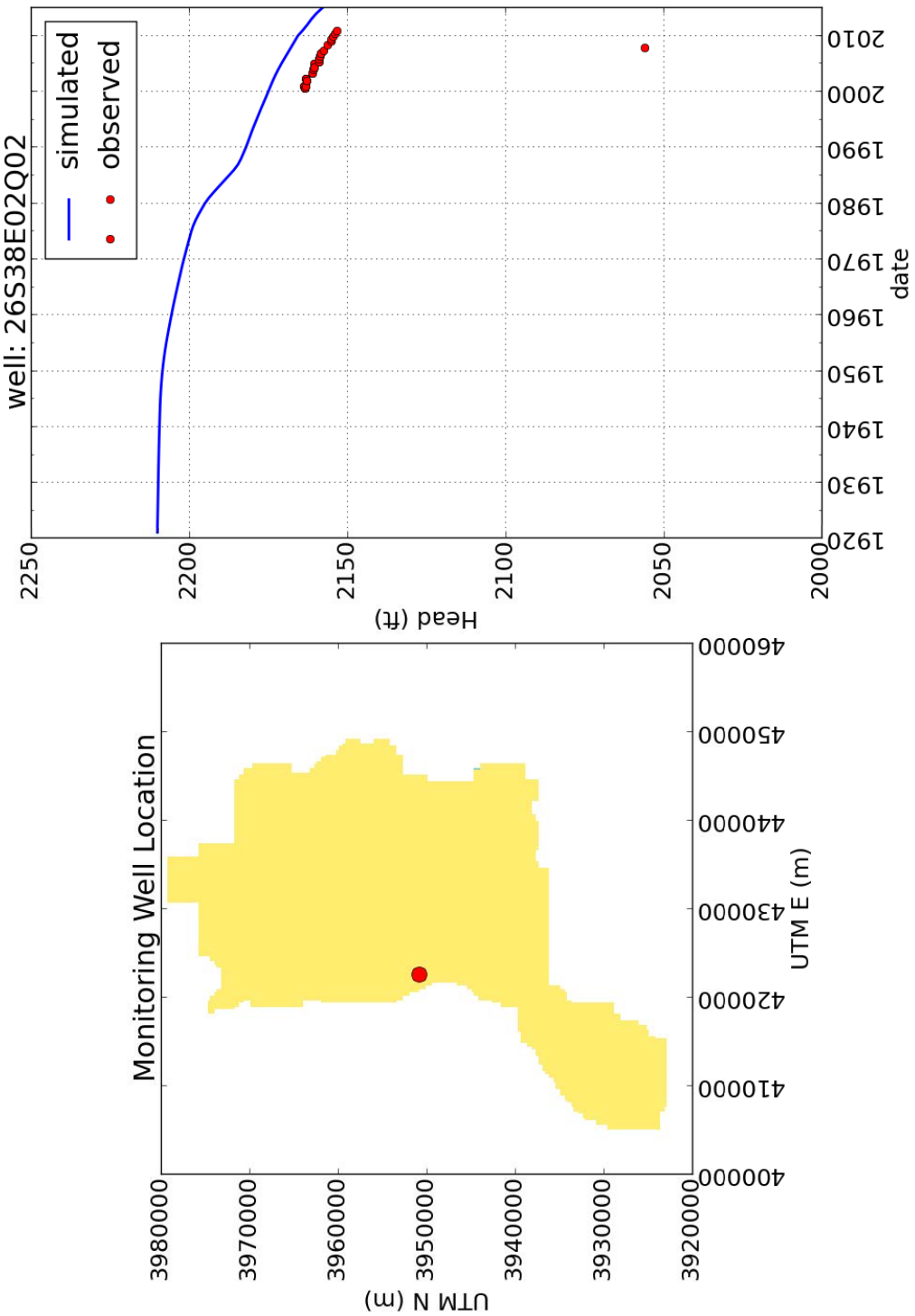
well: 26S38E02Q02
simulated
observed
Head (ft)
date
2250
2200
2150
2100
2050
2000
1920
1930
1940
1950
1960
1970
1980
1990
2000
2010
Monitoring Well Location
UTM N (m)
UTM E (m)
3980000
3970000
3960000
3950000
3940000
3930000
3920000
400000
410000
420000
430000
440000
450000
460000

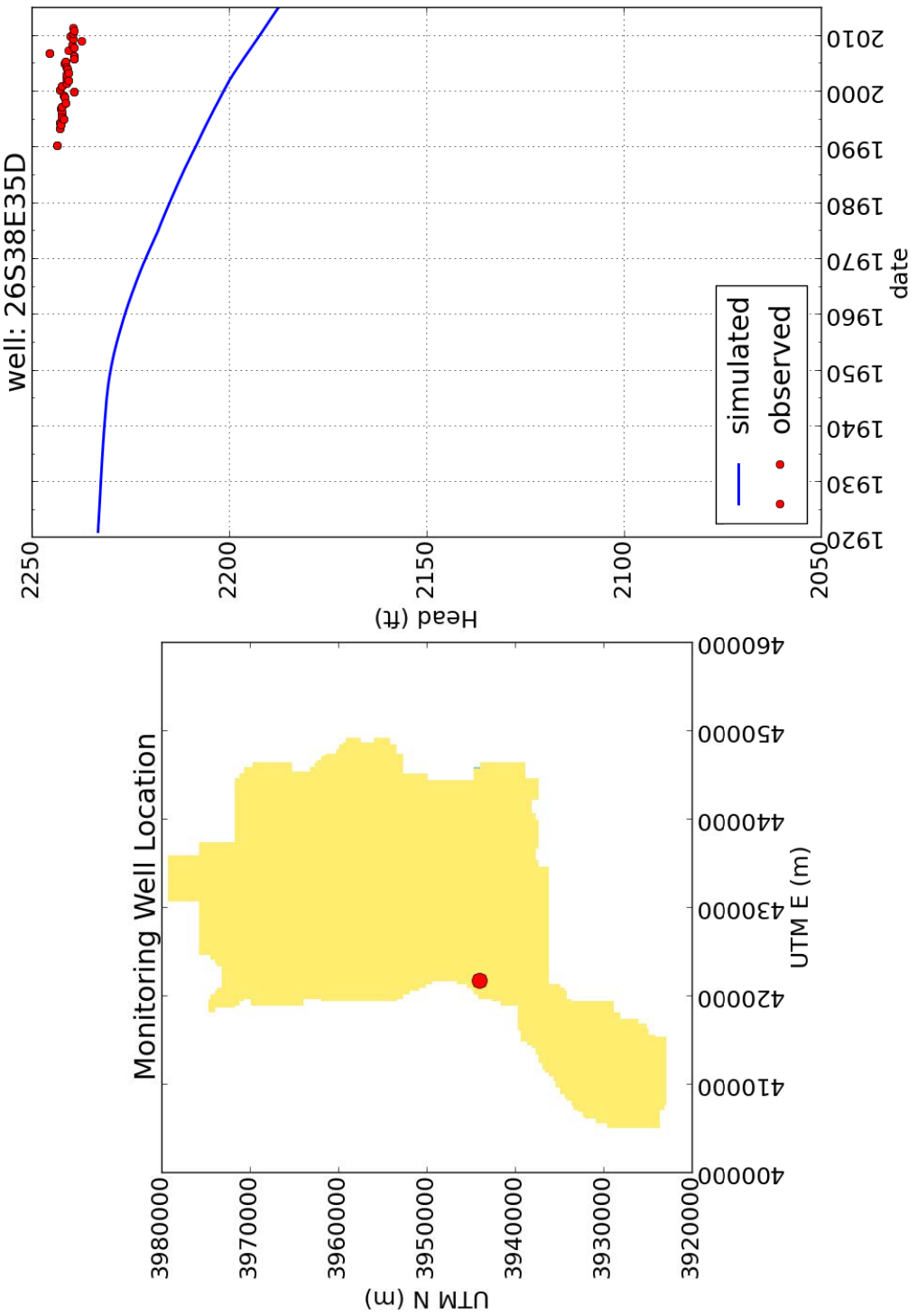
well: 26S38E35D
Head (ft)
2250
2200
2150
2100
2050
date
1920
1930
1940
1950
1960
1970
1980
1990
2000
2010
simulated
observed
Monitoring Well Location
UTM N (m)
3980000
3970000
3960000
3950000
3940000
3930000
3920000
UTM E (m)
400000
410000
420000
430000
440000
450000
460000

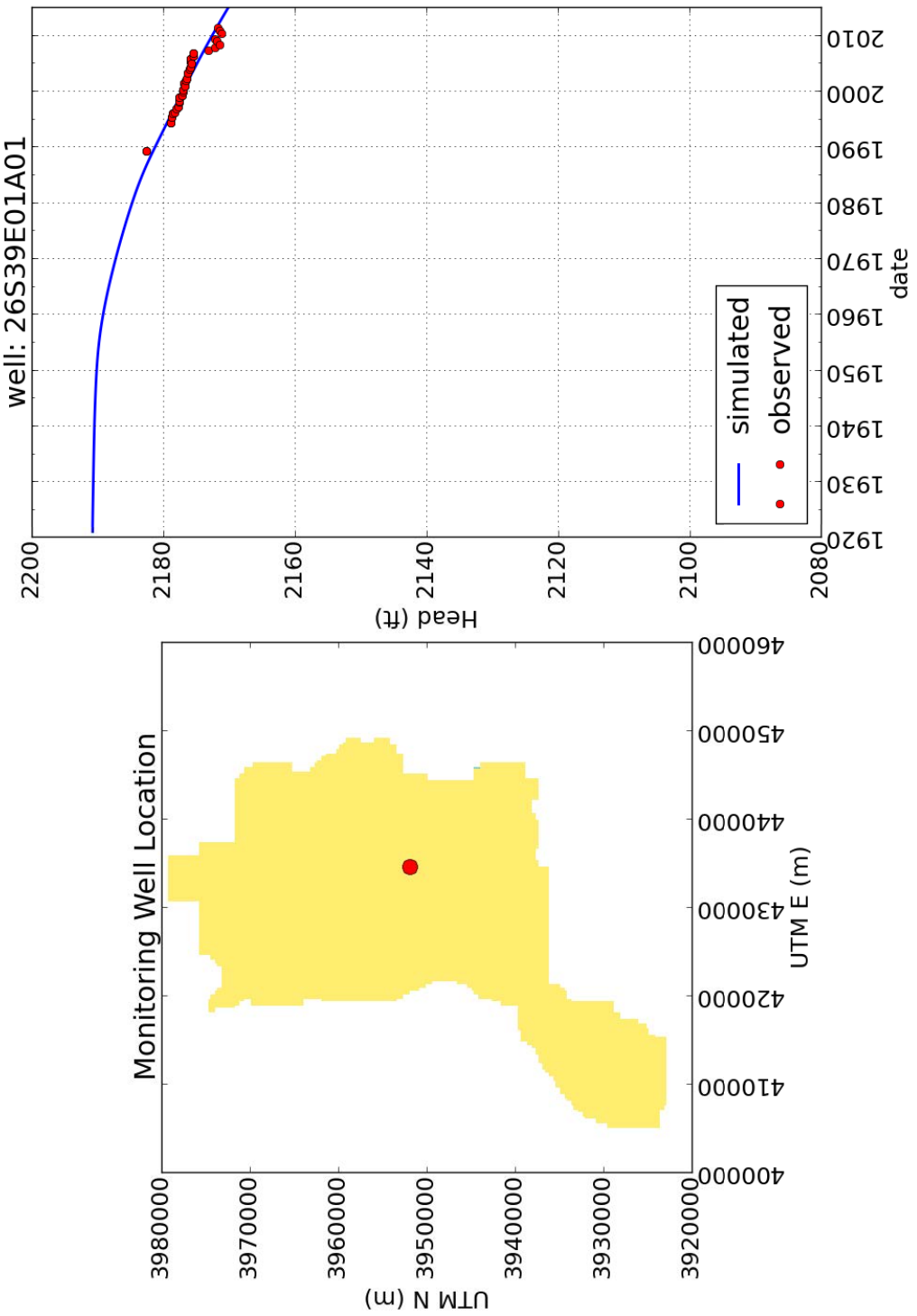
well: 26S39E01A01
Head (ft)
2200
2180
2160
2140
2120
2100
2080
date
1920
1930
1940
1950
1960
1970
1980
1990
2000
2010
simulated
observed
Monitoring Well Location
UTM N (m)
3980000
3970000
3960000
3950000
3940000
3930000
3920000
UTM E (m)
400000
410000
420000
430000
440000
450000
460000

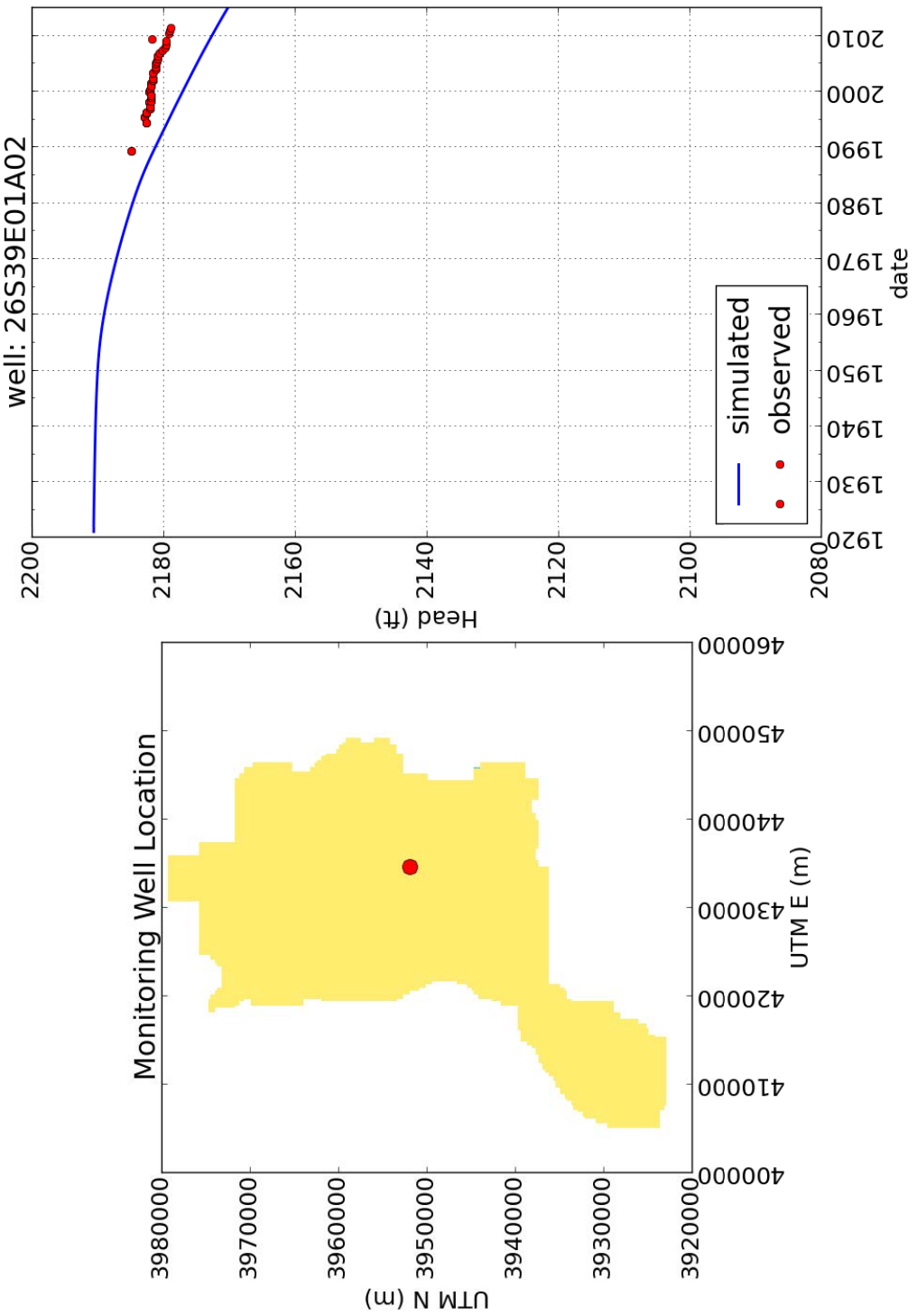
well: 26S39E01A02
Head (ft)
2200
2180
2160
2140
2120
2100
2080
1920
1930
1940
1950
1960
1970
1980
1990
2000
2010
date
simulated
observed
Monitoring Well Location
UTM N (m)
3980000
3970000
3960000
3950000
3940000
3930000
3920000
460000
450000
440000
430000
420000
410000
400000
UTM E (m)

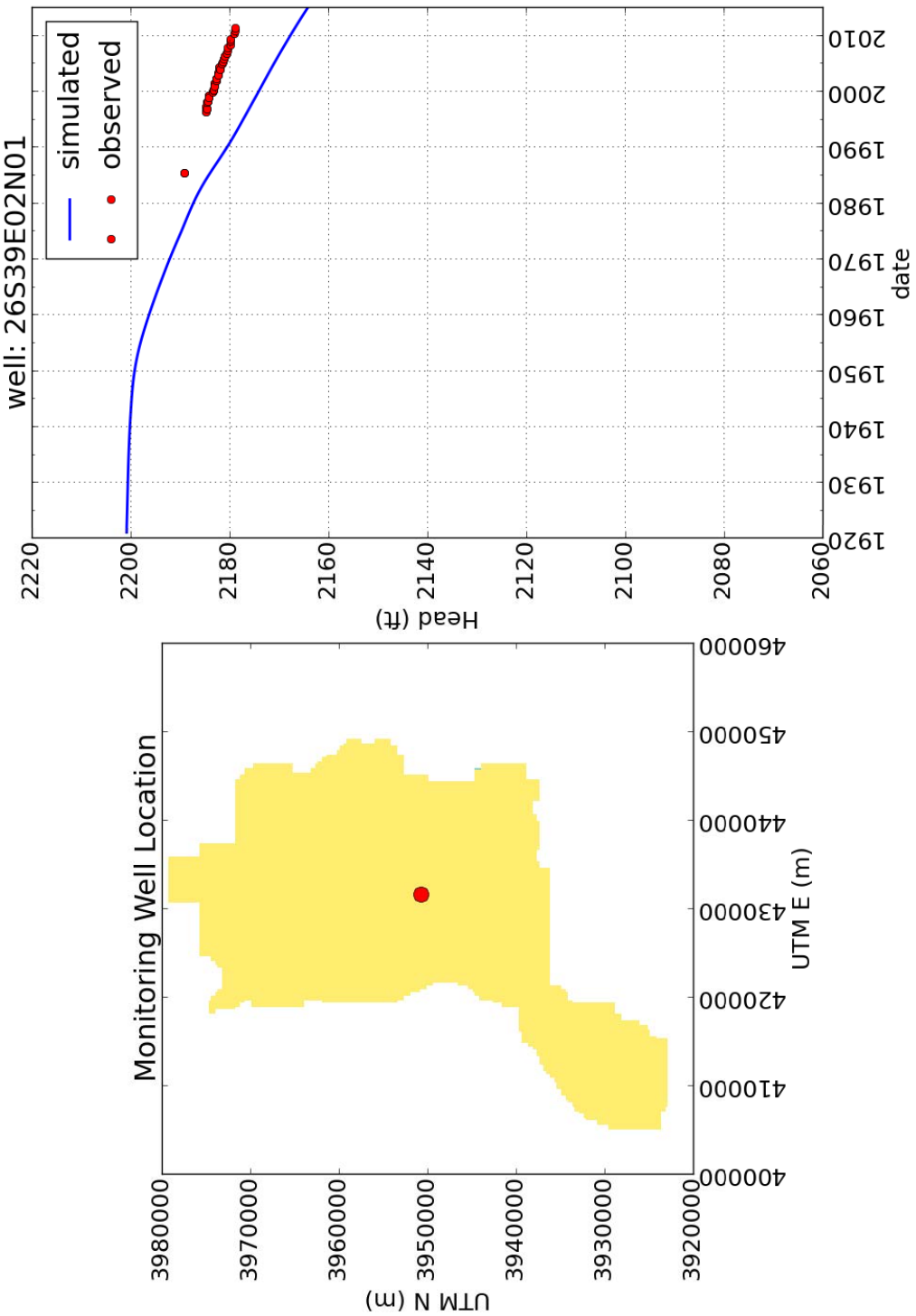
well: 26S39E02N01
simulated
observed
Head (ft)
date
2220
2200
2180
2160
2140
2120
2100
2080
2060
1920
1930
1940
1950
1960
1970
1980
1990
2000
2010
Monitoring Well Location
UTM N (m)
UTM E (m)
3980000
3970000
3960000
3950000
3940000
3930000
3920000
400000
410000
420000
430000
440000
450000
460000

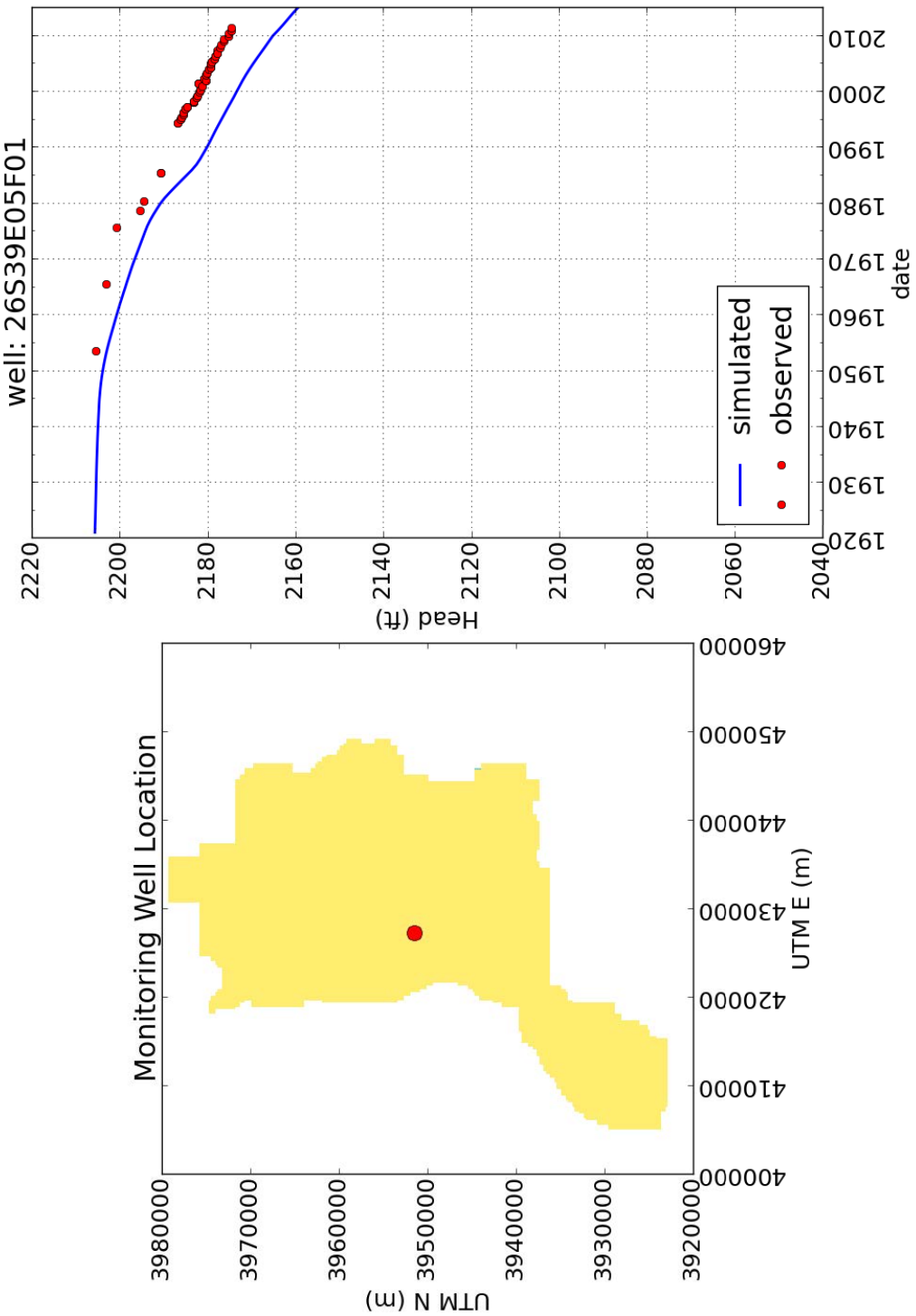
well: 26S39E05F01
Head (ft)
2220
2200
2180
2160
2140
2120
2100
2080
2060
2040
date
1920
1930
1940
1950
1960
1970
1980
1990
2000
2010
simulated
observed
Monitoring Well Location
UTM N (m)
3980000
3970000
3960000
3950000
3940000
3930000
3920000
UTM E (m)
400000
410000
420000
430000
440000
450000
460000

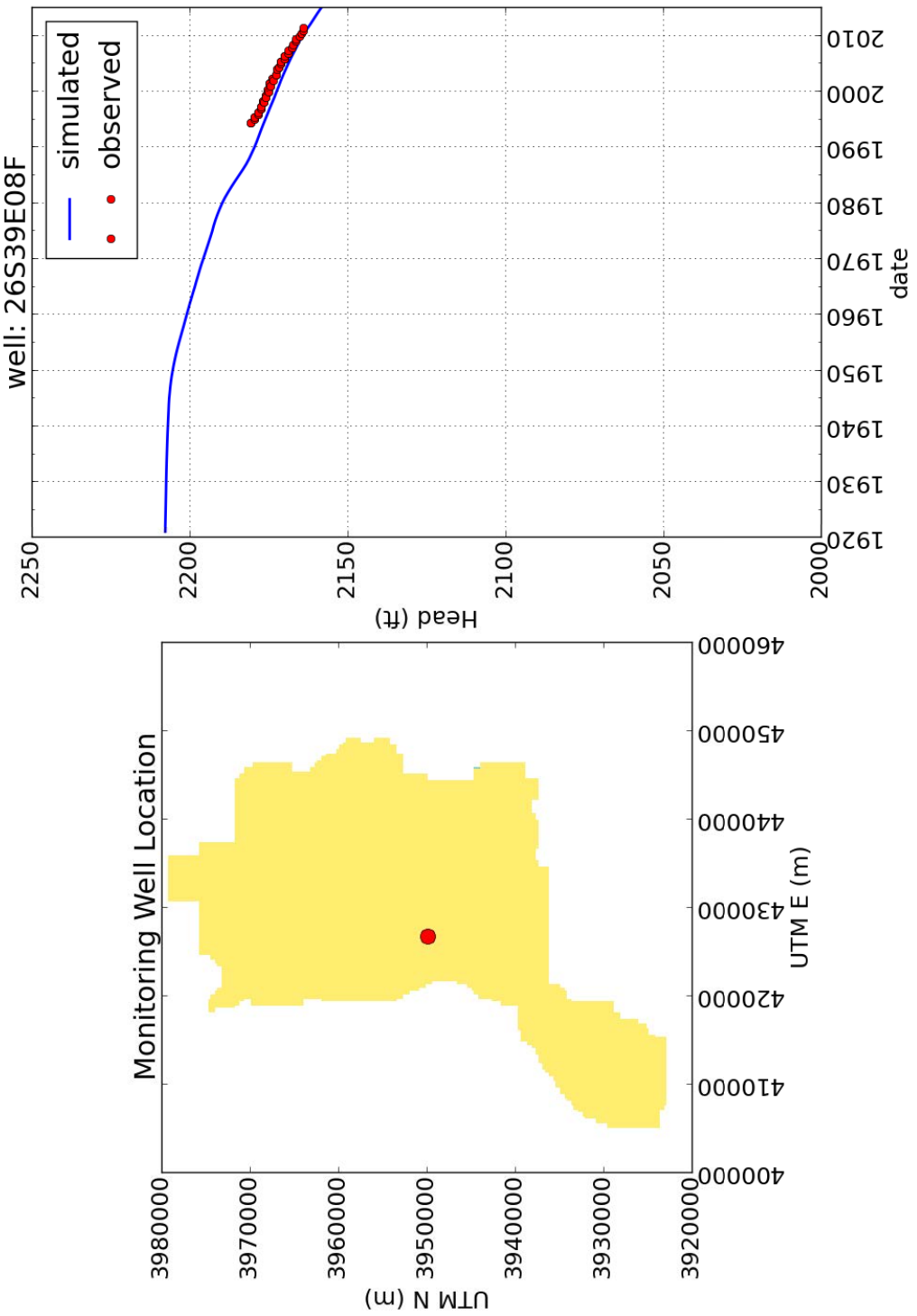
well: 26S39E08F
simulated
observed
Head (ft)
2250
2200
2150
2100
2050
2000
date
1920
1930
1940
1950
1960
1970
1980
1990
2000
2010
Monitoring Well Location
UTM N (m)
3980000
3970000
3960000
3950000
3940000
3930000
3920000
UTM E (m)
400000
410000
420000
430000
440000
450000
460000

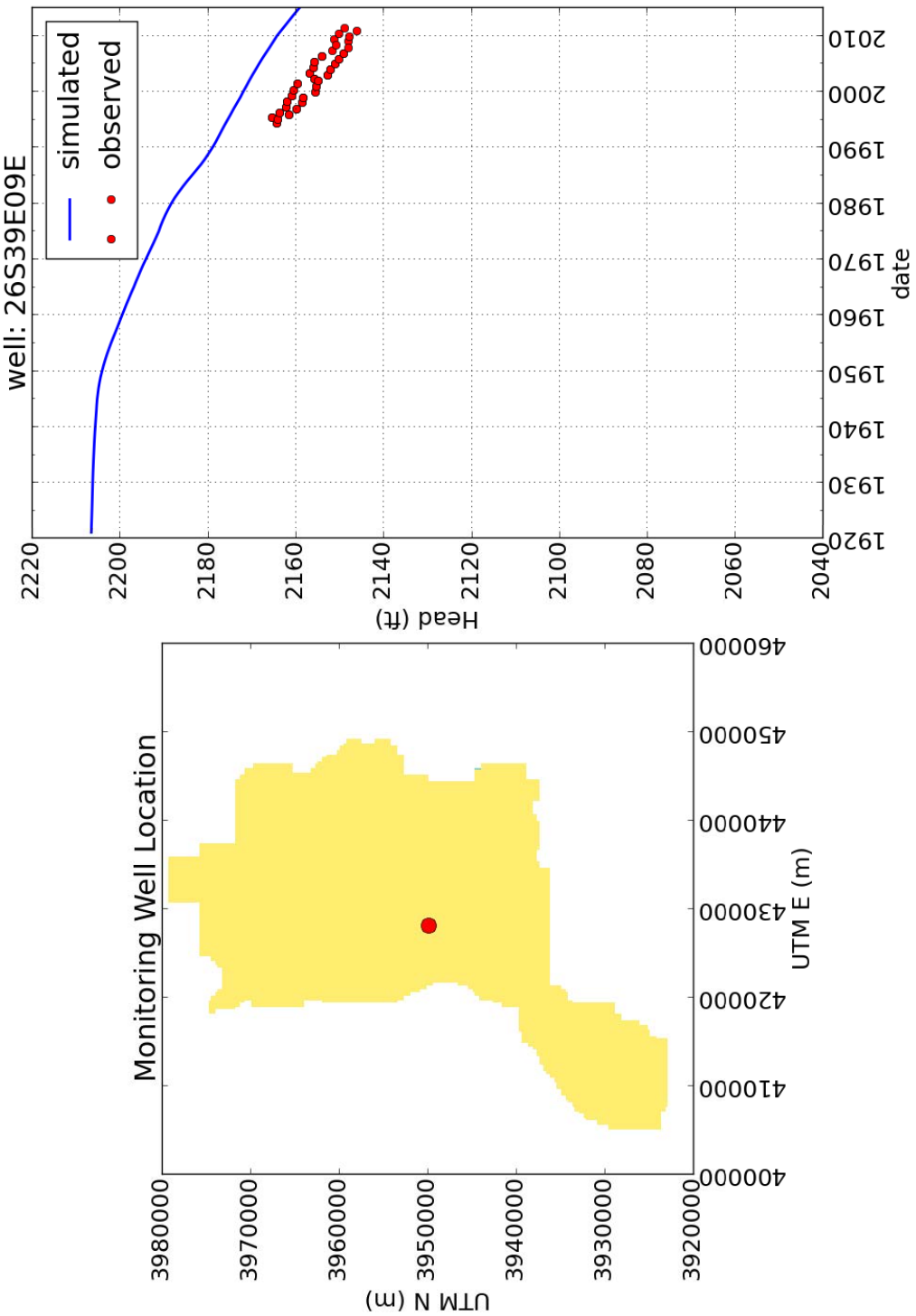
well: 26S39E09E
simulated
observed
Head (ft)
date
2220
2200
2180
2160
2140
2120
2100
2080
2060
2040
1920
1930
1940
1950
1960
1970
1980
1990
2000
2010
Monitoring Well Location
UTM N (m)
UTM E (m)
3980000
3970000
3960000
3950000
3940000
3930000
3920000
400000
410000
420000
430000
440000
450000
460000

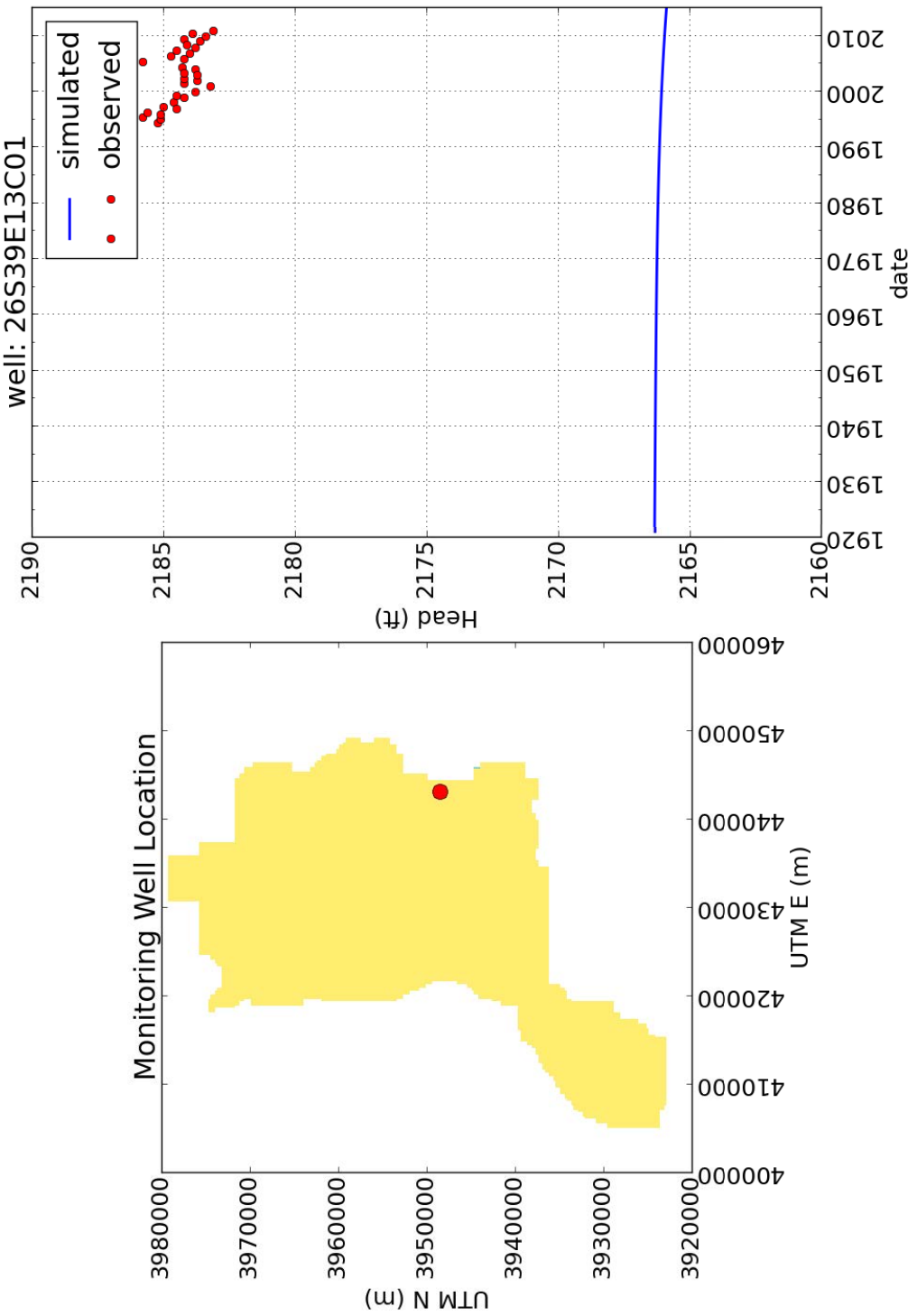
well: 26S39E13C01
simulated
observed
Head (ft)
2190
2185
2180
2175
2170
2165
2160
1920
1930
1940
1950
1960
1970
1980
1990
2000
2010
date
Monitoring Well Location
UTM N (m)
3980000
3970000
3960000
3950000
3940000
3930000
3920000
400000
410000
420000
430000
440000
450000
460000
UTM E (m)

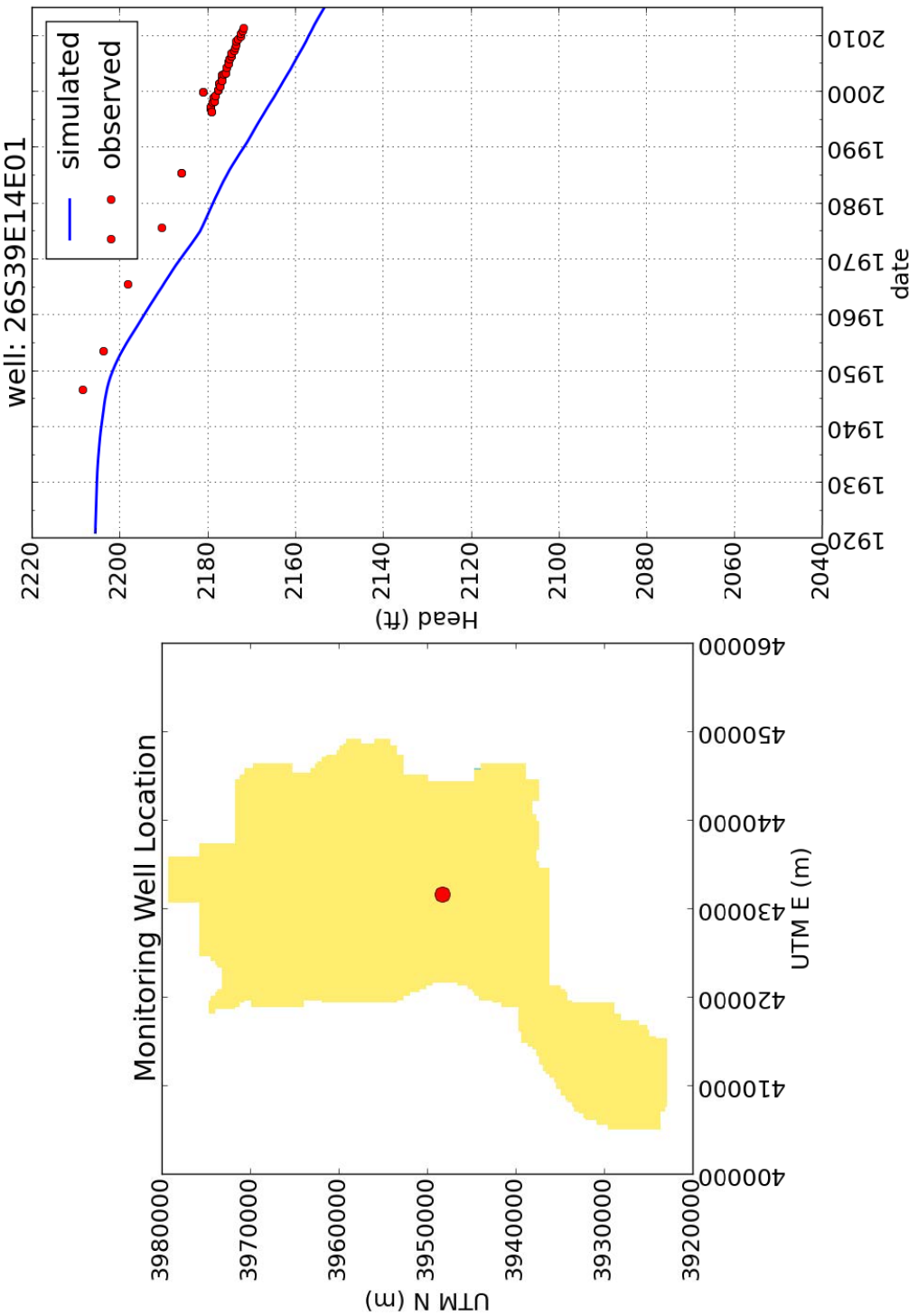
well: 26S39E14E01
simulated
observed
Head (ft)
date
2220
2200
2180
2160
2140
2120
2100
2080
2060
2040
1920
1930
1940
1950
1960
1970
1980
1990
2000
2010
Monitoring Well Location
UTM N (m)
UTM E (m)
3980000
3970000
3960000
3950000
3940000
3930000
3920000
400000
410000
420000
430000
440000
450000
460000

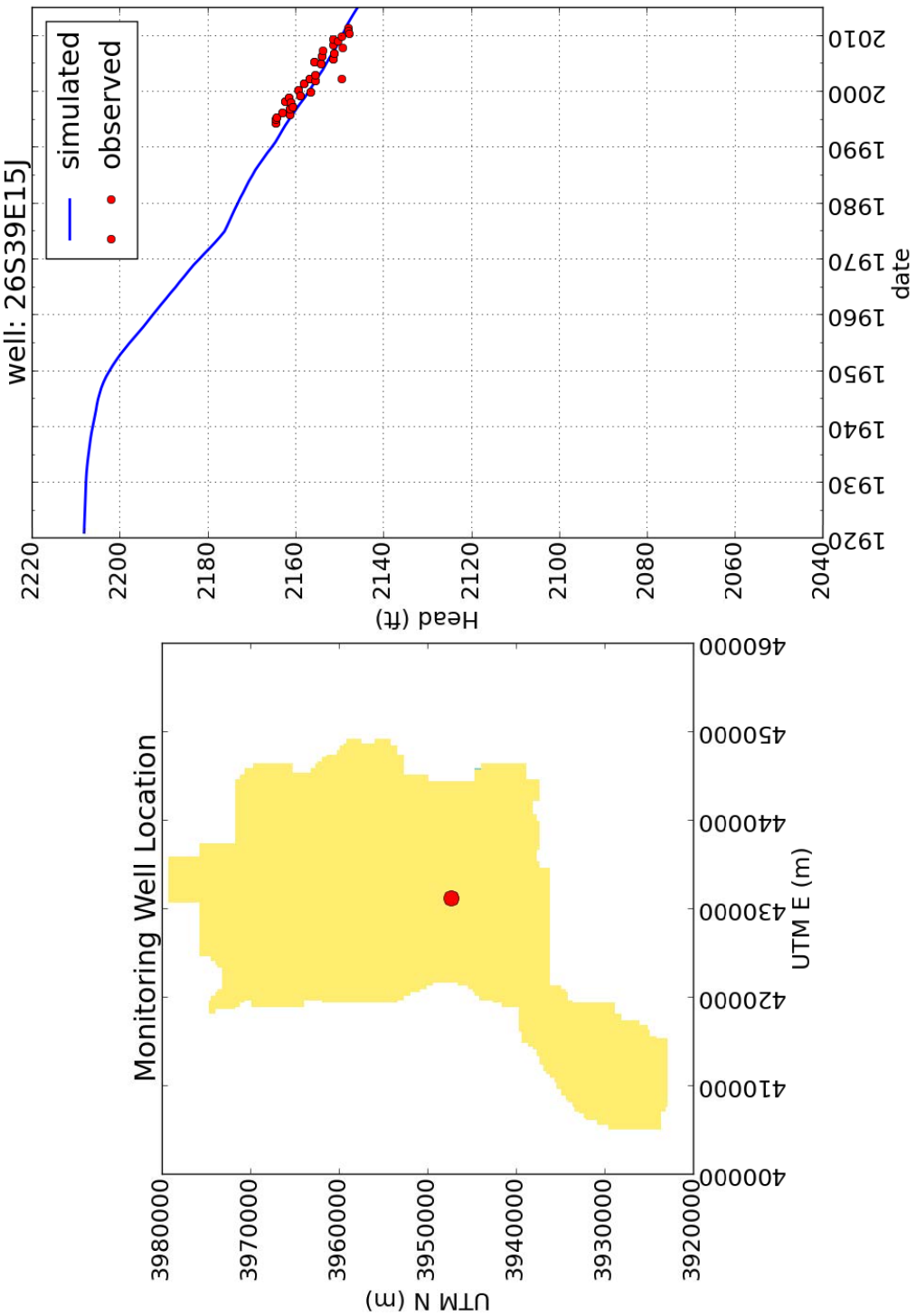
well: 26S39E15J
simulated
observed
Head (ft)
date
2220
2200
2180
2160
2140
2120
2100
2080
2060
2040
1920
1930
1940
1950
1960
1970
1980
1990
2000
2010
Monitoring Well Location
UTM N (m)
UTM E (m)
3980000
3970000
3960000
3950000
3940000
3930000
3920000
400000
410000
420000
430000
440000
450000
460000

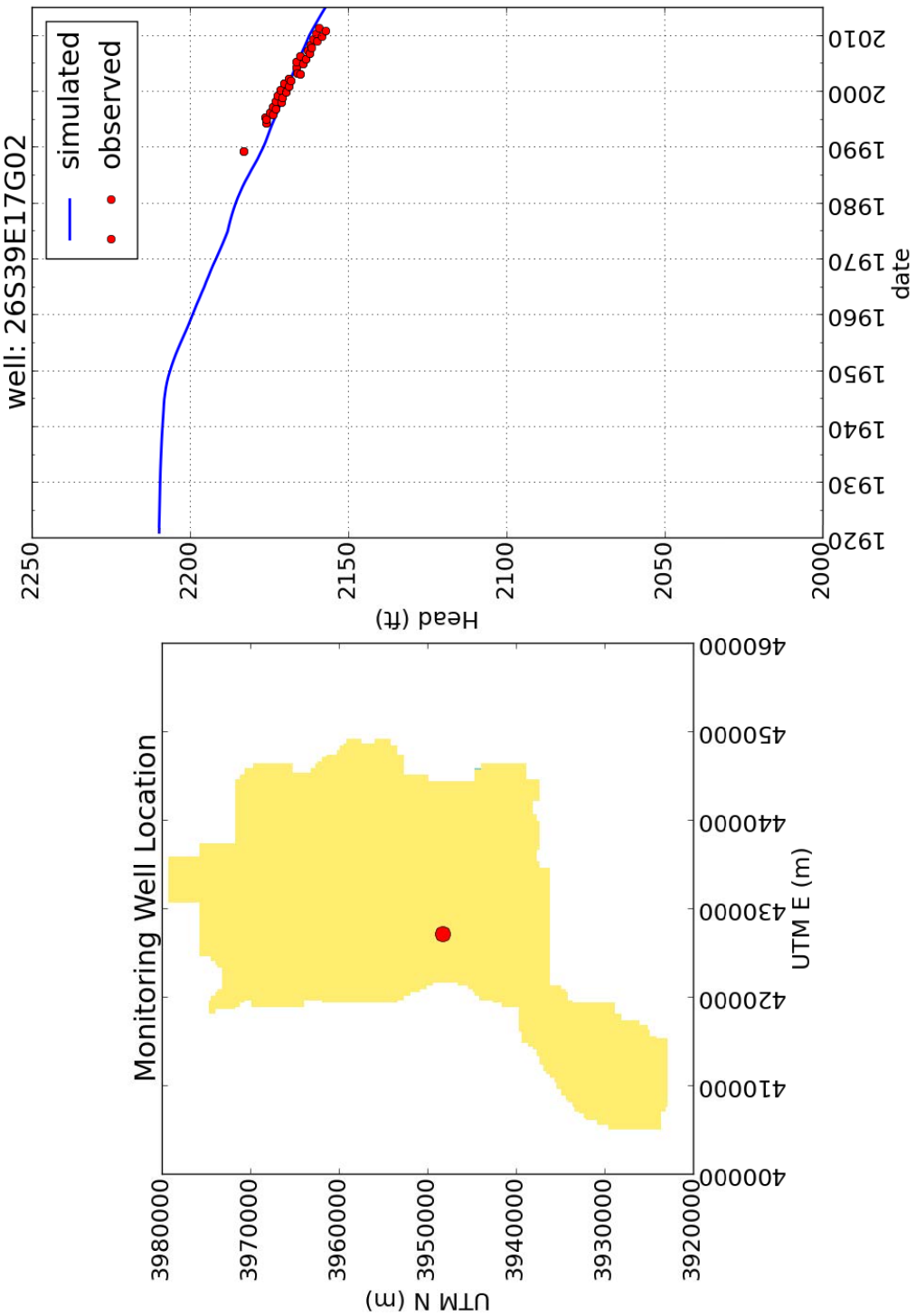
well: 26S39E17G02
simulated
observed
Head (ft)
date
2250
2200
2150
2100
2050
2000
1920
1930
1940
1950
1960
1970
1980
1990
2000
2010
Monitoring Well Location
UTM N (m)
UTM E (m)
3980000
3970000
3960000
3950000
3940000
3930000
3920000
400000
410000
420000
430000
440000
450000
460000

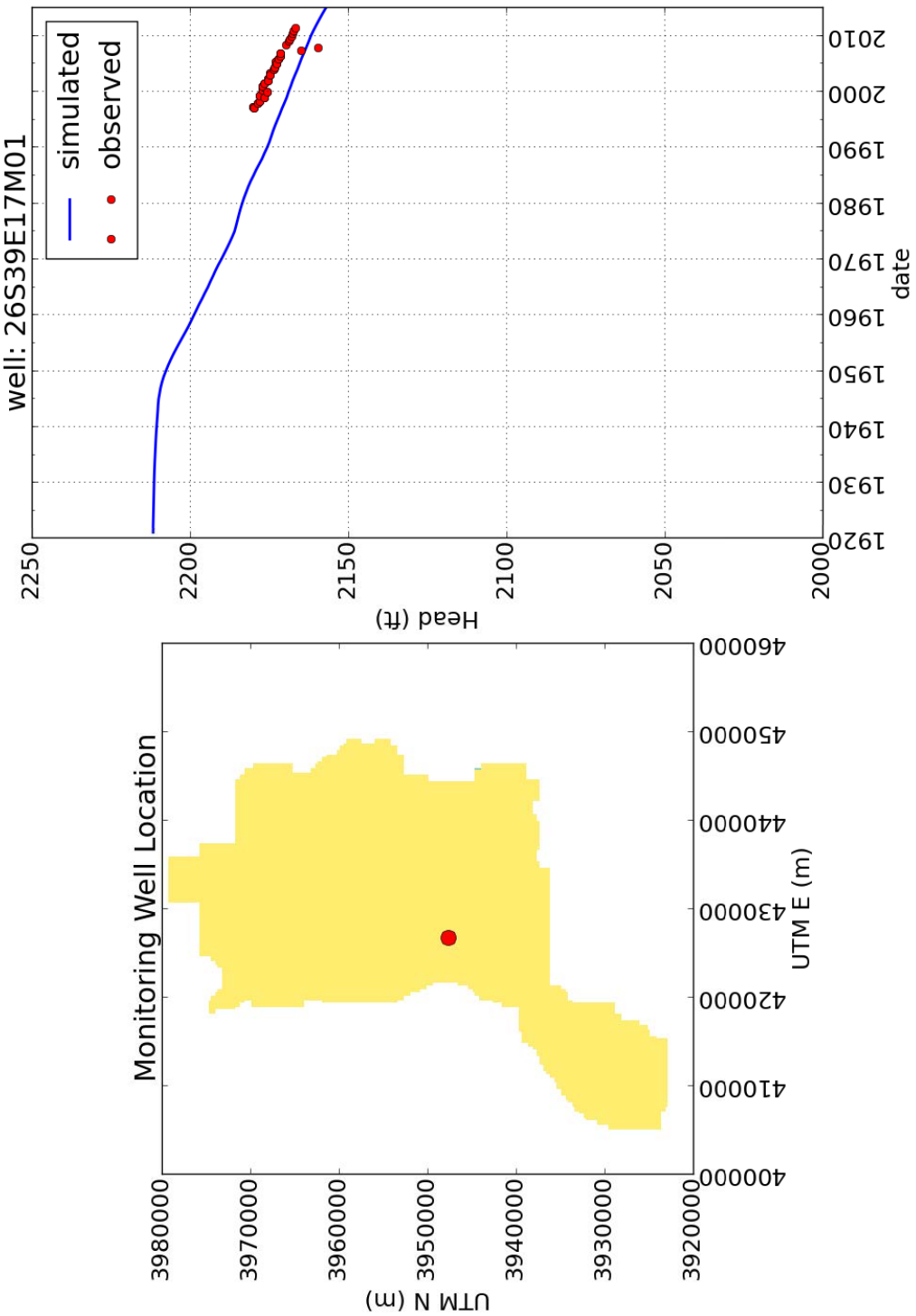
well: 26S39E17M01
simulated
observed
Head (ft)
date
2250
2200
2150
2100
2050
2000
1920
1930
1940
1950
1960
1970
1980
1990
2000
2010
Monitoring Well Location
UTM N (m)
UTM E (m)
3980000
3970000
3960000
3950000
3940000
3930000
3920000
400000
410000
420000
430000
440000
450000
460000

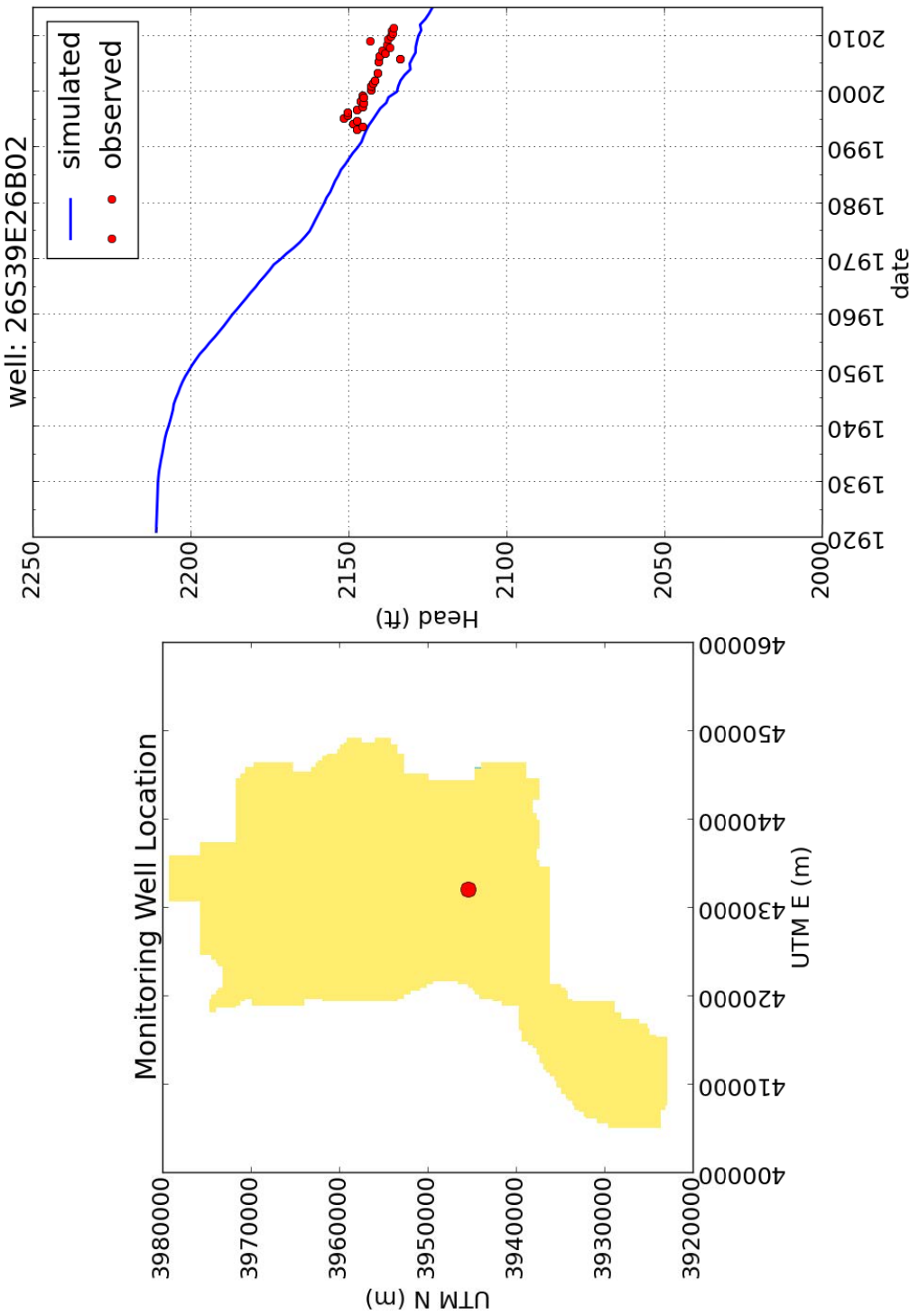
well: 26S39E26B02
simulated
observed
Head (ft)
date
2250
2200
2150
2100
2050
2000
1920
1930
1940
1950
1960
1970
1980
1990
2000
2010
Monitoring Well Location
UTM N (m)
UTM E (m)
3980000
3970000
3960000
3950000
3940000
3930000
3920000
400000
410000
420000
430000
440000
450000
460000

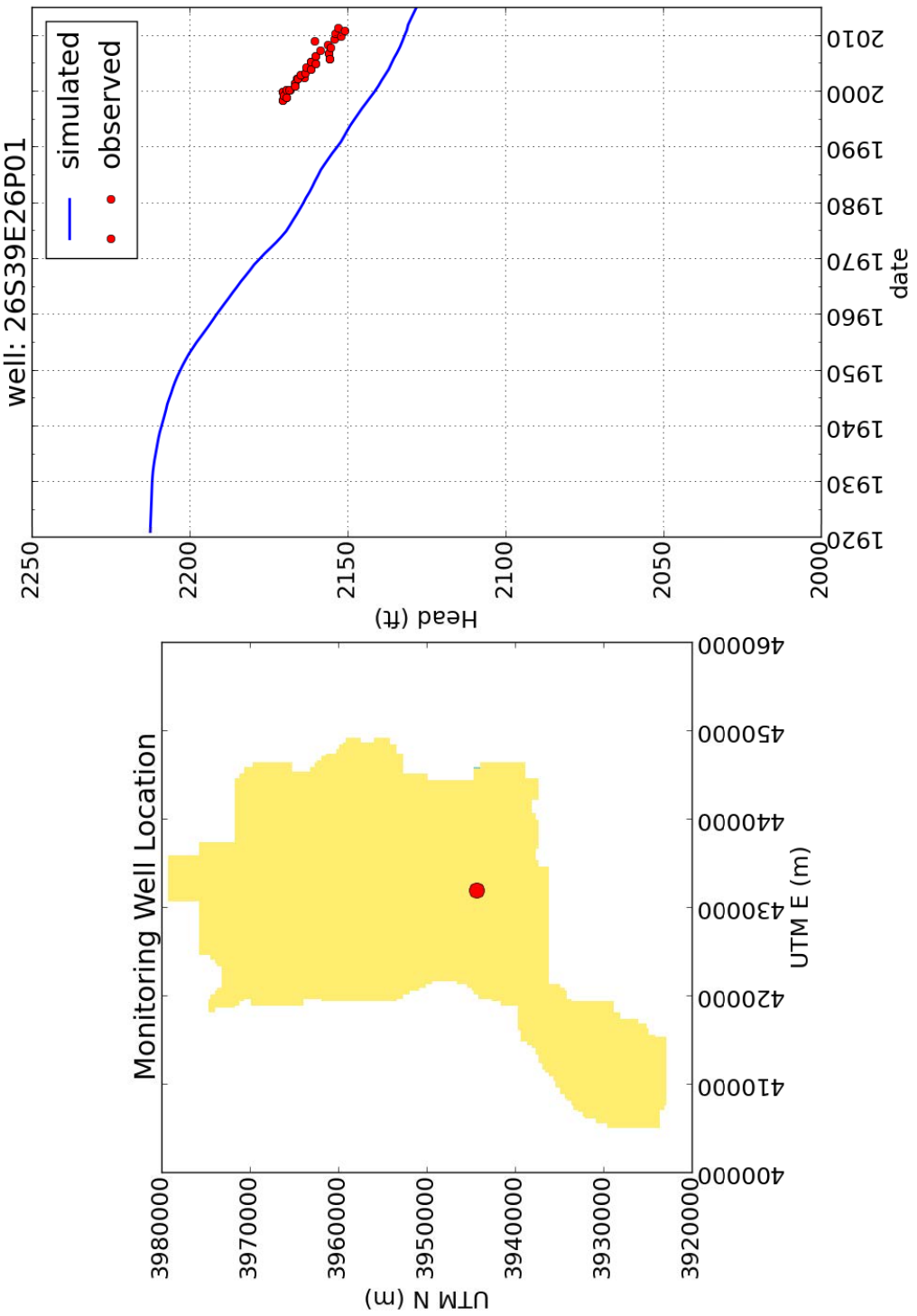
well: 26S39E26P01
simulated
observed
Head (ft)
date
2250
2200
2150
2100
2050
2000
1920
1930
1940
1950
1960
1970
1980
1990
2000
2010
Monitoring Well Location
UTM N (m)
UTM E (m)
3980000
3970000
3960000
3950000
3940000
3930000
3920000
400000
410000
420000
430000
440000
450000
460000

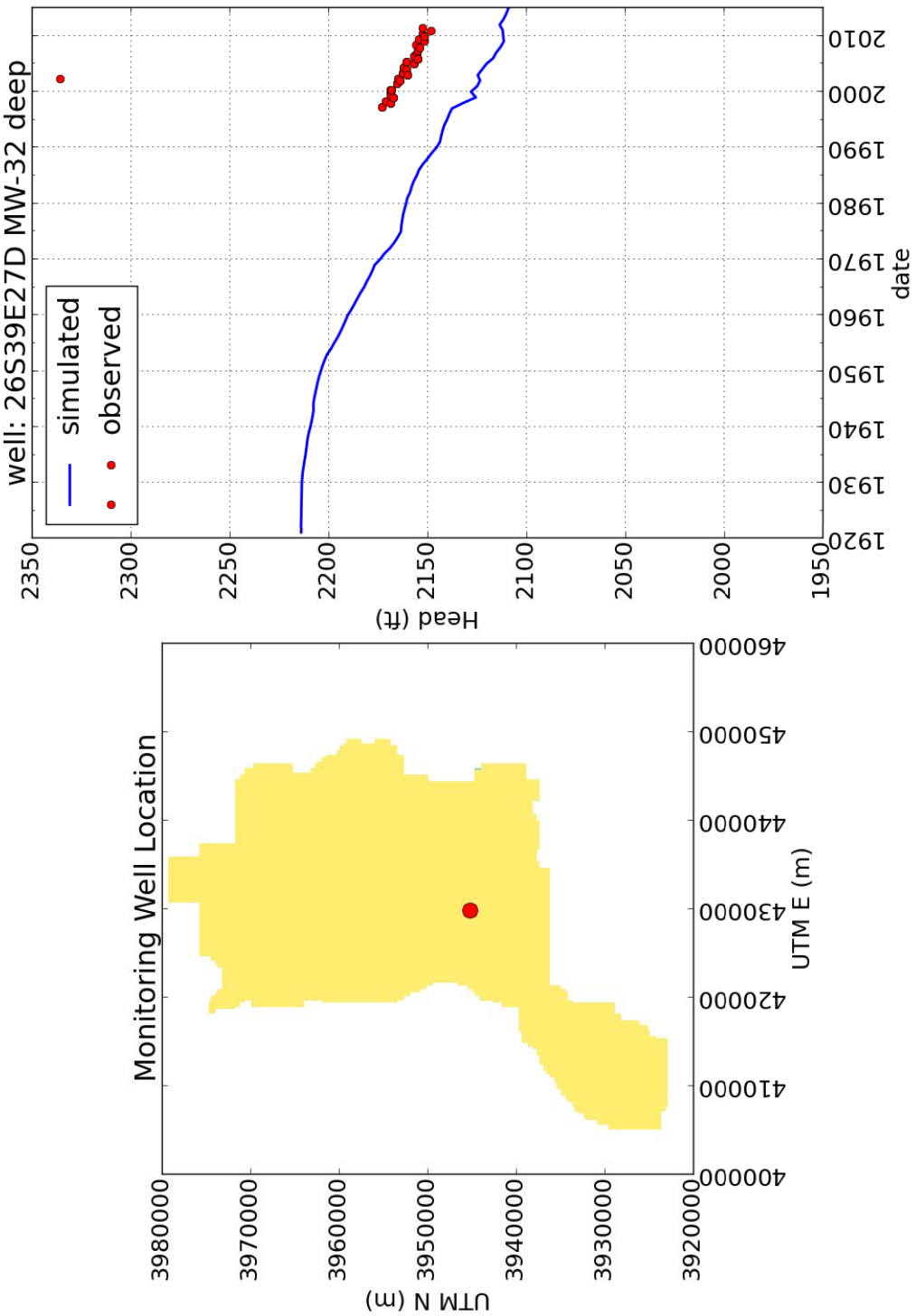
well: 26S39E27D MW-32 deep
simulated
observed
Head (ft)
date
2350
2300
2250
2200
2150
2100
2050
2000
1950
1920
1930
1940
1950
1960
1970
1980
1990
2000
2010
Monitoring Well Location
UTM N (m)
UTM E (m)
3980000
3970000
3960000
3950000
3940000
3930000
3920000
400000
410000
420000
430000
440000
450000
460000

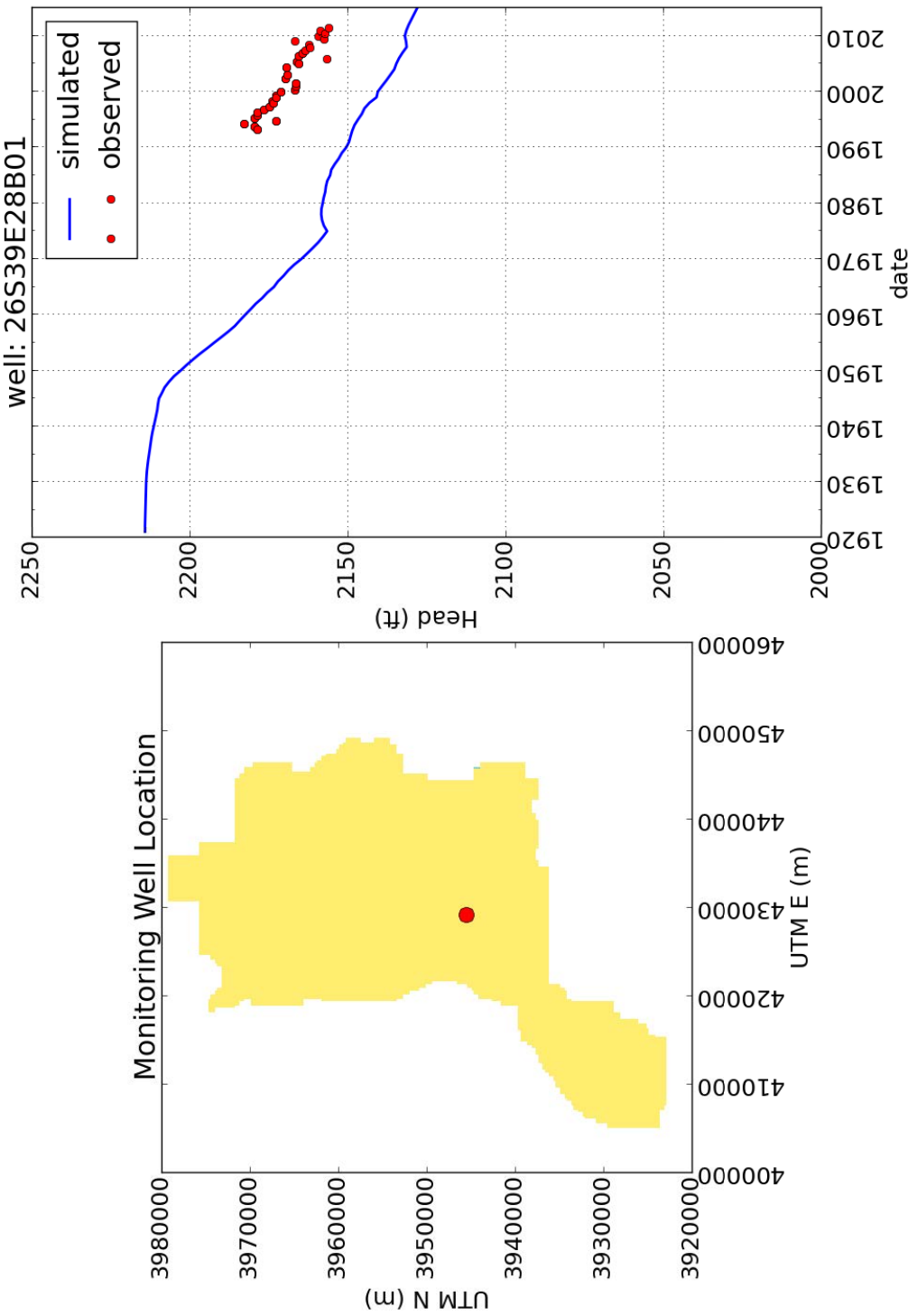
well: 26S39E28B01
simulated
observed
Head (ft)
date
Monitoring Well Location
UTM N (m)
UTM E (m)

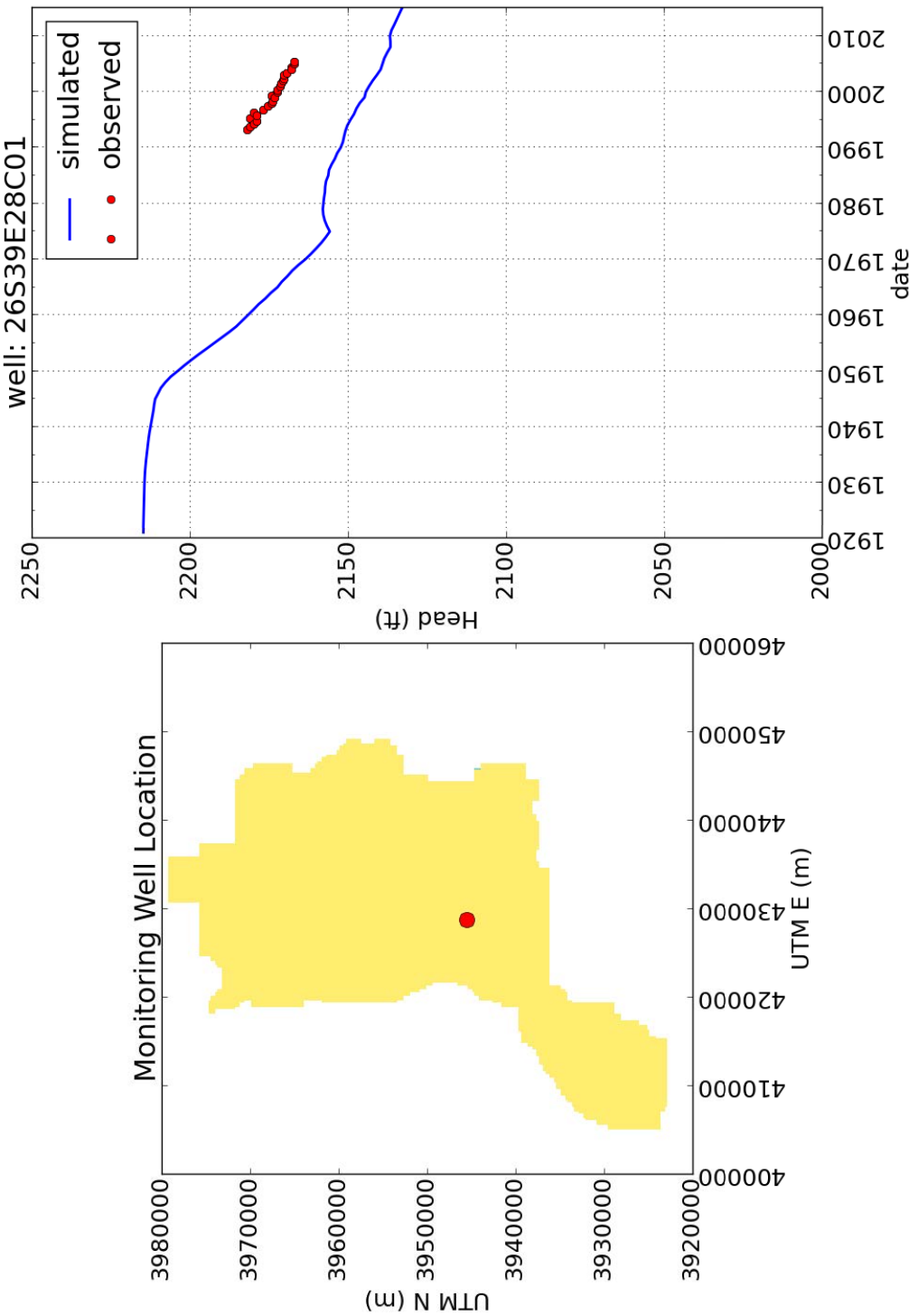
well: 26S39E28C01
simulated
observed
Head (ft)
2250
2200
2150
2100
2050
2000
1920
1930
1940
1950
1960
1970
1980
1990
2000
2010
date
Monitoring Well Location
UTM N (m)
3980000
3970000
3960000
3950000
3940000
3930000
3920000
400000
410000
420000
430000
440000
450000
460000
UTM E (m)

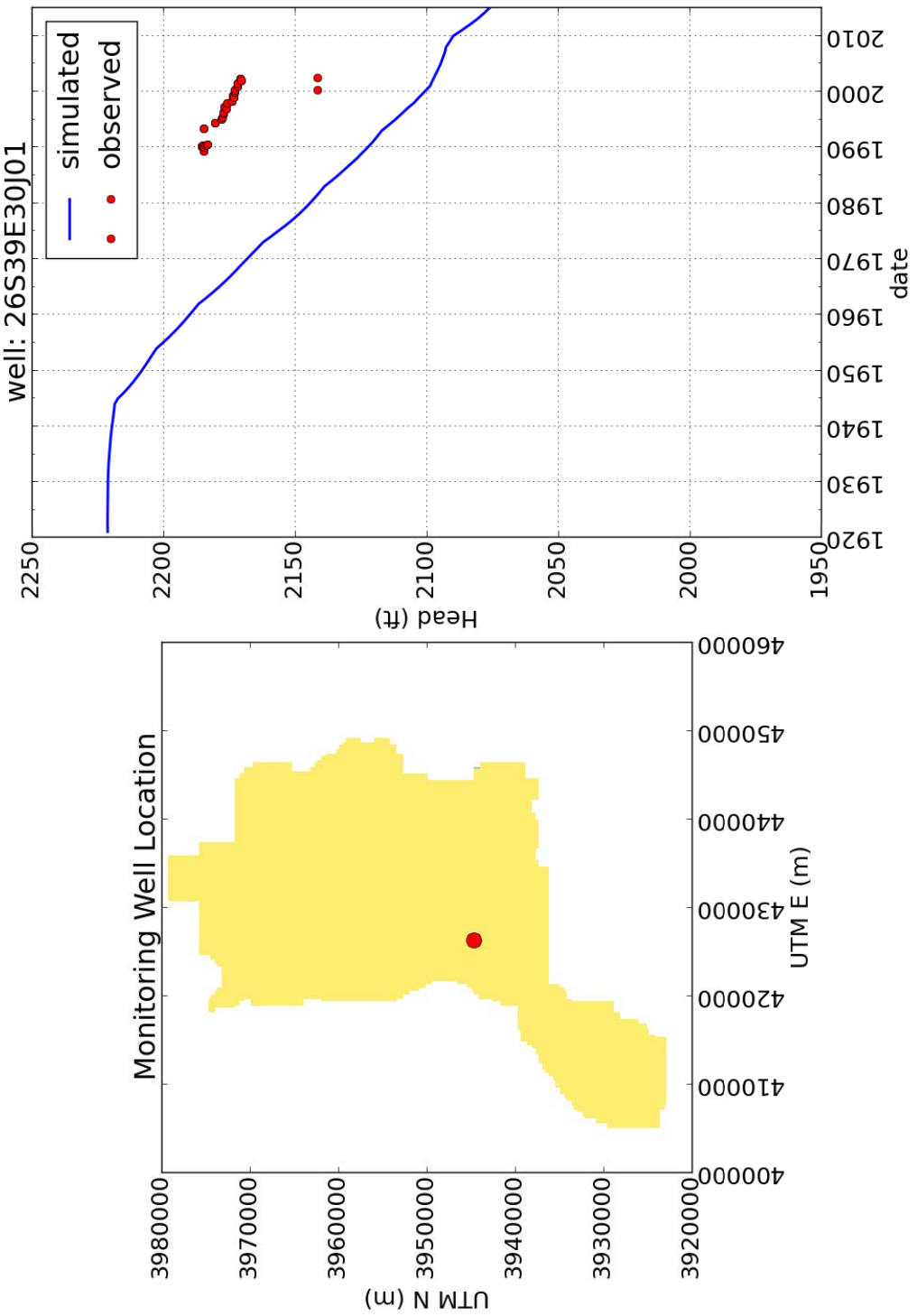
well: 26S39E30J01
simulated
observed
Head (ft)
2250
2200
2150
2100
2050
2000
1950
date
1920
1930
1940
1950
1960
1970
1980
1990
2000
2010
Monitoring Well Location
UTM N (m)
3980000
3970000
3960000
3950000
3940000
3930000
3920000
UTM E (m)
400000
410000
420000
430000
440000
450000
460000

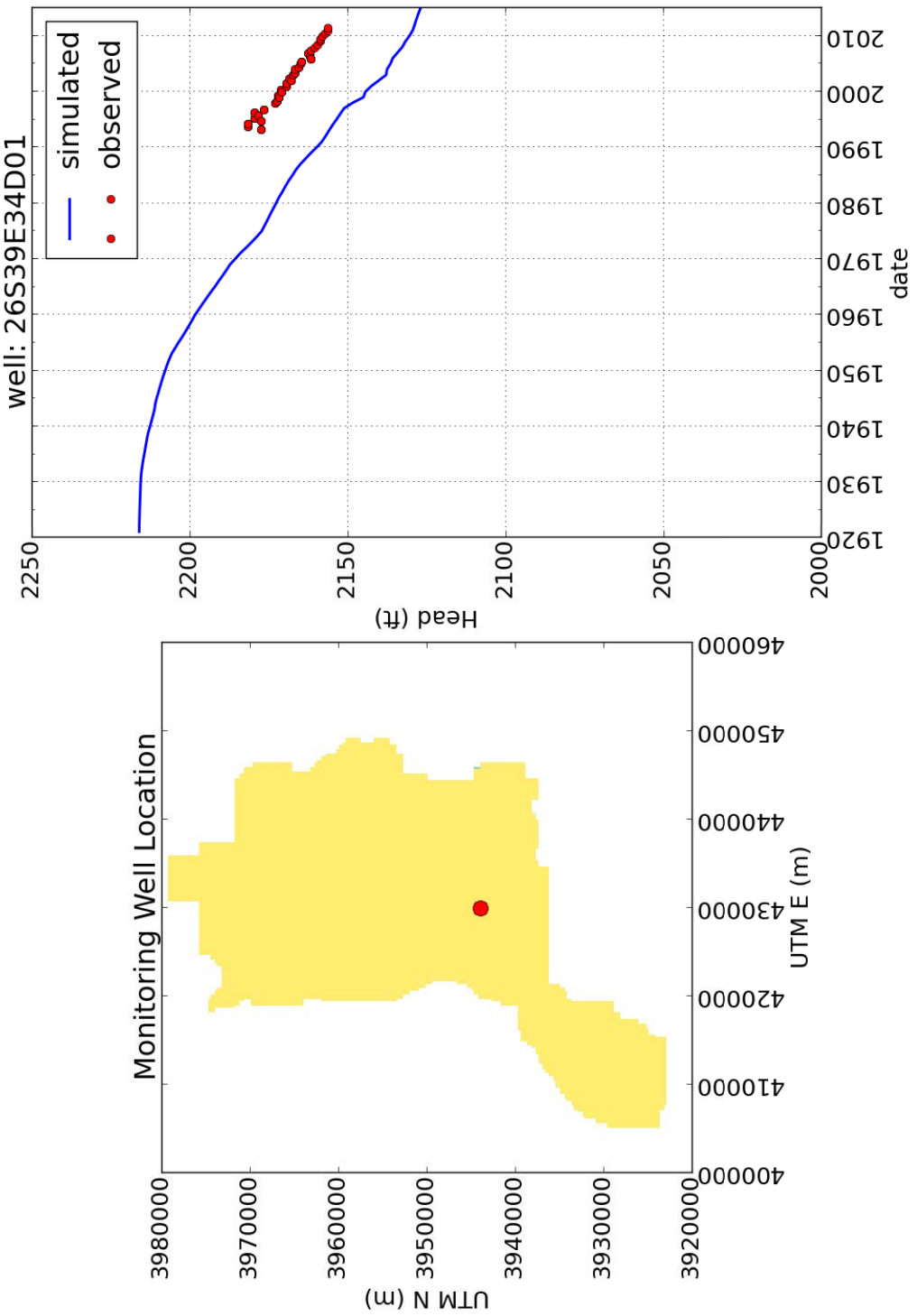
well: 26S39E34D01
simulated
observed
Head (ft)
date
2250
2200
2150
2100
2050
2000
1920
1930
1940
1950
1960
1970
1980
1990
2000
2010
Monitoring Well Location
UTM N (m)
UTM E (m)
3980000
3970000
3960000
3950000
3940000
3930000
3920000
400000
410000
420000
430000
440000
450000
460000

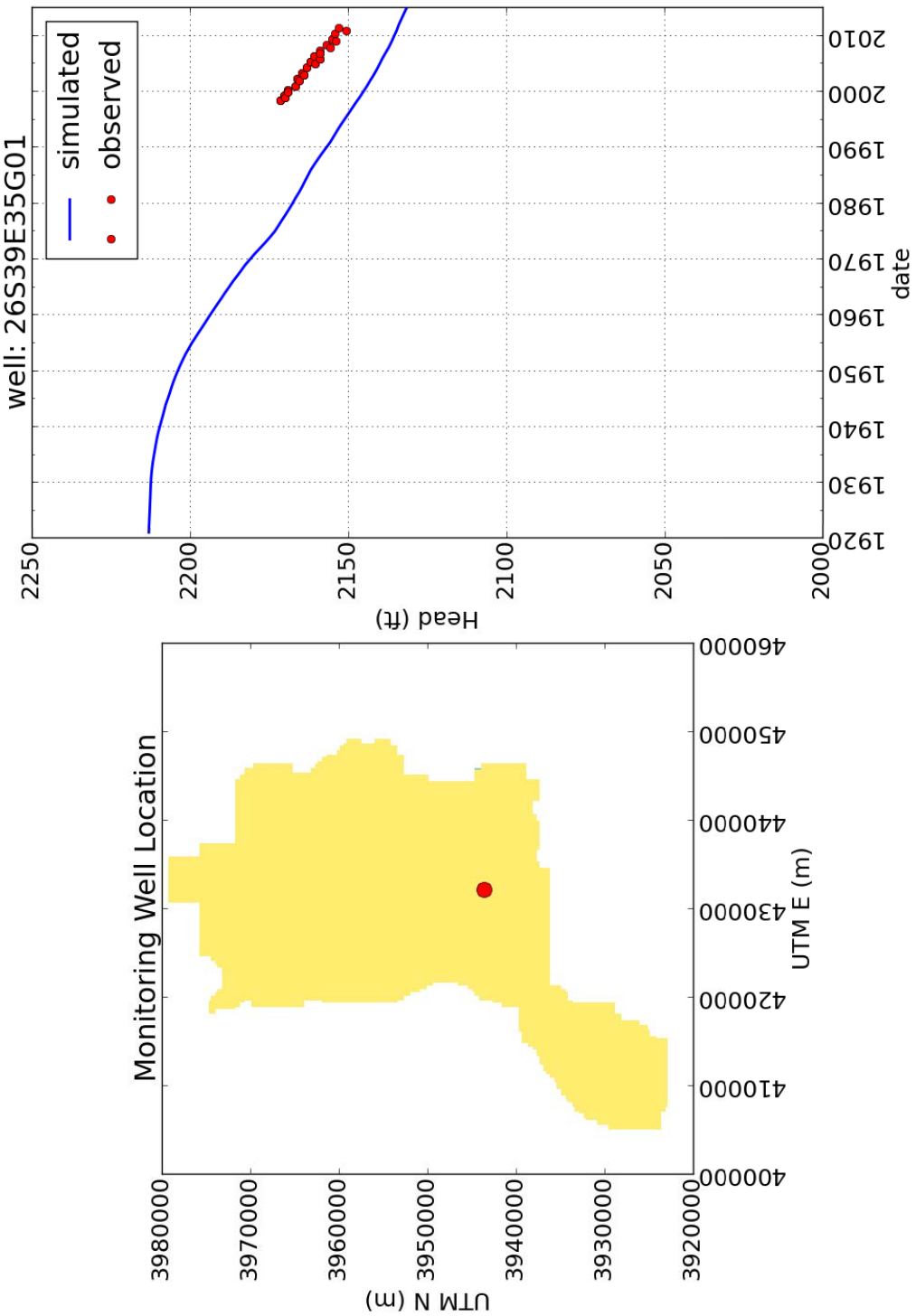
well: 26S39E35G01
simulated
observed
Head (ft)
date
2250
2200
2150
2100
2050
2000
1920
1930
1940
1950
1960
1970
1980
1990
2000
2010
Monitoring Well Location
UTM N (m)
UTM E (m)
3980000
3970000
3960000
3950000
3940000
3930000
3920000
400000
410000
420000
430000
440000
450000
460000

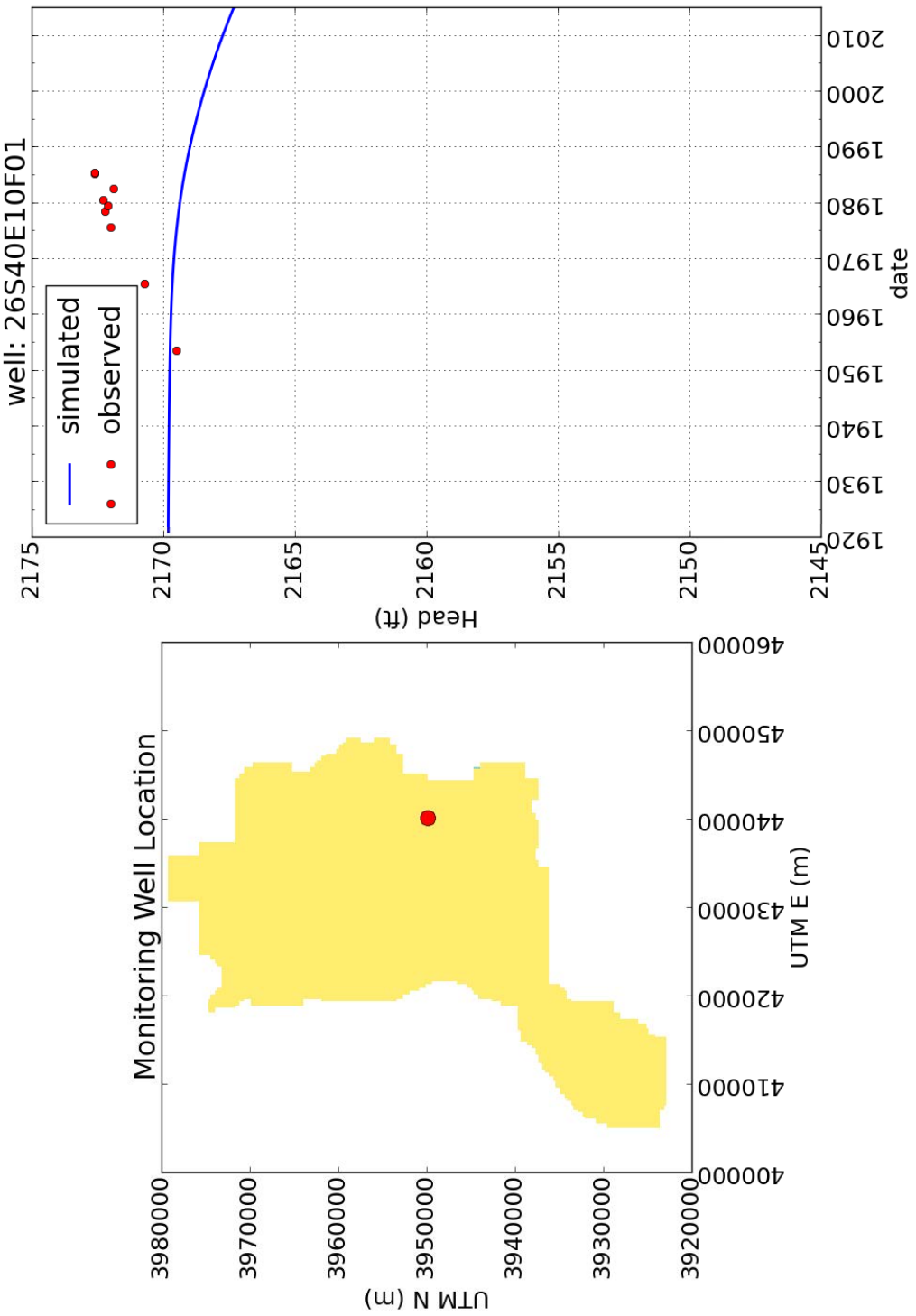
well: 26S40E10F01
simulated
observed
Head (ft)
2175
2170
2165
2160
2155
2150
2145
date
1920
1930
1940
1950
1960
1970
1980
1990
2000
2010
Monitoring Well Location
UTM N (m)
3980000
3970000
3960000
3950000
3940000
3930000
3920000
UTM E (m)
400000
410000
420000
430000
440000
450000
460000

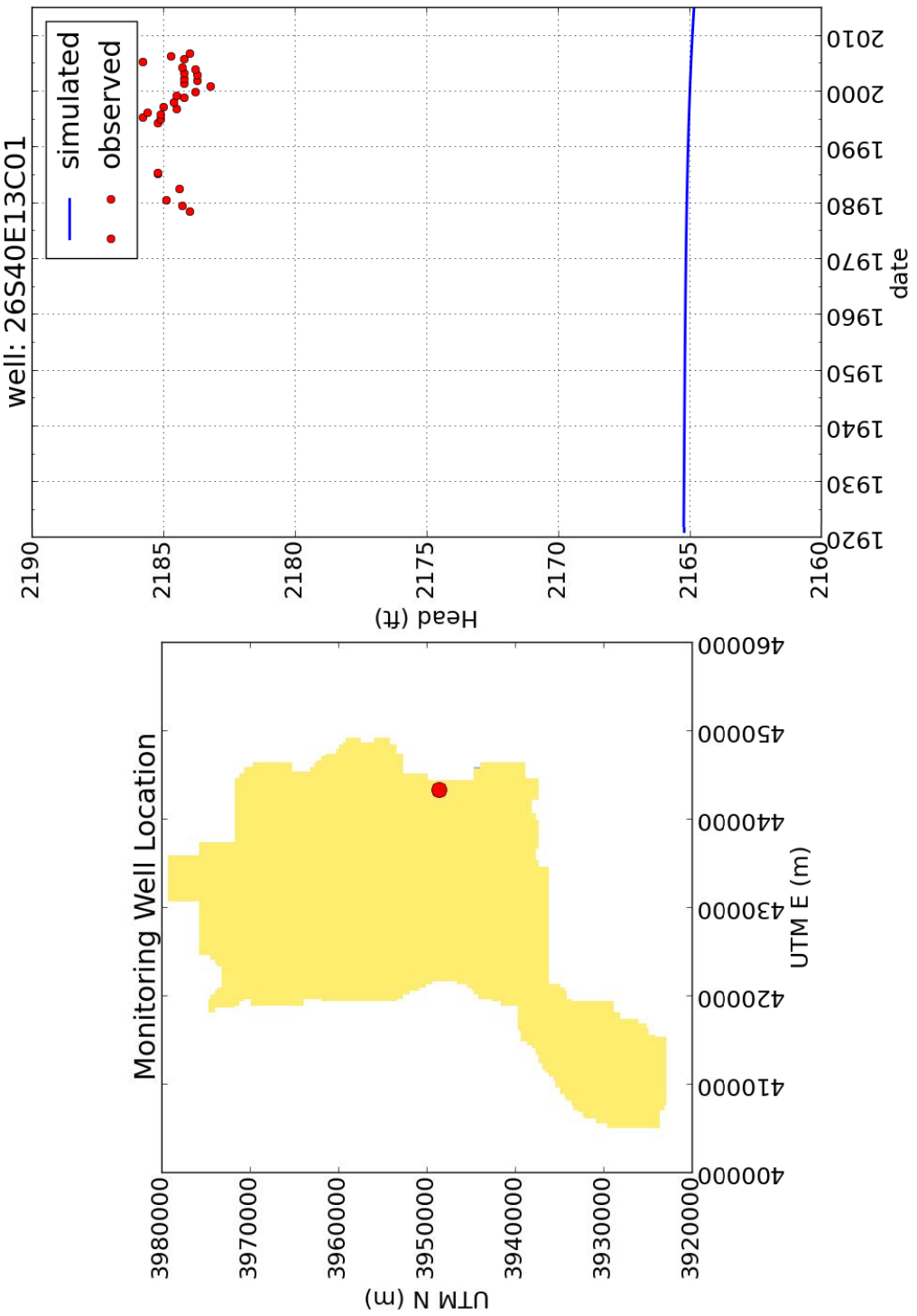
well: 26S40E13C01
simulated
observed
Head (ft)
date
2190
2185
2180
2175
2170
2165
2160
1920
1930
1940
1950
1960
1970
1980
1990
2000
2010
Monitoring Well Location
UTM N (m)
UTM E (m)
3980000
3970000
3960000
3950000
3940000
3930000
3920000
400000
410000
420000
430000
440000
450000
460000

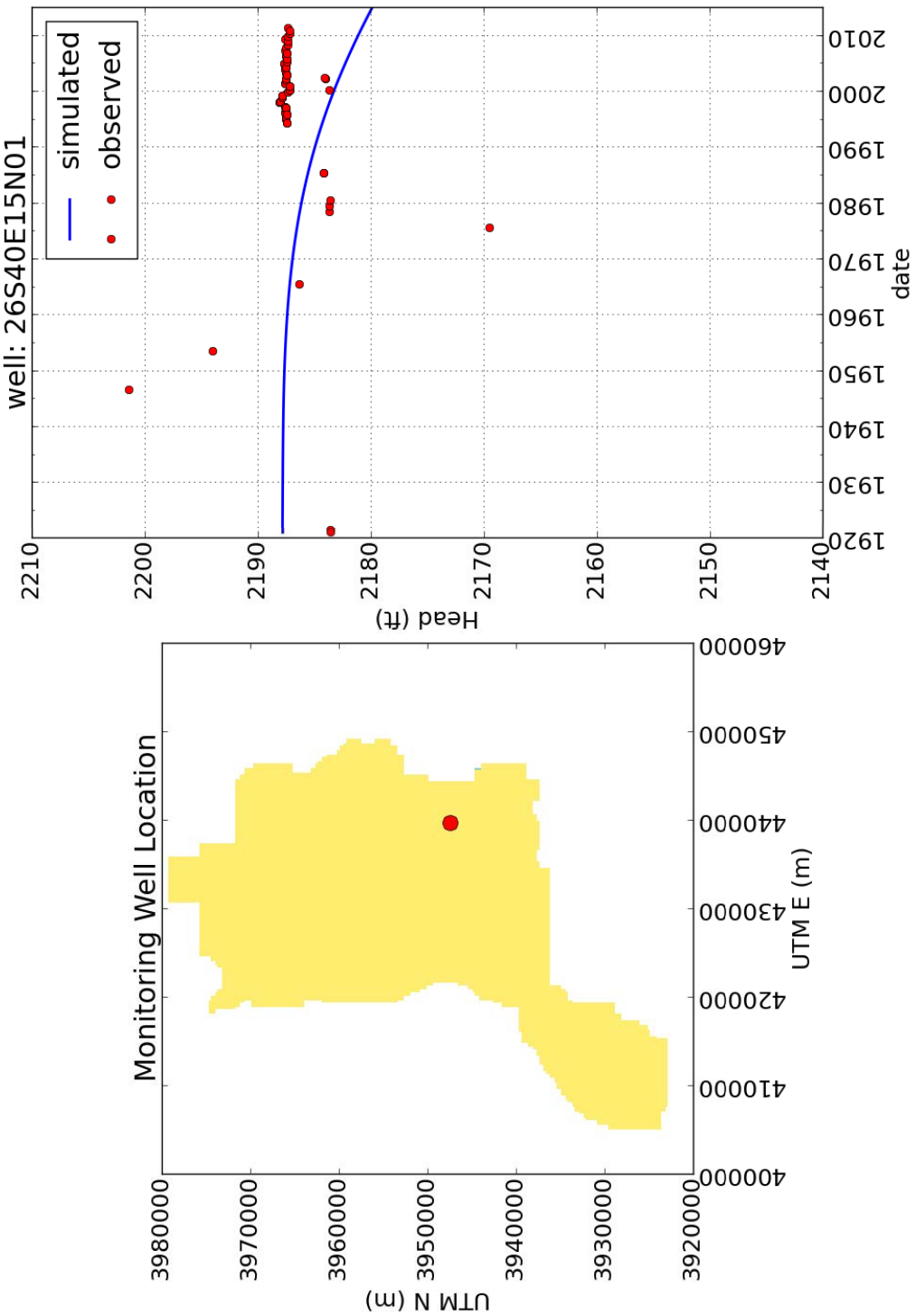
well: 26S40E15N01
simulated
observed
Head (ft)
date
2210
2200
2190
2180
2170
2160
2150
2140
1920
1930
1940
1950
1960
1970
1980
1990
2000
2010
Monitoring Well Location
UTM N (m)
UTM E (m)
3980000
3970000
3960000
3950000
3940000
3930000
3920000
400000
410000
420000
430000
440000
450000
460000

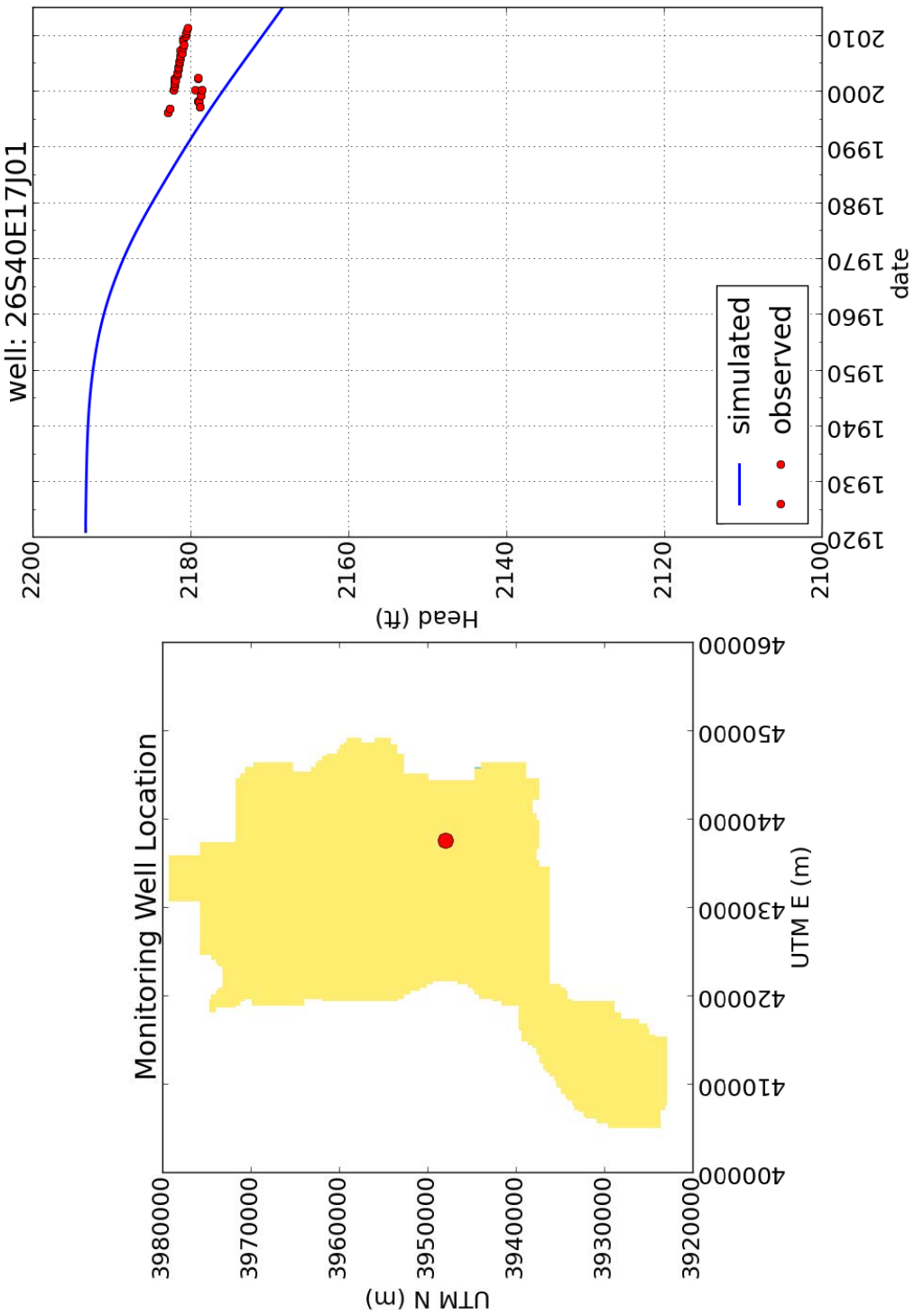
well: 26S40E17J01
Head (ft)
2200
2180
2160
2140
2120
2100
date
1920
1930
1940
1950
1960
1970
1980
1990
2000
2010
simulated
observed
Monitoring Well Location
UTM N (m)
3980000
3970000
3960000
3950000
3940000
3930000
3920000
UTM E (m)
460000
450000
440000
430000
420000
410000
400000

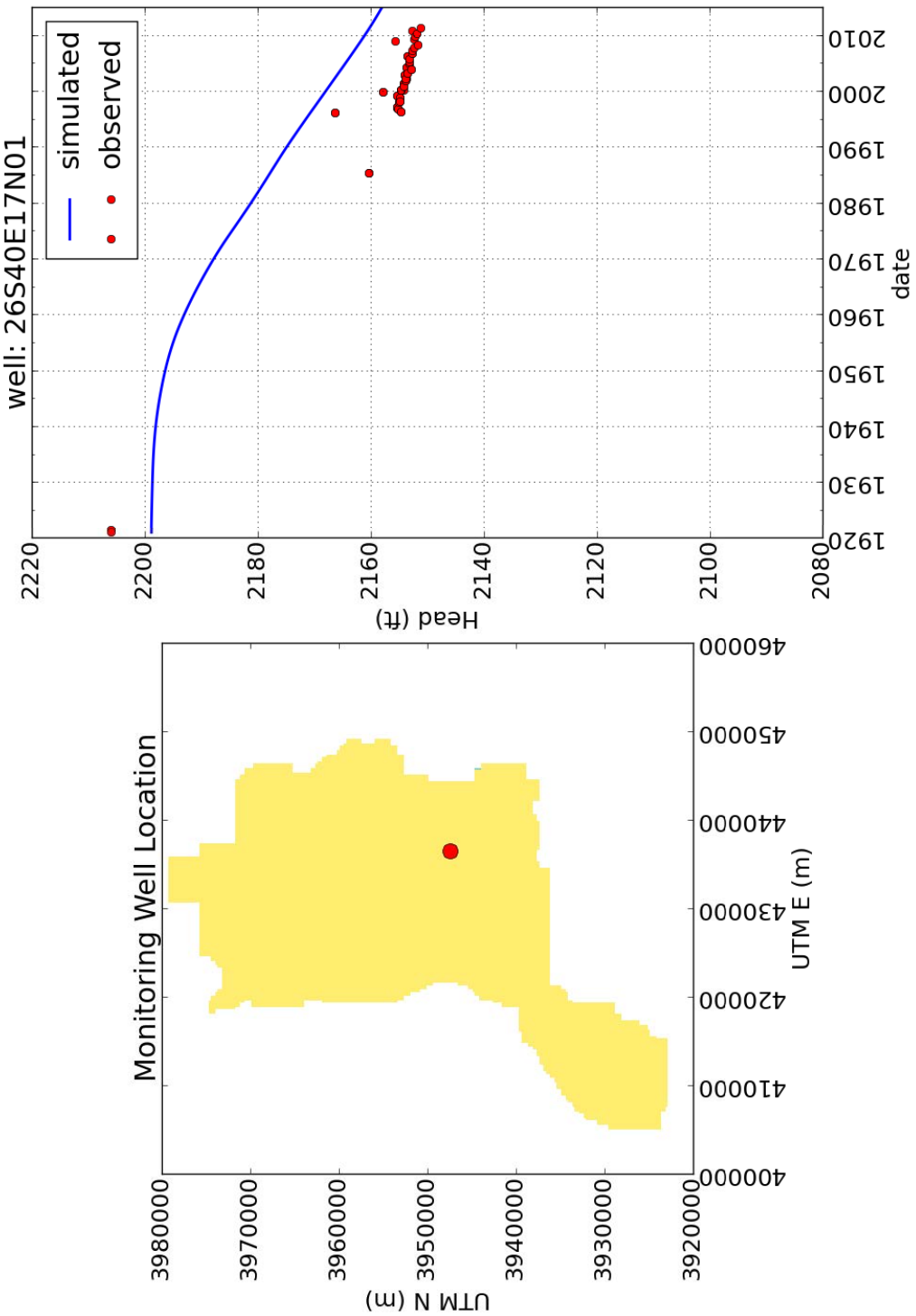
well: 26S40E17N01
simulated
observed
Head (ft)
date
2220
2200
2180
2160
2140
2120
2100
2080
1920
1930
1940
1950
1960
1970
1980
1990
2000
2010
Monitoring Well Location
UTM N (m)
UTM E (m)
3980000
3970000
3960000
3950000
3940000
3930000
3920000
400000
410000
420000
430000
440000
450000
460000

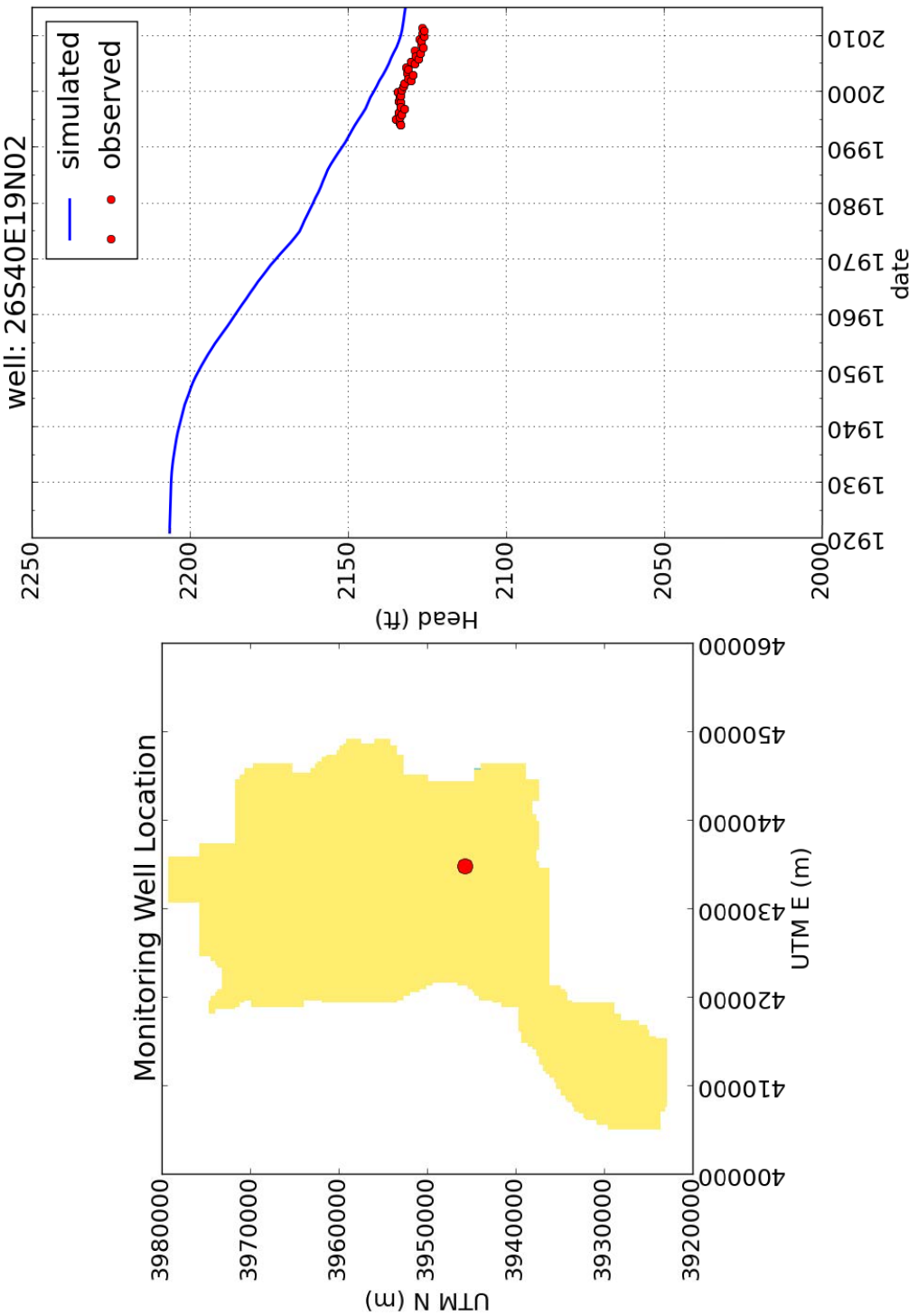
well: 26S40E19N02
simulated
observed
Head (ft)
date
2250
2200
2150
2100
2050
2000
1920
1930
1940
1950
1960
1970
1980
1990
2000
2010
Monitoring Well Location
UTM N (m)
UTM E (m)
3980000
3970000
3960000
3950000
3940000
3930000
3920000
400000
410000
420000
430000
440000
450000
460000

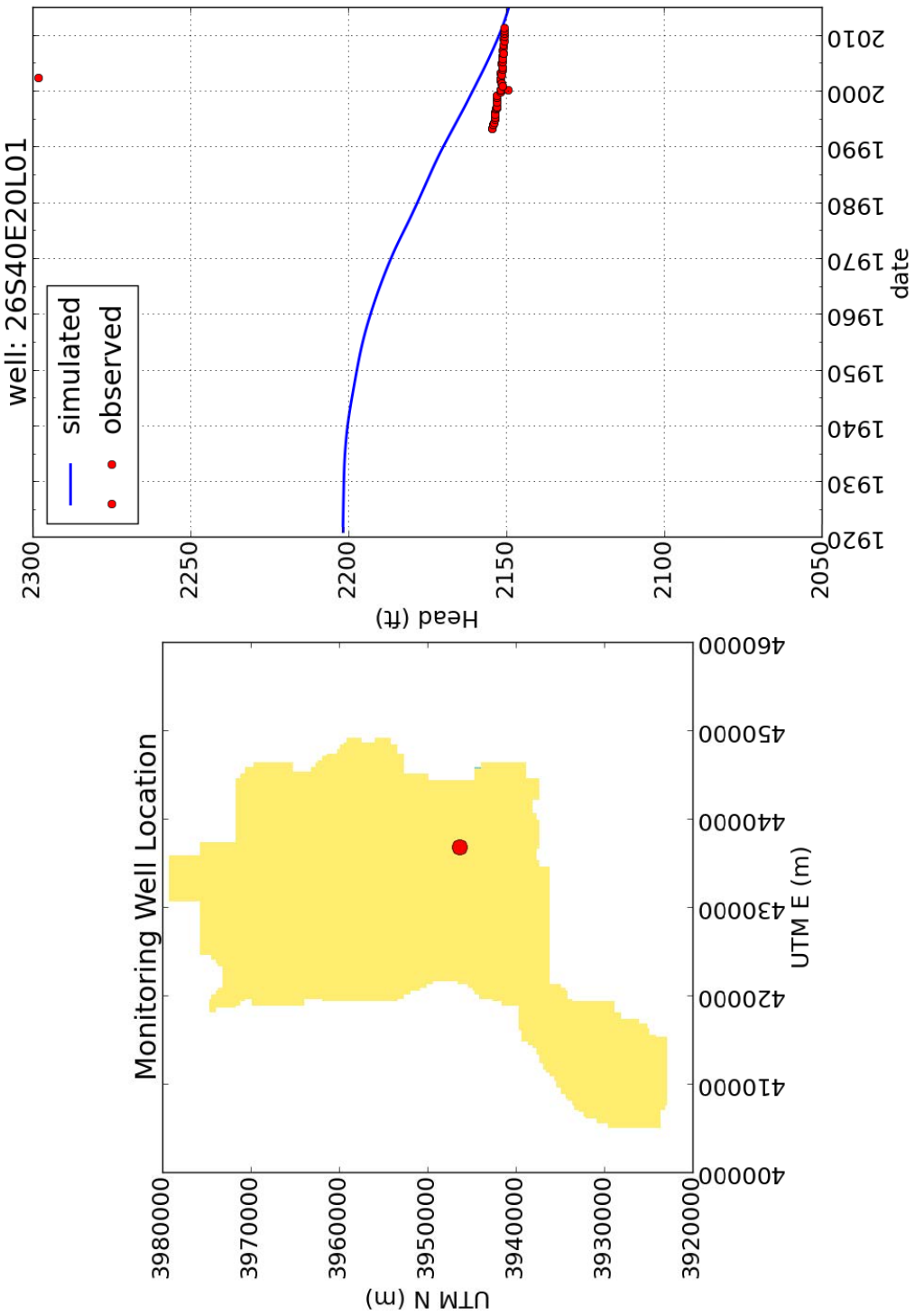
well: 26S40E20L01
simulated
observed
Head (ft)
2300
2250
2200
2150
2100
2050
1920
1930
1940
1950
1960
1970
1980
1990
2000
2010
date
Monitoring Well Location
UTM N (m)
3980000
3970000
3960000
3950000
3940000
3930000
3920000
400000
410000
420000
430000
440000
450000
460000
UTM E (m)

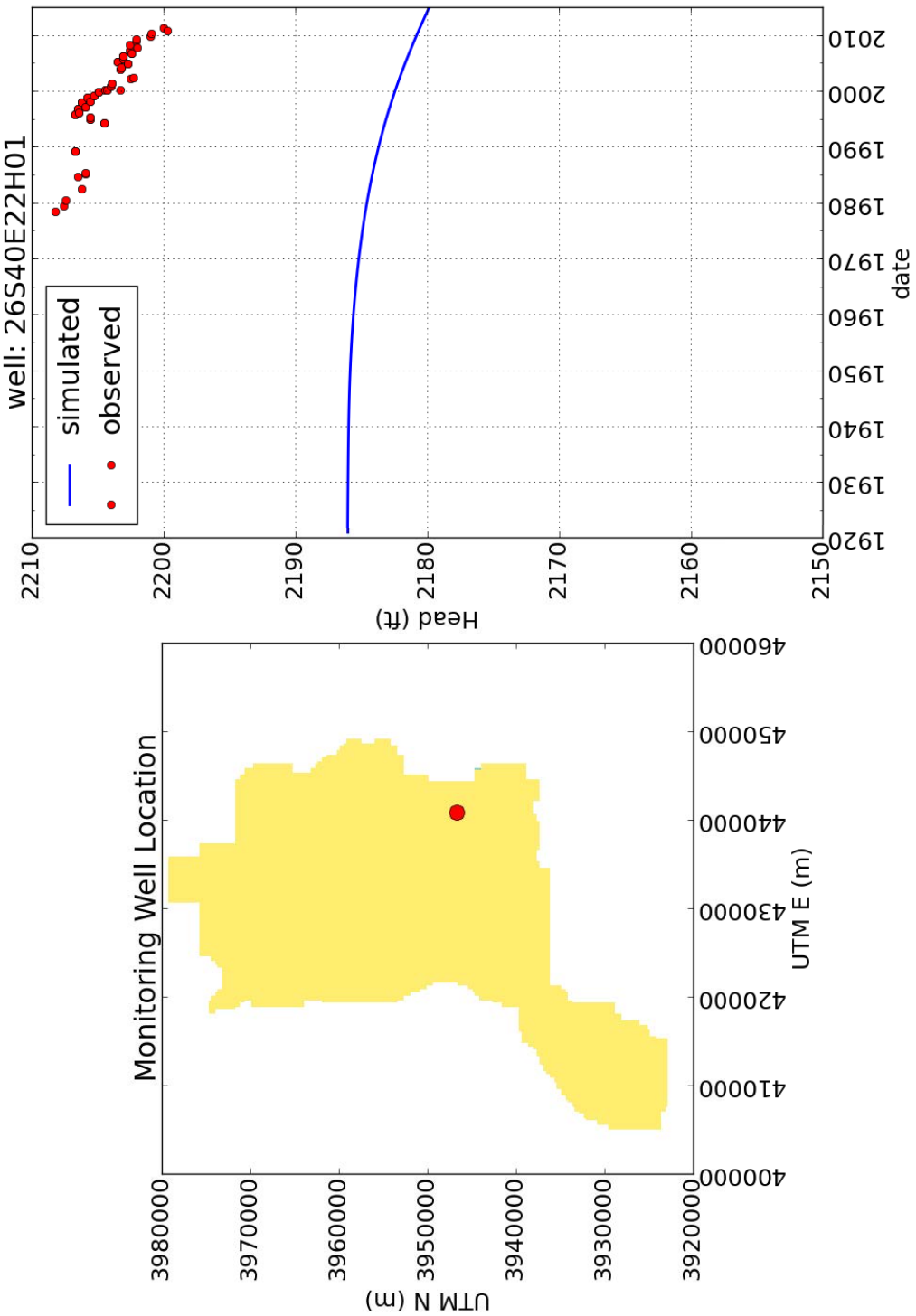
well: 26S40E22H01
simulated
observed
Head (ft)
date
Monitoring Well Location
UTM N (m)
UTM E (m)

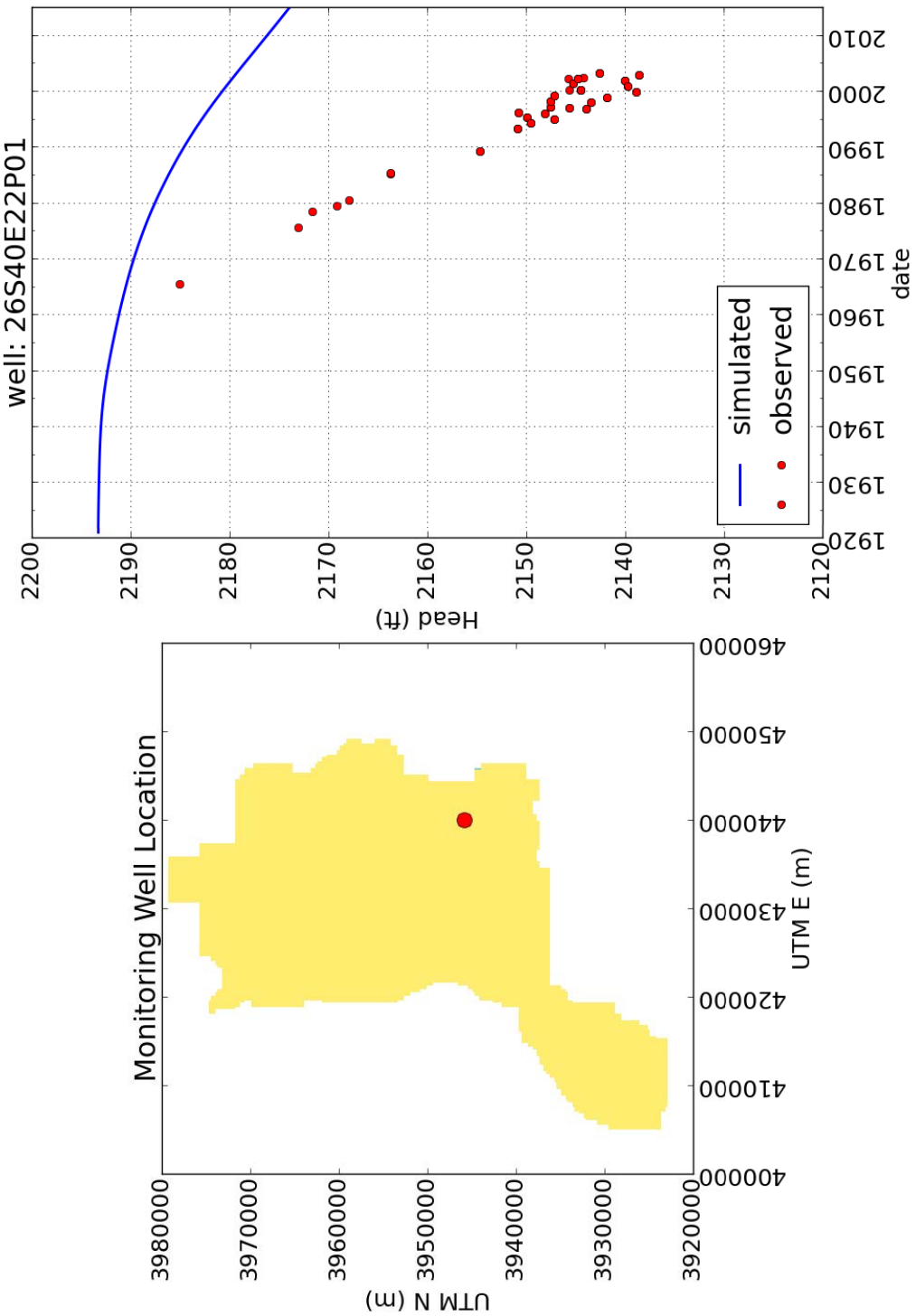
well: 26S40E22P01
Head (ft)
date
simulated
observed
Monitoring Well Location
UTM N (m)
UTM E (m)

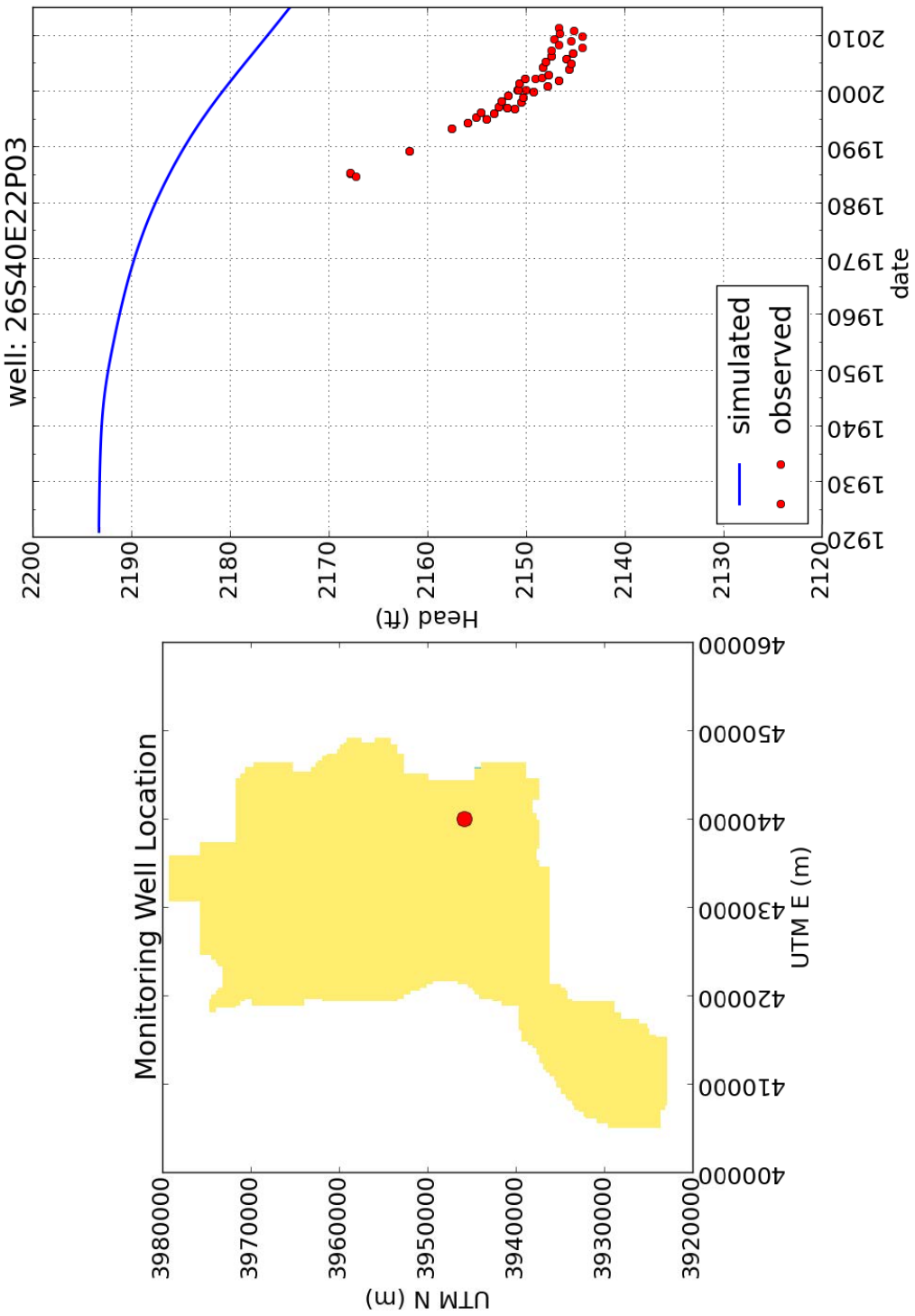
well: 26S40E22P03
Head (ft)
date
simulated
observed
Monitoring Well Location
UTM N (m)
UTM E (m)

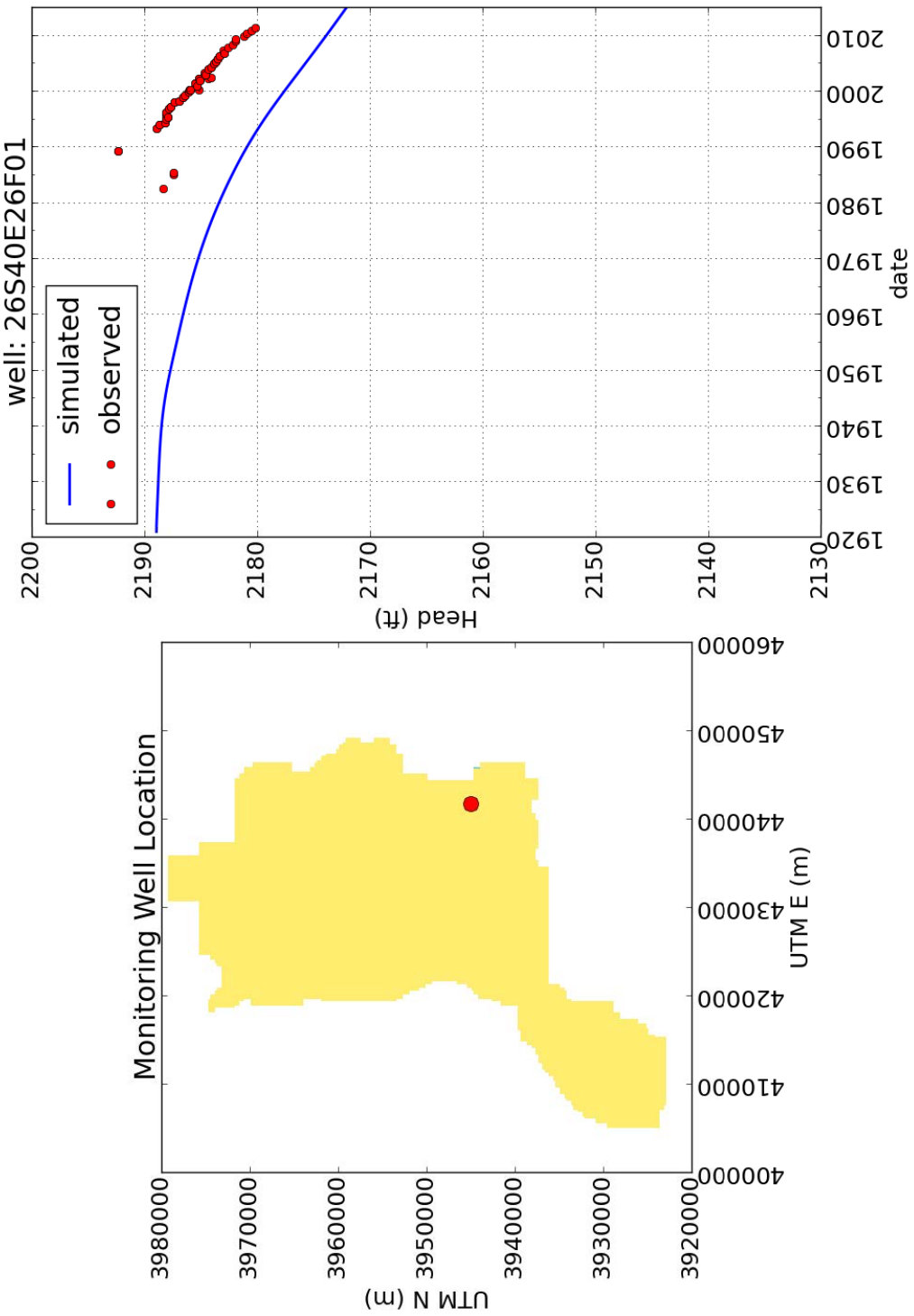
well: 26S40E26F01
simulated
observed
Head (ft)
date
2200
2190
2180
2170
2160
2150
2140
2130
1920
1930
1940
1950
1960
1970
1980
1990
2000
2010
Monitoring Well Location
UTM N (m)
UTM E (m)
3980000
3970000
3960000
3950000
3940000
3930000
3920000
400000
410000
420000
430000
440000
450000
460000

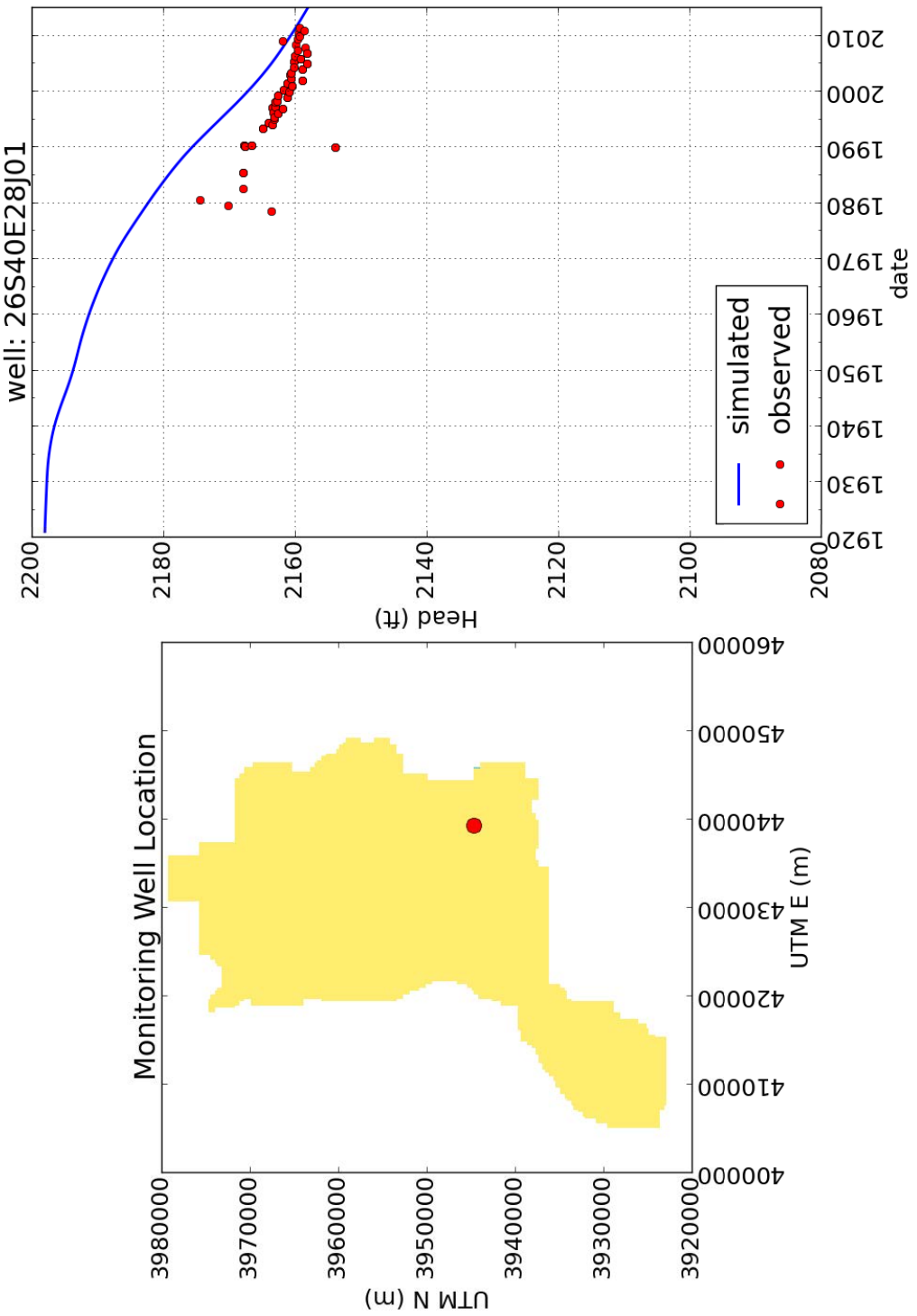
well: 26S40E28J01
Head (ft)
2200
2180
2160
2140
2120
2100
2080
date
1920
1930
1940
1950
1960
1970
1980
1990
2000
2010
simulated
observed
Monitoring Well Location
UTM N (m)
3980000
3970000
3960000
3950000
3940000
3930000
3920000
UTM E (m)
400000
410000
420000
430000
440000
450000
460000

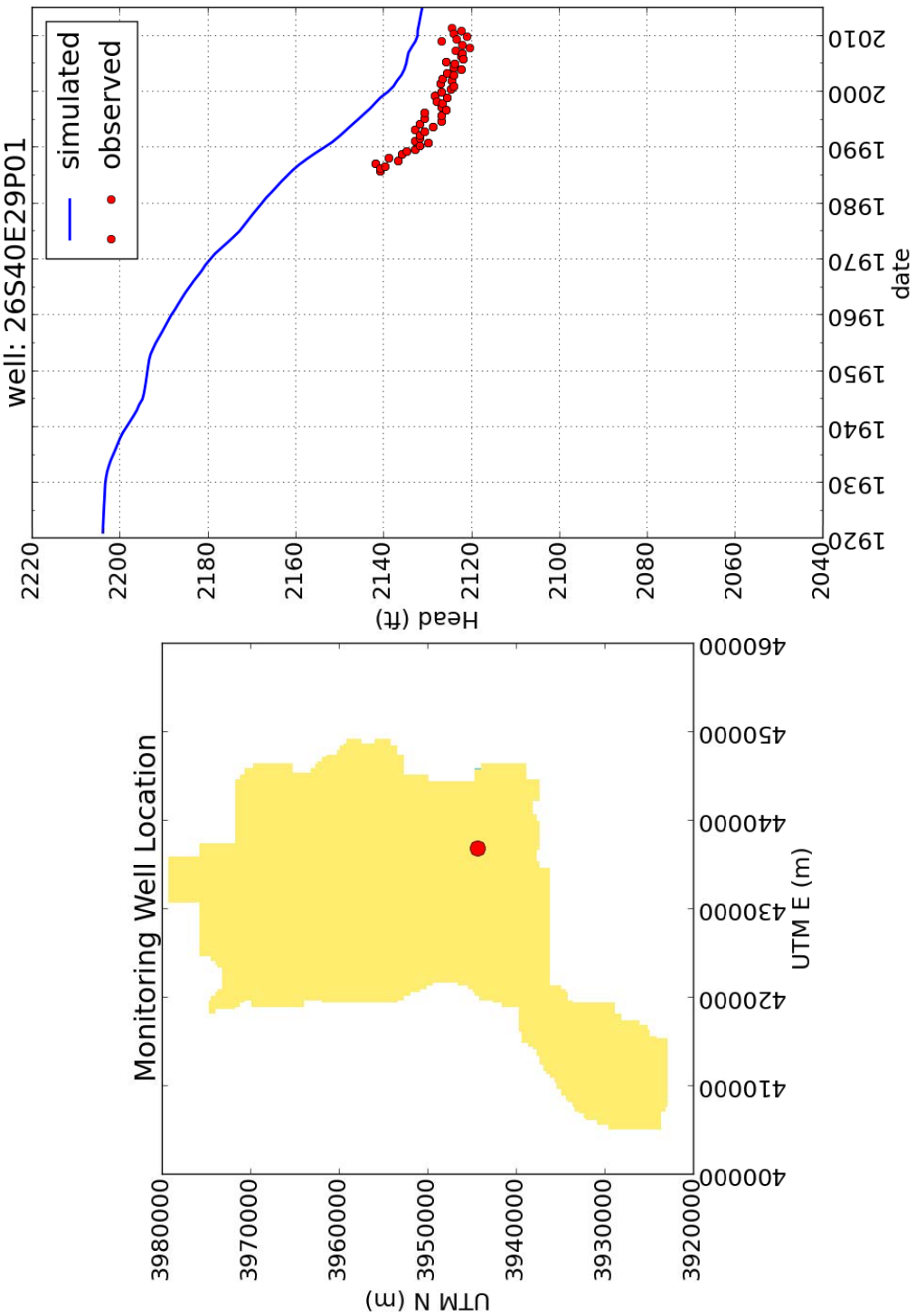
well: 26S40E29P01
simulated
observed
Head (ft)
date
2220
2200
2180
2160
2140
2120
2100
2080
2060
2040
1920
1930
1940
1950
1960
1970
1980
1990
2000
2010
Monitoring Well Location
UTM N (m)
UTM E (m)
3980000
3970000
3960000
3950000
3940000
3930000
3920000
400000
410000
420000
430000
440000
450000
460000

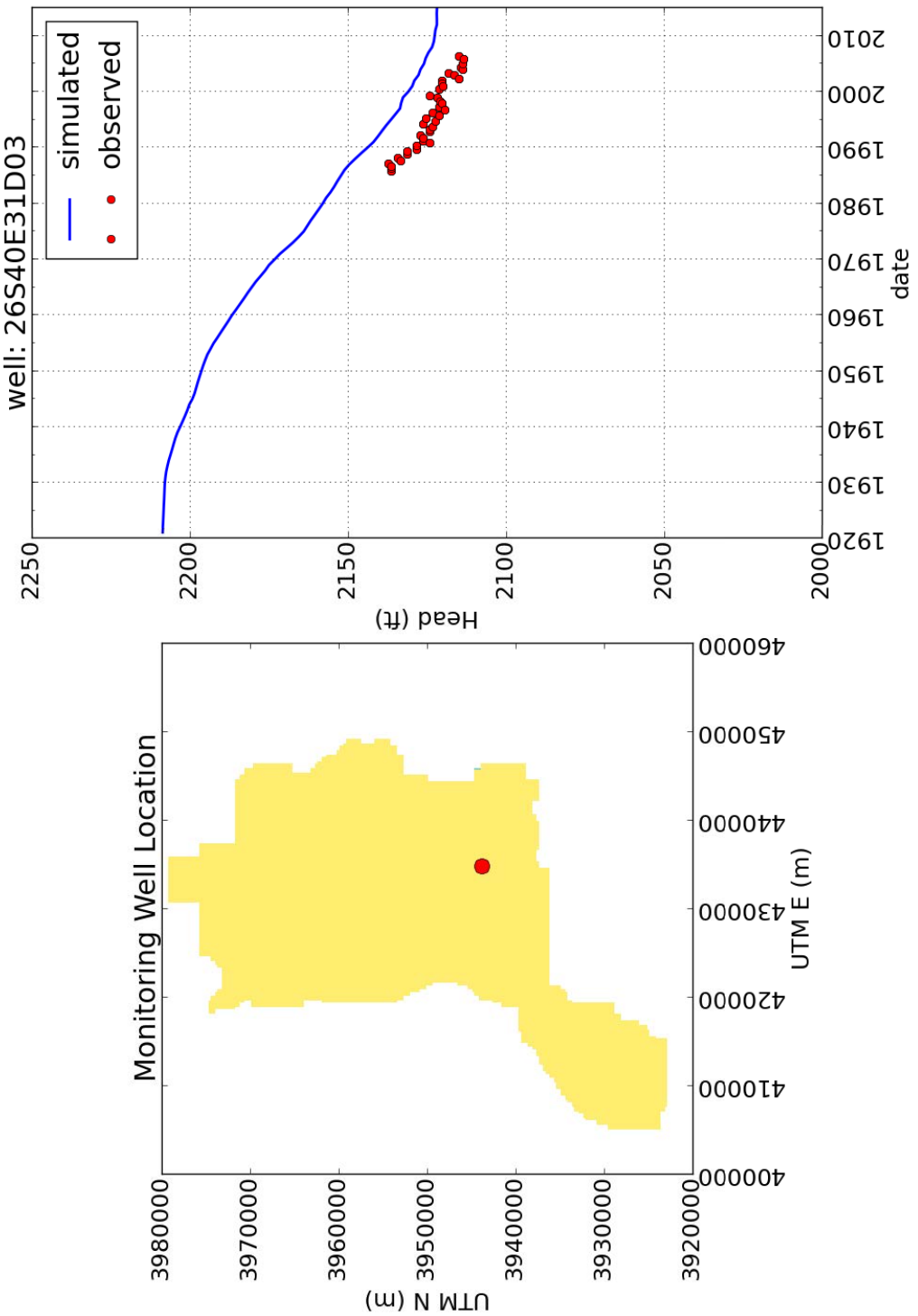
well: 26S40E31D03
simulated
observed
Head (ft)
2250
2200
2150
2100
2050
2000
date
1920
1930
1940
1950
1960
1970
1980
1990
2000
2010
Monitoring Well Location
UTM N (m)
3980000
3970000
3960000
3950000
3940000
3930000
3920000
UTM E (m)
400000
410000
420000
430000
440000
450000
460000

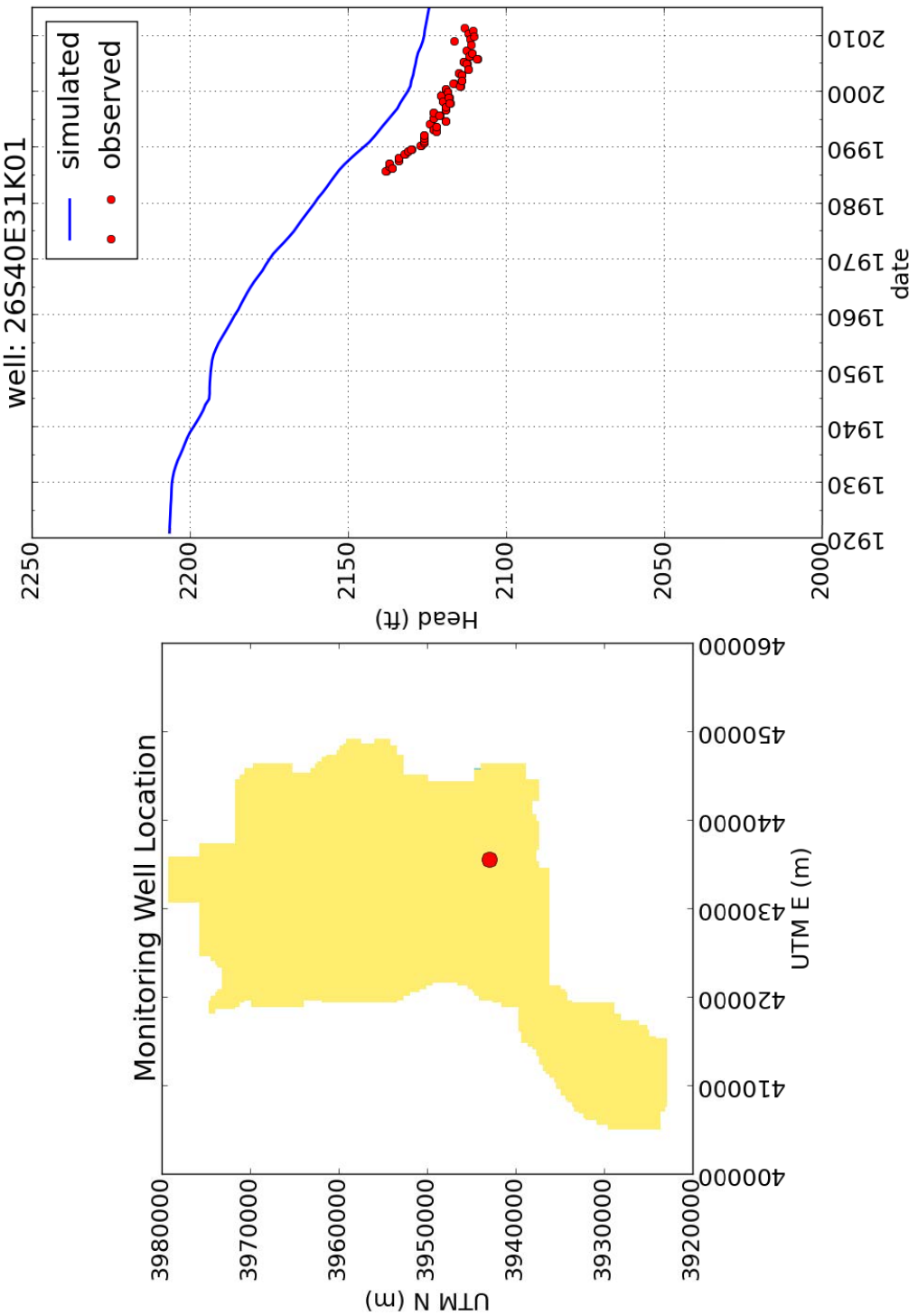
well: 26S40E31K01
simulated
observed
Head (ft)
date
2250
2200
2150
2100
2050
2000
1920
1930
1940
1950
1960
1970
1980
1990
2000
2010
Monitoring Well Location
UTM N (m)
UTM E (m)
3980000
3970000
3960000
3950000
3940000
3930000
3920000
400000
410000
420000
430000
440000
450000
460000

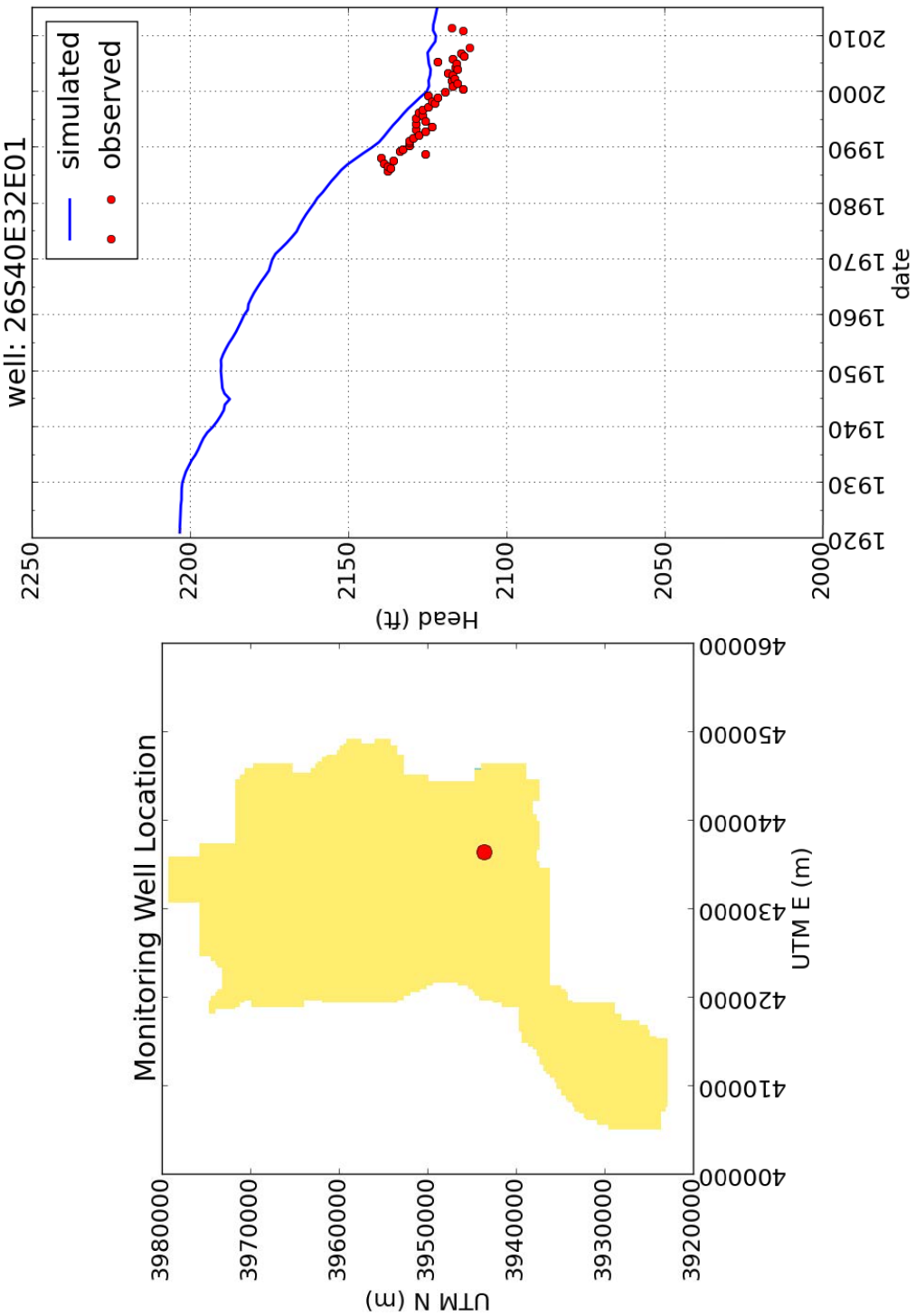
well: 26S40E32E01
simulated
observed
Head (ft)
date
2250
2200
2150
2100
2050
2000
1920
1930
1940
1950
1960
1970
1980
1990
2000
2010
Monitoring Well Location
UTM N (m)
UTM E (m)
3980000
3970000
3960000
3950000
3940000
3930000
3920000
400000
410000
420000
430000
440000
450000
460000

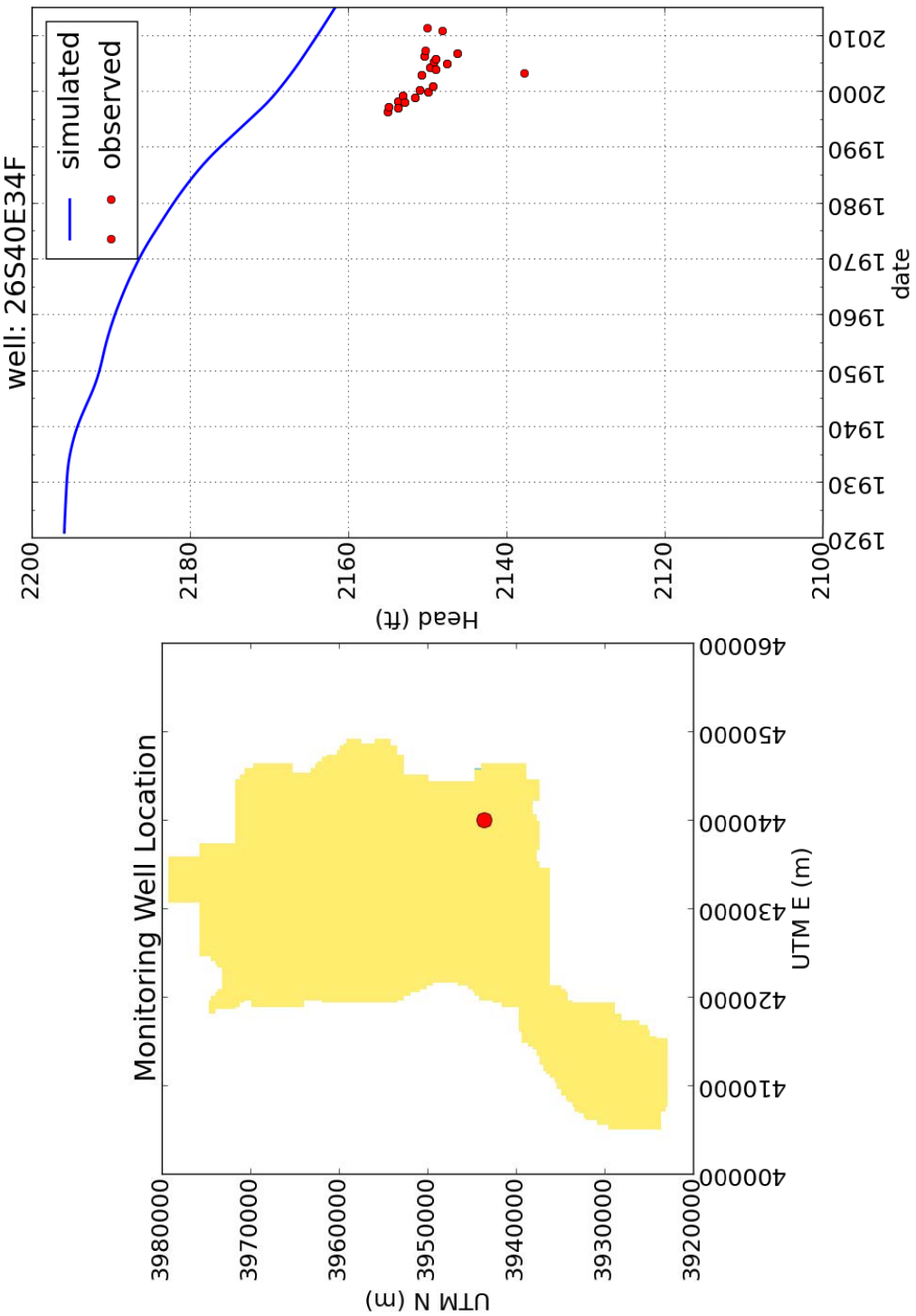
well: 26S40E34F
simulated
observed
Head (ft)
date
2200
2180
2160
2140
2120
2100
1920
1930
1940
1950
1960
1970
1980
1990
2000
2010
Monitoring Well Location
UTM N (m)
UTM E (m)
3980000
3970000
3960000
3950000
3940000
3930000
3920000
400000
410000
420000
430000
440000
450000
460000

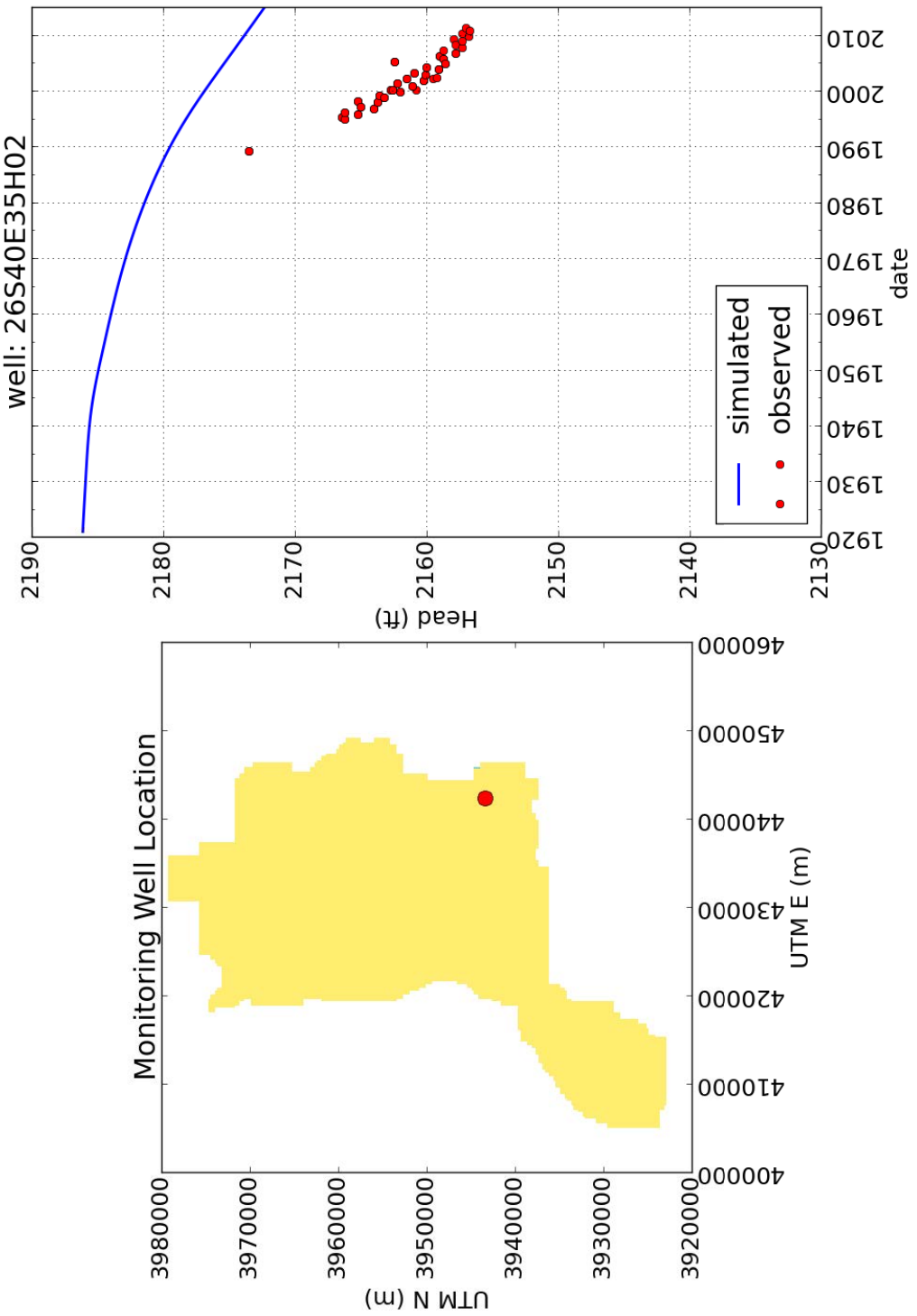
well: 26S40E35H02
Head (ft)
2190
2180
2170
2160
2150
2140
2130
date
1920
1930
1940
1950
1960
1970
1980
1990
2000
2010
simulated
observed
Monitoring Well Location
UTM N (m)
3980000
3970000
3960000
3950000
3940000
3930000
3920000
UTM E (m)
400000
410000
420000
430000
440000
450000
460000

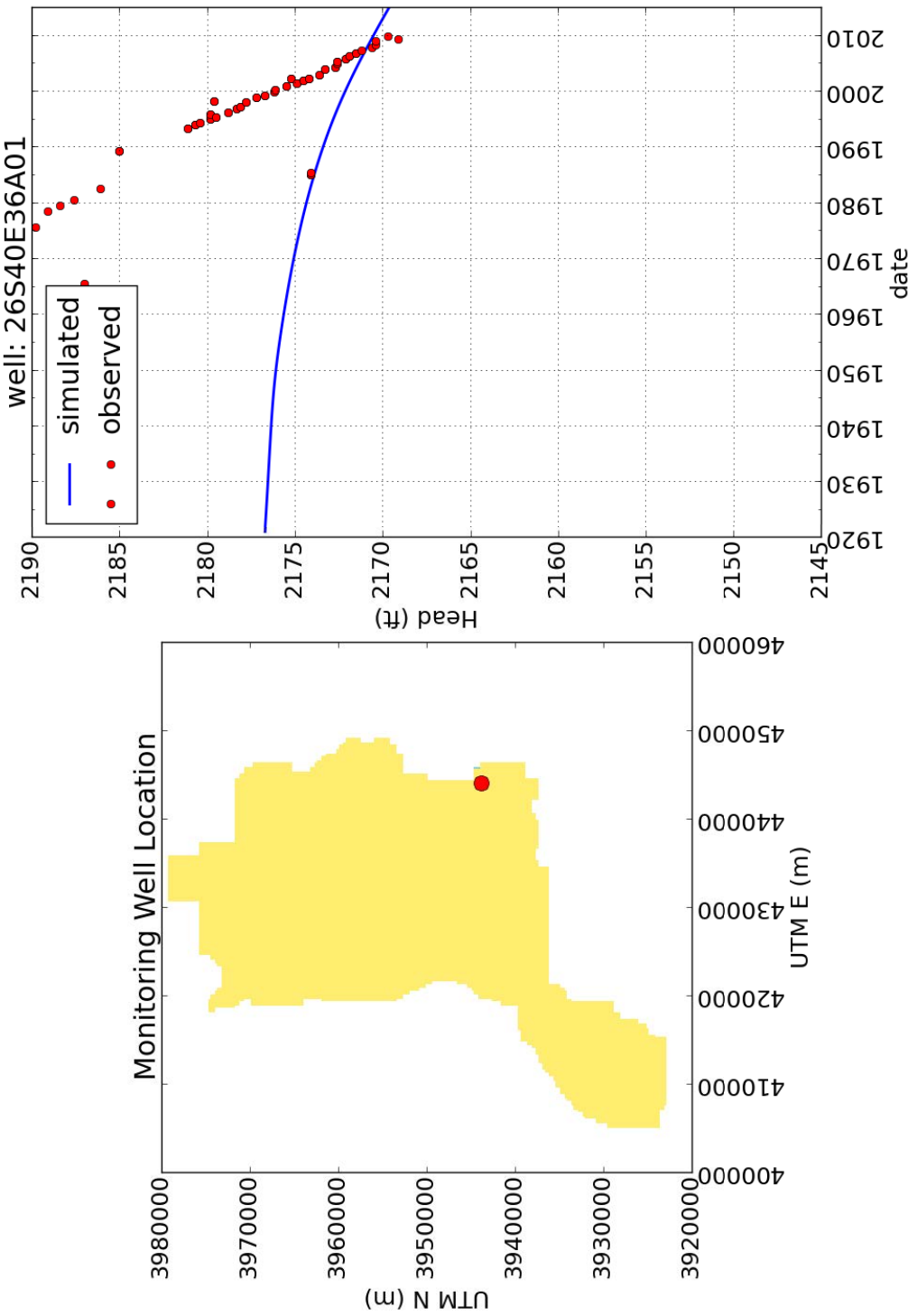
well: 26S40E36A01
simulated
observed
Head (ft)
date
2190
2185
2180
2175
2170
2165
2160
2155
2150
2145
1920
1930
1940
1950
1960
1970
1980
1990
2000
2010
Monitoring Well Location
UTM N (m)
UTM E (m)
3980000
3970000
3960000
3950000
3940000
3930000
3920000
400000
410000
420000
430000
440000
450000
460000

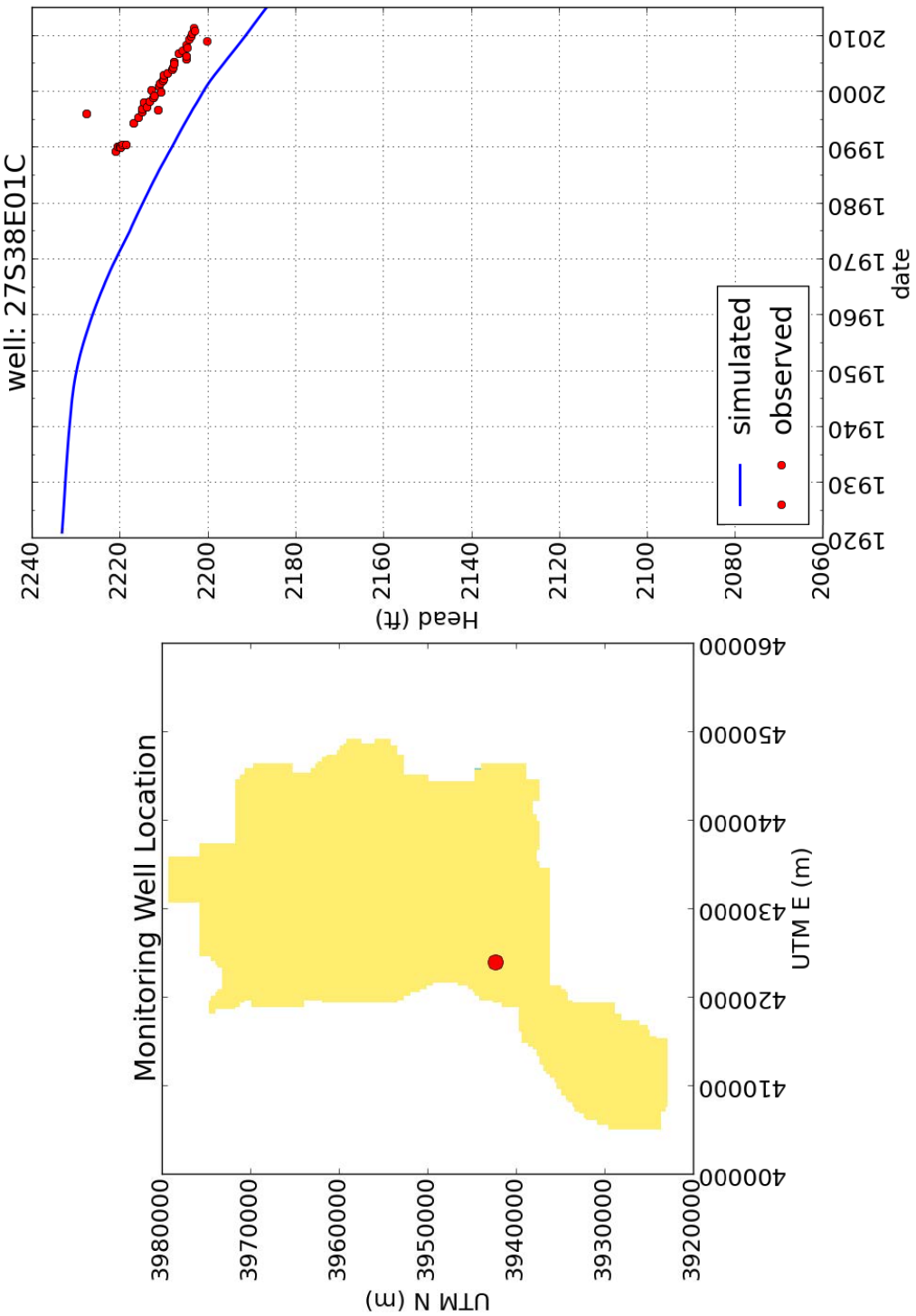
well: 27S38E01C
Head (ft)
2240
2220
2200
2180
2160
2140
2120
2100
2080
2060
date
1920
1930
1940
1950
1960
1970
1980
1990
2000
2010
simulated
observed
Monitoring Well Location
UTM N (m)
3980000
3970000
3960000
3950000
3940000
3930000
3920000
UTM E (m)
400000
410000
420000
430000
440000
450000
460000

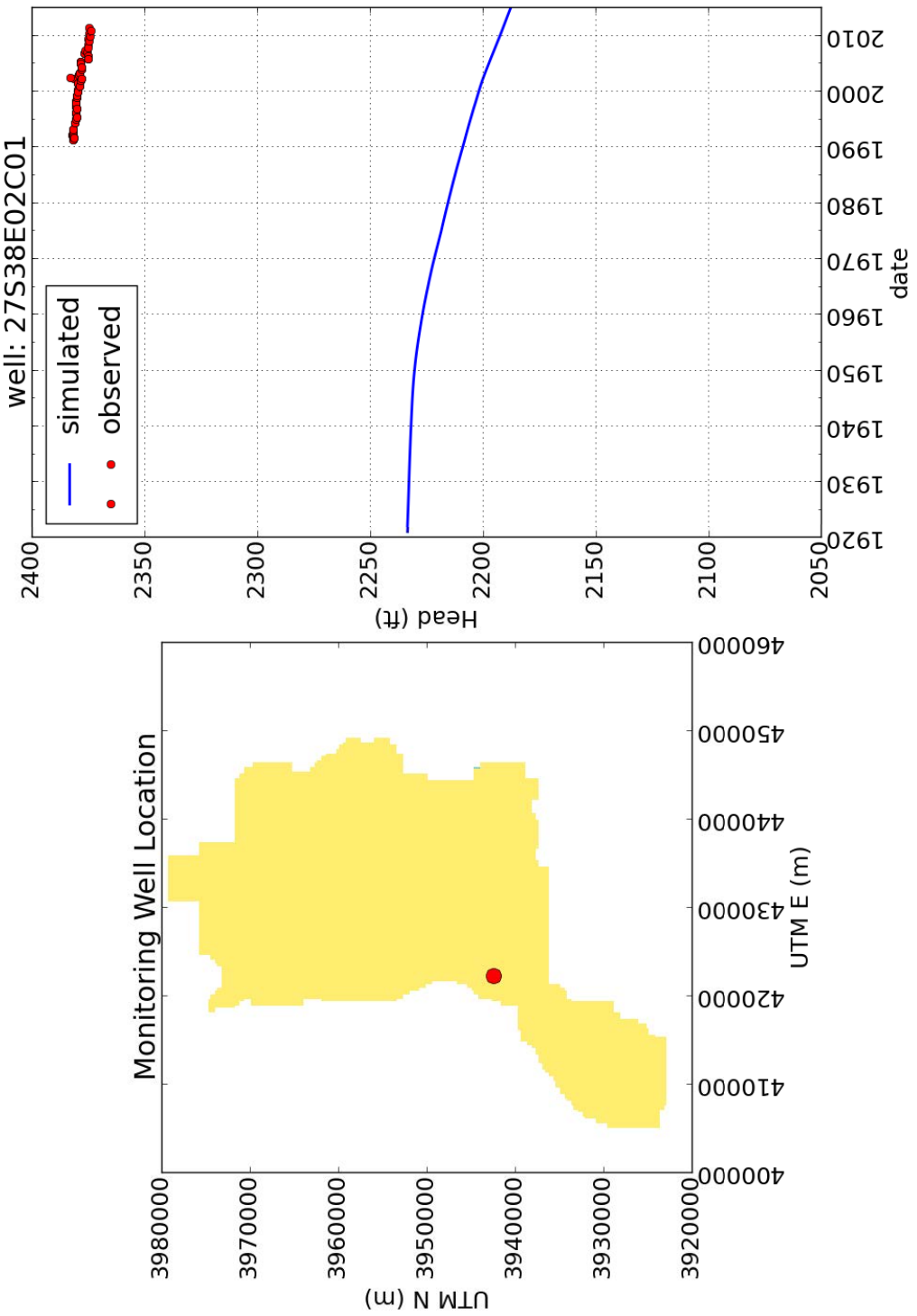
well: 27S38E02C01
simulated
observed
Head (ft)
date
2400
2350
2300
2250
2200
2150
2100
2050
1920
1930
1940
1950
1960
1970
1980
1990
2000
2010
Monitoring Well Location
UTM N (m)
UTM E (m)
3980000
3970000
3960000
3950000
3940000
3930000
3920000
400000
410000
420000
430000
440000
450000
460000

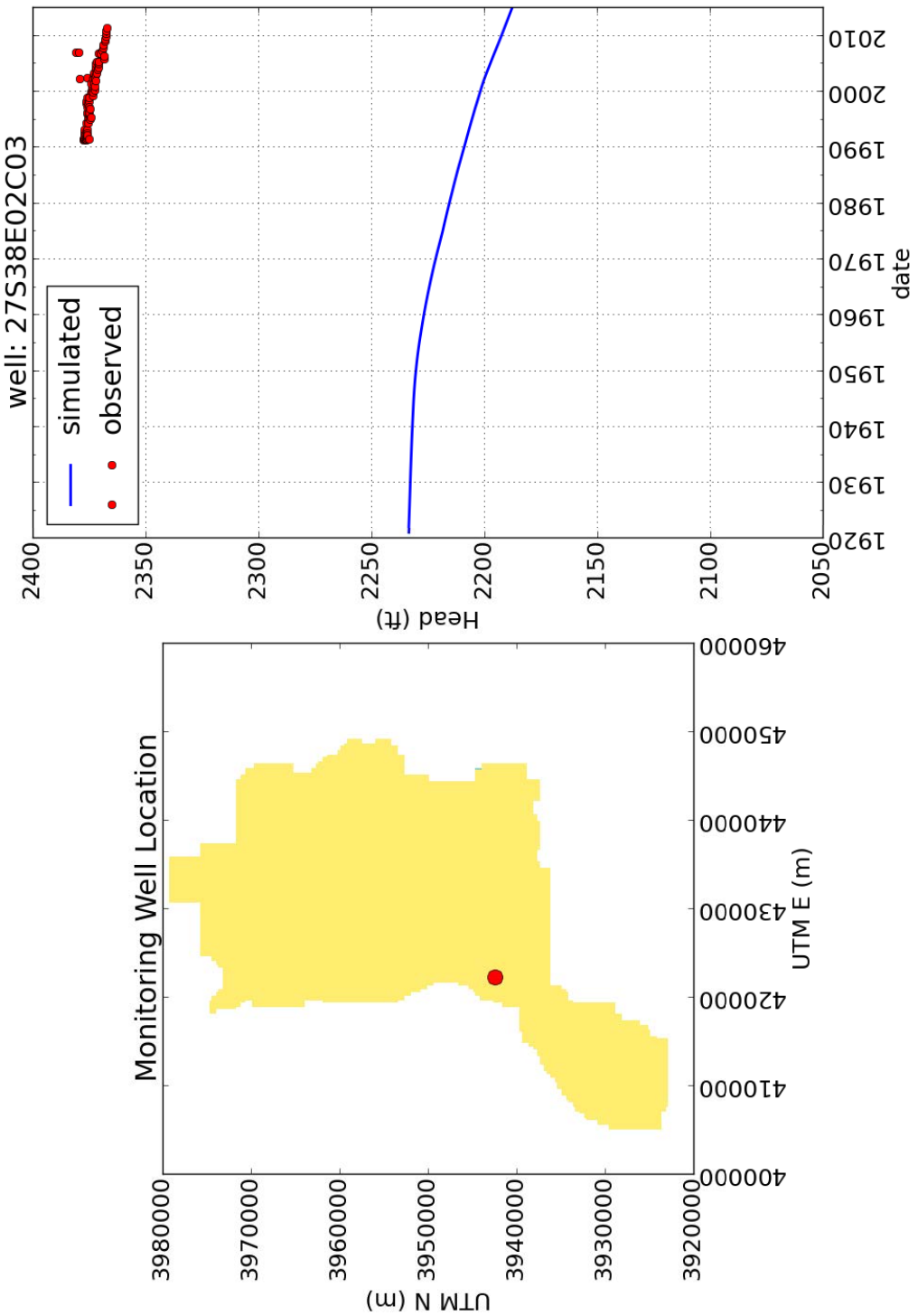
well: 27S38E02C03
simulated
observed
Head (ft)
date
2400
2350
2300
2250
2200
2150
2100
2050
1920
1930
1940
1950
1960
1970
1980
1990
2000
2010
Monitoring Well Location
UTM N (m)
UTM E (m)
3980000
3970000
3960000
3950000
3940000
3930000
3920000
400000
410000
420000
430000
440000
450000
460000

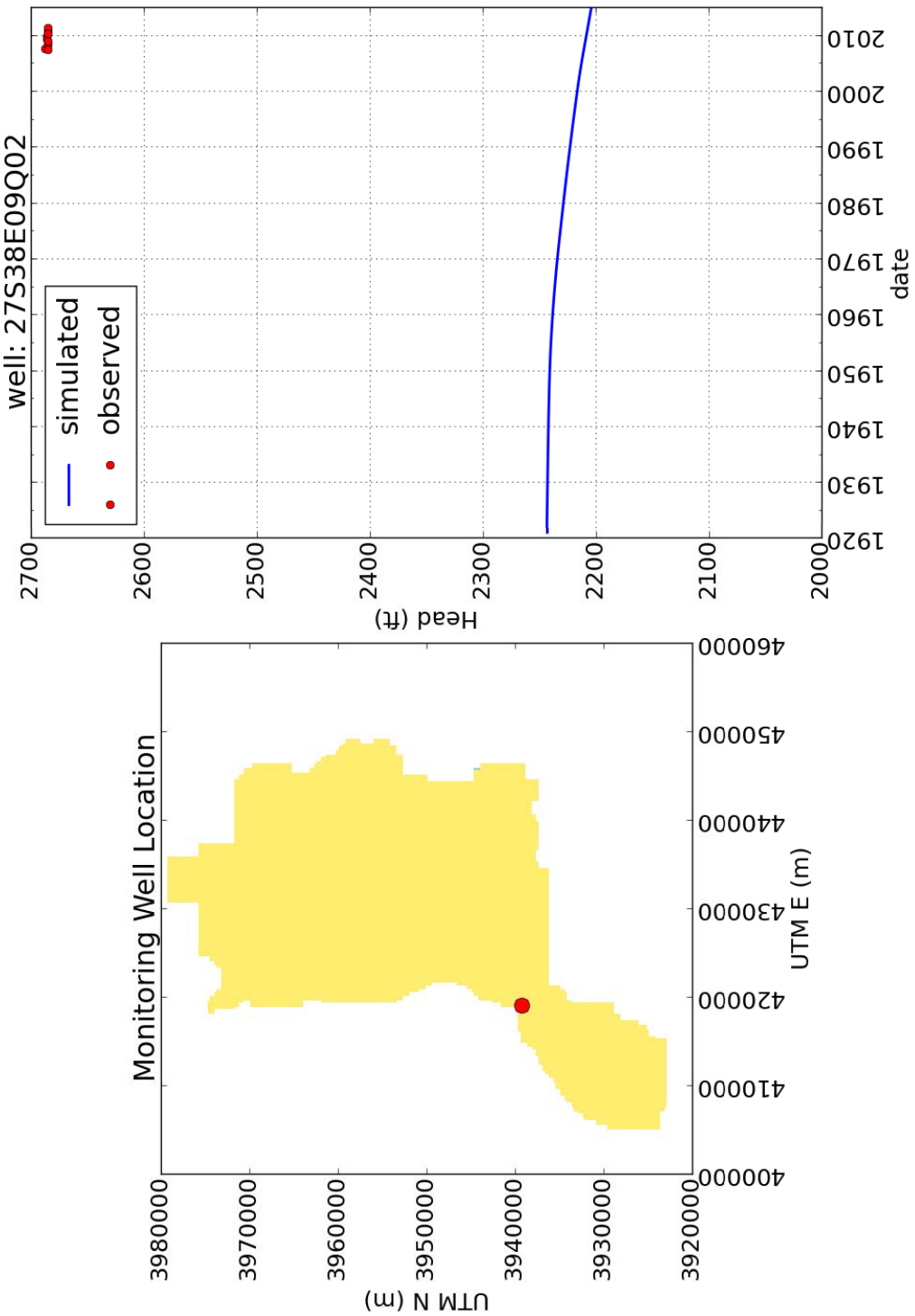
well: 27S38E09Q02
simulated
observed
Head (ft)
2700
2600
2500
2400
2300
2200
2100
2000
date
1920
1930
1940
1950
1960
1970
1980
1990
2000
2010
Monitoring Well Location
UTM N (m)
3980000
3970000
3960000
3950000
3940000
3930000
3920000
UTM E (m)
400000
410000
420000
430000
440000
450000
460000

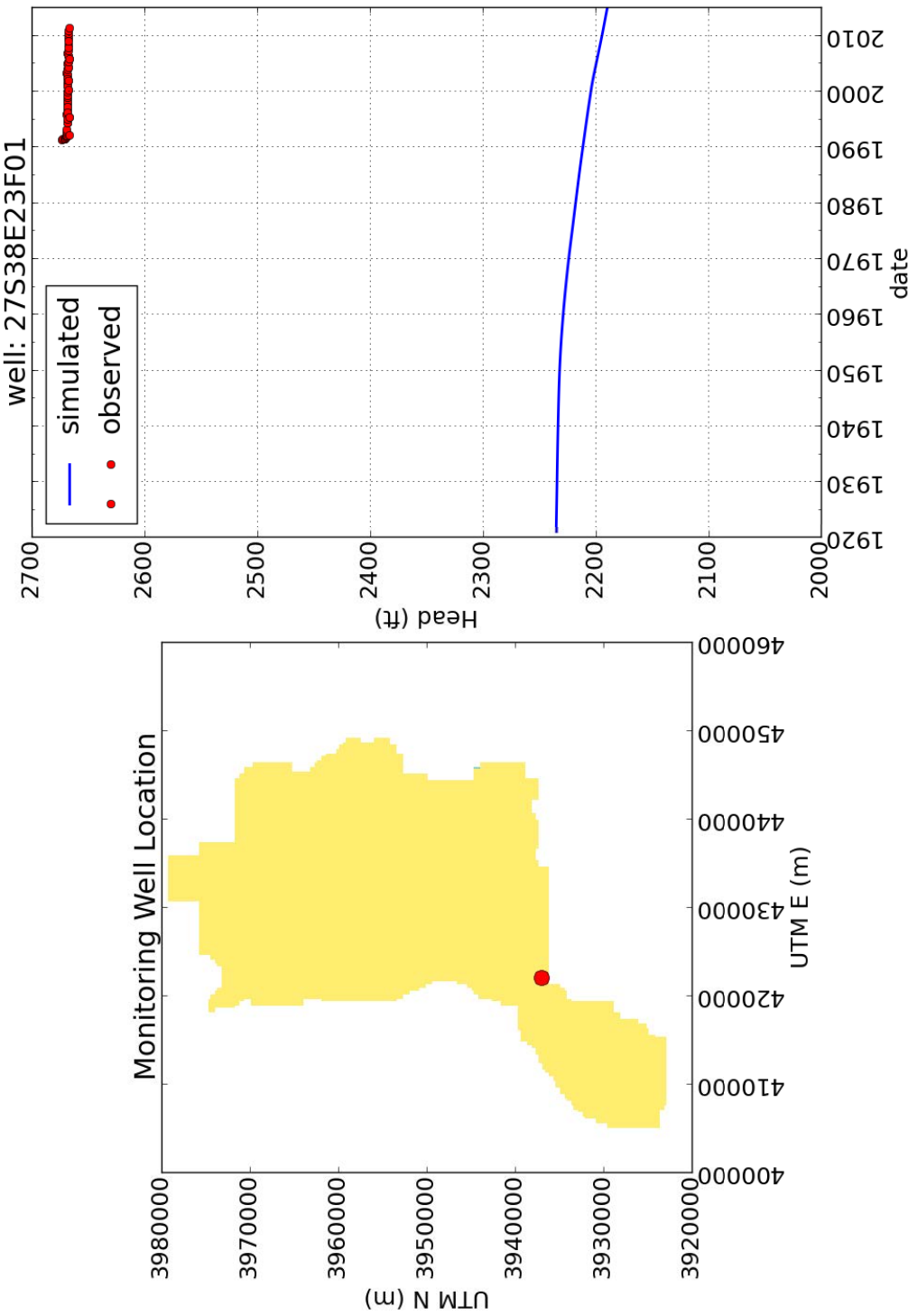
well: 27S38E23F01
simulated
observed
Head (ft)
date
2700
2600
2500
2400
2300
2200
2100
2000
1920
1930
1940
1950
1960
1970
1980
1990
2000
2010
Monitoring Well Location
UTM N (m)
UTM E (m)
3980000
3970000
3960000
3950000
3940000
3930000
3920000
400000
410000
420000
430000
440000
450000
460000

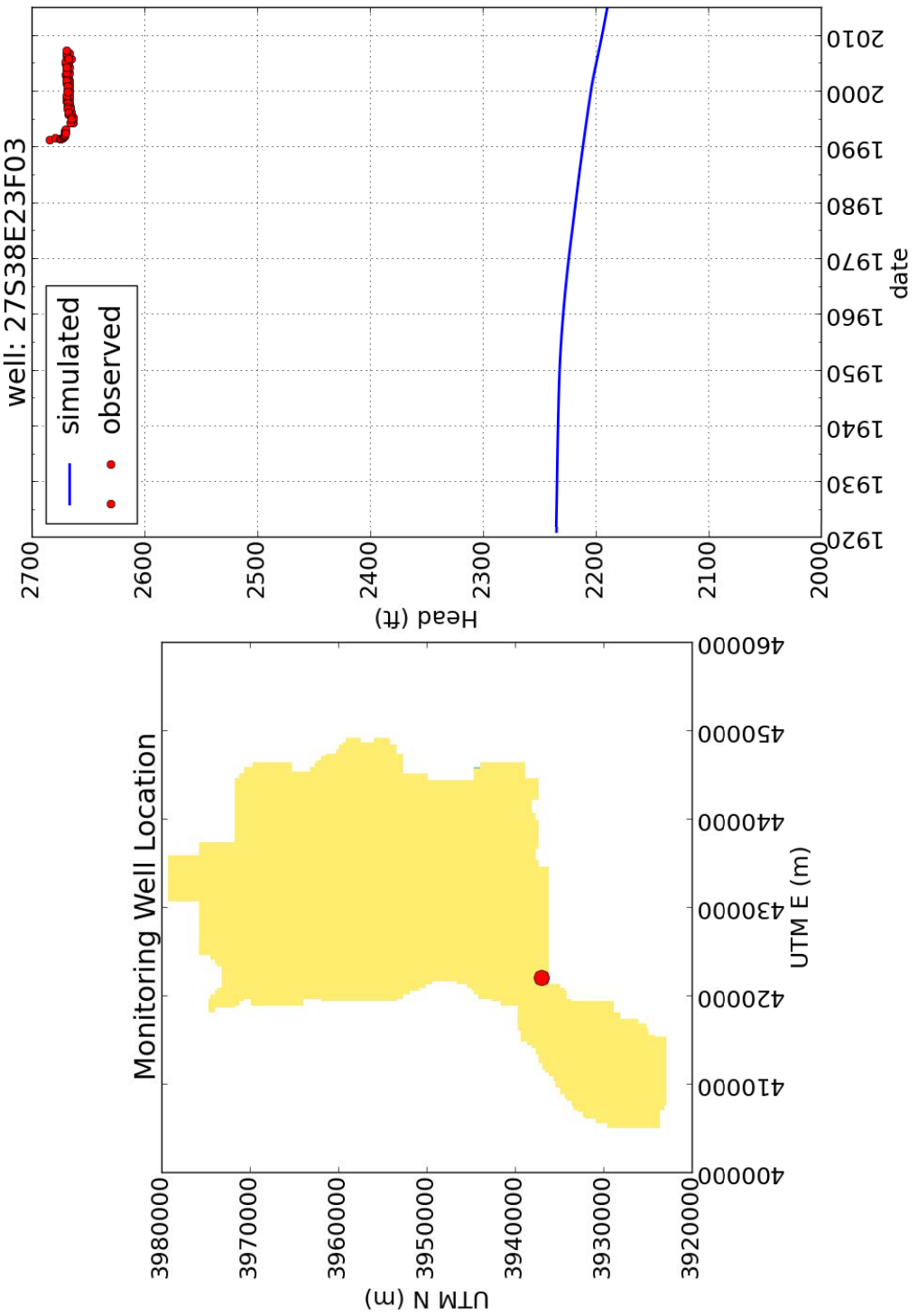
well: 27S38E23F03
simulated
observed
Head (ft)
date
2700
2600
2500
2400
2300
2200
2100
2000
1920
1930
1940
1950
1960
1970
1980
1990
2000
2010
Monitoring Well Location
UTM N (m)
UTM E (m)
3980000
3970000
3960000
3950000
3940000
3930000
3920000
400000
410000
420000
430000
440000
450000
460000

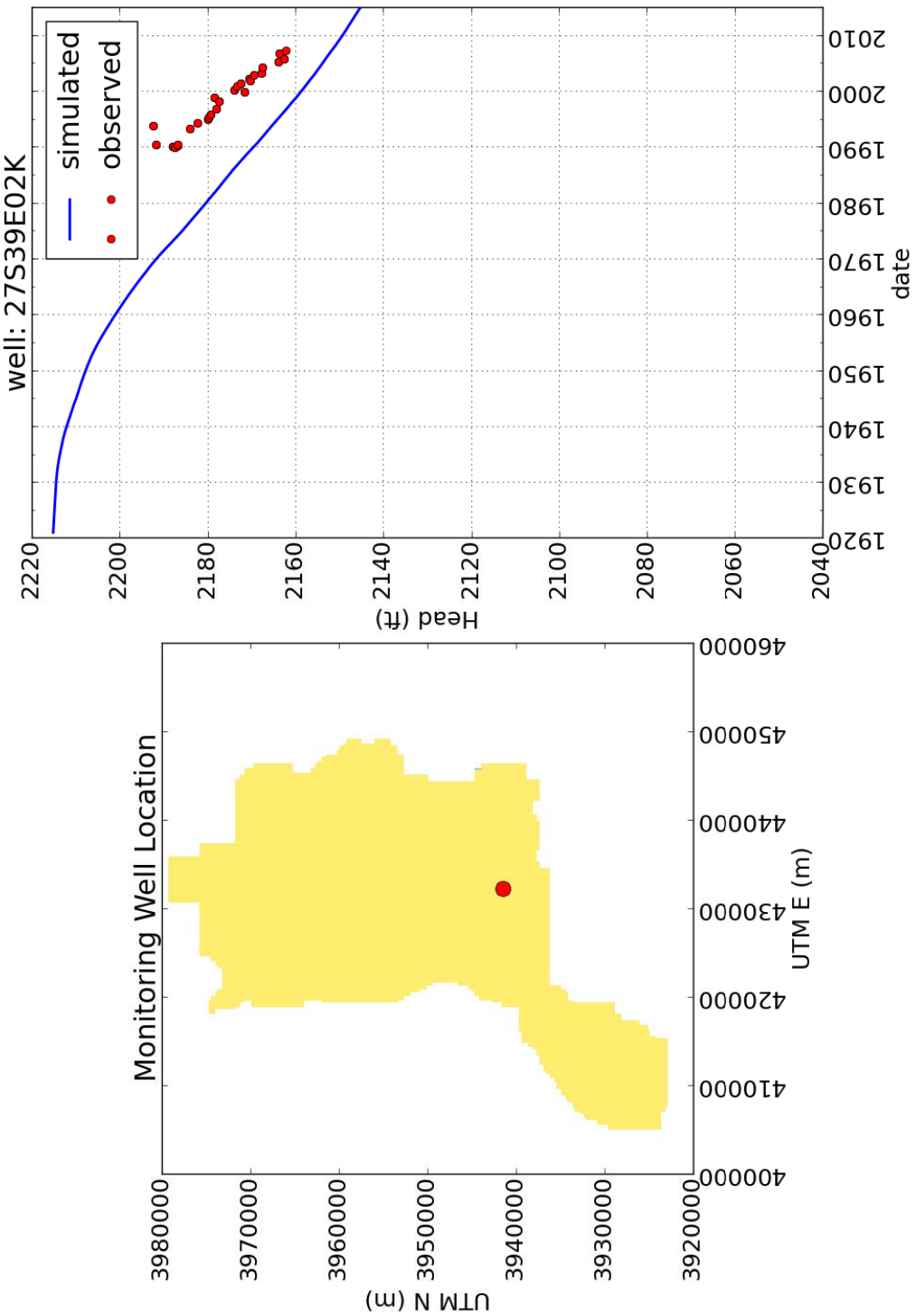
well: 27S39E02K
simulated
observed
Head (ft)
date
2220
2200
2180
2160
2140
2120
2100
2080
2060
2040
1920
1930
1940
1950
1960
1970
1980
1990
2000
2010
Monitoring Well Location
UTM N (m)
UTM E (m)
3980000
3970000
3960000
3950000
3940000
3930000
3920000
400000
410000
420000
430000
440000
450000
460000

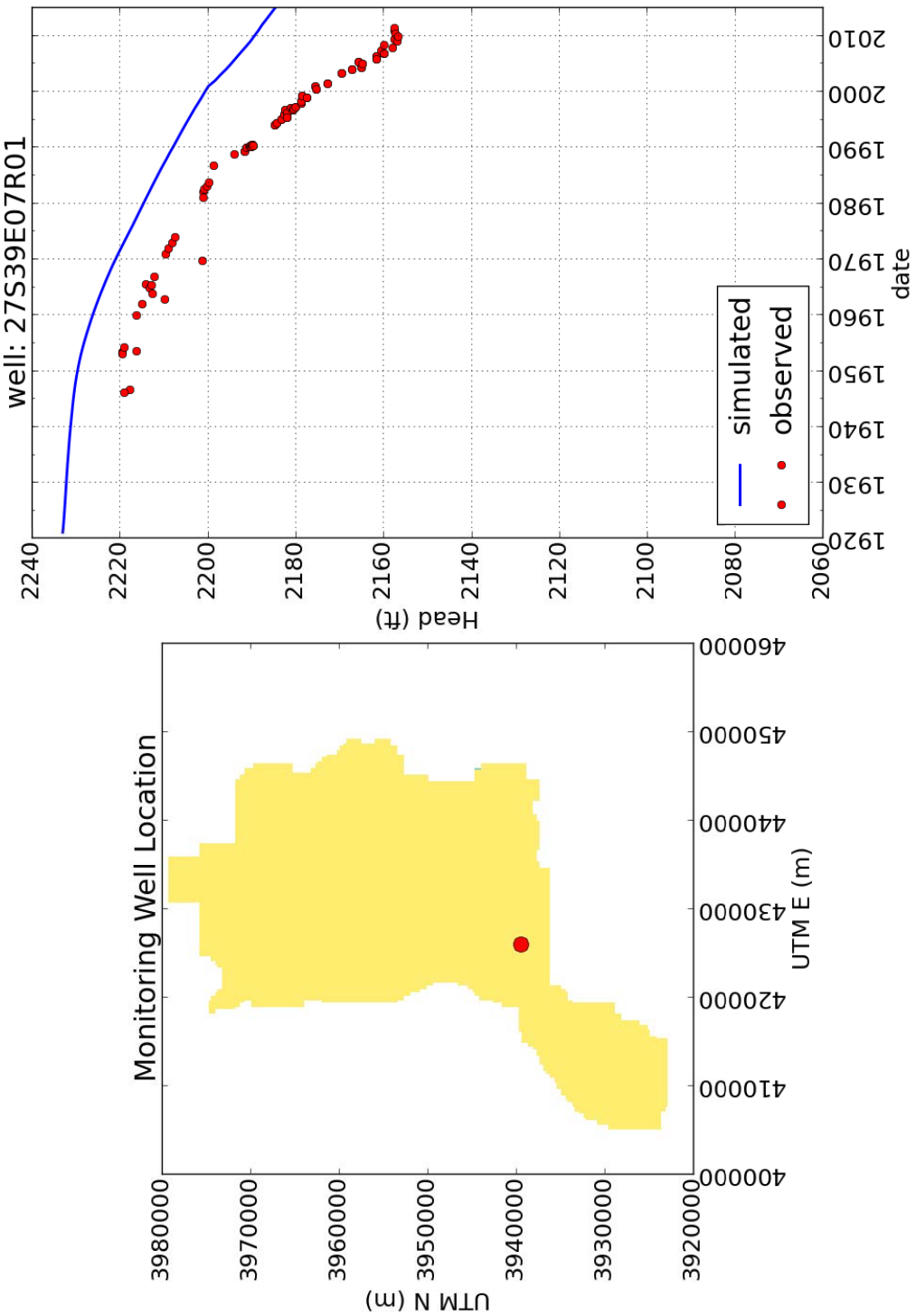
well: 27S39E07R01
Head (ft)
date
simulated
observed
Monitoring Well Location
UTM N (m)
UTM E (m)

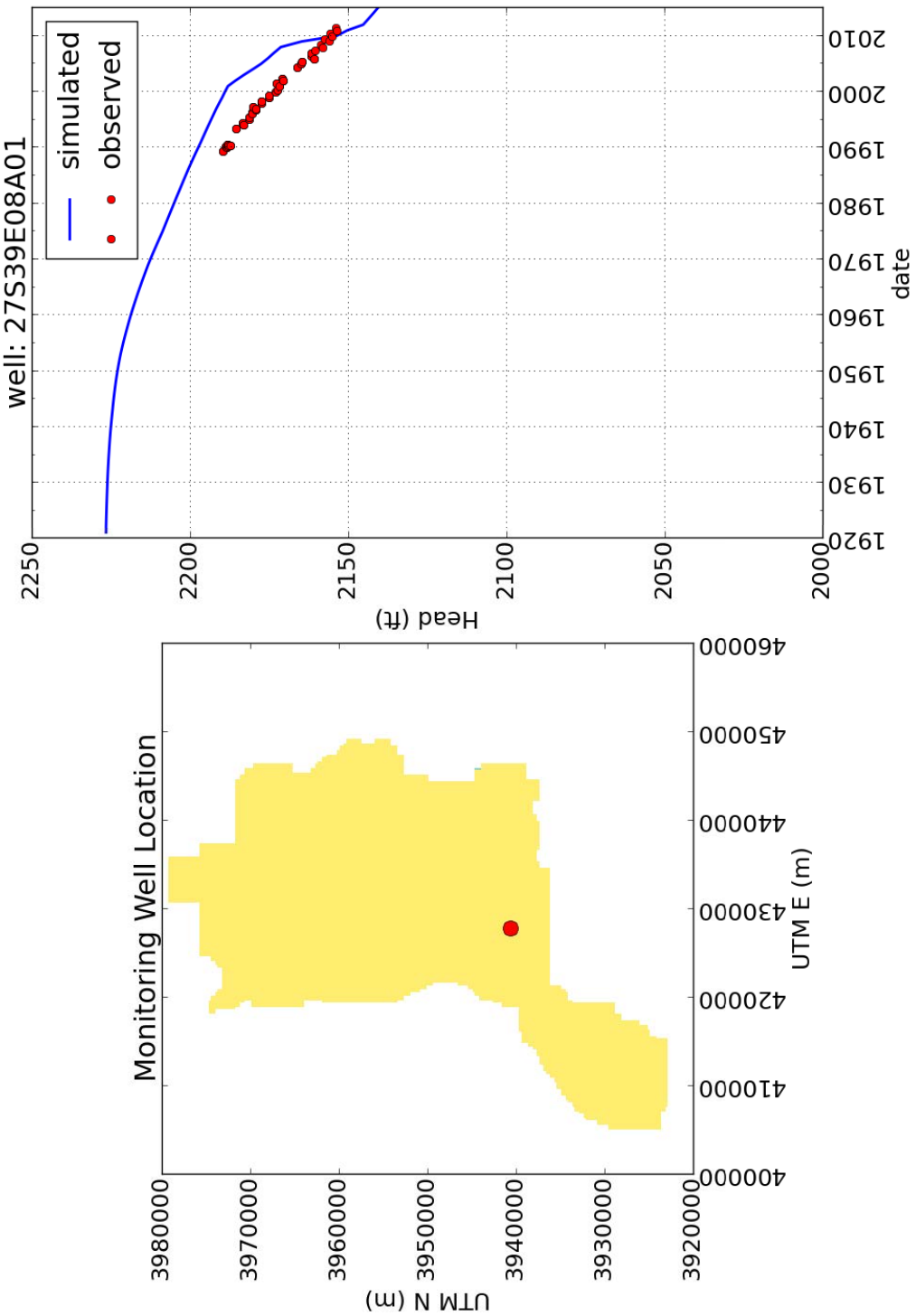
well: 27S39E08A01
simulated
observed
Head (ft)
date
2250
2200
2150
2100
2050
2000
1920
1930
1940
1950
1960
1970
1980
1990
2000
2010
Monitoring Well Location
UTM N (m)
UTM E (m)
3980000
3970000
3960000
3950000
3940000
3930000
3920000
400000
410000
420000
430000
440000
450000
460000

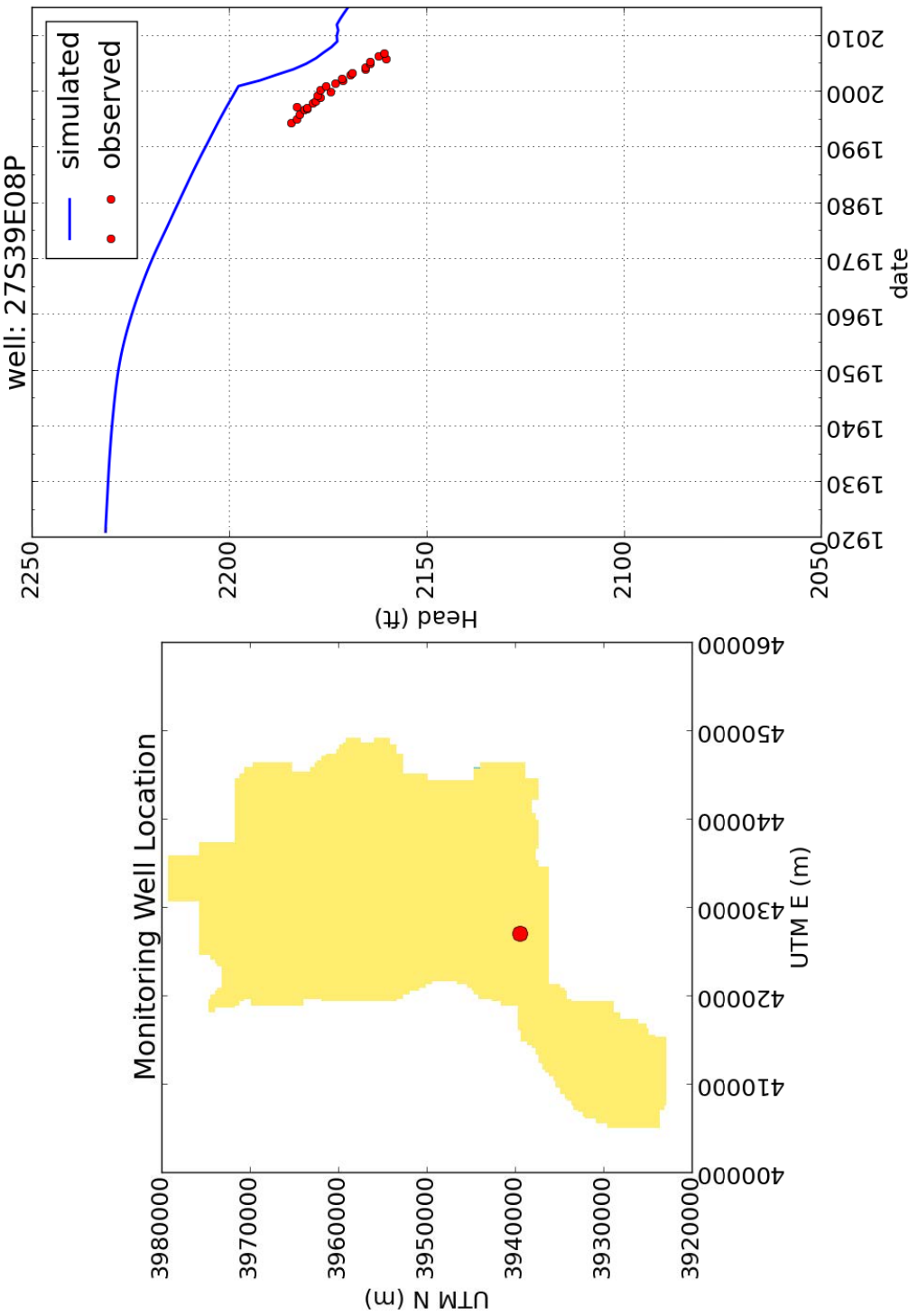
well: 27S39E08P
simulated
observed
Head (ft)
2250
2200
2150
2100
2050
date
1920
1930
1940
1950
1960
1970
1980
1990
2000
2010
Monitoring Well Location
UTM N (m)
3980000
3970000
3960000
3950000
3940000
3930000
3920000
UTM E (m)
400000
410000
420000
430000
440000
450000
460000

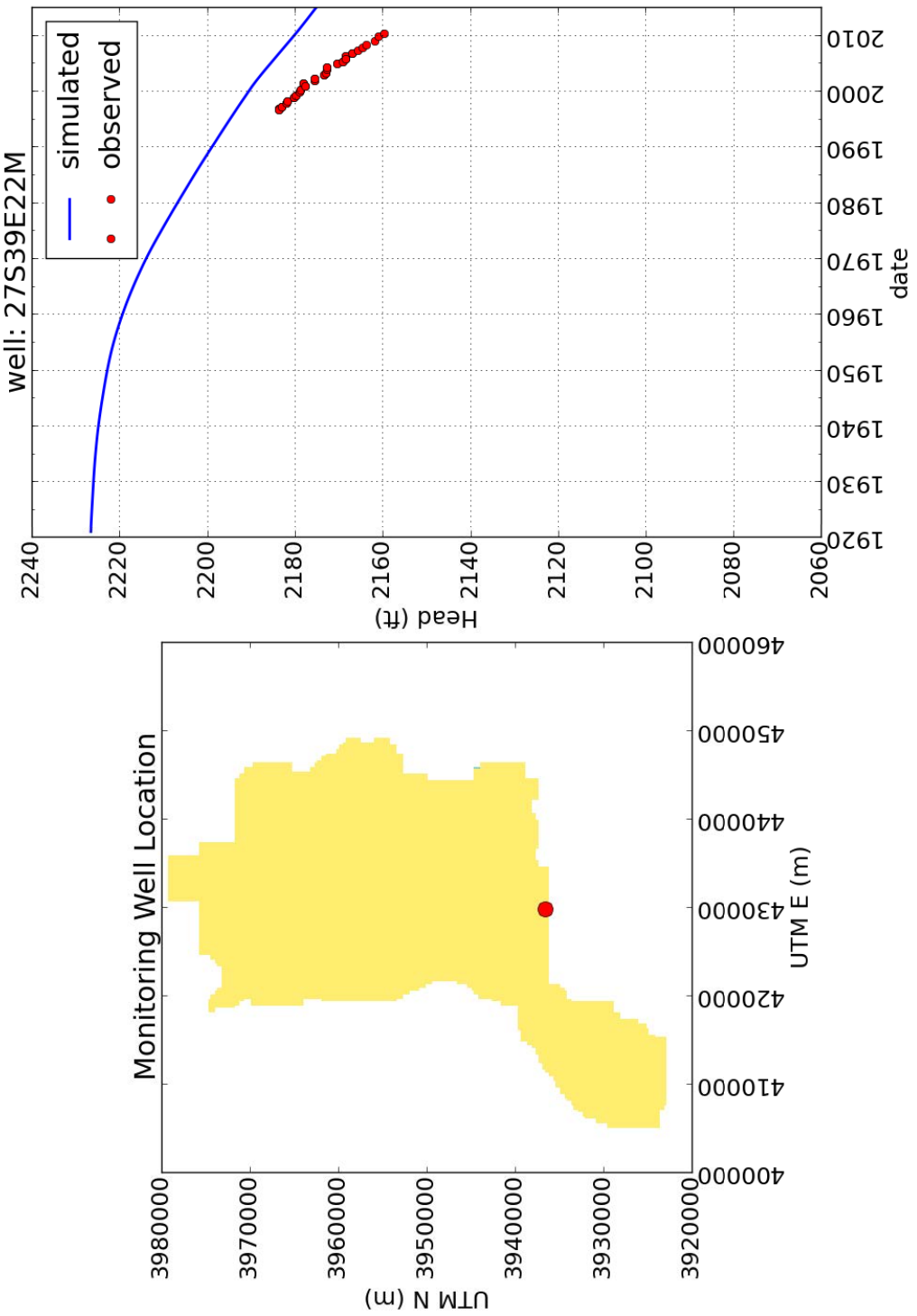
well: 27S39E22M
simulated
observed
Head (ft)
date
2240
2220
2200
2180
2160
2140
2120
2100
2080
2060
1920
1930
1940
1950
1960
1970
1980
1990
2000
2010
Monitoring Well Location
UTM N (m)
UTM E (m)
3980000
3970000
3960000
3950000
3940000
3930000
3920000
400000
410000
420000
430000
440000
450000
460000

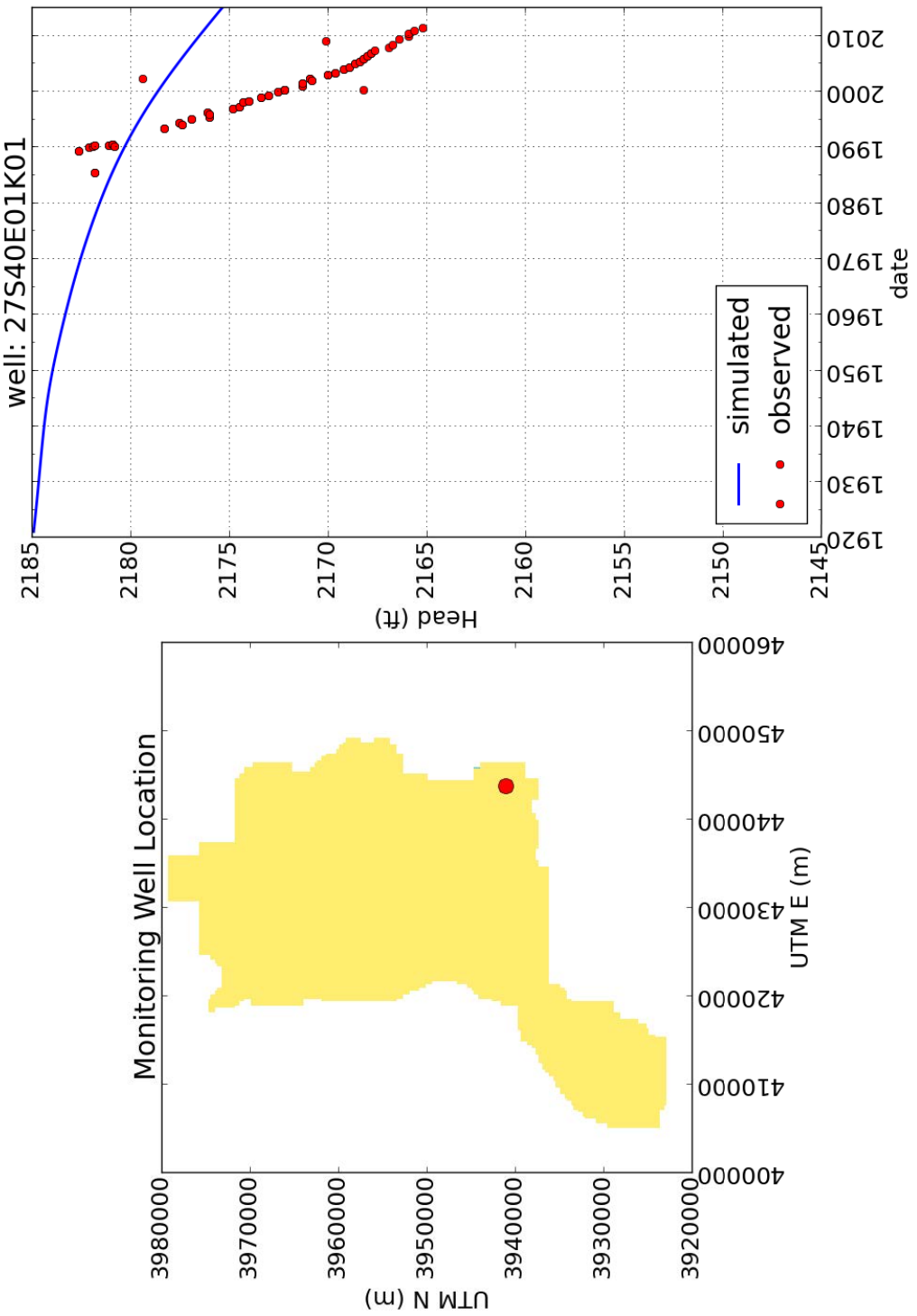
well: 27S40E01K01
Head (ft)
2185
2180
2175
2170
2165
2160
2155
2150
2145
1920
1930
1940
1950
1960
1970
1980
1990
2000
2010
date
simulated
observed
Monitoring Well Location
UTM N (m)
3980000
3970000
3960000
3950000
3940000
3930000
3920000
460000
450000
440000
430000
420000
410000
400000
UTM E (m)

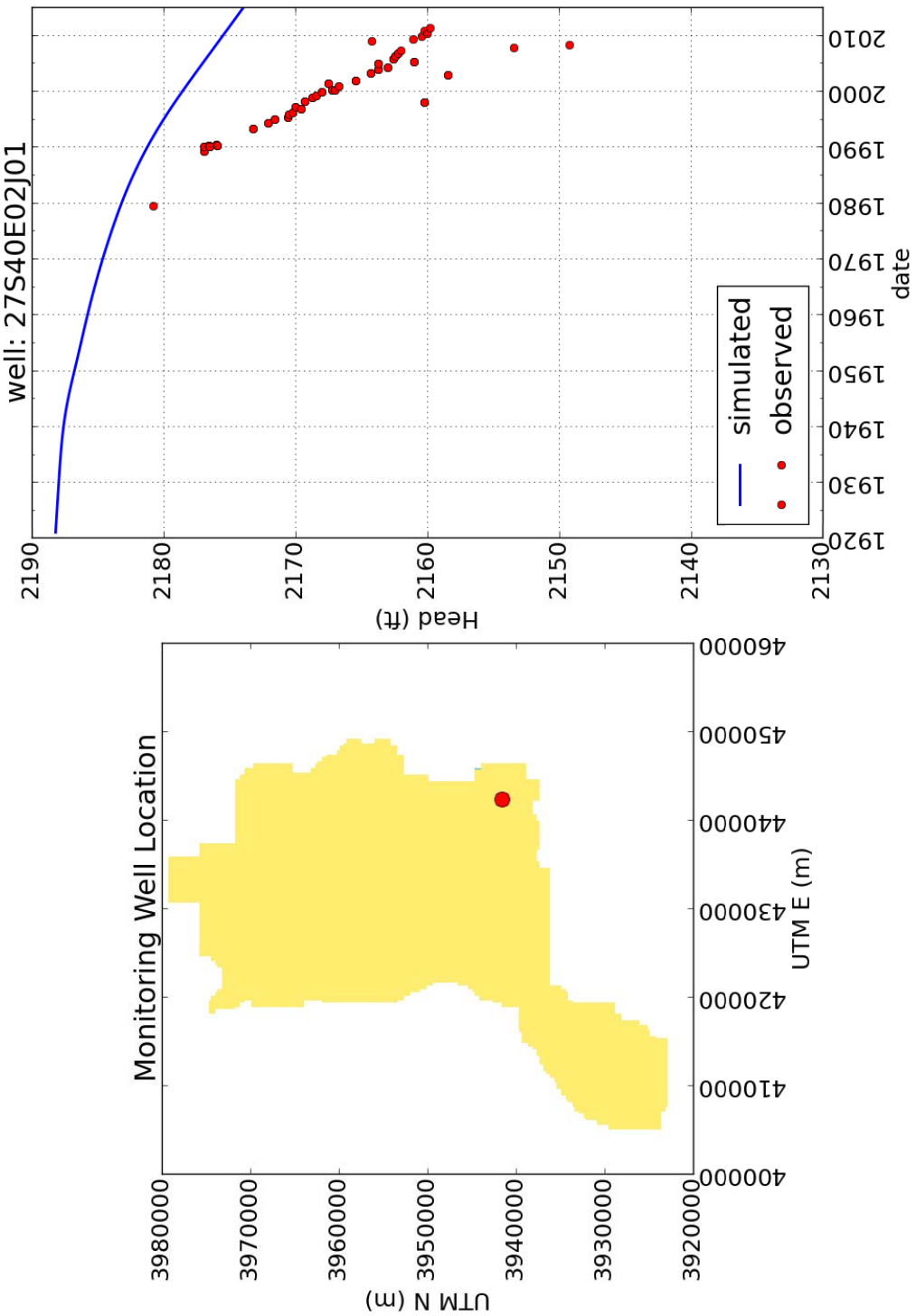
well: 27S40E02J01
Head (ft)
2190
2180
2170
2160
2150
2140
2130
date
1920
1930
1940
1950
1960
1970
1980
1990
2000
2010
simulated
observed
Monitoring Well Location
UTM N (m)
3980000
3970000
3960000
3950000
3940000
3930000
3920000
UTM E (m)
400000
410000
420000
430000
440000
450000
460000

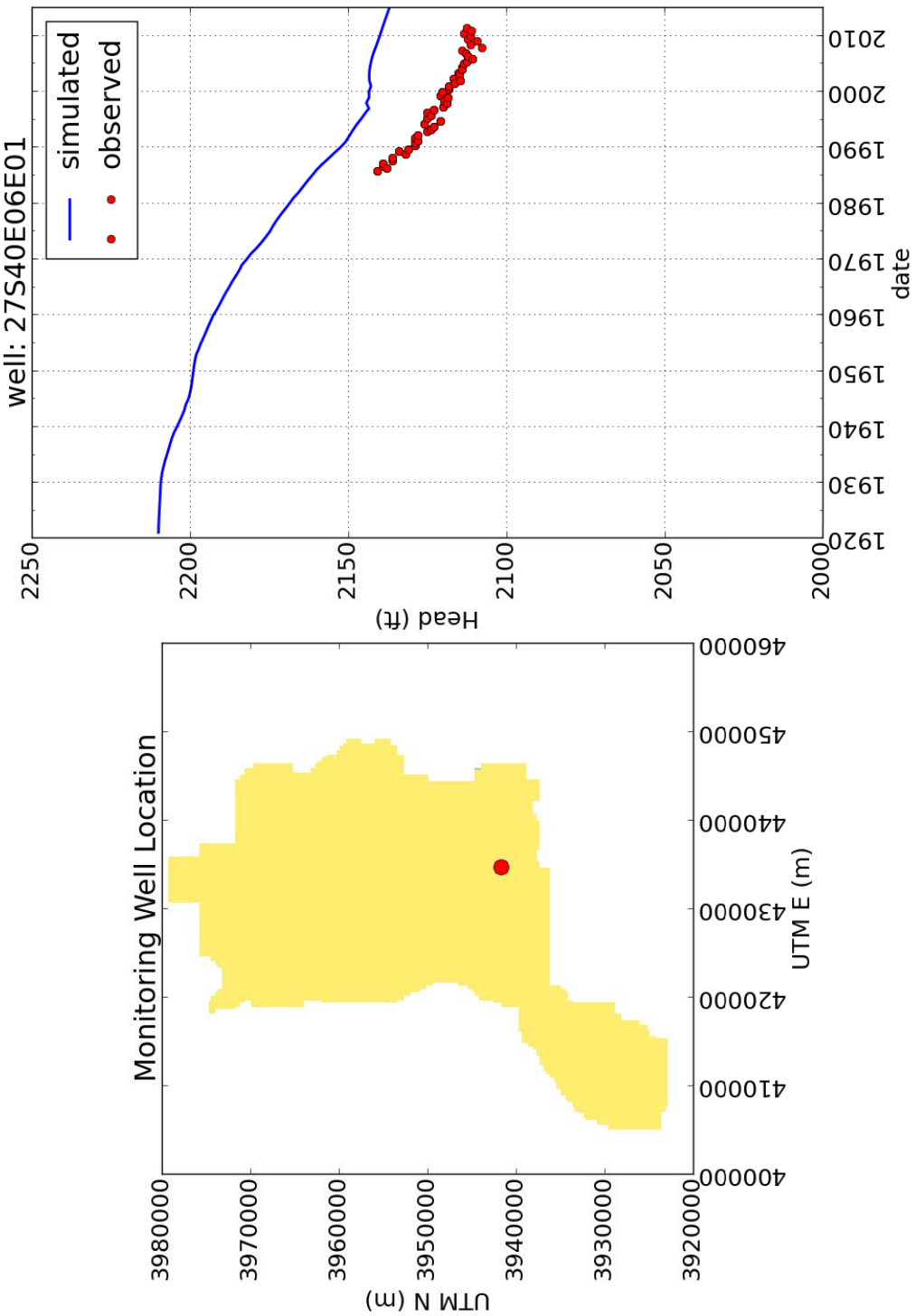
well: 27S40E06E01
simulated
observed
Head (ft)
date
2250
2200
2150
2100
2050
2000
1920
1930
1940
1950
1960
1970
1980
1990
2000
2010
Monitoring Well Location
UTM N (m)
UTM E (m)
3980000
3970000
3960000
3950000
3940000
3930000
3920000
400000
410000
420000
430000
440000
450000
460000

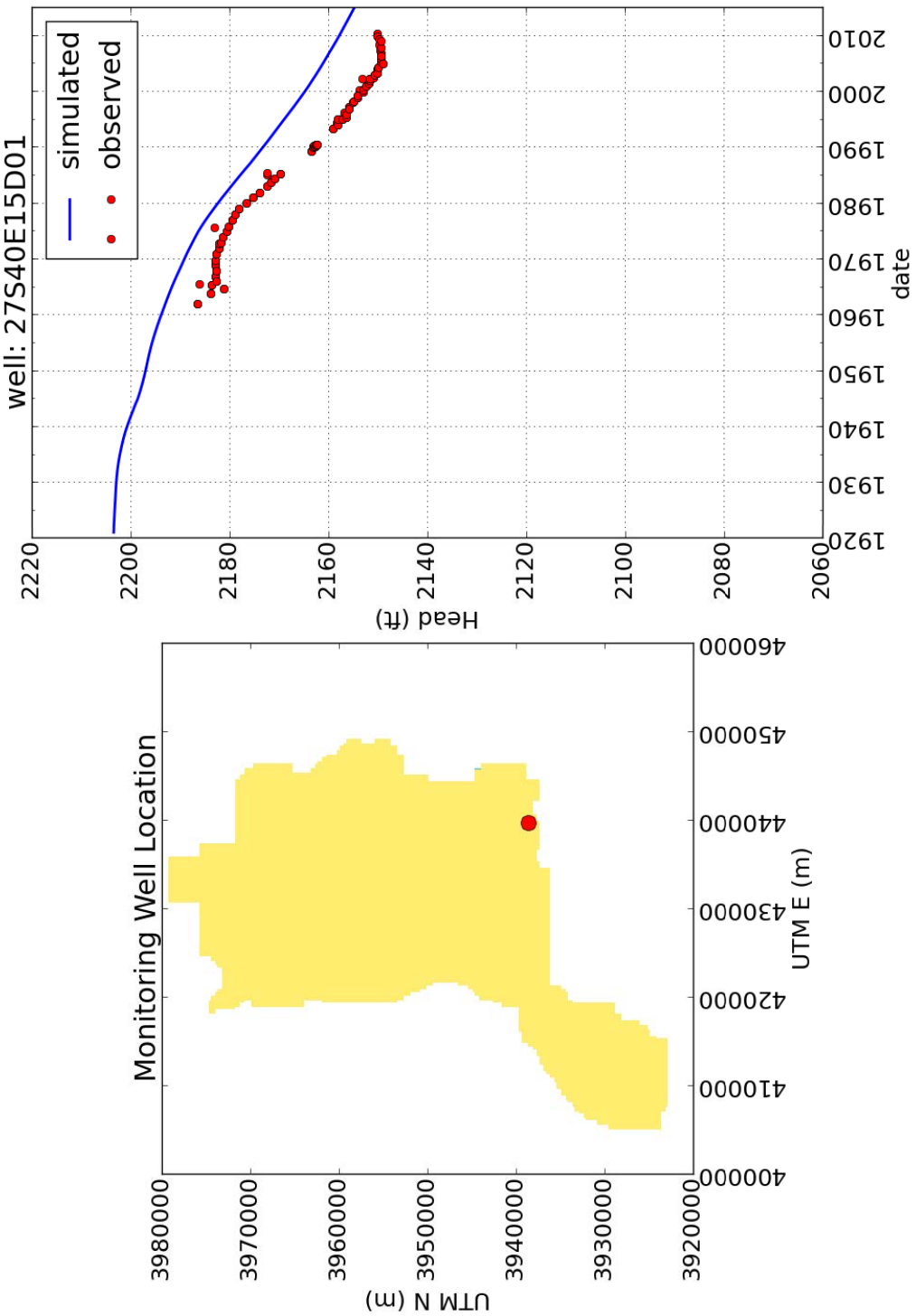
well: 27S40E15D01
simulated
observed
Head (ft)
date
2220
2200
2180
2160
2140
2120
2100
2080
2060
1920
1930
1940
1950
1960
1970
1980
1990
2000
2010
Monitoring Well Location
UTM N (m)
UTM E (m)
3980000
3970000
3960000
3950000
3940000
3930000
3920000
460000
450000
440000
430000
420000
410000
400000

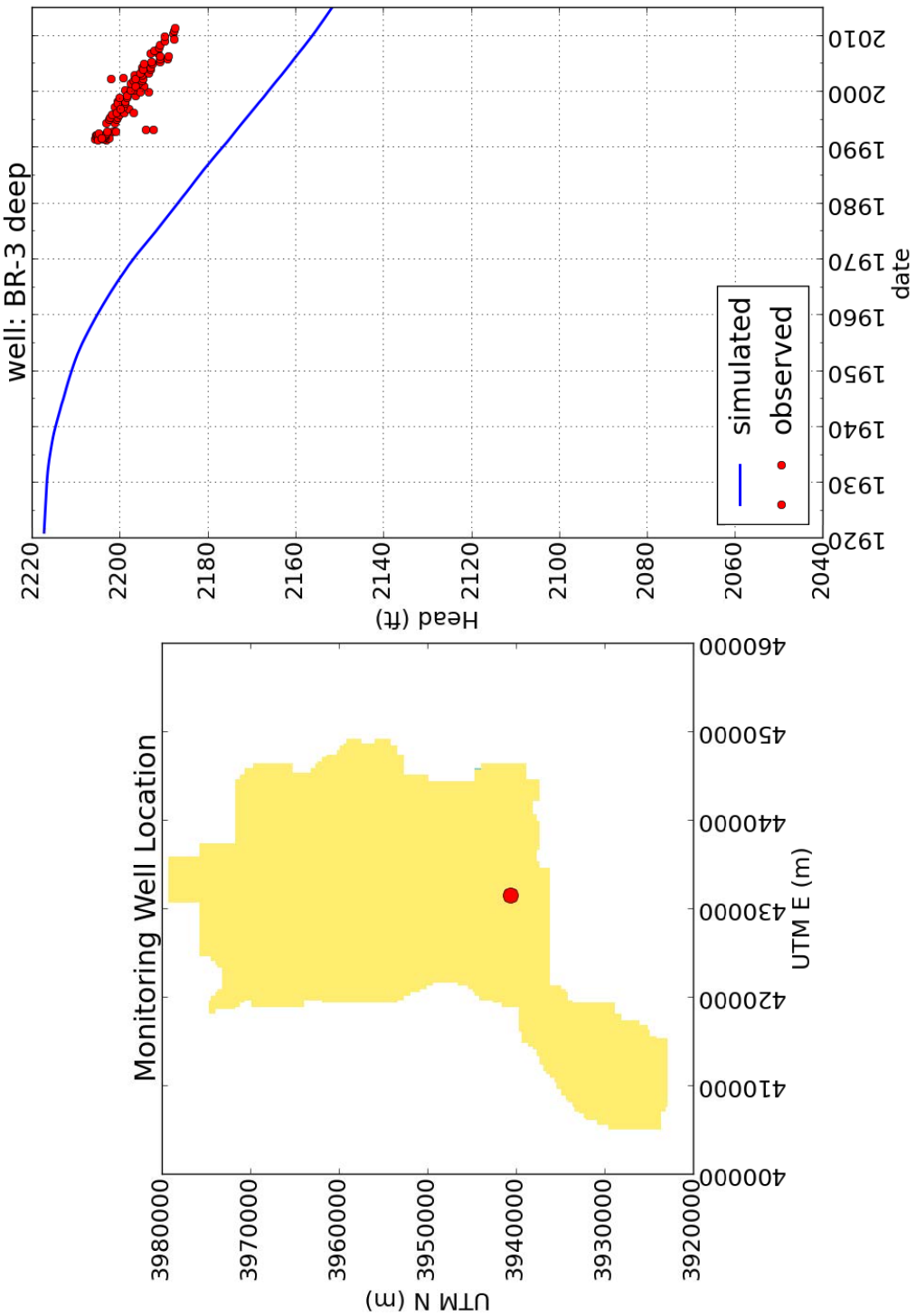
well: BR-3 deep
Head (ft)
2220
2200
2180
2160
2140
2120
2100
2080
2060
2040
date
1920
1930
1940
1950
1960
1970
1980
1990
2000
2010
simulated
observed
Monitoring Well Location
UTM N (m)
3980000
3970000
3960000
3950000
3940000
3930000
3920000
UTM E (m)
400000
410000
420000
430000
440000
450000
460000

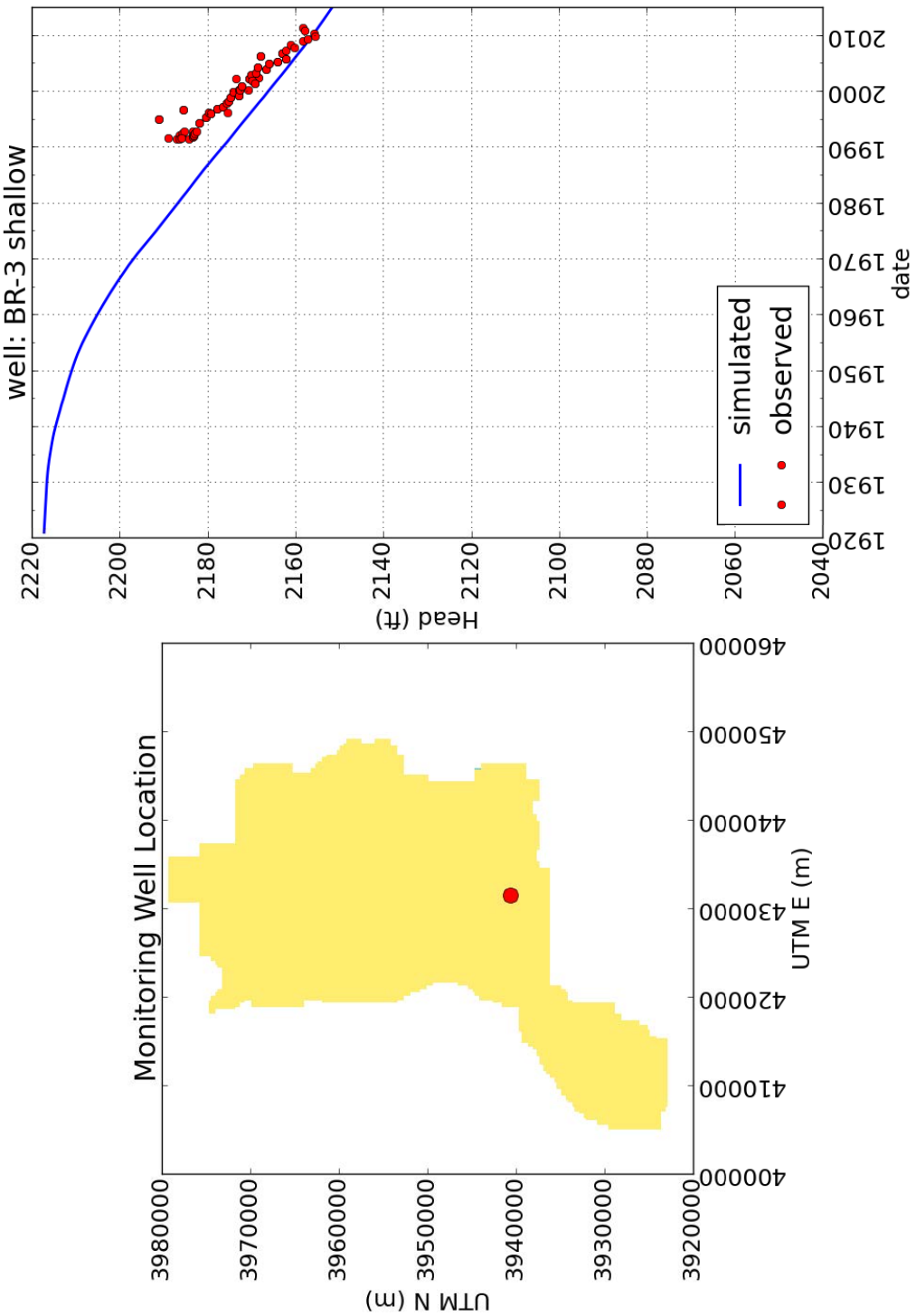
well: BR-3 shallow
Head (ft)
2220
2200
2180
2160
2140
2120
2100
2080
2060
2040
date
1920
1930
1940
1950
1960
1970
1980
1990
2000
2010
simulated
observed
Monitoring Well Location
UTM N (m)
3980000
3970000
3960000
3950000
3940000
3930000
3920000
UTM E (m)
400000
410000
420000
430000
440000
450000
460000

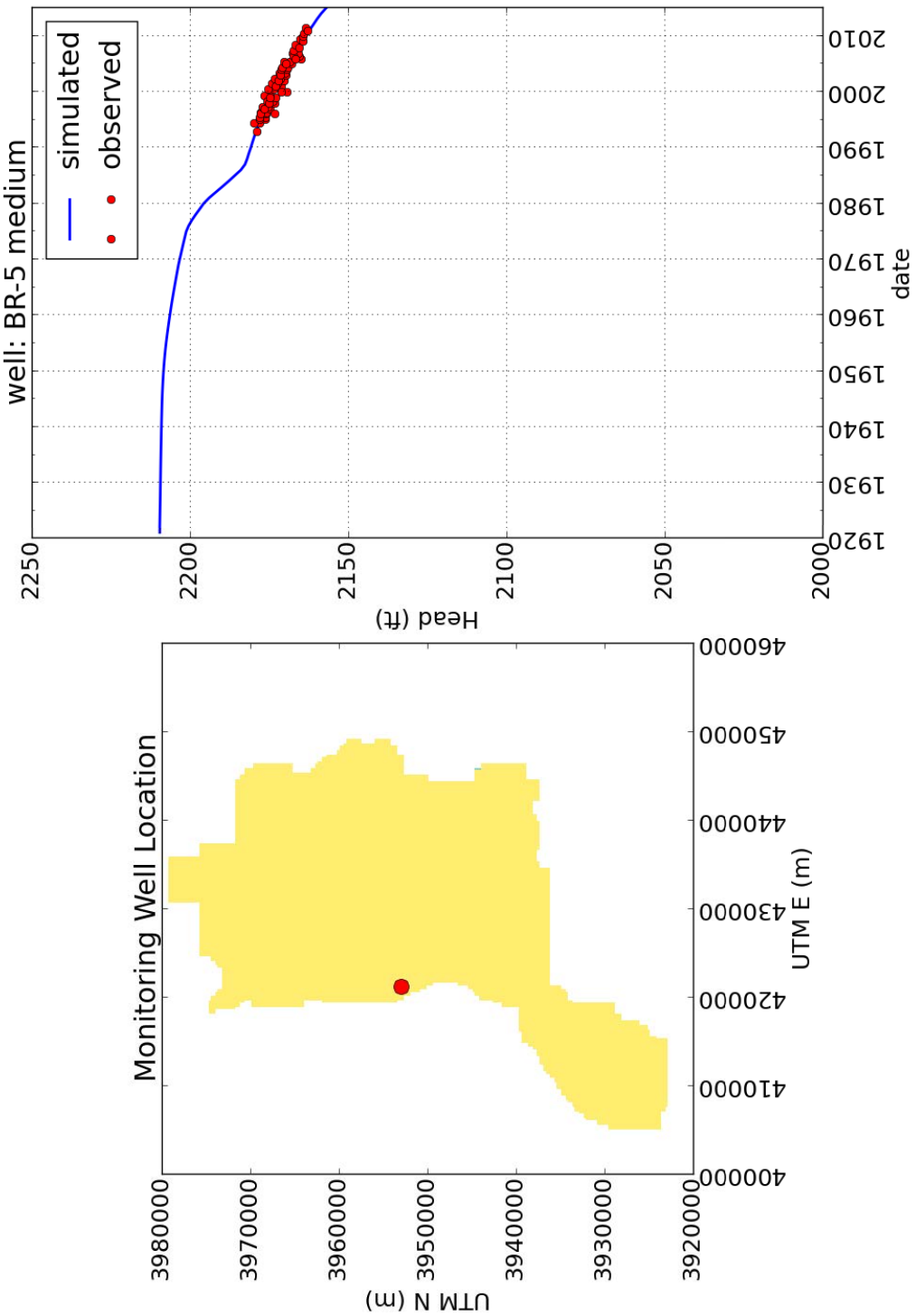
well: BR-5 medium
simulated
observed
Head (ft)
2250
2200
2150
2100
2050
2000
date
1920
1930
1940
1950
1960
1970
1980
1990
2000
2010
Monitoring Well Location
UTM N (m)
3980000
3970000
3960000
3950000
3940000
3930000
3920000
UTM E (m)
400000
410000
420000
430000
440000
450000
460000

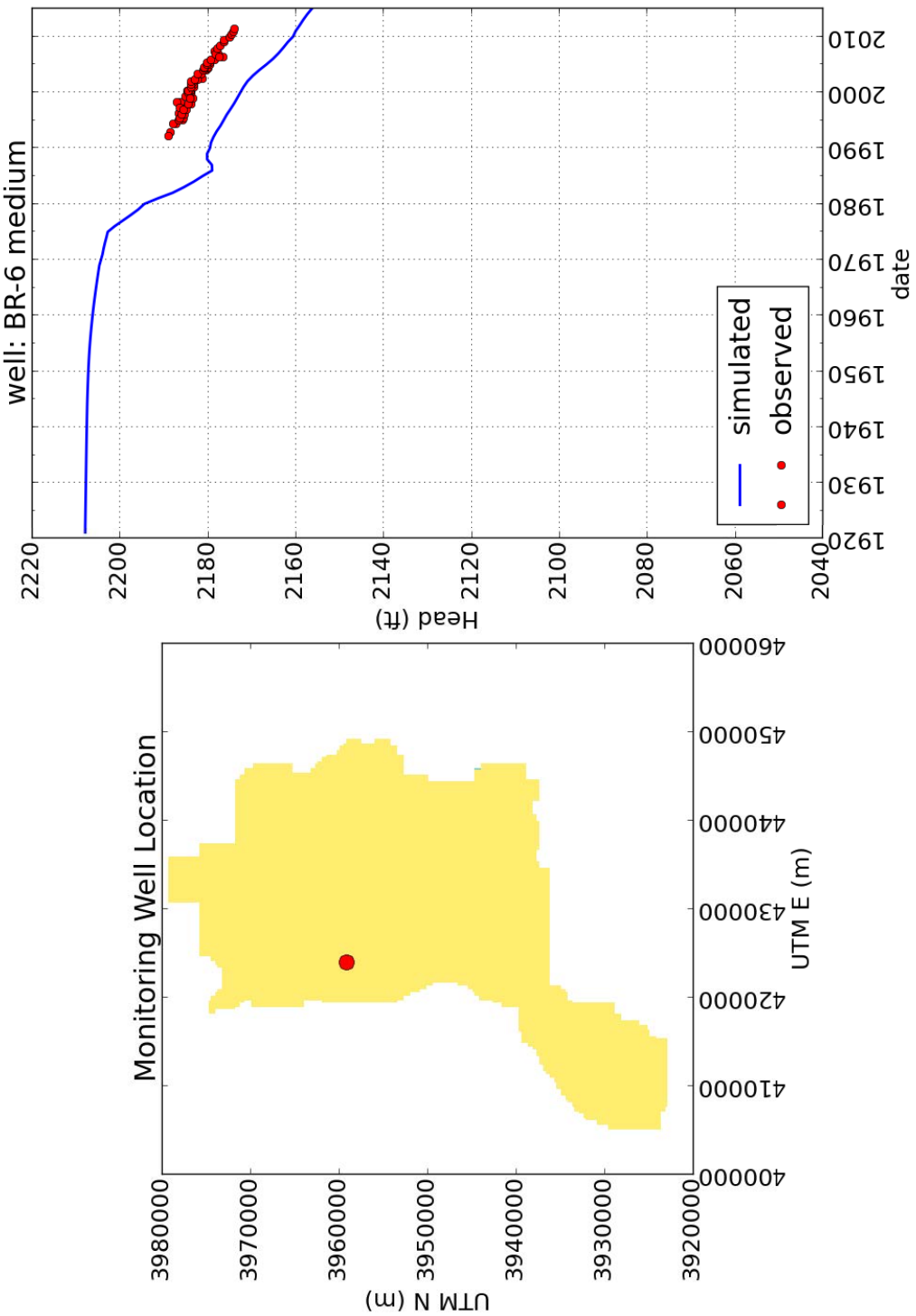
well: BR-6 medium
Head (ft)
2220
2200
2180
2160
2140
2120
2100
2080
2060
2040
date
1920
1930
1940
1950
1960
1970
1980
1990
2000
2010
simulated
observed
Monitoring Well Location
UTM N (m)
3980000
3970000
3960000
3950000
3940000
3930000
3920000
UTM E (m)
400000
410000
420000
430000
440000
450000
460000

This page intentionally left blank.

APPENDIX B: INSAR ANALYSIS OF AQUIFER-SYSTEM RESPONSE TO PUMPING IN INDIAN WELLS VALLEY, CALIFORNIA

InSAR Analysis of Aquifer-System Response to Pumping in the Indian Wells Valley, California

Indian Wells Valley, Kern County, California

Final Technical Report To

The Desert Research Institute Attn: Gregory Pohll

Kurt Katzenstein, Ph. D.
Department of Geology and Geological Engineering South Dakota School of Mines and Technology

January 21, 2015

EXECUTIVE SUMMARY

This report documents the results of an Interferometric Synthetic Aperture Radar (InSAR) study that created 92 interferograms covering the time periods of June 1, 1992 – November 30, 2000, November 24, 2005 – October 14, 2010, and March 16, 2012 – October 8, 2014 for the Indian Wells Valley, CA. The spatial distribution of deformation suggests that it is related to groundwater production in the valley. In some cases, deformation appears to be controlled by existing structure (faults). For each of the time periods evaluated, the best interferograms were stacked (summed), in order to provide an estimate of the cumulative deformation that occurred during each period. When sufficient data were available, multiple stacks covering the same time periods were evaluated in order to minimize noise. Analysis of the stacked interferograms suggests maximum deformation rates of approximately 2.7 – 3.3 mm/yr.

BACKGROUND AND PURPOSE

This study originated through discussions with Dr. Gregory Pohll, Research Professor of Hydrology at the Desert Research Institute (DRI), in December 2013. Dr. Pohll expressed interest in utilizing Interferometric Synthetic Aperture Radar (InSAR) to better understand the impact that groundwater pumping was having on the alluvial aquifer system within the Indian Wells Valley (IWV), CA. In particular, there is interest in investigating the impact that pumping associated with recent pistachio orchard development in the western part of the IWV since 2012. These data would be utilized in calibrating a new groundwater model for the IWV. Similar InSAR studies (such as Amelung and others, 1999, Buckley, 2000 and Katzenstein 2013) have confirmed the applicability of this methodology to groundwater related surface deformation in the arid western United States. This project utilizes Synthetic Aperture Radar (SAR) data from the ERS-1 and ERS-2 platform (1992 – 2000), Envisat platform (2005 – 2010) and Radarsat 2 platform (2012 – 2014). All plausible interferograms from available data were processed and the best continuous interferometric pairs from each archive were stacked (more information below) in order to evaluate cumulative deformation during each of the three time periods studied.

APPROACH

The spaceborne Synthetic Aperture Radar (SAR) data utilized for this study were acquired by the European Space Agency's (ESA) ERS-1, ERS-2 and Envisat satellites as well as the Canadian Radarsat-2 satellite operated by MDA Geospatial Services International. The ERS-1 and ERS-2 data coverage for the IWV spans from June 1, 1992 – November 30, 2000 (last viable scene prior to ERS-2 stability gyroscope failure). Envisat data cover from November 24, 2005 – October 14, 2010. The three Radarsat-2 scenes utilized in this study cover from March 16, 2012 – October 8, 2014.

The ESA radar data were obtained from the WInSAR archive operated by UNAVCO, a federally funded clearing house for space-platform-based research. Figure 1 details the areal extent of the radar frames utilized from each platform. The data utilized from Radarsat-2 does not cover the entire study area because during the dates of acquisition, another client was operating the satellite in a different mode and data for this study could not be acquired concurrently. All products shown later in this report are cropped to show the area of interest.

ERS-1, ERS-2 and Envisat data were processed using the Repeat Orbit Interferometry Package (ROI_Pac) Version 3.0.1 developed by the NASA Jet Propulsion Laboratory. The Radarsat-2 data were processed using the Gamma software package developed by Gamma Remote Sensing. Scene pairs were selected based on two important parameters:

- Perpendicular Baseline Separation: This represents the perpendicular distance (along satellite track) between the two image acquisitions of interest. This value needs to be less than about 250m (ideally less than 100 m).

- Date of Acquisition: In general, shorter time periods will have better coherence (less data dropout). For this study, one year time periods were studied whenever possible; however, due to lack of data and/or lack of data that satisfy the perpendicular baseline separation.

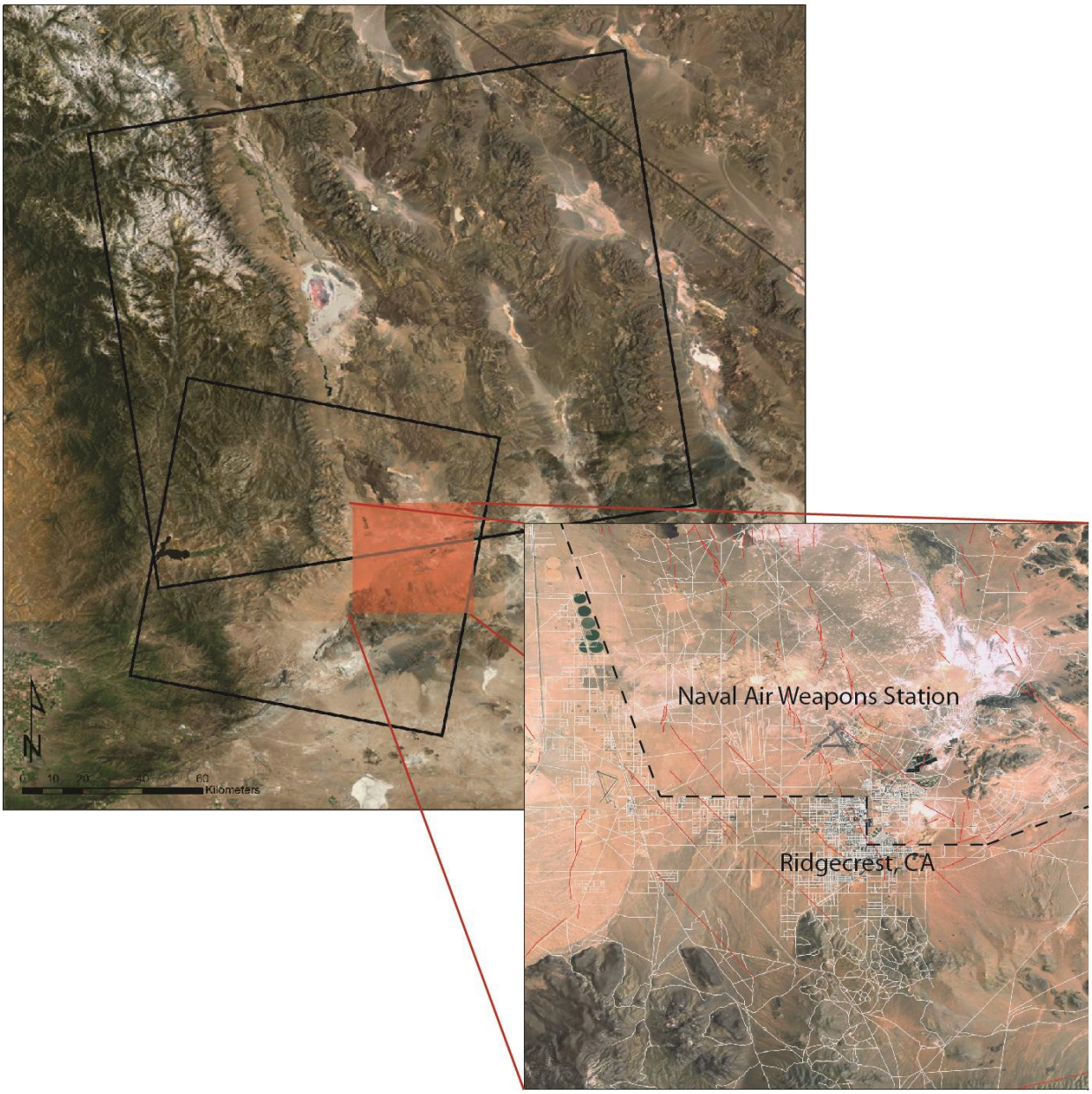

Figure 1. Map showing location of the radar images used in this study. The lower black box represents the aerial extent of the ERS-1, ERS-2 and Envisat scenes used in this study. The larger, upper, black box represents the extent of the Radarsat-2 scene used. The red box and detail image is the approximate extent of the study area figures presented below.

requirement, longer time periods were utilized when necessary. As the IWV sits at quite low elevation and is therefore relatively warm, snow did not preclude the use of winter images for this study. This allowed for 113 interferometric pairs to be attempted (92 were successful).

Two general classes of noise can appear in interferograms created using this processing method: incoherent and coherent noise. Incoherent noise manifests itself as random, speckled (incoherent) pixels while coherent noise manifests itself as a seemingly coherent signal that is inaccurate.

Incoherent noise typically results from:

- Snow cover
- Ground disturbance (common at active mine sites or areas undergoing land use change)
- Adverse vegetative conditions (i.e. agricultural areas or seasonal vegetation)
- Steep terrain
- Seasonal soil moisture changes (or shallow flooding)

With this particular study area, the impact of incoherent noise is automatically reduced due to the desert climate and landscape as well as the wide, flat valley floor of the Indian Wells Valley. However, incoherent noise is present around the margins of the valley where steep terrain exists, as well as near areas of ground surface disturbance related to recent land use change (more discussion on this later).

While sources of coherent noise (seemingly coherent signals in the interferogram that do not represent deformation) were minimized whenever possible, some still exist in the data presented in this report. The majority of these types of signals fall into two categories:

- Topographic Signals: As part of the InSAR processing algorithm, the effect of topography is removed from the final product through the use of a reference Digital Elevation Model (DEM). If the DEM contains inaccuracies (commonly resulting from anthropogenic alteration of topography, often near mine sites), a coherent, erroneous signal will be present in the final product. More commonly, slight errors in the orbital data (the precise location of the satellite during scene acquisition) can also lead to topographic artifacts in the scene. The use of smaller perpendicular baselines reduce the potential topographic signal that may remain in an interferogram as the potential parallax is minimized (larger parallax will accentuate any orbital inaccuracies). Topographic signal can be recognized in an interferogram where a colored fringe pattern exactly corresponds with increasing or decreasing elevation, the rate at which the fringe pattern changes corresponds with the slope of the terrain.
- Atmospheric Signals: While energy from the radar spectrum can easily travel through water vapor, small perturbations in phase can result from SAR arrival time delays resulting from the energy traveling through a heterogeneous turbulent or stratified (due to extreme topography) atmosphere. This can results in a “blotchy” appearance that does not correspond to any real deformation.

Ideally, interferometric pairs using unique scenes can be used to cover roughly the same time period. This allows one to identify which InSAR signals are recurring, and, therefore, represent actual deformation, and which result from the coherent noise listed above.

The initial product of InSAR processing is called a “wrapped interferogram.” A wrapped interferogram is created by subtracting the phase values in each pixel of the “slave” image (usually the later of the two images of interest) from those contained within the “master” image.

The result is an image where each pixel represents phase differences varying from 0 - 2π. These products are often colorized such that one color cycle, or “fringe”, represents one full 2π cycle. In the case of C-band radar such as ERS-1, ERS-2, Envisat and Radarsat-2, this corresponds to a 2.8 cm (1.1 in) magnitude of line of sight (LOS) change.

Next, an algorithm is utilized to create what is called an "unwrapped interferogram." In this step, the phase differences between neighboring pixels in the wrapped interferogram are evaluated on a pixel-by-pixel basis and differences are summed in radians. This can then be converted to an LOS change in any length unit of interest for a particular study. Another advantage of unwrapped interferograms is that multiple interferograms can be added to one another or "stacked" to evaluate deformation over time periods longer than what is covered by any individual interferogram. All of the results presented in this report are generated from unwrapped interferograms.

Post-processing of the InSAR results was conducted using the geospatial software ENVI 4.8 and ArcMap 10.0.

Table 1 lists the 92 interferograms generated for this study. This list does not include interferograms that failed during processing. Once the results were evaluated, the best semi- continuous (covering or nearly covering back-to-back time periods) interferograms for both the ERS (green) and Envisat (yellow) platforms were stacked, or added up to form one interferograms. This is done in order to better quantify surface deformation that occurred during the entire time span covered by each satellite platform. The interferograms chosen for stacking each exhibited the best coherence for the time period covered. The stacks also permitted an estimate of the total areal extent of the deformation that has occurred since 1992. The two stacks are presented here in both raw and masked forms (with an additional stack presented later for the purposes of creating deformation contours). The raw forms include areas where there were not data in all five interferograms thus making the stack a bit "noisier". The masked stacks only contain data in pixels that were coherent in all five interferograms used in the stack. As a result, holes in the data are much larger, but one can feel comfortable that each pixel containing data is more accurate.

RESULTS

A total of seven cumulative, composite, stacked interferograms were created from the results listed in Table 1. There were three stacks each created from the ERS and Envisat results, and one created from the Radarsat-2 data. The time periods for each of the stacks are June 1, 1992 – November 30, 2000, November 24, 2005 – September 9, 2010, and March 16, 2012 – October 8, 2014 for the ERS, Envisat and Radarsat-2 data respectively. In the case of the ERS and Envisat stacks, the three stacks from each dataset were also averaged in an attempt to minimize noise that may have been present. All of these products are shown in Figures 2 - 10. In each stack, pixels that were not coherent in each individual interferogram were masked from the final stacks. This ensured that every coherent pixel in the stack contained data for the entire time period covered by the stack. The grey pixels show areas of incoherent noise that were masked during the unwrapping process, or were masked because they were not coherent in each interferogram comprising a given stack.

All of the interferograms presented are colorized such that each color cycle (fringe) represents 3 cm of LOS change. However, it is important to note that the look angle of SAR data is approximately 23° off of vertical for ERS and Envisat data, and approximately 31° for Radarsat- 2 data. This means that even though we are predominantly looking for what are assumed to be vertical ground motions related to subsidence, the non-vertical LOS direction can be somewhat sensitive (more so with the Radarsat-2 data

Table 1. List of the interferometric pairs processed for this study. Pairs used for the ERS, Envisat and Radarsat-2 Stacks are denoted in the right-hand column.

Scene 1 (YYYYMMDD)	Scene 2 (YYYYMMDD)	Satellite Platform	Utilized in Stack ?
19920601	19921123	ERS	ERS Stack 1, 2, 3
19920914	19931108	ERS	
19921123	19931108	ERS	ERS Stack 1, 2, 3
19931108	19950719	ERS	ERS Stack 3
19931108	19950927	ERS	ERS Stack 1, 2
19950719	19960704	ERS	ERS Stack 3
19950719	19970515	ERS	
19950719	19970724	ERS	
19950927	11951206	ERS	
19950927	19960110	ERS	
19950927	19960704	ERS	ERS Stack 1
19950927	19970515	ERS	ERS Stack 2
19950927	19970724	ERS	
19951101	19960424	ERS	
19960110	19970724	ERS	
19960704	19961017	ERS	
19960704	19970828	ERS	ERS Stack 1, 3
19960704	19980430	ERS	
19961017	19971002	ERS	
19961017	19980430	ERS	
19961017	19990624	ERS	
19970515	19980813	ERS	
19970515	19981126	ERS	
19970515	19990311	ERS	ERS Stack 2
19970828	19980430	ERS	ERS Stack 1, 3
19970828	19990624	ERS	
19971002	19980430	ERS	
19971002	19990624	ERS	
19971002	19991111	ERS	
19980430	19980813	ERS	ERS Stack 1, 3
19980430	19990624	ERS	
19980813	19990311	ERS	ERS Stack 1
19980813	20000504	ERS	
19980813	20000817	ERS	ERS Stack 3
19990311	20001026	ERS	
19990311	20001130	ERS	ERS Stack 1, 2
20000817	20001130	ERS	ERS Stack 3
20051124	20060622	Envisat	Envisat Stack 1, 3
20051124	20071129	Envisat	Envisat Stack 2
20060202	20061005	Envisat	
20060202	20080103	Envisat	
20060622	20070920	Envisat	
20060622	20071129	Envisat	Envisat Stack 1
20060622	20080207	Envisat	Envisat Stack 3

Table 1. List of the interferometric pairs processed for this study. Pairs used for the ERS, Envisat and Radarsat-2 Stacks are denoted in the right-hand column (Continued).

Scene 1 (YYYYMMDD)	Scene 2 (YYYYMMDD)	Satellite Platform	Utilized in Stack ?
20061005	20080103	Envisat	
20070920	20080207	Envisat	
20070920	20080417	Envisat	
20070920	20080904	Envisat	
20070920	20090611	Envisat	
20071129	20080417	Envisat	Envisat Stack 1
20071129	20080626	Envisat	Envisat Stack 2
20071129	20080731	Envisat	
20071129	20080904	Envisat	
20071129	20090611	Envisat	
20080103	20080313	Envisat	
20080207	20080626	Envisat	
20080207	20080731	Envisat	Envisat Stack 3
20080207	20080904	Envisat	
20080207	20090611	Envisat	
20080207	20100211	Envisat	
20080313	20090611	Envisat	
20080313	20091029	Envisat	
20080313	20100318	Envisat	
20080417	20090611	Envisat	Envisat Stack 1
20080417	20091203	Envisat	
20080417	20100211	Envisat	
20080626	20090611	Envisat	
20080626	20091203	Envisat	Envisat Stack 2
20080626	20100701	Envisat	
20080731	20091029	Envisat	Envisat Stack 3
20080731	20091203	Envisat	
20080731	20100701	Envisat	
20080904	20091203	Envisat	
20080904	20100211	Envisat	
20080904	20100701	Envisat	
20080904	20101014	Envisat	
20090611	20100211	Envisat	
20090611	20100909	Envisat	Envisat Stack 1
20091029	20100527	Envisat	
20091029	20100909	Envisat	Envisat Stack 3
20091203	20100527	Envisat	Envisat Stack 2
20091203	20100909	Envisat	
20100211	20101014	Envisat	
20100318	20100909	Envisat	
20100527	20100909	Envisat	Envisat Stack 2
20100701	20101014	Envisat	
20120316	20140517	Radarsat-2	Radarsat-2 Stack 1
20120316	20141008	Radarsat-2	Radarsat-2 Stack 1
20140517	20141008	Radarsat-2	

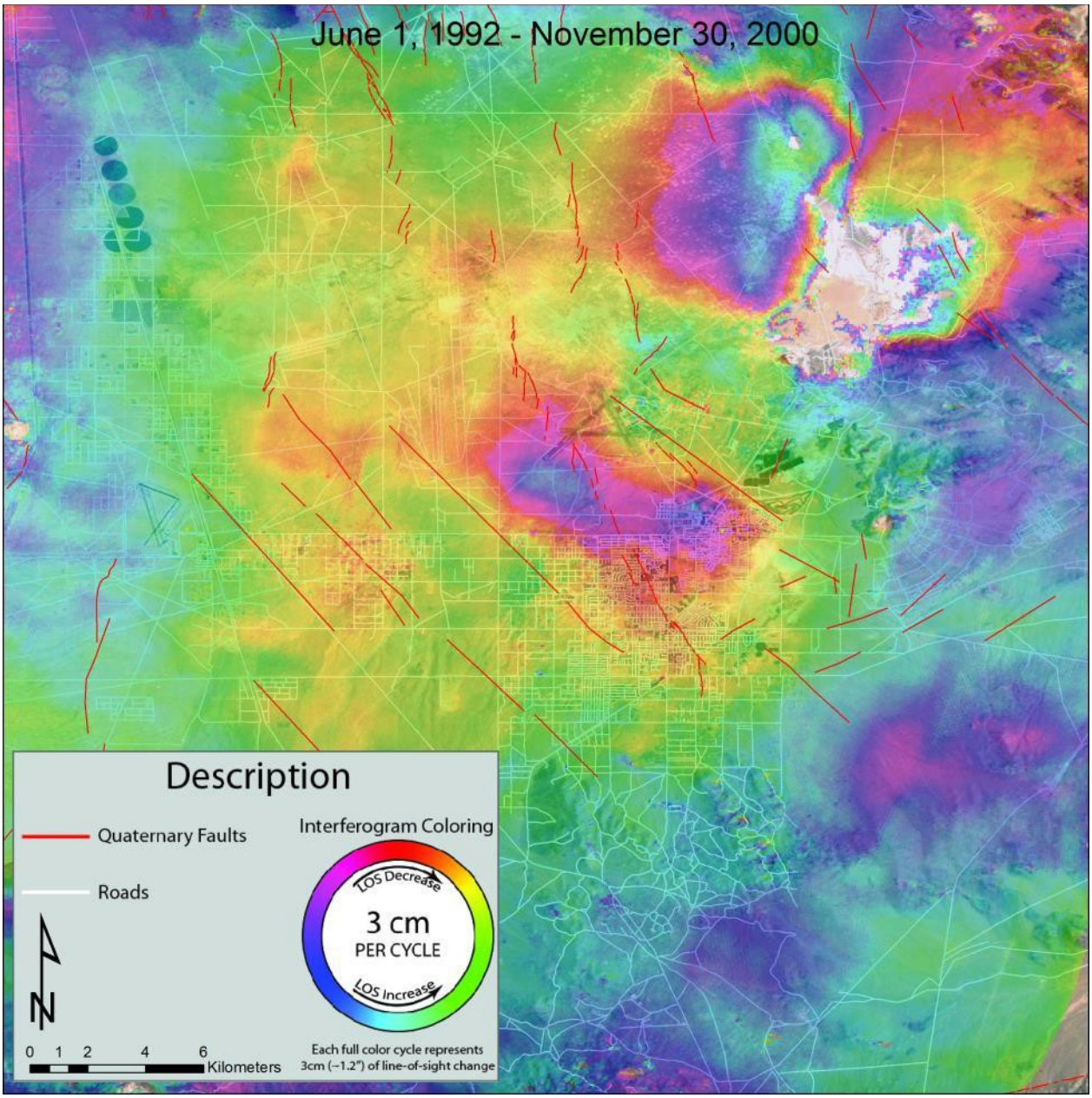

Figure 2 (ERS Stack 1). Cumulative, composite, stacked unwrapped ERS interferogram covering the time period of June 1, 1992 – November 30, 2000. Each full color cycle (fringe) represents 3 cm of LOS change. In addition to the subsidence features located in the central part of the IWV, note the deformation signal related to the 1995 Airport Lake earthquake sequence in the north eastern part of the figure. Fault data are from the USGS Quaternary Fault and Fold database (http://earthquake.usgs.gov/hazards/qfaults/). Road data downloaded from the USGS National Map (http://nationalmap.gov). Base imagery provided by ESRI ArcGIS online (accessed January 20, 2015).

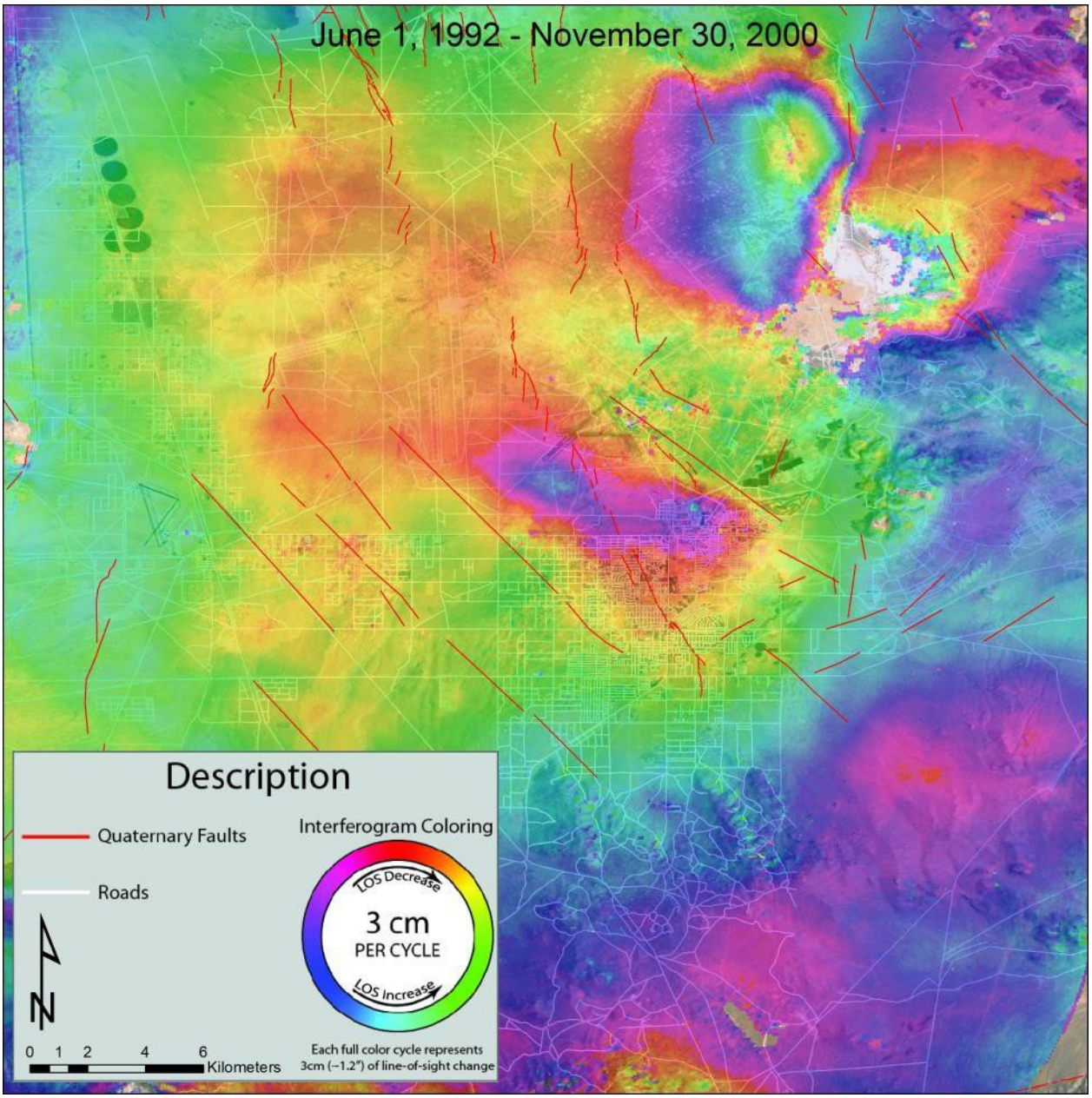

Figure 3 (ERS Stack 2). Cumulative, composite, stacked unwrapped ERS interferogram covering the time period of June 1, 1992 – November 30, 2000. Each full color cycle (fringe) represents 3 cm of LOS change. In addition to the subsidence features located in the central part of the IWV, note the deformation signal related to the 1995 Airport Lake earthquake sequence in the north eastern part of the figure. Fault data are from the USGS Quaternary Fault and Fold database (http://earthquake.usgs.gov/hazards/qfaults/). Road data downloaded from the USGS National Map (http://nationalmap.gov). Base imagery provided by ESRI ArcGIS online (accessed January 20, 2015).

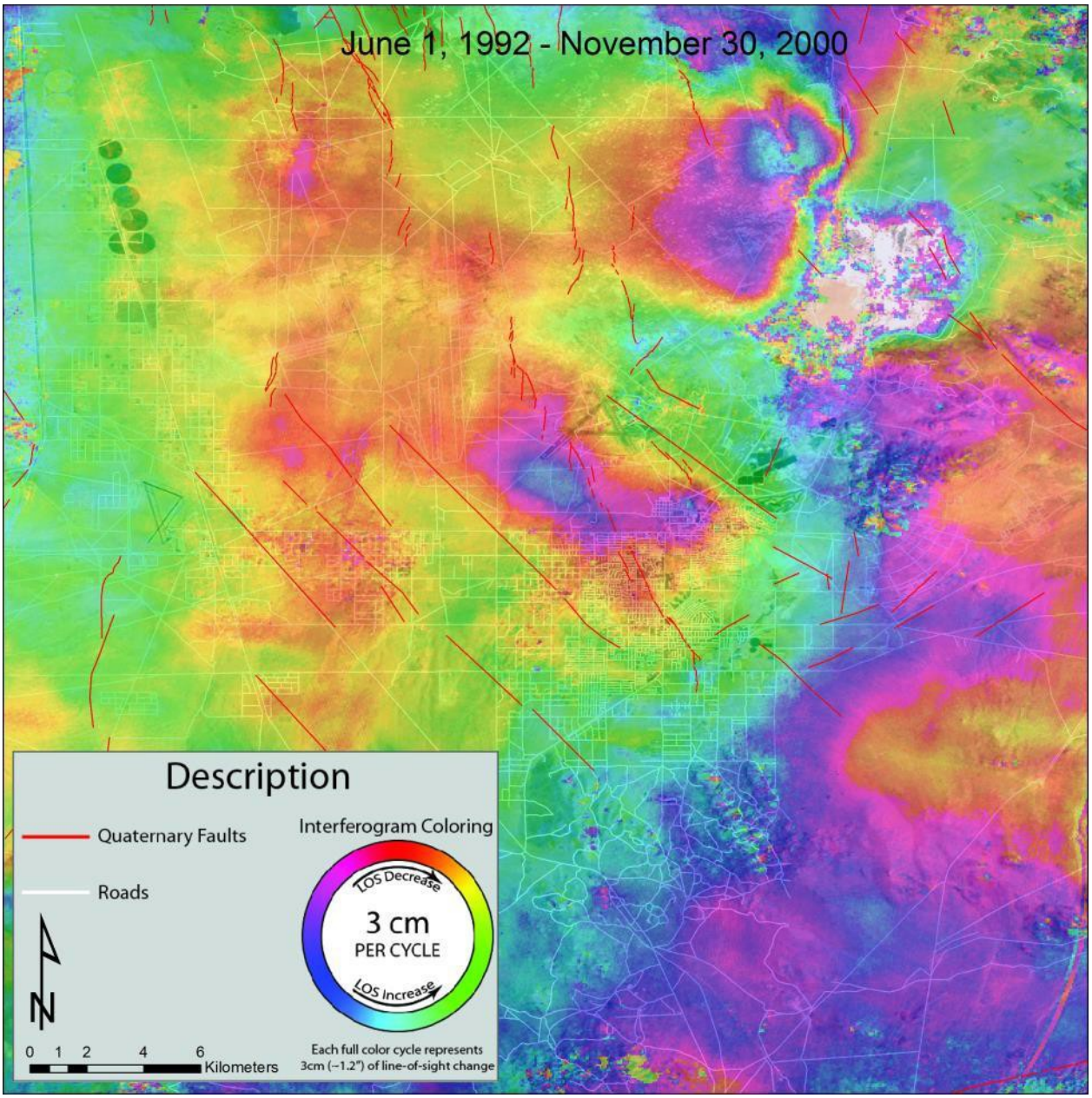

Figure 4 (ERS Stack 3). Cumulative, composite, stacked unwrapped ERS interferogram covering the time period of June 1, 1992 – November 30, 2000. Each full color cycle (fringe) represents 3 cm of LOS change. In addition to the subsidence features located in the central part of the IWV, note the deformation signal related to the 1995 Airport Lake earthquake sequence in the north eastern part of the figure. Fault data are from the USGS Quaternary Fault and Fold database (http://earthquake.usgs.gov/hazards/qfaults/). Road data downloaded from the USGS National Map (http://nationalmap.gov). Base imagery provided by ESRI ArcGIS online (accessed January 20, 2015).

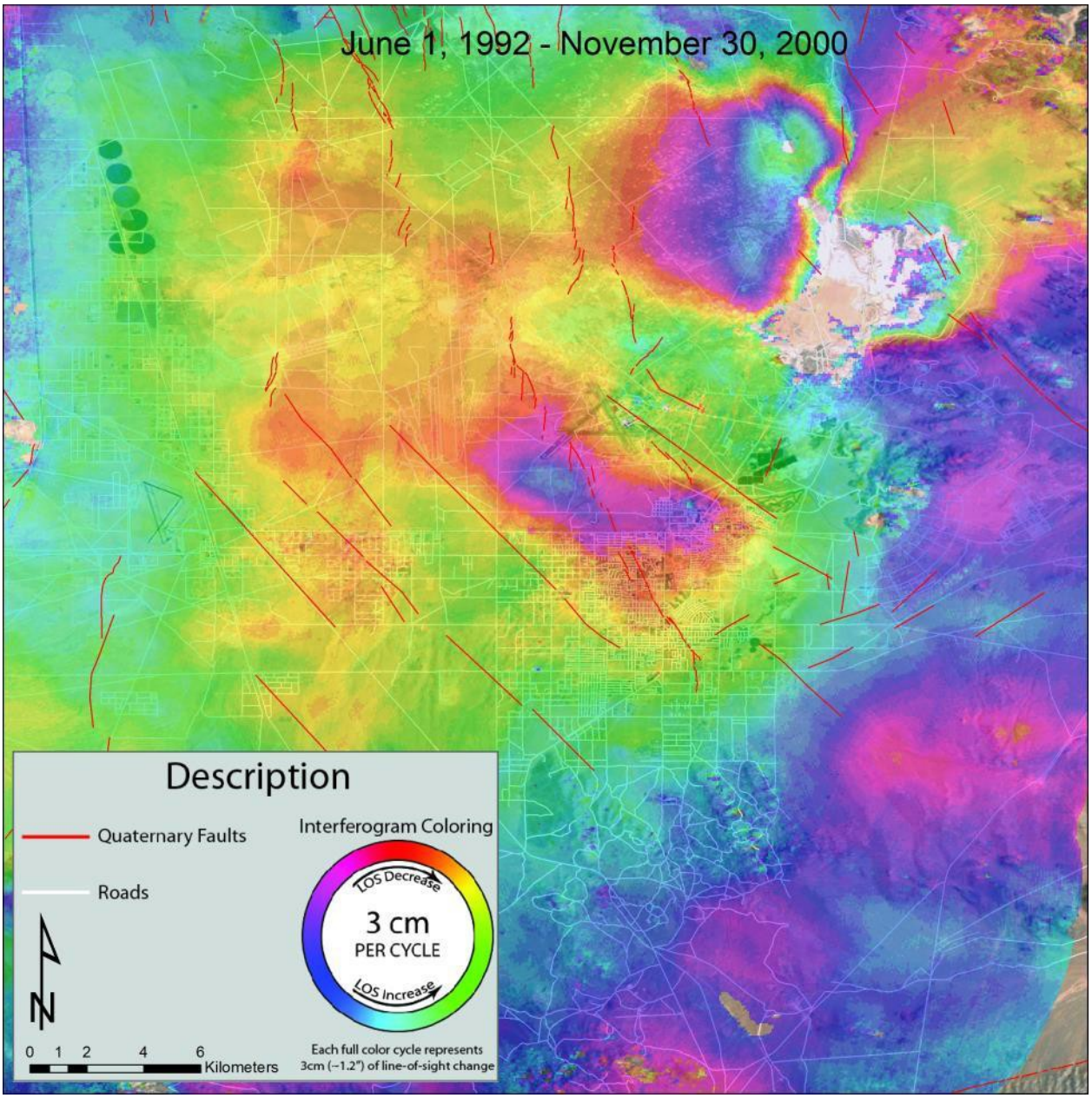

Figure 5 (ERS Averaged Stack). Averaged cumulative, composite, stacked unwrapped ERS interferogram covering the time period of June 1, 1992 – November 30, 2000. This stack is an average of figures 2 – 4. Each full color cycle (fringe) represents 3 cm of LOS change. In addition to the subsidence features located in the central part of the IWV, note the deformation signal related to the 1995 Airport Lake earthquake sequence in the north eastern part of the figure. Fault data are from the USGS Quaternary Fault and Fold database (http://earthquake.usgs.gov/hazards/qfaults/). Road data downloaded from the USGS National Map (http://nationalmap.gov). Base imagery provided by ESRI ArcGIS online (accessed January 20, 2015).

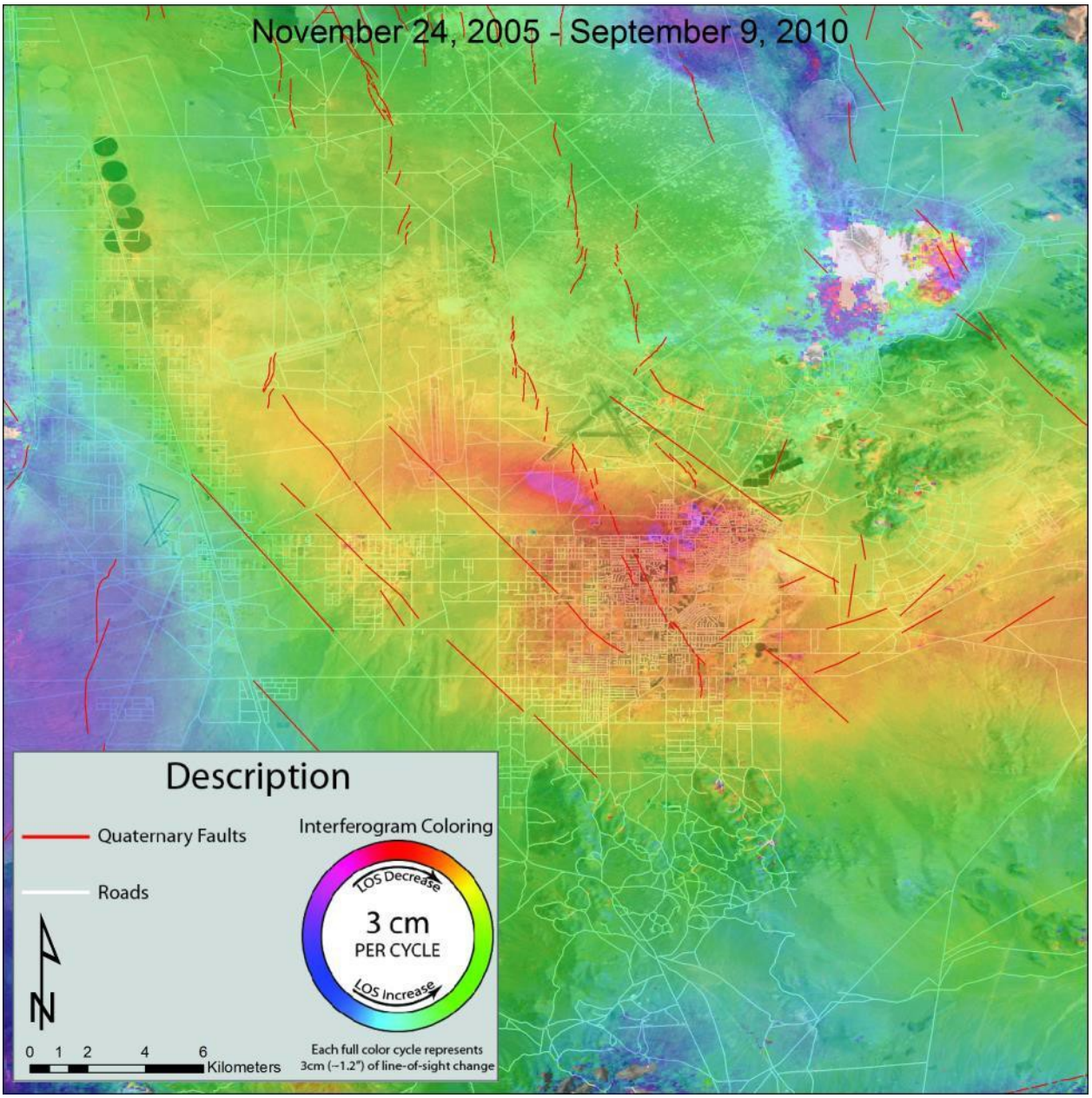

Figure 6 (Envisat Stack 1): Cumulative, composite, stacked unwrapped Envisat interferogram covering the time period of November 24, 2005 – September 9, 2010. Each full color cycle (fringe) represents 3 cm of LOS change. Fault data are from the USGS Quaternary Fault and Fold database (http://earthquake.usgs.gov/hazards/qfaults/). Road data downloaded from the USGS National Map (http://nationalmap.gov). Base imagery provided by ESRI ArcGIS online (accessed January 20, 2015).

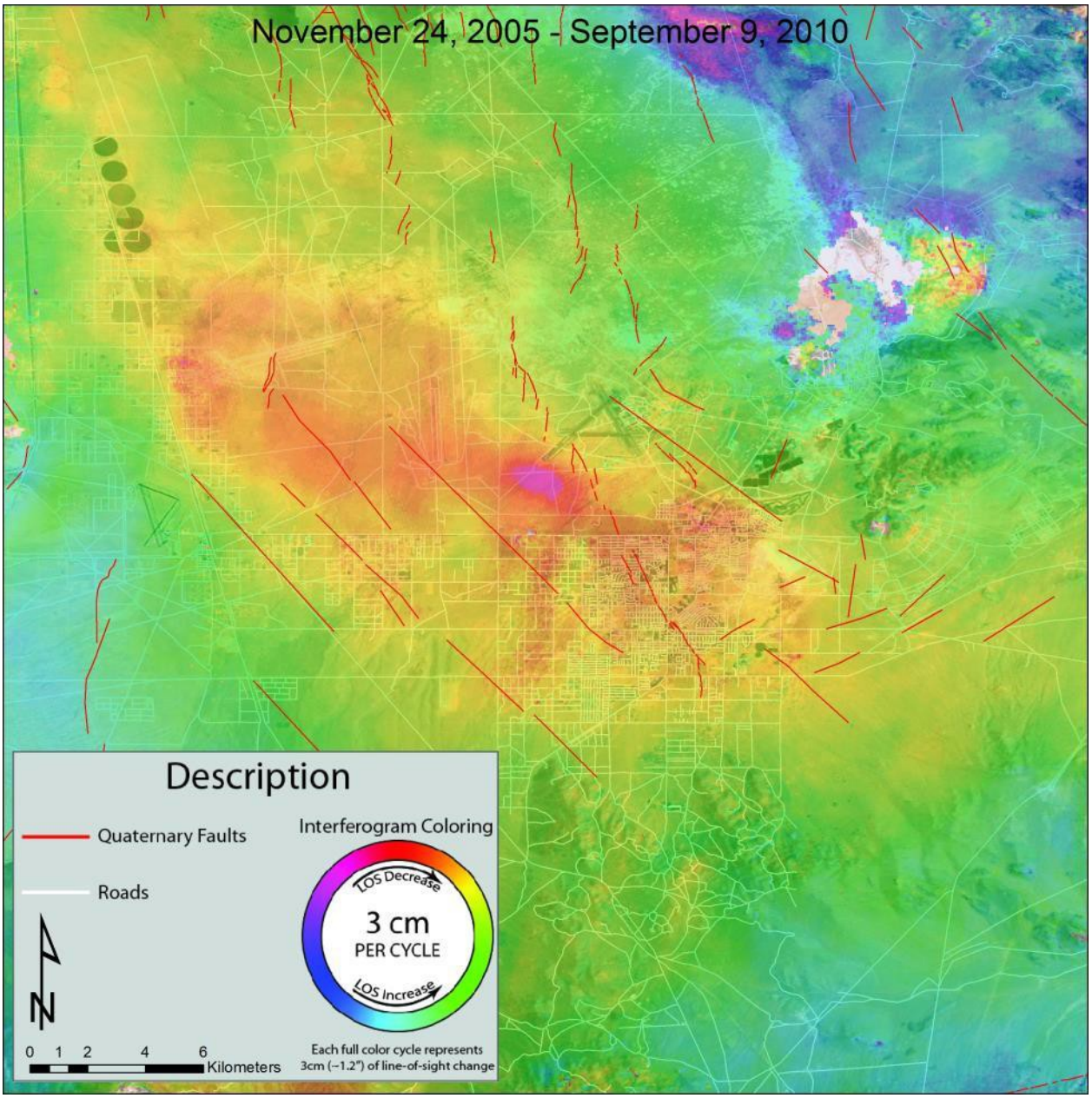

Figure 7 (Envisat Stack 2): Cumulative, composite, stacked unwrapped Envisat interferogram covering the time period of November 24, 2005 – September 9, 2010. Each full color cycle (fringe) represents 3 cm of LOS change. Fault data are from the USGS Quaternary Fault and Fold database (http://earthquake.usgs.gov/hazards/qfaults/). Road data downloaded from the USGS National Map (http://nationalmap.gov). Base imagery provided by ESRI ArcGIS online (accessed January 20, 2015).

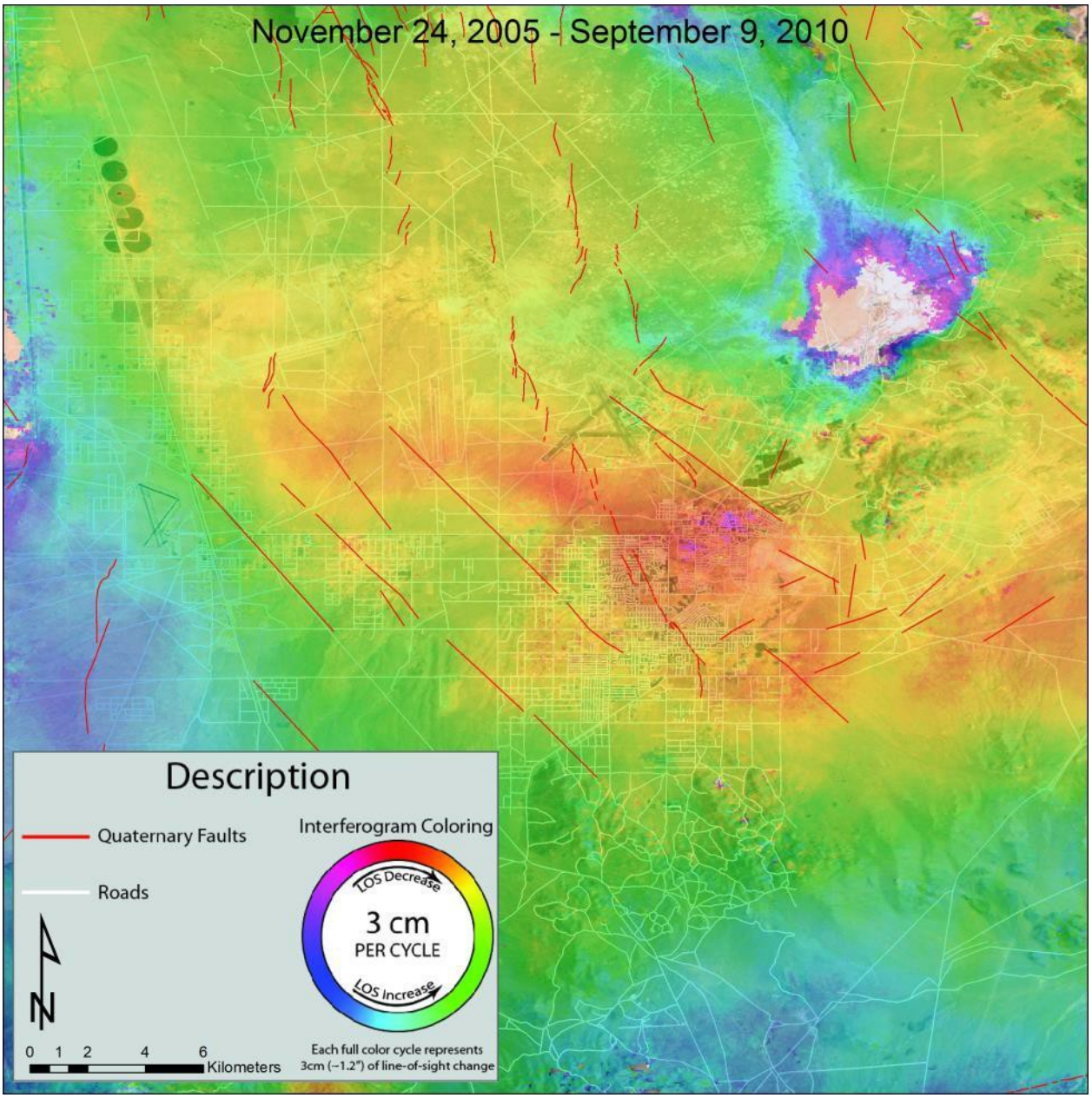

Figure 8 (Envisat Stack 3): Cumulative, composite, stacked unwrapped Envisat interferogram covering the time period of November 24, 2005 – September 9, 2010. Each full color cycle (fringe) represents 3 cm of LOS change. Fault data are from the USGS Quaternary Fault and Fold database (http://earthquake.usgs.gov/hazards/qfaults/). Road data downloaded from the USGS National Map (http://nationalmap.gov). Base imagery provided by ESRI ArcGIS online (accessed January 20, 2015).

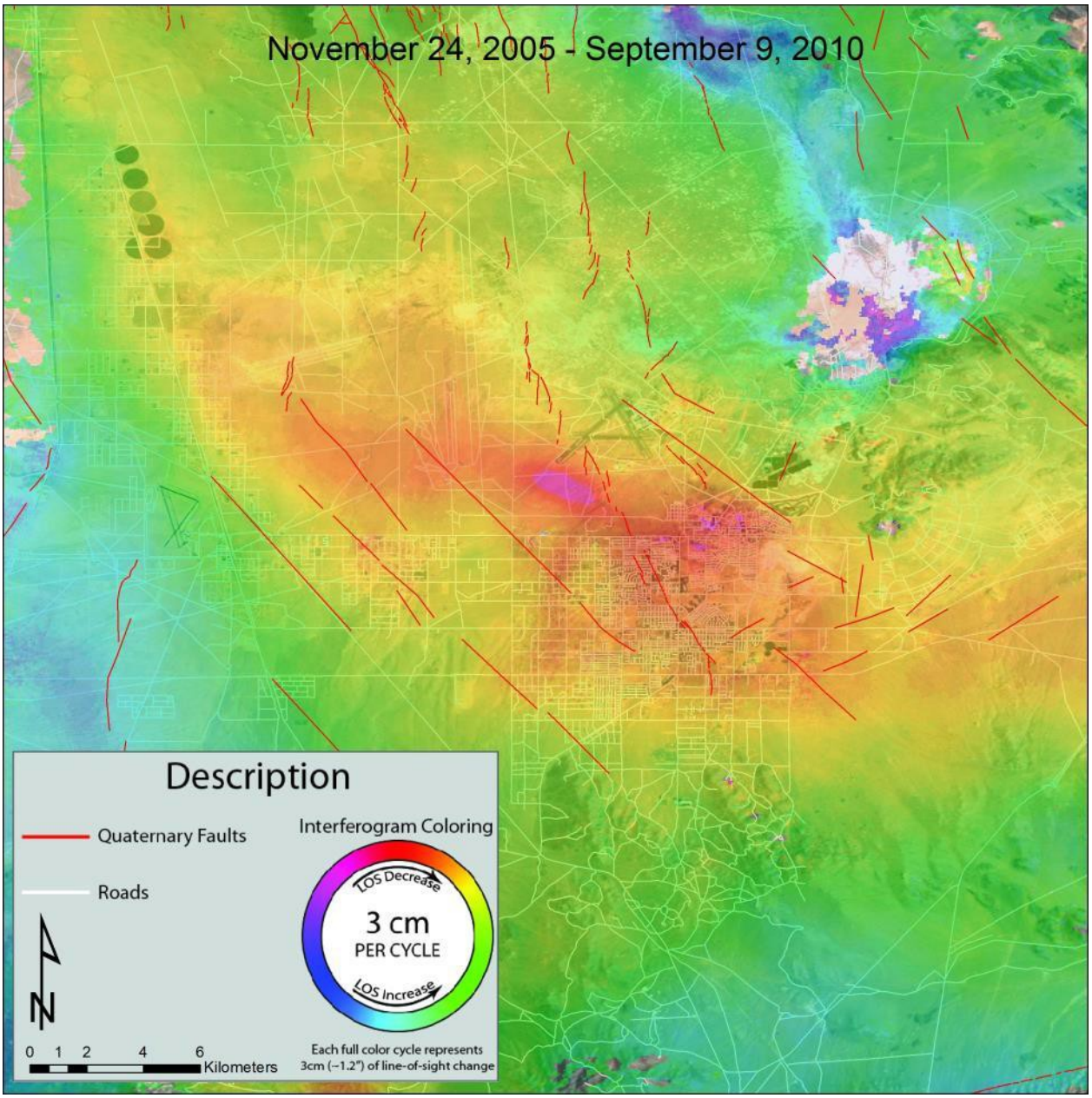

Figure 9 (Envisat Averaged Stack): Averaged cumulative, composite, stacked unwrapped ERS interferogram covering the time period of November 24, 2005 – September 9, 2010. This stack is an average of figures 6-8. Each full color cycle (fringe) represents 3 cm of LOS change. Fault data are from the USGS Quaternary Fault and Fold database (http://earthquake.usgs.gov/hazards/qfaults/). Road data downloaded from the USGS National Map (http://nationalmap.gov). Base imagery provided by ESRI ArcGIS online (accessed January 20, 2015).

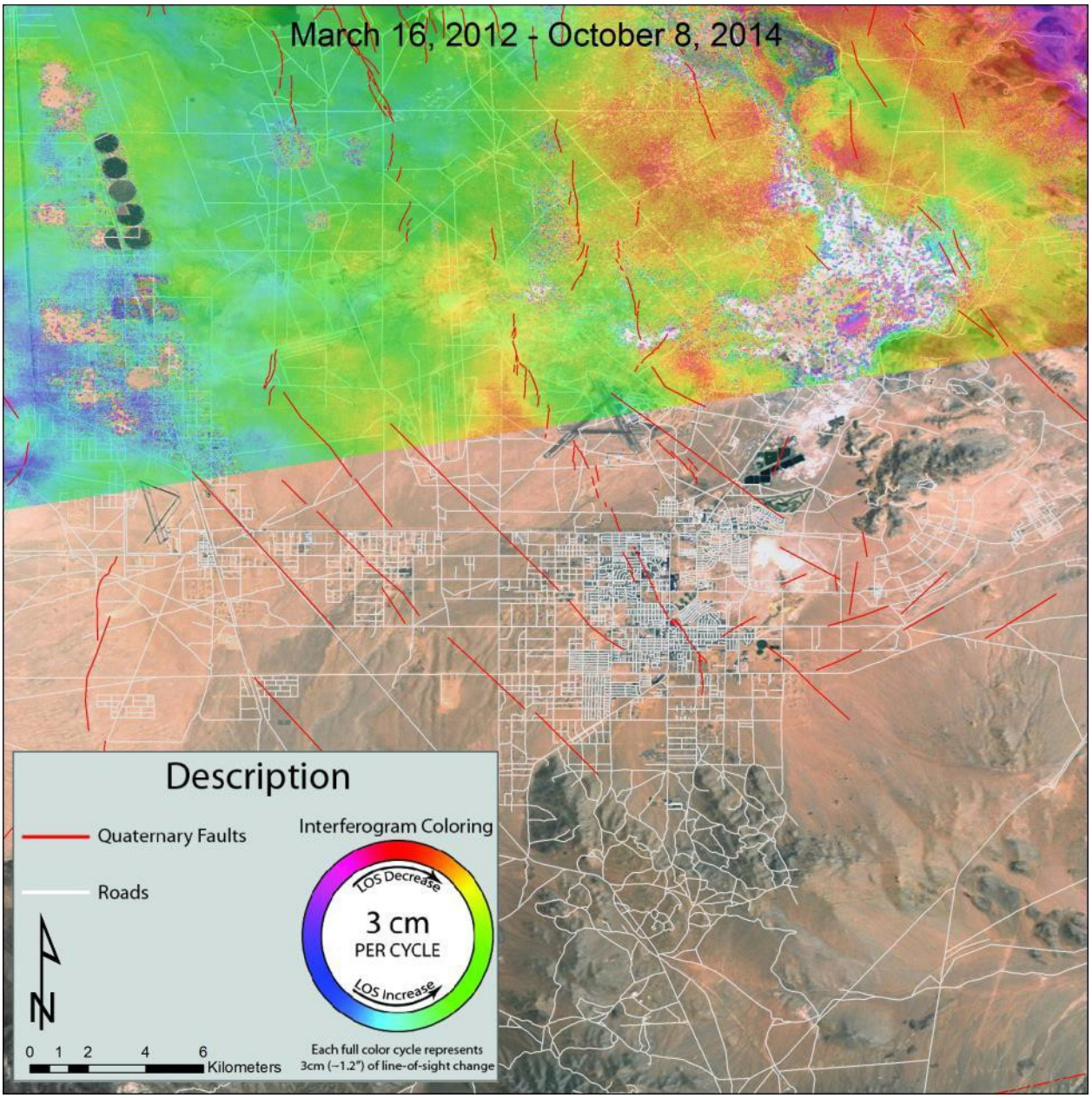

Figure 10 (Radarsat-2 Stack 1): Cumulative, composite, stacked unwrapped Radarsat-2 interferogram covering the time period of March 16, 2012 – October 8, 2014. Each full color cycle (fringe) represents 3 cm of LOS change. Fault data are from the USGS Quaternary Fault and Fold database (http://earthquake.usgs.gov/hazards/qfaults/). Road data downloaded from the USGS National Map (http://nationalmap.gov). Base imagery provided by ESRI ArcGIS online (accessed January 20, 2015).

since the look angle is closer to horizontal) to horizontal motions as well if they are present. Since we do not have multiple radar scenes from adjacent satellite tracks with look angles from multiple directions, it is not possible to resolve vertical vs. horizontal displacements in the results presented below. As such, all results will be discussed in terms of LOS displacements. LOS increases are inferred to be subsidence features, while LOS decreases represent uplift.

ANALYSIS OF INSAR RESULTS

Persistent (in time, location and magnitude) deformation signals are present in all of the ERS and Envisat stacked results. The fact that similar deformation signal shapes and magnitudes occur in stacks that have unique to semi-unique interferograms comprising the stacks provides a high confidence that the deformations signals are legitimate. There appears to be two main areas of subsidence (termed East and West Subsidence Bowls from hence forth, see Figure 11) in the east-central portions of the IWV, with

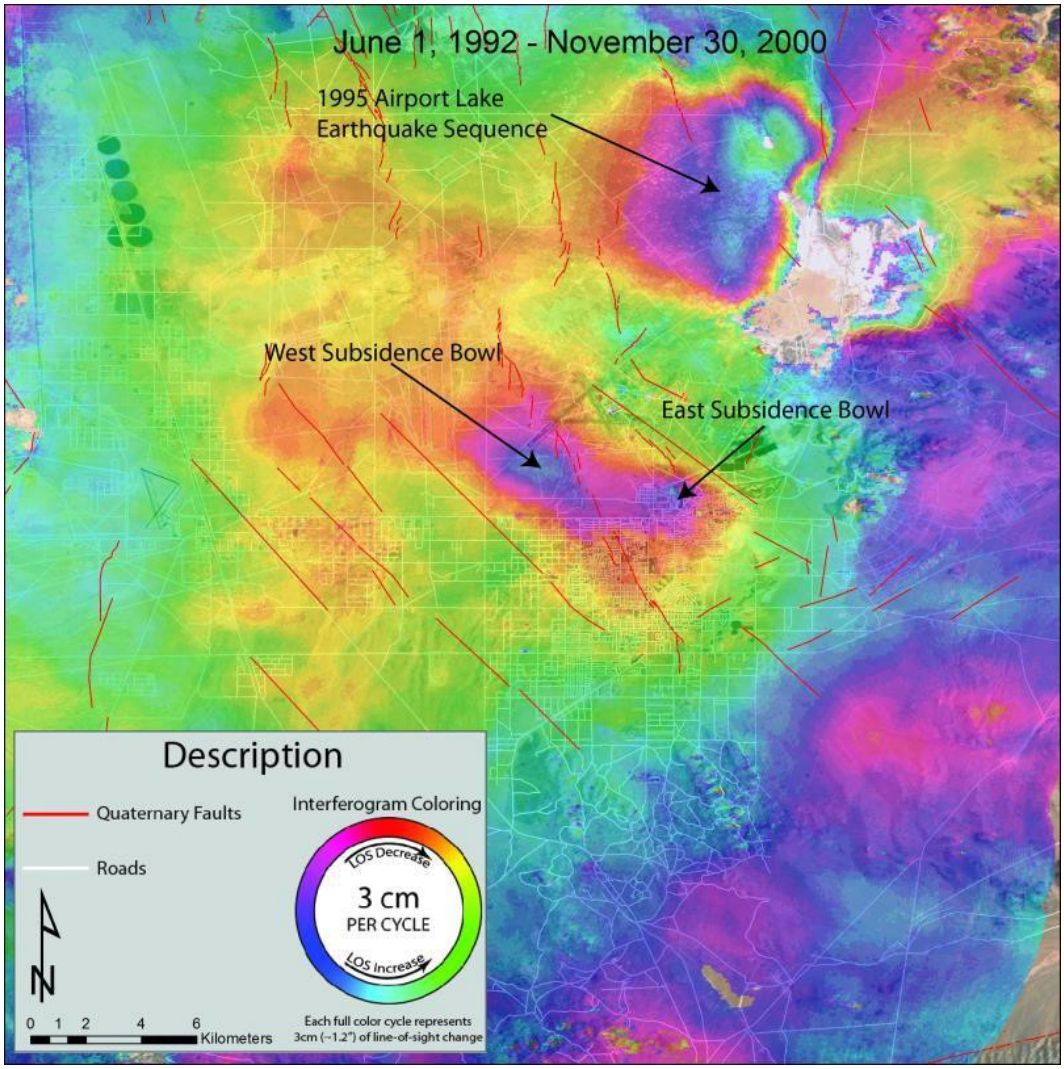

Figure 11. Annotated, average ERS stack showing the location of the West and East Subsidence Bowls, as well as the signal from the 1995 Airport Lake Earthquake Sequence.

smaller magnitudes of subsidence occurring throughout much of the remainder of the valley. The general shape of the main areas of subsidence appear to be somewhat controlled by known Quaternary faults in the valley. Maximum subsidence rates estimated from the averaged stacks from the ERS and Envisat data at both the East and West Subsidence Bowls are similar with time (Table 2). While the Radarsat-2 data do not cover the entire IWV, the data suggest that, at the very least, the West Subsidence Bowl was still deforming between early 2012 and late 2014 (see the yellow/orange colors just west of the NAWS airfield on Figure 10).

Table 2. Subsidence rates estimated from the Averaged ERS and Envisat Stacks as well as the only Radarsat-2 stack. (note while rates are listed as "subsidence rate", the deformation is occurring along the radar LOS)

Stack	West Bowl Max Deformation	West Bowl Subsidence Rate	East Bowl Max Deformation	East Bowl Subsidence Rate
ERS Average Stack	26 mm	3.1 mm/yr	28 mm	3.3 mm/yr
Envisat Average Stack	14 mm	2.9 mm/yr	13 mm	2.7 mm/yr
Radarsat-2 Stack 1	11 mm*	4.3 mm/yr*	No data	No data

*minimum estimates, entire deformation signal is not well defined due to lack of data coverage in the southern portions of the IWV.

In order to provide a better representation of the subsidence across the entire IWV, deformation profiles were constructed from each of the ERS and Envisat stacks (4 total for both the ERS and Envisat data, including the average). The locations of these profiles are shown in Figures 12a and 12b. Plots of these profiles are shown in Figures 13 and 14 (vertical scales are the same for both plots for consistency). Again, note the consistency of the spatial location and magnitudes of the deformation signals on the individual stacked interferograms.

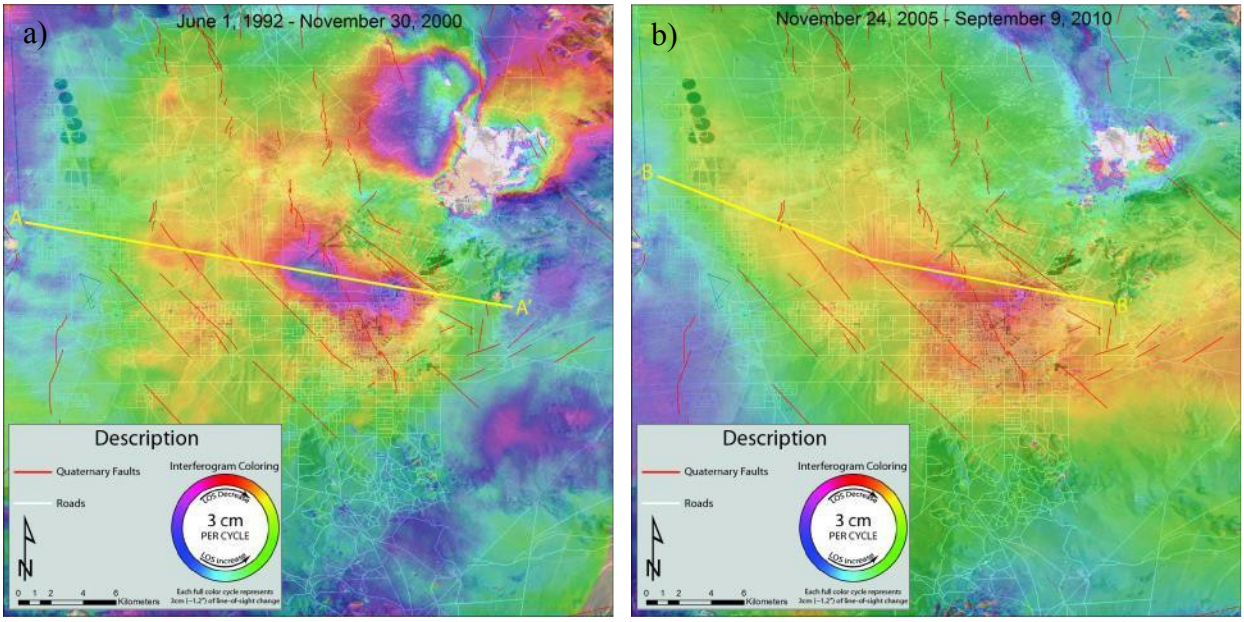

Figures 12a (left) and 12b (right): Sample stacked interferograms showing the profiles A – A' and B – B' for the ERS and Envisat stacked interferograms respectively. Deformation profiles are shown in Figures 13 and 14.

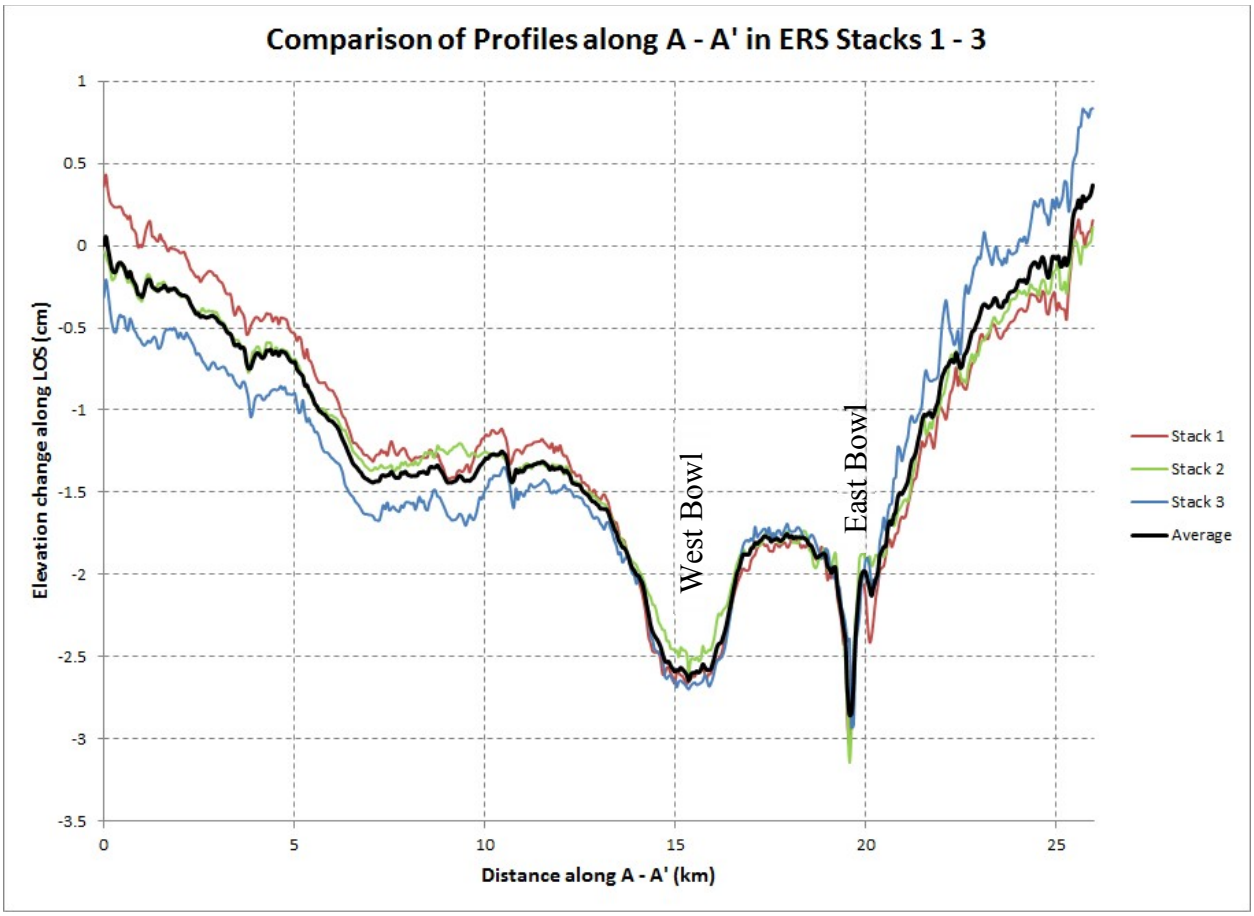

Figure 13. Deformation profiles along A-A' for the three ERS cumulative, composite stacks as well as the average of those three stacks.

The Radarsat-2 data were purchased and processed in order to assess the impact that new pumping related to pistachio orchards is having on the aquifer system in the western side of the IWV. Unfortunately, as mentioned above, the satellite could not be programmed to begin acquiring data until it had crossed roughly half (the southern half) of the IWV. However, there is data coverage over the location of the recently added (since 2012) pistachio orchards (Figure 15). Since the only data that were in the Radarsat-2 archive prior to the initiation of this study were from 2012, there is a 2+ year gap in data availability (as this study requested the May and October 2014 scenes be acquired). As such, there appears to be incoherent noise related to the tilling and re-grading of the land where the orchards were planted. This change in the nature of the ground surface has caused the pixels in the direct vicinity of the orchards to decorrelate. The signal around the areas of decorrelation actually suggest a hint of uplift in the general area of the pistachio orchards; however the magnitude of this uplift is very small and could be some type of coherent noise. (Ideally we would check this with other unique interferogram pairs, but the lack of available SAR data precludes this).

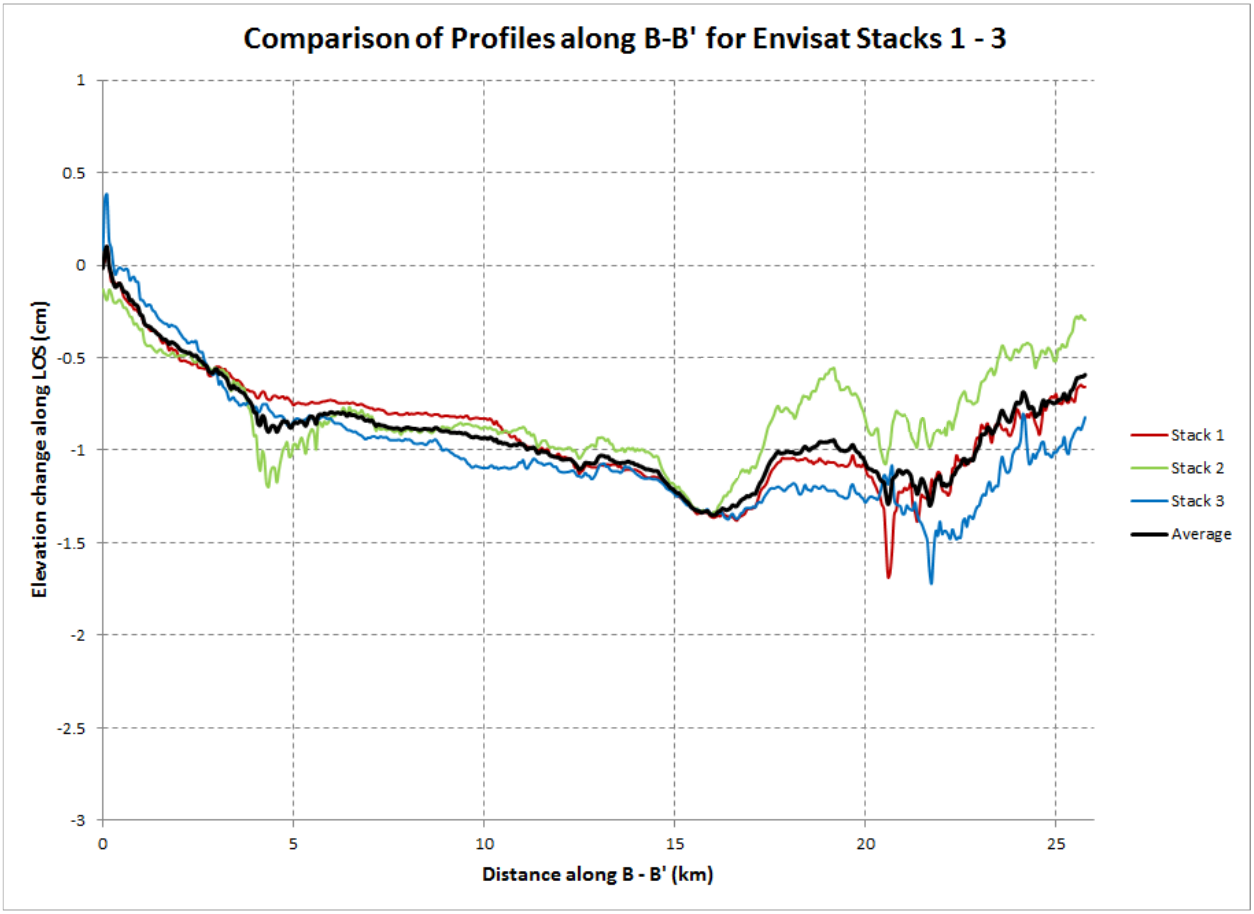

Figure 14. Deformation profiles along A-A' for the three ERS cumulative, composite stacks as well as the average of those three stacks.

CONCLUSIONS

It appears as though the ground subsidence related to aquifer-system response to groundwater pumping in the IWV has remained active since 1992. Subsidence rates are generally constant, although the Radarsat-2 data suggest that subsidence rates at the West Subsidence Bowl may be increasing (although further data would need to be processed to confirm this). It also appears that known Quaternary faults may play a role in the shape and distribution of the subsidence related to groundwater production. Initial investigation of potential subsidence in the vicinity of newly established pistachio orchards was somewhat inconclusive, but should be monitored in the future.

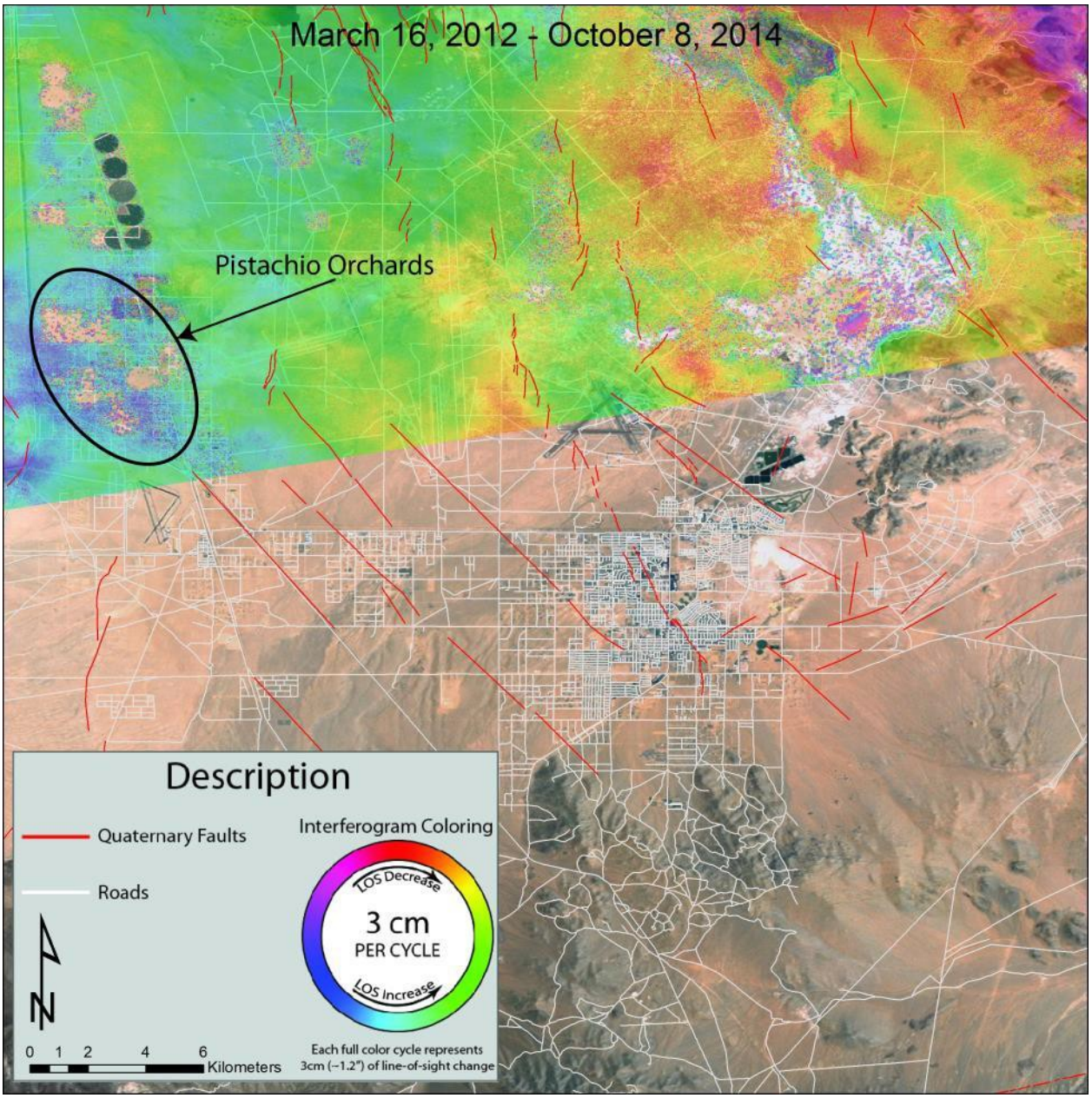

Figure 15. Radarsat-2 Stack with the general vicinity of the new (since 2012) pistachio orchards shown. Note the areas of incoherent noise related to ground surface disturbance from the planting of the pistachio trees.

REFERENCES

Amelung, F., Galloway, D. L., Bell, J. W., Zebker, H. A., and Laczniak, R. J., 1999, Sensing the ups and downs of Las Vegas: InSAR reveals structural control of land subsidence and aquifer- system deformation, Geology, v. 27, no. 6, p. 483 – 486.

Buckley, S. M., 2000, Radar interferometry measurement of urban land subsidence, University of Texas at Austin, Ph. D., dissertation, 229 p.

Katzenstein, K. W., 2013, InSAR analysis of ground surface deformation in Cedar Valley, Iron County, Utah, Utah Geological Survey Miscellaneous Publication 13-5, 44 pages.

This page intentionally left blank.

INITIAL DISTRIBUTION

6 Naval Air Weapons Station, China Lake, CA
  CDR B. Longbottom (3)
  CAPT R. Wiley (3)
5 Naval Facilities Engineering Command–Southwest, China Lake, CA
  S. Bork (2)
  A. Sabin (3)
2 Naval Facilities Engineering Command–Southwest, San Diego, CA (L. Sinfield)
5 Navy Region Southwest, San Diego, CA
  S. Chung (2)
  M. Faryan (3)
1 Defense Technical Information Center, Fort Belvoir, VA
4 Desert Research Institute, Las Vegas, NV (J. Chapman)
4 Desert Research Institute, Reno, NV (G. Pohll)

ON-SITE DISTRIBUTION

4 Code 4G0000D (archive and file copies)
44 Code 52000MD, M. Boggs